

NON-EQUILIBRIUM CHEMISTRY AND COOLING IN SIMULATIONS OF GALAXY FORMATION

PROEFSCHRIFT

ter verkrijging van
de graad van Doctor aan de Universiteit Leiden,
op gezag van de Rector Magnificus Prof. mr. C. J. J. M. Stolker,
volgens besluit van het College voor Promoties
te verdedigen op dinsdag 8 december 2015
klokke 11.15 uur

door
Alexander J. Richings
geboren te Huntingdon, Verenigd Koninkrijk
in 1988

Promotiecommissie

Promotor: Prof. dr. J. Schaye

Overige leden: Prof. dr. E. F. van Dishoeck
Dr. C. L. Dobbs (University of Exeter)
Dr. S. C. O. Glover (University of Heidelberg)
Prof. dr. H. J. A. Röttgering
Prof. dr. A. G. G. M. Tielens

Cover: Image showing the gas distribution in a simulation of an isolated disc galaxy, viewing the disc of the galaxy face-on. This is taken from simulation 'low-ISRF', presented in Chapter 4 of this thesis.

To Grandpa

TABLE OF CONTENTS

1	INTRODUCTION	1
1.1	Galaxies: An historical overview	2
1.2	A modern picture of galaxy formation	3
1.3	The role of chemistry in galaxy formation	5
1.3.1	Gas cooling rates	6
1.3.2	Observational diagnostics	6
1.4	Computational simulations	7
1.5	Thesis outline	9
	References	14
2	NON-EQUILIBRIUM CHEMISTRY AND COOLING IN THE DIFFUSE INTERSTEL- LAR MEDIUM - I. OPTICALLY THIN REGIME	19
2.1	Introduction	20
2.2	The chemical model	22
2.2.1	Numerical implementation	24
2.2.2	Photochemical reactions	25
2.2.3	Cosmic ray ionisation	27
2.2.4	Dust grain physics	28
2.2.5	CO model	30
2.3	Thermal processes	31
2.3.1	Metal line cooling	31
2.3.2	H ₂ rovibrational cooling	33
2.3.3	CO, H ₂ O and OH cooling	34
2.3.4	Photoheating	35
2.3.5	Photoelectric heating	35
2.4	Equilibrium chemistry and cooling in the ISM	36
2.4.1	Dominant coolants	37
2.4.2	Molecular abundances	40
2.4.3	Impact of cosmic rays on ionisation balance and cooling	43
2.5	Cooling in non-equilibrium interstellar gas	43
2.5.1	Cooling from $T = 10^4$ K	45
2.5.2	Cooling from $T = 10^6$ K	47
2.6	Conclusions	50
2.7	Appendix A: Dust temperature	52
2.8	Appendix B: Chemical reactions	55
	References	57
3	NON-EQUILIBRIUM CHEMISTRY AND COOLING IN THE DIFFUSE INTERSTEL- LAR MEDIUM - II. SHIELDED GAS	63
3.1	Introduction	64
3.2	Thermochemical Model	65
3.2.1	Chemistry	66
3.2.2	Thermal processes	67
3.3	Shielding processes	68

TABLE OF CONTENTS

3.3.1	Photoionisation	69
3.3.2	Photodissociation	72
3.3.3	Photoheating	75
3.4	Chemistry and cooling in shielded gas	76
3.4.1	Comparison with CLOUDY	77
3.4.2	Importance of turbulence for H ₂ self-shielding	81
3.4.3	Atomic to molecular transition in thermal and pressure equilibrium	82
3.5	Comparison with published approximations for H ₂ formation	86
3.5.1	Gnedin09 model	86
3.5.2	KMT model	88
3.5.3	Results	89
3.6	Conclusions	92
3.7	Appendix A: Shielding approximations	94
3.8	Appendix B: H ₂ self-shielding function	96
	References	98
4	THE EFFECTS OF METALLICITY, UV RADIATION AND NON-EQUILIBRIUM CHEMISTRY IN HIGH-RESOLUTION SIMULATIONS OF GALAXIES	103
4.1	Introduction	104
4.2	Subgrid Physics Models	106
4.2.1	Chemistry and radiative cooling	107
4.2.2	Star formation	109
4.2.3	Stellar feedback	110
4.2.4	Jeans limiter	111
4.3	Simulations	112
4.3.1	Initial conditions	112
4.3.2	Morphology and star formation	114
4.3.3	Outflows	120
4.3.4	Phase structure of the ISM	127
4.4	Observable Line Emission	134
4.4.1	CII fine-structure line emission	136
4.4.2	CO line emission	139
4.5	Conclusions	145
	References	148
5	CHEMICAL EVOLUTION OF GIANT MOLECULAR CLOUDS IN SIMULATIONS OF GALAXIES	153
5.1	Introduction	154
5.2	Simulations	156
5.2.1	Chemistry and subgrid models	157
5.2.2	Initial conditions	158
5.3	Analysis methods	160
5.3.1	Clump finding algorithm	160
5.3.2	Cloud mass evolution	163
5.3.3	CO emission maps	167

5.4	Cloud scaling relations	169
5.5	Chemical evolution	178
5.5.1	Molecular hydrogen	178
5.5.2	Carbon monoxide	182
5.6	CO emission and the X_{CO} factor	184
5.7	Conclusions	189
5.8	Appendix A: Effects of the pressure floor	193
	References	200
6	THESIS SUMMARY AND FUTURE OUTLOOK	203
6.1	This thesis	204
6.2	Future outlook	207
	Nederlandse Samenvatting	211
	Publications	219
	Curriculum Vitae	221
	Acknowledgments	223

INTRODUCTION

While galaxies such as Andromeda (M31) have been observed for many hundreds of years, it is only in the last century or so that it has been established that these are extragalactic systems of stars and gas, external to our own galaxy. In recent decades, many advances have been made in understanding how these galaxies form and evolve. Numerical simulations, using supercomputers with hundreds or thousands of CPUs, are an important tool for understanding galaxy formation, as they enable us to model the wide range of scales (both spatial and temporal) and the wide range of physical processes that are involved. With the ongoing development of more powerful supercomputers, we can push these simulations to cover a wider range of scales, and to include more detailed, and more computationally demanding, physical models.

On the smallest scales, chemical processes involve reactions between ions and molecules. These chemical processes on atomic scales influence galaxy formation in two ways: firstly, by determining the rate at which gas can cool radiatively, and secondly, by determining the observable line emission from individual chemical species. Existing simulations of galaxy formation typically assume chemical equilibrium. However, this may not be valid if the physical conditions of the gas are evolving rapidly, on time-scales shorter than the chemical time-scales. In this thesis, we develop a chemical model to follow the non-equilibrium evolution of ion and molecule abundances, which we incorporate into hydrodynamic simulations of galaxies. We then use this model to explore how non-equilibrium chemistry affects galaxy formation, both dynamically, via its impact on gas cooling rates, and observationally, via its impact on emission line diagnostics.

1.1 Galaxies: An historical overview

Galaxies are gravitationally bound systems made up of stars, gas and dark matter. Our own galaxy, the Milky Way, can be seen by the naked eye on a clear night as a band of diffuse light extending across the sky. This band of light was recognised by the Ancient Greeks (*'kyklos galaktikos'*, from which we get the word 'galaxy'), and the Romans (*'Via Lactea'*). However, the existence of other such systems beyond the Milky Way has only been firmly established within the last century or so.

The idea that nebulae, which appear as diffuse clouds in the night sky, may be stellar systems similar to the Milky Way, but at very large distances, was first proposed by Wright (1750). This 'island universes' theory was taken up and extended by Kant (1755). Early observations of some nebulae, for example by William Herschel, were able to resolve individual stars, which supported this theory that they are stellar systems like our own galaxy. Using a 72" telescope (the largest in the world at the time), William Parsons, the third Earl of Rosse, found spiral structures in M51 and other 'spiral nebulae' (Rosse 1850). This suggested that such spiral nebulae are rotating, which supported Kant's idea that island universes, along with the Milky Way, are flattened systems supported against gravity by rotation.

However, not all nebulae can be resolved into individual stars. Huggins & Miller (1864) used spectroscopic observations to demonstrate that nebulae could be divided into two distinct classes: those made up of gas, and those consisting of stars. There were also several other arguments against the island universes theory. For example, Proctor (1869) showed that nebulae are preferentially found away from the plane of the Milky Way, which, he argued, indicates a physical connection between the Milky Way and the nebular system.

Harlow Shapley's model of the Milky Way (Shapley 1918, 1919a,b) cast further doubt on the island universes theory. One of the earliest attempts at modelling the distribution of stars in the Milky Way was made by Sir William Herschel, who counted stars in different regions of the sky (Herschel 1785). In the early twentieth century, Jacobus Kapteyn and his collaborators used photography to refine this approach, measuring the brightness of individual stars from photographic plates, and measuring their proper motions from observations taken years apart, and their line of sight velocities from spectroscopic observations. This ultimately led to the 'Kapteyn Universe' model of the Milky way (Kapteyn & van Rhijn 1920; Kapteyn 1922), which placed the Sun near the centre of an oblate spheroidal distribution of stars, a few kpc across. However, their approach of counting stars in different parts of the sky and measuring their brightness assumed that the stars are not obscured by intervening material, and thus any dimming of the stars' apparent brightness is due solely to their distance from the observer. In reality, we now know that the apparent position of the Sun at the centre of the Milky Way in the Kapteyn Universe model is an artifact of interstellar absorption, which prevents us from seeing stars on the far side of the Milky Way's disc. However, the importance of interstellar absorption was not fully appreciated until much later (Trumpler 1930). The Kapteyn Universe model therefore underestimated the true size of the Milky Way.

Harlow Shapley's model of the Milky Way was based on the distribution of

globular clusters. He found that they are evenly distributed either side of the Galactic plane, but are not evenly distributed in galactic longitude, with more globular clusters concentrated towards Sagittarius. He argued that, if these globular clusters are associated with the Milky Way system, the centre of the globular cluster distribution should coincide with the Galactic centre. Hence, unlike in the Kapteyn Universe, Shapley's model did not place the Sun at the centre of the Milky Way. By measuring the apparent brightness of Cepheid variable stars in globular clusters, and using the known relation between the period and luminosity of Cepheids (Leavitt & Pickering 1912), he was able to measure the distances to the globular clusters, and hence deduced that the Sun is ≈ 15 kpc from the Galactic centre. He also determined that the size of the Milky Way system is ≈ 100 kpc, much larger than previously thought. If spiral nebulae were stellar systems similar to the Milky Way, as proposed by the island universes theory, then, given their apparent sizes on the sky, this would require that they are much farther away than previously thought. Such huge distances were inconceivable at the time, which led many (including Shapley) to doubt the island universes theory.

The arguments for and against culminated in the 'Great Debate' in April 1920. The debate actually consisted of two lectures, one by Harlow Shapley, who argued against the theory, and the other by Heber Curtis, who presented the arguments in favour (Shapley & Curtis 1921). However, the question was only settled a few years later by Edwin Hubble. Using the 100" Mount Wilson telescope, he discovered Cepheid variable stars in the Andromeda Nebula. By measuring their apparent brightness, and using the period–luminosity relation of Cepheid stars (Leavitt & Pickering 1912), he deduced that the Andromeda Nebula is 285 kpc from the Sun (Hubble 1925). While modern estimates place it at ≈ 770 kpc (e.g. Karachentsev 2004), this was nevertheless enough to confirm that Andromeda is indeed an island universe outside of the Milky Way, and similar in size to our own galaxy. Hence the existence of galactic systems beyond the Milky Way was established.

1.2 A modern picture of galaxy formation

The basic picture that we have of how galaxies form was originally proposed by White & Rees (1978). The main stages in this process are illustrated in Fig. 1.1. In this model, most of the mass in the Universe is in non-gaseous 'dark matter', which dominates the large-scale structure of the Universe. This dark matter component is dissipationless, meaning that it only interacts via gravity, and so the distribution of this dissipationless matter on large scales arises from scale-free 'hierarchical clustering', driven by gravity alone (e.g. Press & Schechter 1974). However, gas is dissipative, and can cool radiatively (e.g. Rees & Ostriker 1977; Silk 1977). As the gas cools, it falls to the centre of the gravitational potentials of the dark matter haloes that formed via gravitational clustering (stages 1 and 2 in Fig. 1.1). Additionally, the gas will have angular momentum, due to tidal torques, so, as it collapses to the centre of the halo, it will rotate faster and form a galactic disc (Fall & Efstathiou 1980; stage 3). As the gas continues to cool, it will fragment on the

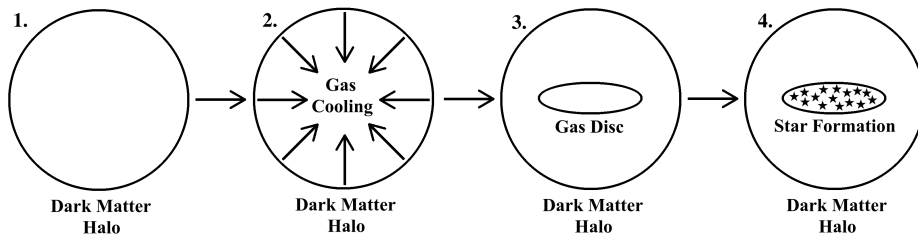


Figure 1.1: Diagram showing the main stages in galaxy formation.

Jeans scale, which is smaller in colder gas (Jeans 1902), thus forming molecular clouds and ultimately stars (stage 4).

This simple picture explains how gas can come together and form collections of stars that we see as galaxies, and it explains the large-scale distribution of galaxies, such as their arrangement in a ‘Cosmic Web’ (Bond et al. 1996; Erdođdu et al. 2004). However, there are many additional baryonic processes that complicate this picture, and which prove to be crucial for understanding the detailed properties of galaxy populations.

Firstly, in the above theory of galaxy formation, as gas falls into the gravitational potential of a dark halo, it is shock-heated to the virial temperature of the halo. This is often called ‘hot mode accretion’ (e.g. Kereš et al. 2005). However, haloes below a critical mass of a few times $10^{11} M_{\odot}$ are unable to maintain a stable shock front at the virial radius (Birnboim & Dekel 2003). Thus, gas is able to fall onto low-mass haloes without being shock-heated. Additionally, if the gas is falling in as dense clumps or filaments, it is less likely to be shocked, because the cooling time is shorter in dense gas, which again prevents the formation of a stable shock front. Therefore, these dense clumps and filaments can penetrate the hot gaseous atmospheres of massive haloes (e.g. Dekel et al. 2009). These modes of accretion are generally termed ‘cold mode accretion’ (Kereš et al. 2005). These different modes of accretion affect how the galaxy, and ultimately star formation within the galaxy, is fuelled (Dekel & Birnboim 2006; Ocvirk et al. 2008; Kereš et al. 2009; van de Voort et al. 2011).

Secondly, there is a wealth of evidence that the Universe underwent an ‘epoch of reionisation’ at high redshift ($z \gtrsim 6$), where the intergalactic medium became ionised by UV radiation from star-forming galaxies and/or quasars (Becker et al. 2001; Fan et al. 2006; Komatsu et al. 2009; Bouwens et al. 2015; Planck Collaboration XIII 2015). After this reionisation epoch, galaxies were illuminated by a (redshift-dependent) background of ionising radiation from quasars and other galaxies (Haardt & Madau 2001; Faucher-Giguère et al. 2009). This radiation can heat the gas, which reduces the net cooling rate and thus inhibits the cooling of gas onto low-mass dark haloes (Efstathiou 1992). Additionally, the gravitational potential of low-mass haloes is too weak to hold onto gas that is heated by ionising radiation (Rees 1986). Hence there is a critical dark halo mass below which galaxy formation is strongly suppressed after the epoch of reionisation (Benítez-Llambay et al. 2015; Sawala et al. 2015).

Thirdly, as stars form in a galaxy, they inject energy and momentum into the surrounding gas, in the form of stellar winds, photoionisation heating, radiation pressure and supernovae (Dale et al. 2005; Krumholz & Matzner 2009; Hopkins et al. 2011; Dalla Vecchia & Schaye 2012; Geen et al. 2015; Rosdahl et al. 2015). These processes can disrupt the natal gas cloud, disrupting further star formation. They can also drive galactic-scale outflows of gas, which deplete the galaxy's gas reservoir, further inhibiting star formation, and which interact with the inflows of fresh gas, thereby inhibiting the accretion of new material needed to fuel star formation.

Another source of energetic feedback can come from Active Galactic Nuclei (AGN), which are powered by accreting Supermassive Black Holes (SMBHs). SMBHs are ubiquitous in the centres of massive galaxies (Kormendy & Richstone 1995; Ferrarese & Merritt 2000). As they accrete gas from the galaxy, some of the rest energy of this accreted material is released by the SMBH and can couple to the surrounding interstellar medium (ISM). This can drive powerful outflows (Chartas et al. 2002; Pounds et al. 2003; King 2010; Costa et al. 2015), and is a likely candidate for explaining how star formation in the most massive galaxies becomes quenched (Silk & Rees 1998; Di Matteo et al. 2003; Bower et al. 2006; Sijacki & Springel 2006; Fabian 2012; Gaspari et al. 2012).

The interplay between these various baryonic processes is highly complex, and modelling them all self-consistently is made more challenging by the wide range of scales that they cover, from atomic scales (e.g. radiative cooling) up to Mpc scales (e.g. accretion and shock heating of gas falling onto galaxy clusters). However, it has been shown that all of these processes are necessary in models of galaxy formation to reproduce observed populations of galaxies (Baugh 2006; Schaye et al. 2010; Vogelsberger et al. 2013; Crain et al. 2015).

1.3 The role of chemistry in galaxy formation

As discussed in the previous section, the physical processes that are involved in the formation of galaxies cover a tremendous range of scales. Of these, chemical processes occur on the smallest scales, as they deal with the reactions between individual atoms, ions and molecules. To model these processes, we can make use of chemical reaction networks (e.g. Le Petit et al. 2006; Glover et al. 2010; Ferland et al. 2013; McElroy et al. 2013). These networks contain information about the chemical reactions between different species, and their reaction rates. From these networks, we get the rate equations, which are a system of coupled differential equations that describe the rate of change of abundance of each species. By integrating the rate equations in time, we can follow the evolution of the chemical abundances.

In this section, we summarise why the chemistry of ions, atoms and molecules is important for modelling galaxy formation.

1.3.1 Gas cooling rates

We saw in section 1.2 that galaxy formation is sensitive to the cooling rate of gas, as this determines how the gas collapses to the centre of dark matter haloes, and how it ultimately fragments to form molecular clouds and stars. Radiative cooling of gas is driven by collisional excitation and collisional ionisation of ions and molecules in the gas, through collisions with other ions/molecules or free electrons. This excitation removes thermal energy from the gas, which is subsequently radiated away when the ion/molecule de-excites (assuming that the gas is optically thin to the emitted photon, so that the energy is not re-absorbed). In this way, gas is able to radiate away its thermal energy and hence cool.

The collisional excitation rate of an ion or molecule will depend on the energy level structure of that species and its cross-sectional area to collisions with a given species, along with the gas density and temperature. Thus different species (for example, different ionisation states of a given element, or different molecules) will radiate away energy at different rates. Therefore, to calculate the net cooling rate of gas, we need to know the chemical abundances and the physical conditions of the gas (i.e. the density, temperature, metallicity, radiation field etc.). In this way, chemistry affects the net cooling rate of gas, and hence the dynamics of galaxy formation.

1.3.2 Observational diagnostics

Observations of galaxies often focus on line emission from particular chemical species. For example, line emission from transitions between the rotational states of the CO molecule are often used to trace molecular gas (e.g. Solomon et al. 1987; Heyer et al. 2001; Bolatto et al. 2008; Leroy et al. 2009). While molecular hydrogen is the most abundant molecule, it is difficult to detect in emission at the low temperatures typical of molecular clouds (~ 10 K), because the lowest rotational transition of H_2 has an excitation energy of $E/k_B = 510$ K (Dabrowski 1984), so it is difficult to excite H_2 at low temperatures. The CO molecule is more easily excited at these low temperatures, and thus is more easily detected. The CO intensity is then converted to an H_2 column density using an assumed conversion factor, the X_{CO} factor (see Bolatto et al. 2013 for a recent review). Recently, such observations have suggested that the star formation rate of a galaxy correlates closely with its molecular gas content (Wong & Blitz 2002; Kennicutt et al. 2007; Bigiel et al. 2008), although the more fundamental correlation may be with the cold gas content (Schaye 2004; Krumholz et al. 2011; Glover & Clark 2012).

Fine structure line emission from metals in low ionisation states, such as CII and OI, are also important observational diagnostics. Note that, in astronomy, ‘metals’ refer to any elements other than hydrogen or helium. These low-ionisation species dominate the cooling rate in the neutral ISM. Therefore, by measuring line emission from these species, we can probe the total cooling rate in the neutral gas in a galaxy, and thus we can probe the cooling and heating processes and the physical conditions in the neutral ISM phases (Malhotra et al. 2001; Kennicutt et al. 2011; Croxall et al. 2012).

Line emission from higher ionisation states, such as OIII and NII, trace the ionised phases of the ISM. The line ratios of these species contain information about the source of ionisation in this gas. For example, if the gas is photoionised, the line ratios will depend on the shape of the UV spectrum. These diagnostics can thus be used to determine whether the main source of ionisation is from the UV radiation of young stars, as we would expect in a star-forming galaxy, or from a harder source of UV radiation, such as an AGN (Baldwin et al. 1981; Veilleux & Osterbrock 1987; Kauffmann et al. 2003; Kewley et al. 2013).

To make predictions for these observations from our models of galaxy formation, we need to compute the chemical abundances, and thus we need to understand the chemistry of the gas. We can then compare our predictions for these observable diagnostics with the observations to test our models. Additionally, by comparing the observations to the models, we can help interpret what is seen in the observations. For example, we can use such comparisons to deduce the physical conditions that are being traced by a particular emission line.

1.4 Computational simulations

A common approach to model the formation of galaxies is to use computational simulations. Due to the large range of scales, both spatial and temporal, that are involved in galaxy formation, such simulations typically require supercomputers with hundreds or thousands of CPUs.

The simplest type of simulation that we can run is an N-body simulation that follows only the dark matter component of the Universe (Davis et al. 1985; Springel et al. 2005; Boylan-Kolchin et al. 2009). Dark matter dominates the large-scale structure of the Universe, and it is relatively simple to model, as it only interacts via gravity. The formation and evolution of galaxies within the large-scale structure of the Universe can then be modelled on top of these simulations, assuming that the baryons do not influence the dark matter distribution. For example, we can populate the simulated dark matter haloes with galaxies using the (sub-)halo abundance matching technique (Frenk et al. 1988; Behroozi et al. 2013; Moster et al. 2013), in which we take a population of galaxies that follow an observed luminosity function and match them to simulated dark matter haloes by assuming a one-to-one correlation between halo mass and galaxy luminosity. Alternatively, we can model galaxies using a semi-analytic treatment (Kauffmann et al. 1999; Bower et al. 2006; Croton et al. 2006; Guo et al. 2011). This approach takes the merger histories of haloes from dark matter only simulations as input, and then uses a set of coupled equations that describe baryonic processes, such as cooling of gas onto the galaxy, star formation and outflows, to model the evolution of the galaxy.

The advantage of dark matter only simulations is that they are relatively fast, which allows us to simulate large volumes of the Universe at high resolution. However, they neglect the effects of baryonic processes on the dark matter distribution (Blumenthal et al. 1986; Gnedin et al. 2004; van Daalen et al. 2011; Sawala et al. 2013; Velliscig et al. 2014). To explicitly model baryonic processes,

and self-consistently include their impact on the dark matter distribution, we can use hydrodynamic simulations, which include the dark matter and baryonic components of the Universe. However, some baryonic processes, such as star formation and feedback from supernovae, occur on scales that are too small to be resolved. For these, we need to rely on subgrid models that describe how these processes influence the gas on scales that we do resolve.

Chemical processes in hydrodynamic simulations of galaxies are often treated by assuming that the gas is in chemical equilibrium, by which we mean that the abundances of individual ions and molecules have reached an equilibrium or steady state. For example, to compute the net cooling rate, these simulations typically make use of cooling tables, which tabulate the cooling rate as a function of gas density, temperature etc., for a given radiation field (e.g. Wiersma et al. 2009). This greatly reduces the computational cost, as the cooling rates are pre-computed, and thus we do not need to integrate the chemical rate equations throughout the simulation. However, the assumption of chemical equilibrium will not be valid if the physical conditions of the gas are evolving quickly, on time-scales shorter than the chemical time-scale. This may occur if the cooling time is short (Kafatos 1973; Sutherland & Dopita 1993; Gnat & Sternberg 2007; Oppenheimer & Schaye 2013a), if the UV radiation field is varying rapidly (Oppenheimer & Schaye 2013b), or in the presence of turbulence (Gray et al. 2015).

Additionally, pre-computed cooling tables often assume a uniform radiation field. To include a fluctuating radiation field, for example from the evolution of young stars, we could potentially require many frequency bins, each of which adds another dimension to the cooling tables, to fully capture the changing shape of the UV spectrum. This would make the tables unfeasibly large, although Gnedin & Hollon (2012) find that they can capture the shape of the spectrum with just three additional dimensions in the tables.

The treatment of chemical processes in large-scale galactic and cosmological simulations is often fairly simple. However, on smaller scales, much work has gone into modelling the chemical processes in individual molecular clouds and photodissociation regions (PDRs). These models are used to determine the chemical structure of clouds and where in the cloud certain transitions, such as the transition from atomic to molecular hydrogen, occur, and how they depend on physical properties, such as gas density and incident UV radiation.

Fig.1.2 illustrates the chemical structure of a typical one-dimensional PDR model. Nearby sources of UV radiation, such as massive stars, irradiate the cloud from the left in this diagram. Once the photons above 13.6 eV are absorbed, hydrogen is no longer photoionised, and it becomes neutral ($\text{HII} \rightarrow \text{HI}$), which marks the edge of the PDR. The Lyman-Werner radiation, which dissociates H_2 , is then shielded by dust and by self-shielding of H_2 , which allows the hydrogen to become molecular ($\text{HI} \rightarrow \text{H}_2$). Once the C I-ionising radiation is absorbed, the carbon becomes neutral ($\text{CI} \rightarrow \text{C I}$). Finally, the CO-dissociating radiation is shielded by dust, H_2 and CO, and the carbon forms CO ($\text{C I} \rightarrow \text{CO}$). If we extend the diagram to the right, i.e. to higher column densities, we would also find additional molecular transitions, as more complex molecules form.

Tielens & Hollenbach (1985) used one-dimensional PDR models to study how

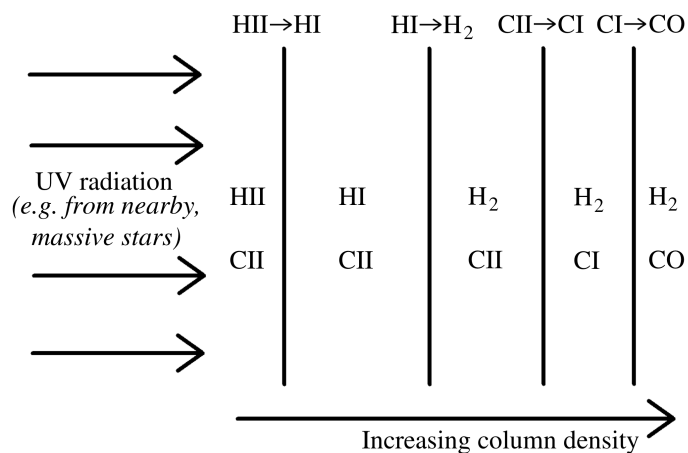


Figure 1.2: Diagram showing the basic chemical structure of a one-dimensional photodissociation region (PDR). The cloud is illuminated from the left of the diagram by UV radiation, e.g. from nearby, massive stars. The main hydrogen and carbon species in each layer are shown, and the vertical lines indicate the main chemical transitions within the cloud.

the chemical and temperature structure of a cloud depends on physical parameters such as gas density and incident UV radiation field. They computed the abundances of atoms and molecules in chemical equilibrium as a function of depth into the cloud using a chemical model of 41 species, including HI, H₂, CI, CII and CO. They also considered several heating and cooling processes, including photoelectric heating from dust grains and cooling from fine-structure metal lines and molecules, and they computed the equilibrium temperature as a function of depth. Using these models, they then determined the line and continuum emission, which can be compared with observed clouds.

van Dishoeck & Black (1988) focussed on the photodissociation and chemistry of CO in PDR models of diffuse clouds, including common CO isotopologues such as ¹³CO, C¹⁸O and ¹³C¹⁸O. Visser et al. (2009) presented a model for the chemistry and photodissociation of CO and its isotopologues, based on more recent spectroscopic data, and they applied their model to diffuse clouds, PDRs and circumstellar discs. Wolfire et al. (2010) used PDR models to investigate the mass fraction of molecular gas in clouds that is ‘CO-dark’, i.e. in the H₂-CI or CII layer, where molecular hydrogen is not traced by CO. Recently, Sternberg et al. (2014) presented a detailed study of the HI→H₂ transition in clouds, using both analytic theory and numerical PDR calculations.

1.5 Thesis outline

In this thesis we develop a chemical model to follow the evolution of ion and molecule abundances in non-equilibrium, and we incorporate this model into hydrodynamic simulations of galaxies. This allows us to relax the assumption of

chemical equilibrium that is often used in galaxy formation models. We then use these simulations to explore how non-equilibrium chemistry affects galaxy formation, both through the dynamical effects due to its impact on gas cooling rates, and through the effect it has on observational diagnostics.

For this study we are particularly interested in the transition from the warm ($\sim 10^4$ K) to the cold ($\sim 10^2$ K) ISM phase. The existence of distinct ISM phases arises due to thermal instabilities, which allow gas to cool rapidly to the cold phase. As discussed in section 1.4, these short cooling times may drive non-equilibrium effects in the chemistry. Additionally, as we will see in Chapters 4 and 5, molecules in the cold phase typically have relatively long formation time-scales, which can also drive non-equilibrium effects.

Large-scale cosmological simulations are unable to explicitly follow the multi-phase ISM, as they are unable to resolve the Jeans scale in the cold ISM phase. Therefore, in this thesis we apply our model to high-resolution simulations of isolated disc galaxies, in which we can resolve the warm-to-cold transition in the ISM. These Smoothed Particle Hydrodynamics (SPH) simulations have a particle mass of $750 M_{\odot}$, with a gravitational softening of 3.1 pc (see Chapter 4).

The remainder of this thesis is organised as follows:

Chapter 2: Non-equilibrium chemistry and cooling in the diffuse interstellar medium - I. Optically thin regime

We develop a chemical model that follows the non-equilibrium evolution of the abundances of all ionisation states of the 11 elements¹ that dominate the cooling rate, and 20 molecular species². This chemical network contains 157 species in total, and includes chemical reactions on dust grains, photoelectric heating from dust grains, collisional gas phase reactions such as collisional ionisation, recombination and charge transfer reactions, cosmic ray ionisation and heating, and photochemical reactions. This model is applicable to temperatures $10^2 \text{ K} \leq T \leq 10^9 \text{ K}$ and densities $n_{\text{H}} \leq 10^4 \text{ cm}^{-3}$.

We then apply this model to a range of physical conditions that are typical for the diffuse ISM, with densities $10^2 \text{ cm}^{-3} \leq n_{\text{H}} \leq 10^4 \text{ cm}^{-3}$, temperatures $10^2 \text{ K} \leq T \leq 10^4 \text{ K}$, and for different UV radiation fields: the local interstellar radiation field (ISRF) of Black (1987), ten times this ISRF, the redshift zero extragalactic UV background (UVB) of Haardt & Madau (2001), and in the absence of UV radiation. For this chapter, we consider only optically thin gas. We compare the abundances and the cooling and heating rates predicted by our model in chemical equilibrium to those computed using the photoionisation code CLOUDY, version 13.01³ (Ferland et al. 2013). We generally find good agreement between our model and CLOUDY. We also identify which chemical species contribute most to the cooling rate. We find that CII, SiII and FeII are important coolants in the physical conditions that we consider here, along with OI and H₂ at densities $n_{\text{H}} \gtrsim 10^2 \text{ cm}^{-3}$.

¹H, He, C, N, O, Ne, Mg, Si, S, Ca & Fe.

²H₂, H₂⁺, H₃⁺, OH, H₂O, C₂, O₂, HCO⁺, CH, CH₂, CH₃⁺, CO, CH⁺, CH₂⁺, OH⁺, H₂O⁺, H₃O⁺, CO⁺, HOC⁺, O₂⁺.

³<http://nublado.org/>

Finally, we use our chemical model to investigate how non-equilibrium chemistry can affect the cooling rate in idealised scenarios of gas that is cooling either isochorically or isobarically. At temperatures $T > 10^4$ K, we find that non-equilibrium effects tend to suppress the cooling rate, similar to what has been found previously (e.g. Oppenheimer & Schaye 2013a). This is due to recombination lags, which leave ions in a higher ionisation state than they would have in equilibrium. These higher ionisation states are more difficult to collisionally excite, and so the radiative cooling rate is lower. However, at $T < 10^4$ K, non-equilibrium chemistry enhances the cooling rate by up to two orders of magnitude, rather than suppress it. This is because the recombination lags also enhance the electron abundance, which increases the number of collisions between electrons and ions, thereby increasing the collisional excitation rate and hence increasing the radiative cooling rate.

Chapter 3: Non-equilibrium chemistry and cooling in the diffuse interstellar medium - II. Shielded gas

We extend the chemical model presented in Chapter 2 to account for shielding from the UV radiation field. This shielding is modelled by attenuating the photochemical and photoheating rates by dust and gas, including shielding by HI, H₂, HeI, HeII and CO, where appropriate.

We apply our model to a simple photodissociation region (PDR) set-up, in which a one-dimensional plane-parallel slab of gas is irradiated from one side by the Black (1987) ISRF. We consider gas either at constant density and temperature, or in thermal and pressure equilibrium. We then use our model to investigate which heating and cooling processes dominate in different regions of the cloud, as the gas becomes shielded from UV radiation. Near the edge of the cloud, at low column densities, cooling is primarily from ionised metals, e.g. SiII, FeII, FeIII and CII, while heating is primarily from photoionisation of HI. Once the HI column density is high enough to shield the ionising radiation above 1 Ryd, the thermal balance is dominated by CII cooling versus photoelectric dust heating. Finally, at the highest column densities that we consider here ($N_{\text{H,tot}} \gtrsim 10^{22} \text{ cm}^{-2}$), carbon forms CO. In this fully shielded region, the thermal balance is primarily driven by molecular cooling, from H₂ and CO, versus cosmic ray heating.

We also use these PDR models to investigate the HI-to-H₂ transition. The column density at which this transition occurs is lower at higher density and at higher metallicity, in agreement with previous PDR models (e.g. Black & van Dishoeck 1987; Krumholz et al. 2009).

Chapter 4: The effects of metallicity, UV radiation and non-equilibrium chemistry in high-resolution simulations of galaxies

We incorporate the chemical model developed in Chapters 2 and 3 into the Tree/Smoothed Particle Hydrodynamics (SPH) code GADGET3 (last described in Springel 2005). We then use this to run a series of hydrodynamic simulations of isolated disc galaxies with an initial stellar mass of $10^9 M_{\odot}$ and a virial mass of $10^{11} M_{\odot}$. These simulations have a resolution of $750 M_{\odot}$ per particle, with a gravitational

softening of 3.1 pc, which is sufficient to resolve the transition from the warm (10^4 K) to the cold (10^2 K) ISM phase.

We run simulations at different metallicities ($0.01 \leq Z/Z_{\odot} \leq 1.0$), which is held fixed throughout the simulation, with dust abundances that are assumed to scale linearly with metallicity. We include a uniform UV radiation field (either the Black 1987 ISRF, ten per cent of this ISRF, or the redshift zero UVB of Haardt & Madau 2001), along with our prescription for self-shielding by gas and dust, plus one run using the Haardt & Madau (2001) UVB without self-shielding. By considering a wide range of metallicities and UV radiation fields, we can explore how they affect the properties of our model galaxies. We also repeat all of these simulations using tabulated cooling rates computed assuming chemical equilibrium. We compare these to the corresponding simulations run with the full non-equilibrium chemical model to investigate the impact of non-equilibrium chemistry on galaxy formation.

The gas in these simulations is initially in a smooth, rotating disc, at a temperature of 10^4 K. However, as the gas cools, it fragments and collapses to form cold ($\sim 10^2$ K), dense clouds, due to thermal and gravitational instabilities. These dense clouds can then form stars.

The total star formation rates and mass outflow rates are higher at higher metallicity and in the presence of a weaker radiation field, because in both cases it is easier for gas to cool to a cold star-forming phase. However, the wind mass loading factor (i.e. the ratio of mass outflow rate to star formation rate) is generally independent of metallicity and radiation field, tending towards a value of ≈ 10 at late times in the simulation.

Contrary to the effects of varying the metallicity and radiation field, non-equilibrium chemistry generally has no strong effect on the total star formation rates or the outflow properties of the galaxy. However, it does have an impact on the abundances of individual chemical species, particularly for molecules. We find that this is important for modelling molecular outflows. If we consider gas particles that are moving vertically away from the mid-plane of the galactic disc, i.e. that are outflowing, then the mass of H_2 that is outflowing with a vertical velocity $> 50 \text{ km s}^{-1}$ is enhanced by a factor ≈ 20 in non-equilibrium.

We then compute maps of line emission from CII and CO from our simulations in post-processing, using the publicly available Monte Carlo radiative transfer code RADMC-3D⁴ (version 0.38). CII emission is stronger for higher metallicities and stronger radiation fields, while CO emission is stronger for higher metallicities and weaker radiation fields. CII emission is generally unaffected by non-equilibrium chemistry, while CO emission varies by a factor of $\approx 2-4$ compared to equilibrium. Additionally, the X_{CO} factor, which is defined as the ratio of the H_2 column density to the velocity-integrated CO intensity, is lowered by up to a factor ≈ 2.3 in non-equilibrium.

⁴<http://www.ita.uni-heidelberg.de/~dullemond/software/radmc-3d/>

Chapter 5: Chemical evolution of giant molecular clouds in simulations of galaxies

We study Giant Molecular Clouds (GMCs) in the hydrodynamic simulations presented in Chapter 4. In particular, we look at the evolution of molecular abundances in these GMCs to investigate the time-scales over which molecules form and to see whether young GMCs tend to be out of chemical equilibrium, and we explore the implications that this has for CO emission and the X_{CO} factors of individual clouds.

We consider two different cloud definitions in our simulations, one that is physically motivated and one that is observationally motivated. Firstly, we define clouds to be regions above a density threshold of $n_{\text{H}} = 10 \text{ cm}^{-3}$. Gas particles above this threshold are grouped together into clouds using a Friends of Friends (FoF) algorithm, with a linking length of 10 pc. We then consider an observationally motivated definition in which we restrict the clouds to regions with a velocity-integrated CO intensity above a threshold of 0.25 K km s^{-1} , which corresponds to the 3σ intensity threshold for the Small Magellanic Cloud in the observations of Leroy et al. (2011). Properties such as cloud radius are then computed in projection, in 2d.

We find cloud lifetimes up to $\approx 40 \text{ Myr}$, with a median of 13 Myr, consistent with observations (e.g. Bash et al. 1977; Kawamura et al. 2009; Murray 2011; Miura et al. 2012, but see Elmegreen 2000 and Scoville et al. 1979 for examples that find shorter and longer GMC lifetimes, respectively). Our simulated clouds follow a mass-size relation $M \propto R^2$, as observed in molecular clouds (e.g. Solomon et al. 1987; Roman-Duval et al. 2010), with a normalisation that is a factor of four and two below the observed relation using our density- and CO-based cloud definitions, respectively. Our clouds also follow the observed velocity dispersion-size relation (Solomon et al. 1987), albeit with a large scatter that correlates with distance from the galactic centre, with clouds in the central 1 kpc showing higher velocity dispersions. All clouds in our simulations have virial parameters $\alpha > 1$, i.e. they are not virialised, and most have $\alpha > 2$, i.e. most are unbound. However, this is partly due to the pressure floor that we impose to ensure that the Jeans scale is well-resolved, as this pressure floor prevents low-mass ($\lesssim 3 \times 10^5 M_{\odot}$) clouds from becoming gravitationally bound.

At ten per cent solar metallicity, young clouds, with ages $\lesssim 10 - 15 \text{ Myr}$, have H_2 and CO fractions that are below chemical equilibrium, by a factor of ≈ 3 and 1 – 2 orders of magnitude, respectively, while at solar metallicity they reach equilibrium faster, within $\approx 1 \text{ Myr}$.

We then compute CO $J = 1 - 0$ line emission from each cloud in post-processing, using RADMC-3D. The CO intensity, I_{CO} , is suppressed towards low dust extinction, A_{v} , and possibly saturates towards high A_{v} . This agrees with the $I_{\text{CO}} - A_{\text{v}}$ relation that has been observed in the Milky Way, for example in the Pipe nebula (Lombardi et al. 2006) and the Perseus cloud (Pineda et al. 2008). The $I_{\text{CO}} - A_{\text{v}}$ relation in our simulations shifts towards higher A_{v} for higher metallicities and, to a lesser extent, for stronger radiation fields.

We find no strong trends of X_{CO} with A_{v} , except at high A_{v} where the scatter in

X_{CO} is greatly reduced, with values within a factor two of the Milky Way value. At ten per cent solar metallicity, the median X_{CO} factor in bins of age decreases by an order of magnitude from 0 to 15 Myr, albeit with a large scatter at fixed age, and we find no strong trends of X_{CO} with age at solar metallicity.

Final remarks

While the simulations presented in this thesis include one of the most detailed treatments of non-equilibrium chemistry so far used in galactic-scale simulations, they still contain several limitations. Firstly, the limited resolution of these simulations mean that we are likely missing small-scale turbulence. Turbulence can drive chemical abundances out of equilibrium if the gas density is changing rapidly, and it can accelerate the formation of H_2 , as gas forms dense clumps. Additionally, CO emission is often concentrated in dense, compact structures. If we do not fully resolve these structures, the CO emission, and hence the X_{CO} factor, will be uncertain.

Another limitation of our simulations is that we use a uniform UV radiation field, and we do not model the effects of local sources of radiation, such as young stars. A fluctuating radiation field, that varies both spatially and temporally, may drive non-equilibrium effects in the chemistry, if it varies rapidly. Also, if local sources are included, the radiation field will depend on the star formation rate. This could act as a feedback mechanism. For example, as the star formation rate increases, the radiation field increases, which will heat the gas and inhibit further star formation. These effects are missing from our simulations.

References

- Baldwin J. A., Phillips M. M., Terlevich R., 1981, *PASP*, 93, 5
Bash F. N., Green E., Peters W. L., III, 1977, *ApJ*, 217, 464
Baugh C. M., 2006, *Rep. Prog. Phys.*, 69, 3101
Becker R. H. et al., 2001, *AJ*, 122, 2850
Behroozi P. S., Wechsler R. H., Conroy C., 2013, *ApJ*, 770, 57
Benítez-Llambay A., Navarro J. F., Abadi M. G., Gottlöber S., Yepes G., Hoffman Y., Steinmetz M., 2015, *MNRAS*, 450, 4207
Bigiel F., Leroy A., Walter F., Brinks E., de Blok W. J. G., Madore B., Thornley M. D., 2008, *AJ*, 136, 2846
Birnboim Y., Dekel A., 2003, *MNRAS*, 345, 349
Black J. H., 1987, *ASSL*, 134, 731
Black J. H., van Dishoeck E. F., 1987, *ApJ*, 322, 412
Blumenthal G. R., Faber S. M., Flores R., Primack J. R., 1986, *ApJ*, 301, 27
Bolatto A. D., Leroy A. K., Rosolowsky E., Walter F., Blitz L., 2008, *ApJ*, 686, 948
Bolatto A. D., Wolfire M., Leroy A. K., 2013, *ARA&A*, 51, 207
Bond J. R., Kofman L., Pogosyan D., *Nature*, 380, 603
Bower R. G. et al., 2006, *MNRAS*, 370, 645
Bouwens R. J., Illingworth G. D., Oesch P. A., Caruana J., Holwerda B., Smit R., Wilkins S., 2015, arXiv:1503.08228

- Boylan-Kolchin M., Springel V., White S. D. M., Jenkins A., Lemson G., 2009, *MNRAS*, 398, 1150
- Chartas G., Brandt W. N., Gallagher S. C., Garmire G. P., 2002, *ApJ*, 579, 169
- Costa T., Sijacki D., Haehnelt M. G., 2015, *MNRAS*, 448, L30
- Crain R. A. et al., 2015, *MNRAS*, 450, 1937
- Croton D. J. et al., 2006, *MNRAS*, 365, 11
- Croxall K. V. et al., 2012, *ApJ*, 747, 81
- Dabrowski I., 1984, *Can. J. Phys.*, 62, 1639
- Dale J. E., Bonnell I. A., Clarke C. J., Bate M. R., 2005, *MNRAS*, 358, 291
- Dalla Vecchia C., Schaye J., 2012, *MNRAS*, 426, 140
- Davis M., Efstathiou G., Frenk C. S., White S. D. M., 1985, *ApJ*, 292, 371
- Dekel A., Birnboim Y., 2006, *MNRAS*, 368, 2
- Dekel A. et al., 2009, *Nature*, 457, 451
- Di Matteo T., Croft R. A. C., Springel V., Hernquist L., 2003, *ApJ*, 593, 56
- Efstathiou G., 1992, *MNRAS*, 256, 43
- Elmegreen B. G., 2000, *ApJ*, 530, 277
- Erdođdu P. et al., 2004, *MNRAS*, 352, 939
- Fabian A. C., 2012, *ARA&A*, 50, 455
- Fall S. M., Efstathiou G., 1980, *MNRAS*, 193, 189
- Fan X. et al., 2006, *AJ*, 132, 117
- Faucher-Giguère C.-A., Lidz A., Zaldarriaga M., Hernquist L., 2009, *ApJ*, 703, 1416
- Ferland G. J. et al., 2013, *RMxAA*, 49, 137
- Ferrarese L., Merritt D., *ApJ*, 539, L9
- Frenk C. S., White S. D. M., Davis M., Efstathiou G., 1988, *ApJ*, 327, 507
- Gaspari M., Brighenti F., Temi P., 2012, *MNRAS*, 424, 190
- Geen S., Rosdahl J., Blaizot J., Devriendt J., Slyz A., 2015, *MNRAS*, 448, 3248
- Glover S. C. O., Federrath C., Mac Low M.-M., Klessen R. S., 2010, *MNRAS*, 404, 2
- Glover S. C. O., Clark P. C., 2012, *MNRAS*, 421, 9
- Gnat O., Sternberg A., 2007, *ApJS*, 168, 213
- Gnedin O. Y., Kravtsov A. V., Klypin A. A., Nagai D., 2004, *ApJ*, 616, 16
- Gnedin N. Y., Hollon N., 2012, *ApJS*, 202, 13
- Gray W. J., Scannapieco E., Kasen D., 2015, *ApJ*, 801, 107
- Guo Q. et al., 2011, *MNRAS*, 413, 101
- Haardt F., Madau P., 2001, in Neumann D. M., Tran J. T. V., eds, *XXIst Moriond Astrophys. Meeting, Clusters of Galaxies and the High Redshift Universe Observed in X-rays Editions Frontieres, Paris*, 64
- Herschel W., 1785, *Phil. Trans. R. Soc.*, 75, 213
- Heyer M. H., Carpenter J. M., Snell R. L., 2001, *ApJ*, 551, 852
- Hopkins P. F., Quataert E., Murray N., 2011, *MNRAS*, 417, 950
- Hubble E. P., 1925, *Pop. Astr.*, 33, 252
- Huggins W., Miller W. A., 1864, *Phil. Trans. R. Soc.*, 154, 437
- Jeans J. H., 1902, *Phil. Trans. R. Soc.*, 199, 1
- Kafatos M., 1973, *ApJ*, 182, 433
- Kant I., 1755, *Allgemeine Naturgeschichte und Theorie des Himmels*

- Kapteyn J. C., van Rhijn P. J., 1920, *ApJ*, 52, 23
Kapteyn J. C., 1922, *ApJ*, 55, 302
Karachentsev I. D., Karachentseva V. E., Huchtmeier W. K., Makarov D. I., 2004, *AJ*, 127, 2031
Kauffmann G., Colberg J. M., Diaferio A., White S. D. M., 1999, *MNRAS*, 303, 188
Kauffmann G. et al., 2003, *MNRAS*, 346, 1055
Kawamura et al., 2009, *ApJS*, 184, 1
Kennicutt R. C. Jr. et al., 2007, *ApJ*, 671, 333
Kennicutt R. C. Jr. et al., 2011, *PASP*, 123, 1347
Kereš D., Katz N., Weinberg D. H., Davé R., 2005, *MNRAS*, 363, 2
Kereš D., Katz N., Fardal M., Davé R., Weinberg D. H., 2009, *MNRAS*, 395, 160
Kewley L. J., Maier C., Yabe K., Ohta K., Akiyama M., Dopita M. A., Yuan T., 2013, *ApJ*, 774, L10
King A. R., 2010, *MNRAS*, 402, 1516
Komatsu E. et al., 2009, *ApJS*, 180, 330
Kormendy J., Richstone D., 1995, *ARA&A*, 33, 581
Krumholz M. R., Matzner C. D., 2009, *ApJ*, 703, 1352
Krumholz M. R., McKee C. F., Tumlinson J., 2009, *ApJ*, 693, 216
Krumholz M. R., Leroy A. K., McKee C. F., 2011, *ApJ*, 731, 25
Leavitt H. S., Pickering E. C., 1912, *Harvard Coll. Obs. Circ.*, 173, 1
Le Petit F., Nehmé C., Le Bourlot J., Roueff E., 2006, *ApJS*, 164, 506
Leroy A. K. et al., 2009, *AJ*, 137, 4670
Leroy A. K. et al., 2011, *ApJ*, 737, 12
Lombardi M., Alves J., Lada C. J., 2006, *A&A*, 454, 781
Malhotra S. et al., 2001, *ApJ*, 561, 766
McElroy D., Walsh C., Markwick A. J., Cordiner M. A., Smith K., Millar T. J., 2013, *A&A*, 550, 36
Miura R. E. et al., 2012, *ApJ*, 761, 37
Moster B. P., Naab T., White S. D. M., 2013, *MNRAS*, 428, 3121
Murray N., 2011, *ApJ*, 729, 133
Ocvirk P., Pichon C., Teyssier R., 2008, *MNRAS*, 390, 1326
Oppenheimer B. D., Schaye J., 2013a, *MNRAS*, 434, 1043
Oppenheimer B. D., Schaye J., 2013b, *MNRAS*, 434, 1063
Pineda J. E., Caselli P., Goodman A. A., 2008, *ApJ*, 679, 481
Planck Collaboration XIII, 2015, [arXiv:1502.01589](https://arxiv.org/abs/1502.01589)
Pounds K. A., Reeves J. N., King A. R., Page K. L., O'Brien P. T., Turner M. J. L., 2003, *MNRAS*, 345, 705
Press W. H., Schechter P., 1974, *ApJ*, 187, 425
Proctor R. A., 1869, *MNRAS*, 29, 337
Rees M. J., Ostriker J. P., 1977, *MNRAS*, 179, 541
Rees M. J., 1986, *MNRAS*, 218, 25
Roman-Duval J., Jackson J. M., Heyer M., Rathborne J., Simon R., 2010, *ApJ*, 723, 492
Rosdahl J., Schaye J., Teyssier R., Agertz O., 2015, *MNRAS*, 451, 4553
Rosse, The Earl of, 1850, *Phil. Trans. R. Soc.*, 140, 499

-
- Sawala T., Frenk C. S., Crain R. A., Jenkins A., Schaye J., Theuns T., Zavala J., 2013, *MNRAS*, 431, 1366
- Sawala T. et al., 2015, *MNRAS*, 448, 2941
- Schaye J., 2004, *ApJ*, 609, 667
- Schaye J. et al., 2010, *MNRAS*, 402, 1536
- Scoville N. Z., Solomon P. M., Sanders D. B., 1979, in Burton W. D., ed., *Proc. IAU Symp. 84, The Large-Scale Characteristics of the Galaxy*, Reidel, Dordrecht, p. 277
- Shapley H., 1918, *PASP*, 30, 42
- Shapley H., 1919a, *ApJ*, 49, 249
- Shapley H., 1919b, *ApJ*, 49, 311
- Shapley H., Curtis H. D., 1921, *Bull. Nat. Res. Coun.*, 2, 171
- Sijacki D., Springel V., 2006, *MNRAS*, 366, 397
- Silk J., 1977, *ApJ*, 211, 638
- Silk J., Rees M. J., 1998, *A&A*, 331, L1
- Solomon P. M., Rivolo A. R., Barrett J., Yahil A., 1987, *ApJ*, 319, 730
- Springel V., 2005, *MNRAS*, 364, 1105
- Springel V. et al., 2005, *Nature*, 435, 629
- Sternberg A., Le Petit F., Roueff E., Le Bourlot J., 2014, *ApJ*, 190, 10
- Sutherland R. S., Dopita M. A., 1993, *ApJS*, 88, 253
- Tielens A. G. G. M., Hollenbach D., 1985, *ApJ*, 291, 722
- Trumpler R. J., 1930, *Lick Obs. Bull.*, 14, 154
- van Daalen M. P., Schaye J., Booth C. M., Dalla Vecchia C., 2011, *MNRAS*, 415, 3649
- van Dishoeck E. F., Black J. H., 1988, *ApJ*, 334, 771
- van de Voort F., Schaye J., Booth C. M., Haas M. R., Dalla Vecchia C., 2011, *MNRAS*, 414, 2458
- Veilleux S., Osterbrock D. E., 1987, *ApJS*, 63, 295
- Velliscig M., van Daalen M. P., Schaye J., McCarthy I. G., Cacciato M., Le Brun A. M. C., Dalla Vecchia C., 2014, *MNRAS*, 442, 2641
- Visser R., van Dishoeck E. F., Black J. H., 2009, *A&A*, 503, 323
- Vogelsberger M., Genel S., Sijacki D., Torrey P., Springel V., Hernquist L., 2013, *MNRAS*, 436, 3031
- White S. D. M., Rees M. J., 1978, *MNRAS*, 183, 341
- Wiersma R. P. C., Schaye J., Smith B. D., 2009, *MNRAS*, 393, 99
- Wolfire M. G., Hollenbach D., McKee C. F., 2010, *ApJ*, 716, 1191
- Wong T., Blitz L., 2002, *ApJ*, 569, 157
- Wright T., 1750, *An Original Theory or New Hypothesis of the Universe*

NON-EQUILIBRIUM CHEMISTRY AND COOLING IN THE DIFFUSE INTERSTELLAR MEDIUM - I. OPTICALLY THIN REGIME

An accurate treatment of the multiphase interstellar medium (ISM) in hydrodynamic galaxy simulations requires that we follow not only the thermal evolution of the gas, but also the evolution of its chemical state, including its molecular chemistry, without assuming chemical (including ionisation) equilibrium. We present a reaction network that can be used to solve for this thermo-chemical evolution. Our model follows the evolution of all ionisation states of the 11 elements that dominate the cooling rate, along with important molecules such as H_2 and CO , and the intermediate molecular species that are involved in their formation (20 molecules in total). We include chemical reactions on dust grains, thermal processes involving dust, cosmic ray ionisation and heating and photochemical reactions. We focus on conditions typical for the diffuse ISM, with densities of $10^{-2} \text{ cm}^{-3} \lesssim n_{\text{H}} \lesssim 10^4 \text{ cm}^{-3}$ and temperatures of $10^2 \text{ K} \lesssim T \lesssim 10^4 \text{ K}$, and we consider a range of radiation fields, including no UV radiation. In this paper we consider only gas that is optically thin, while paper II considers gas that becomes shielded from the radiation field. We verify the accuracy of our model by comparing chemical abundances and cooling functions in chemical equilibrium with the photoionisation code CLOUDY. We identify the major coolants in diffuse interstellar gas to be CII , SiII and FeII , along with OI and H_2 at densities $n_{\text{H}} \gtrsim 10^2 \text{ cm}^{-3}$. Finally, we investigate the impact of non-equilibrium chemistry on the cooling functions of isochorically or isobarically cooling gas. We find that, at $T < 10^4 \text{ K}$, recombination lags increase the electron abundance above its equilibrium value at a given temperature, which can enhance the cooling rate by up to two orders of magnitude. The cooling gas also shows lower H_2 abundances than in equilibrium, by up to an order of magnitude.

Alexander J. Richings, Joop Schaye and Benjamin D. Oppenheimer
Monthly Notices of the Royal Astronomical Society
Volume 440, Issue 4, pp. 3349-3369 (2014)

2.1 Introduction

Understanding the chemical evolution of the interstellar medium (ISM) is imperative for the accurate modelling of the radiative cooling rate of interstellar gas, and hence for the dynamics of the ISM. However, a full treatment of the ISM chemistry can involve hundreds of chemical species and thousands of reactions (e.g. the UMIST database for astrochemistry¹; Le Teuff et al. 2000) and the computational cost of such a complex treatment renders it impractical for use within large-scale 3D hydrodynamical simulations of galaxy formation. This problem is further compounded by the fact that chemical rate equations are typically stiff and so must be integrated implicitly, with a computational cost that scales with the cube of the number of species involved.

To avoid these issues, existing cosmological hydrodynamical simulations typically make use of simplifying assumptions to model the gas cooling rate. For example, the cosmological simulations run as part of the Overwhelmingly Large Simulations project (OWLS) (Schaye et al. 2010) use pre-computed cooling functions tabulated by temperature, density and abundances of individual elements, which were calculated using CLOUDY (Ferland et al. 1998, 2013) assuming ionisation equilibrium in the presence of the UV background of Haardt & Madau (2001) (see Wiersma et al. 2009). Note that ‘equilibrium’ here means that the abundances of individual chemical species have reached an equilibrium or steady state. However, such an approach has a number of disadvantages. Firstly, it assumes that the gas is in ionisation equilibrium, which may not be valid when the cooling or dynamical time-scale of the gas is shorter than its chemical time-scale (e.g. Kafatos 1973; Gnat & Sternberg 2007; Oppenheimer & Schaye 2013a; Vasiliev 2013) or in the presence of a time variable radiation field (e.g. Oppenheimer & Schaye 2013b). Secondly, one needs to rely on simple assumptions about the UV radiation field that is present. For example, many authors tabulate the cooling rate assuming that the gas is in collisional ionisation equilibrium i.e. they neglect the UV radiation altogether (e.g. Cox & Tucker 1969; Sutherland & Dopita 1993; Smith et al. 2008). Other studies such as Wiersma et al. (2009) assume the presence of a uniform UV background, thus neglecting local sources as well as shielding effects. De Rijcke et al. (2013) account for the self shielding of gas by exponentially suppressing the hydrogen ionising part of the UV background spectrum at high HI densities above a threshold $n_{\text{HI}} = 0.007 \text{ cm}^{-3}$, while Vogelsberger et al. (2013) use the fitting function of Rahmati et al. (2013) for the hydrogen ionisation rate as a function of density. Such simplifying assumptions are used because correctly accounting for the UV radiation field would require additional dimensions in the pre-computed tables of cooling rates, and reproducing the spectral shape of the radiation potentially requires tabulating in many frequency bins, which would greatly increase the size of the tables (although a recent study by Gnedin & Hollon 2012 suggests that this can be achieved with just 3 or 4 frequency bins).

An alternative approach is to solve the ISM chemistry within hydrodynamical simulations using a greatly simplified reaction network that captures the most

¹<http://www.udfa.net/>

important features of the chemical evolution while avoiding the complexity of more complete networks. Such a model was used by Glover & Jappsen (2007) to investigate low-metallicity gas, and Glover et al. (2010) used a similar model including the CO chemistry to study the formation of molecular clouds in the turbulent ISM. Grassi et al. (2011) have developed a model of the ISM that they implemented in numerical simulations by first evaluating their model on a large grid of input parameters and then using this to train an artificial neural network to behave like their gas model, and Grassi et al. (2014) present a package for embedding chemistry in hydrodynamical simulations. There are also methods to optimise a chemical network by selecting only the species and/or reactions from the network that are relevant to the particular physical conditions that one is interested in (e.g. Tupper 2002; Wiebe et al. 2003; Grassi et al. 2012).

We present a new chemical and thermal model of the ISM that covers a wide range of physical conditions, and is accurate for temperatures $10^2 \text{ K} \leq T \leq 10^9 \text{ K}$ and densities $n_{\text{H}} \leq 10^4 \text{ cm}^{-3}$. At higher densities and lower temperatures additional molecular species not included in our model may become important. We intend to apply this model to hydrodynamic galaxy simulations in which it is important that we are able to resolve the Jeans mass of the gas. Colder gas has a smaller Jeans mass ($M_J \propto T^{3/2}$), making it difficult to resolve gas at very low temperatures. We therefore choose not to consider gas below 10^2 K , which approximately corresponds to the smallest Jeans mass that can be resolved in current simulations of galaxy formation.

We are primarily interested in the regime of the diffuse ISM, with typical densities of $10^{-2} \text{ cm}^{-3} \lesssim n_{\text{H}} \lesssim 10^4 \text{ cm}^{-3}$ and temperatures of $10^2 \text{ K} \lesssim T \lesssim 10^4 \text{ K}$. Our model enables us to calculate the radiative cooling rate in the diffuse ISM without assuming ionisation or chemical equilibrium. Additionally, we will also be able to study the formation of some of the simplest molecules in the ISM, particularly H_2 and CO. Molecular hydrogen is known to be an important coolant below 10^4 K in primordial (e.g. Saslaw & Zipoy 1967; Peebles & Dicke 1968; Lepp & Shull 1984; Puy et al. 1993) and low-metallicity gas (e.g. Omukai et al. 2005; Santoro & Shull 2006; Jappsen et al. 2007).

By following the evolution of the CO abundance in our model, we will be able to simulate mock observations of CO emission, which will help us to compare our simulations to observations. This will also allow us to investigate how the X_{CO} factor, which relates the observable CO emission to the abundance of molecular hydrogen, evolves in our simulations. Additionally, cooling from heavy molecular species such as CO, H_2O and OH, which are all included in our network, can also contribute to the cooling rate of diffuse interstellar gas (e.g. Neufeld & Kaufman 1993; Neufeld et al. 1995).

Beyond this regime of the diffuse ISM, we are also interested in gas that is at higher temperatures, above 10^4 K , and/or at lower densities, below 10^{-2} cm^{-3} . For such gas we include the species and reactions from the chemical model of Oppenheimer & Schaye (2013a) for metal-enriched gas in the intergalactic medium (IGM), which includes higher ionisation states. This enables us to self-consistently follow the full chemical evolution of gas as it cools from the IGM and the circumgalactic medium (CGM) onto the ISM, and also to accurately model interstellar

gas that is irradiated by a strong UV radiation field from local sources.

In this paper we shall focus on photoionised gas in the optically thin regime. The chemistry and cooling properties of shielded gas, in which the incident radiation field becomes attenuated by dust and by the gas itself, will be important for the cold phase of the ISM, in particular for molecular clouds. We will present results for such shielded conditions, along with the methods that we use to calculate the attenuation of the photochemical reactions by dust and gas, in a companion paper to this work (hereafter paper II).

Throughout this paper we use the default solar abundances used by CLOUDY, version 13.01 (see for example table 1 in Wiersma et al. 2009). In particular, we take the solar metallicity to be $Z_{\odot} = 0.0129$. This paper is organised as follows. In sections 2.2 and 2.3 we describe the details of our chemical and thermal models respectively (readers who are not interested in the details of our methods may skip these two sections). In section 2.4 we compare the abundances and cooling functions predicted by our model in chemical equilibrium with CLOUDY to confirm its validity in the range of physical conditions that we are interested in, and we highlight the most important processes and the dominant coolants in this regime. In section 2.5 we investigate what impact non-equilibrium chemistry can have on the cooling of interstellar gas, and we discuss our results and conclusions in section 2.6.

2.2 The chemical model

To reproduce the gas cooling rate in the diffuse ISM, we will need to ensure that we include all of the most important coolants for the range of physical conditions that we are interested in. In non-primordial gas the cooling rate below 10^4 K is typically dominated by fine structure line emission from metals (e.g. Maio et al. 2007). Glover & Jappsen (2007) considered the contribution of various neutral and singly ionised metal species to the cooling rate at temperatures $50\text{K} < T < 10^4$ K and densities $10^{-3}\text{ cm}^{-3} < n < 10^2\text{ cm}^{-3}$ at a metallicity of $0.1 Z_{\odot}$. They identified the most important coolants to be C I, C II, O I and Si II, contributing at least 25% to the cooling rate somewhere within these ranges, in addition to inverse Compton cooling (at high redshift) and Ly α cooling. They also included cooling from molecular hydrogen, which dominates below 10^4 K in primordial gas and remains important in low-metallicity gas. We therefore take the reaction network used by Glover & Jappsen (2007) as the basis for our chemical model, supplemented with additional reactions for the primordial chemistry, and more recent rate coefficients for some existing reactions, taken from Glover & Abel (2008) and others. Glover & Jappsen (2007) follow 18 chemical species including the coolants described above and those species that have a significant impact on their abundances. They also include cooling from the HD molecule, which can become important in primordial and very low metallicity gas at low temperatures $T < 200$ K and densities $n_{\text{H}} > 10^4\text{ cm}^{-3}$ (Flower et al. 2000; Omukai et al. 2005; Glover et al. 2006). However, as we are interested in the diffuse ISM rather than dense molecular clouds, we do not explore temperatures below 10^2 K, nor do we consider densities above

10^4 cm^{-3} . We therefore decide to neglect HD cooling, which allows us to remove the deuterium chemistry from the reaction network.

In addition to tracking the coolants described above, we are also interested in following the abundance of CO in our model. Modelling the CO chemistry can become very complicated as a large number of intermediate molecular species are involved in its formation and destruction. Glover & Clark (2012) compare a number of simplified models that aim to approximate the CO chemistry in giant molecular clouds. We include the molecular CO network of Glover et al. (2010) (the most complex model considered by Glover & Clark 2012, although still a significant simplification compared to the full UMIST database), with some modifications as described in section 2.2.5. We demonstrate in section 2.4.2 that this model produces equilibrium CO fractions that are in good agreement with those calculated using version 13.01 of CLOUDY (Ferland et al. 2013) in the physical regimes that we are interested in here, i.e. those relevant to the diffuse ISM. We also include cooling from the molecular species CO, H₂O and OH in our thermal model.

Finally, we extend our chemical network to include the higher ionisation states that are relevant in the circumgalactic medium, the warm and hot ISM, and in regions with a strong interstellar radiation field. We combine the chemical reactions involving molecules and low ionisation states described above with the model of Oppenheimer & Schaye (2013a), which includes all ionisation states of the 11 elements² tabulated by Wiersma et al. (2009) and used in the cosmological simulations of the OWLS project (Schaye et al. 2010). Oppenheimer & Schaye (2013a) have tabulated the temperature dependence of the rate coefficients for collisional ionisation, radiative and di-electronic recombination and charge transfer reactions, based on the rates used by CLOUDY, which we make use of in our model, although we recalculate the photoionisation rates (including Auger ionisation) so that we can apply this model to any general UV radiation field, rather than just the extragalactic UV background models used by Oppenheimer & Schaye (2013a) (see section 2.2.2). Also, while Oppenheimer & Schaye (2013a) only include the charge transfer ionisation and recombination of metals by hydrogen and helium, we supplemented these with a small number of charge transfer reactions between metal species, which we take from the UMIST database.

We now have a chemical model that follows 157 species. These are the molecules H₂, H₂⁺, H₃⁺, OH, H₂O, C₂, O₂, HCO⁺, CH, CH₂, CH₃⁺, CO, CH⁺, CH₂⁺, OH⁺, H₂O⁺, H₃O⁺, CO⁺, HOC⁺ and O₂⁺, along with electrons and all ionisations states of H, He, C, N, O, Ne, Si, Mg, S, Ca and Fe (including H⁻, C⁻ and O⁻). The 907 reactions included in our model are summarised in table 2.3 in Appendix B. We describe some of these reactions, and the rates that we use for them, in more detail in sections 2.2.2 to 2.2.5 below.

To confirm the validity of our chemical model, we compare it to the photoionisation code CLOUDY, version 13.01³ (Ferland et al. 2013), which simulates the ionisation and molecular state of gas in chemical (including ionisation) equilibrium, along with the thermal state and the level populations of each species, and

²H, He, C, N, O, Ne, Mg, Si, S, Ca & Fe

³<http://nublado.org/>

hence predicts the spectrum of the gas. CLOUDY uses a more extensive chemical network than our model, including all ionisation states of the 30 lightest elements, and a molecular network that incorporates 83 molecules. CLOUDY includes a detailed treatment of the microphysical processes involved with molecular hydrogen, including the level populations of 1893 rovibrational states (for details of the microphysics of the H₂ molecule implemented in CLOUDY, see Shaw et al. 2005). CLOUDY also follows the radiative transfer of radiation through the gas, although we only consider optically thin gas in this paper, so we compare one-zone calculations in CLOUDY to our model in chemical equilibrium. CLOUDY is applicable to a wide range of physical conditions, e.g. densities up to $n_{\text{H}} \sim 10^{15} \text{ cm}^{-3}$ and temperatures up to $\sim 10^{10}$ K. See Röllig et al. (2007) for a comparison of several PDR codes, including CLOUDY.

2.2.1 Numerical implementation

We follow the non-equilibrium abundances of the chemical species in our network by integrating the rate equations from the initial conditions using the backward difference formula method and Newton iteration, implemented in CVODE (a part of the SUNDIALS⁴ suite of non-linear differential/algebraic equation solvers). We use a relative tolerance of 10^{-6} and an absolute tolerance of 10^{-13} . The abundances are also subject to the following constraint equations:

$$x_{\text{e}} = \sum_{i,n} n x_{i^{n+}} - \sum_j x_{j^-}, \quad (2.1)$$

$$x_{i^0} = x_{i,\text{tot}} - \sum_n x_{i^{n+}} - x_{i^-} - \sum_{\text{mol}} s_{i,\text{mol}} x_{\text{mol}}, \quad (2.2)$$

where $s_{i,\text{mol}}$ is the number of atoms of element i in the molecular species mol , and the abundance $x_{i^{n+}}$ of ion species i^{n+} is defined with respect to the total number density of hydrogen, $n_{\text{H,tot}}$, i.e. $x_{i^{n+}} \equiv n_{i^{n+}}/n_{\text{H,tot}}$. Be aware that these abundances are number fractions, not mass fractions. Glover & Jappsen (2007) use these constraint equations to reduce the number of rate equations that need to be integrated. However, following Oppenheimer & Schaye (2013a), we track all of the species from their rate equations and use the above constraint equations as an independent check on the accuracy of the CVODE solver. If the sum of species of a given element differs from its constraint by more than 1%, then these abundances are renormalised by multiplying the abundances of each species by the ratio of their constraint to their sum. Similarly, if the electron abundance differs from the sum of charged species as given in equation 2.1, then it is also renormalised.

⁴<https://computation.llnl.gov/casc/sundials/main.html>

2.2.2 Photochemical reactions

Photoionisation

The optically thin photoionisation rate Γ for an incident spectrum with an intensity per unit solid angle per unit frequency J_ν is given by the equation:

$$\Gamma_{\text{thin}} = \int_{\nu_0}^{\infty} \frac{4\pi J_\nu \sigma_\nu}{h\nu} d\nu, \quad (2.3)$$

where ν_0 is the ionisation threshold frequency of the ion.

Equation 2.3 does not include the effect of secondary ionisations, which can be significant if the ionising radiation is dominated by X-rays (e.g. Abel et al. 1997). We use the values for the number of secondary ionisations of hydrogen per primary ionisation tabulated by Furlanetto & Stoeber (2010) as a function of primary electron energy and ionised hydrogen fraction x_{HII} (see section 2.2.3) to calculate how important secondary ionisations would be for the photoionisation of hydrogen by the interstellar radiation field of Black (1987) and the redshift zero extragalactic UV background of Haardt & Madau (2001). We found that, for these two spectra, the secondary ionisation rate of hydrogen was just 0.02% and 0.08% of the primary ionisation rate respectively at an HII abundance $x_{\text{HII}} = 10^{-4}$, and even less at higher HII abundances. We therefore choose to neglect secondary ionisations from UV photoionisation in our model, although we find that we do need to consider them for cosmic rays (see section 2.2.3).

We can replace the frequency dependent cross section σ_ν with an average cross section $\bar{\sigma}$ using the optically thin grey approximation. Then the photoionisation rate of species i is given by the equation:

$$\Gamma_{i,\text{thin}} = \bar{\sigma}_i \int_{\nu_{0,i}}^{\infty} \frac{4\pi J_\nu}{h\nu} d\nu, \quad (2.4)$$

where:

$$\bar{\sigma}_i = \frac{\int_{\nu_{0,i}}^{\infty} \frac{4\pi J_\nu \sigma_{\nu,i}}{h\nu} d\nu}{\int_{\nu_{0,i}}^{\infty} \frac{4\pi J_\nu}{h\nu} d\nu}. \quad (2.5)$$

The integral on the right hand side of equation 2.4 gives the number of hydrogen ionising photons per unit area and time. Once we have specified the spectral shape of the incident UV radiation field through J_ν , we can calculate the average cross sections $\bar{\sigma}_i$ using equation 2.5. We use the frequency dependent cross sections $\sigma_{\nu,i}$ from Verner & Yakovlev (1995) and Verner et al. (1996), as used by CLOUDY. The number of hydrogen ionising photons per unit area and time, which determines the intensity of the UV radiation field, is an input parameter to our model, hence we can calculate the photoionisation rates using equation 2.4.

The photoionisation of inner shell electrons can lead to the ejection of multiple electrons by a single photon (Auger ionisation). We therefore multiply the cross sections calculated using equation 2.5 for each subshell of every ion by the electron vacancy distribution probabilities from Kaastra & Mewe (1993), and then sum over all subshells to obtain the Auger ionisation rates for each species.

Photodissociation

Molecular hydrogen in the ground electronic state can be dissociated by photons in the Lyman Werner band ($11.2 \text{ eV} < h\nu < 13.6 \text{ eV}$) via the two step Solomon process. The absorbed photon excites the H_2 into an electronically and vibrationally excited state, and when it decays back to the ground electronic state there is a probability that it will dissociate. An accurate treatment of the Solomon process would require us to follow the level populations of the rovibrational states of H_2 , which would be computationally expensive. However, there are approximations that we can use to estimate the photodissociation rate. Abel et al. (1997) argue that photodissociation of H_2 occurs mainly via absorptions in the very narrow energy band $12.24 \text{ eV} < h\nu < 13.51 \text{ eV}$. Therefore, if the UV spectrum is approximately constant in this range, the photodissociation rate will be proportional to the spectral intensity J_ν , evaluated at $h\nu = 12.87 \text{ eV}$ (corresponding to the vibrational state $v = 13$). They then derive this rate to be:

$$\Gamma_{\text{H}_2, \text{thin}} = 1.38 \times 10^9 \text{ s}^{-1} \left(\frac{J_\nu(h\nu = 12.87 \text{ eV})}{\text{erg s}^{-1} \text{cm}^{-2} \text{Hz}^{-1} \text{sr}^{-1}} \right). \quad (2.6)$$

This rate is also used by Glover & Jappsen (2007) (their equation 49).

To investigate the accuracy of this approximation, we calculated the photodissociation rate in CLOUDY using its ‘big H2’ model for the molecular hydrogen, in which the level populations of 1893 rovibrational states of H_2 are followed and dissociation from these states via the Solomon process is calculated self-consistently (see Shaw et al. 2005 for a description of how the microphysics of molecular hydrogen is implemented in CLOUDY). We considered three different UV spectra, the interstellar radiation field of Black (1987), the redshift zero extragalactic UV background of Haardt & Madau (2001) and a black body spectrum with a temperature 10^5 K , and compared the photodissociation rates estimated by equation 2.6 with those from CLOUDY for the range of densities $1 \text{ cm}^{-3} \leq n_{\text{H}} \leq 10^4 \text{ cm}^{-3}$. We found that the rates from CLOUDY were generally higher than those estimated using equation 2.6, by a factor ~ 2 . Furthermore, the dissociation rates calculated by CLOUDY did not scale exactly with $J_\nu(h\nu = 12.87 \text{ eV})$. We considered different ways to parameterise the dependence of the photodissociation rate on the UV spectrum, and we found that the most robust method was to assume that it scales with the number density of photons in the energy band $12.24 \text{ eV} < h\nu < 13.51 \text{ eV}$, $n_{12.24-13.51 \text{ eV}}$. We normalised this relation to the average rate calculated by CLOUDY over the density range $1 \text{ cm}^{-3} \leq n_{\text{H}} \leq 10^4 \text{ cm}^{-3}$ in the presence of the Black (1987) interstellar radiation field. The optically thin photodissociation rate of H_2 is then:

$$\Gamma_{\text{H}_2, \text{thin}} = 7.5 \times 10^{-11} \text{ s}^{-1} \left(\frac{n_{12.24-13.51 \text{ eV}}}{2.256 \times 10^{-4} \text{ cm}^{-3}} \right). \quad (2.7)$$

There remains a dependence of the photodissociation rate on the density that we are unable to capture in this approximation, as we do not follow the level populations of the rovibrational states of H_2 . This introduces errors of up to $\sim 25\%$ over the density range $1 \text{ cm}^{-3} \leq n_{\text{H}} \leq 10^4 \text{ cm}^{-3}$.

For the molecular species from the CO network we use the photoionisation and photodissociation rates given by van Dishoeck et al. (2006) and Visser et al. (2009)

where available, or Glover et al. (2010) otherwise, as calculated for the interstellar radiation field of Draine (1978). This radiation field has a field strength $G_0 = 1.7$, where the dimensionless parameter G_0 is defined as the ratio of the energy density in the UV radiation field in the energy range 6 eV to 13.6 eV with respect to the Habing (1968) field:

$$G_0 \equiv \frac{u_{6-13.6\text{eV}}}{5.29 \times 10^{-14} \text{ erg cm}^{-3}}. \quad (2.8)$$

We assume that the photoionisation and photodissociation rates of these molecular species are proportional to G_0 , so we multiply these rates calculated for the Draine (1978) interstellar radiation field by $G_0/1.7$.

The above photochemical rates are valid in the optically thin regime. In paper II we will consider the impact of shielding on these rates.

2.2.3 Cosmic ray ionisation

The ionisation rate of different species due to cosmic rays depends on the spectrum of the cosmic rays. This spectrum is, however, still uncertain both at high redshifts and even in the local ISM. Following the approach of Glover & Jappsen (2007), we allow the primary ionisation rate of atomic hydrogen due to cosmic rays, ζ_{HI} , to be a free parameter in our model. For example, the default value used by CLOUDY for the galactic background is $\zeta_{\text{HI}} = 2.5 \times 10^{-17} \text{ s}^{-1}$ (Williams et al. 1998). We then scale the primary ionisation rates of other species linearly with this parameter. Glover & Jappsen (2007) assume that the ratios of the ionisation rates of the other elements with respect to hydrogen are equal to the ratios of the values given in the UMIST database for astrochemistry (Le Teuff et al. 2000) where these rates are available. For SiII and SiIII, whose cosmic ray ionisation rates are not included in this database, they obtain the cosmic ray ionisation rate with respect to ζ_{HI} using the method from Langer (1978), who use the following equation from Silk (1970):

$$\zeta_i = \bar{\xi}_i \left(\frac{\chi_{\text{H}}}{\chi_i} \right) \zeta_{\text{HI}}, \quad (2.9)$$

where $\bar{\xi}_i$ is the effective number of electrons in the outer shell and χ_{H} and χ_i are the ionisation energies of hydrogen and the ion species i respectively. $\bar{\xi}_i$ can be calculated using the equations in Lotz (1967):

$$\bar{\xi} = \bar{\chi} \sum_{j=1}^2 (\xi_j / \chi_j), \quad (2.10)$$

where the summation is over the two outermost (sub-) shells, with ξ_j electrons and ionisation potential χ_j . $\bar{\chi}$ is a weighted average of these ionisation potentials, given by:

$$\ln \bar{\chi} = \frac{\sum_{j=1}^2 (\xi_j / \chi_j) \ln \chi_j}{\sum_{j=1}^2 (\xi_j / \chi_j)}. \quad (2.11)$$

Many of the species that we have added from the model of Oppenheimer & Schaye (2013a) are not included in the UMIST database, so for these we also use the above equations to calculate their cosmic ray ionisation rates in terms of ζ_{HI} . We note that cosmic ray ionisation is only important for species in low ionisation states, as the ionisation rates calculated above become very small for higher ionisation states.

In addition to the primary ionisations described above, the highly energetic ejected electrons can ionise further atoms. Furlanetto & Stoeber (2010) used Monte Carlo simulations to calculate the fraction of the primary electron energy E that is deposited as heat, in collisional ionisation of HI, HeI or HeII, and in collisional excitation of HI. They tabulate these energy deposition fractions as functions of E and of the ionisation fraction, $x_i = x_{\text{HII}}$. We therefore calculate the ionisation rates of HI and HeI due to secondary ionisations by interpolating the tables of Furlanetto & Stoeber (2010) as a function of the ionised hydrogen fraction x_{HII} . For the primary electron energy we take a typical mean value $E = 35$ eV (Spitzer 1978; Wolfire et al. 1995). At this energy, the secondary ionisation rate of HeII is zero, as it is below the HeII ionisation energy of 54.4 eV.

Note that this introduces a dependence on the ionisation fraction, as Coulomb interactions can reduce the energy of the primary electron if the electron abundance is high, thereby reducing the number of secondary ionisations. If we only include primary ionisations, then we miss this dependence, which we find does have a small but noticeable effect on the ionisation balance at low densities and low ionisation fractions.

We were unable to find equivalent calculations for the secondary ionisation rates of metal species in the literature, so we only include primary cosmic ray ionisations for these species.

Glover et al. (2010) also include a number of ionisation and dissociation reactions of molecules from cosmic ray induced UV emission, which we have also included in our model. These are summarised in table 2.3 in Appendix B, and are labelled as ' γ_{cr} '.

2.2.4 Dust grain physics

Our model includes a number of reactions that occur on the surface of dust grains. The most important of these is the formation of molecular hydrogen on dust, which typically dominates over the gas phase reactions except in dust free or very low metallicity environments. For this reaction we use the rate from Cazaux & Tielens (2002), as given by their equation 18:

$$R_{\text{H}_2} = \frac{1}{2} n_{\text{HI}} v_{\text{H}}(T_{\text{gas}}) n_{\text{d}} \sigma_{\text{d}} \epsilon_{\text{H}_2}(T_{\text{dust}}) S_{\text{H}}(T_{\text{gas}}, T_{\text{dust}}) \text{ cm}^{-3} \text{ s}^{-1}, \quad (2.12)$$

where n_{HI} is the number density of neutral hydrogen, $v_{\text{H}}(T_{\text{gas}})$ is the thermal velocity of the gas at temperature T_{gas} and $n_{\text{d}} \sigma_{\text{d}}$ is the total cross sectional area of dust grains per unit volume. Following Krumholz et al. (2011), we use a cross sectional area of $10^{-21} Z/Z_{\odot} \text{ cm}^2$ per H nucleus, which is intermediate between the values from the models of Weingartner & Draine (2001a) for the Milky Way (with

a ratio of visual extinction to reddening $R_v = 3.1$ or 5.5), the Large Magellanic Cloud and the Small Magellanic Cloud, and assumes that the dust content of the gas scales linearly with metallicity. The dimensionless recombination efficiency $\epsilon_{\text{H}_2}(T_{\text{dust}})$ is given in equation 13 of Cazaux & Tielens (2002). For the dimensionless sticking probability, $S_{\text{H}}(T_{\text{gas}}, T_{\text{dust}})$, we use equation 3.7 from Hollenbach & McKee (1979).

Equation 2.12 depends on the temperatures of both the gas and the dust, so we need to make an assumption about the dust temperature. Glover & Clark (2012) calculate the dust temperature by assuming that it is in thermal equilibrium and then solving the thermal balance equation for the dust grains (their equation A2). However, we find that for the physical conditions that we are interested in, i.e. those relevant to the diffuse ISM, the molecular hydrogen abundance is insensitive to the temperature of the dust (see Appendix A). Therefore, to reduce the computational cost of our model, we shall simply assume a constant dust temperature of 10 K.

Following Glover & Jappsen (2007), we include the recombination of HII , HeII , CII , OII and SiII on dust grains, along with FeII , MgII , SII , CaII and CaIII , which were not present in the model of Glover & Jappsen (2007). We use the rate coefficients quoted in table 3 of their paper, where present, which are based on calculations by Hollenbach & McKee (1979) and Weingartner & Draine (2001b). For the reactions not included in Glover & Jappsen (2007), we take the rate coefficients directly from Weingartner & Draine (2001b). These reactions are typically one or two orders of magnitude smaller than the radiative recombination rates, although the two can become comparable at temperatures above a few thousand Kelvin.

There are several additional dust grain processes that we do not currently include in our model. In particular, we do not explicitly follow the creation and destruction of dust, assuming instead that the dust-to-gas ratio simply scales linearly with the metallicity. More importantly for the gas cooling rates, we also do not model the depletion of metal atoms onto dust grains. This can reduce the gas phase abundances of metals by factors of a few. For example, Jenkins (2009) investigates the variation in the depletion factors (i.e. the fraction of a species remaining in the gas phase) of metals along different sight lines in the local ISM. The depletion factors of carbon and oxygen that they find are typically $\sim 0.6 - 0.8$ and $\sim 0.6 - 1.0$ respectively, while heavily depleted elements such as iron can have depletion factors below one per cent. Thus the rates of metal line cooling, particularly from iron, could be significantly affected by depletion onto dust grains.

Since these depletion factors are highly uncertain, we do not include them in our model, and we aim to address these issues in a future work. However, in figure 2.1 we illustrate the impact that metal depletion onto dust grains could potentially have on the cooling function of interstellar gas. We show the cooling rates of gas at a density $n_{\text{H}} = 1 \text{ cm}^{-3}$ in the presence of the redshift zero Haardt & Madau (2001) extragalactic UV background, plotted as a function of temperature. These were calculated using our model with element abundances at solar metallicity (solid curves), and with the solar abundances of C, N, O, Mg, Si and Fe reduced by the depletion factors given in column seven of table 4 in Jenkins

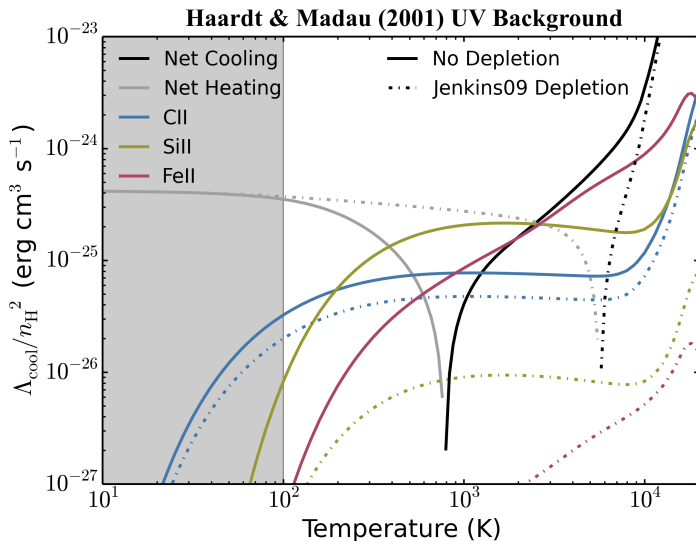


Figure 2.1: Comparison of the cooling functions of interstellar gas at solar metallicity without depletion of metal atoms onto dust grains (*solid curves*) and including the depletion factors from Jenkins (2009) for C, N, O, Mg, Si and Fe. These cooling functions were calculated using our model at a density $n_{\text{H}} = 1 \text{ cm}^{-3}$ in the presence of the redshift zero Haardt & Madau (2001) extragalactic UV background. The shaded grey region indicates temperatures below 100 K that are outside the range of temperatures that we are primarily interested in, but we include this regime here for completeness. We see that, in this example, the depletion of metal atoms onto dust grains can increase the thermal equilibrium temperature from $T_{\text{eq}} \sim 800 \text{ K}$ to $T_{\text{eq}} \sim 5600 \text{ K}$.

(2009) (dot-dashed curves). We see that, in this example, cooling from CII, SiII and FeII are important to balance the heating from the photoionisation of HI. However, these elements can be strongly depleted, particularly Si and Fe. Therefore, when we include the depletion factors of Jenkins (2009), the thermal equilibrium temperature, at which the total cooling and heating rates are equal, increases from $T_{\text{eq}} \sim 800 \text{ K}$ to $T_{\text{eq}} \sim 5600 \text{ K}$.

2.2.5 CO model

We base our model for CO chemistry on the reaction network of Glover et al. (2010), as we find that this is able to reproduce the molecular fraction of CO in the diffuse ISM fairly well, as predicted by CLOUDY, without requiring the full complexity of more complete networks (see section 2.4.2). For the photochemical reaction rates they assume the interstellar radiation field of Draine (1978), with a radiation field strength (see equation 2.8) of $G_0 = 1.7$ in units of the Habing (1968) field. To generalise these rates to any UV radiation field, we multiply them by $G_0/1.7$.

Our comparisons with CLOUDY showed that it is necessary to include four ad-

ditional reactions in our network (reactions 111, 283, 303 and 304 in table 2.3) that were not included in the model of Glover et al. (2010). We also updated the rates for a small number of reactions in Glover et al. (2010) to improve agreement with CLOUDY, and we updated some of the photodissociation rates using the values from van Dishoeck et al. (2006) and Visser et al. (2009); see Appendix B.

2.3 Thermal processes

Once we have calculated the abundance of each species, we can evaluate its contribution to the net cooling rate. The processes that we include in our model are summarised in Table 2.1, and some of these are discussed in more detail below.

2.3.1 Metal line cooling

Oppenheimer & Schaye (2013a) have tabulated the radiative cooling rates from the nine metal species that we include in our model (see section 2.2), along with hydrogen and helium, as a function of temperature using CLOUDY (they use version 10.00 in their paper, but they have since updated these tables using version 13.01 of CLOUDY⁵). See their section 2.2 for more details of their method. We use these tabulated cooling rates for most of these species. However, they note that these rates assume that the radiative cooling is dominated by electron-ion collisions and that this assumption can break down at temperatures $T \lesssim 10^3$ K for some species, for example OI.

We indeed find that their tabulated cooling rates for OI and CI are unable to reproduce CLOUDY's cooling curves at low temperatures, so for these two species we calculate the radiative cooling rates following the same method as Glover & Jappsen (2007). They consider only the three lowest fine-structure energy levels of each species, although for CI we found it necessary to extend their method to include the nine lowest energy levels, using transition probabilities from the NIST Atomic Spectra Database (ver. 5.0)⁶ and effective collision strengths from Péquignot & Aldrovandi (1976) and Dunseath et al. (1997). We tabulate these cooling rates in 55 temperature bins from 10 K to 10^4 K and 30 bins each in HI, HII and electron densities from 10^{-8} cm⁻³ to 10^5 cm⁻³. By tabulating in four dimensions in this way we are able to follow the radiative cooling rates of these species in regimes that are dominated by collisions with HI or HII, as well as when electron-ion collisions dominate. We use these new cooling rates for OI and CI at temperatures below 10^4 K, and revert back to the cooling rates tabulated by Oppenheimer & Schaye (2013a) at higher temperatures.

We also found that for some low-ionisation metal species there was an extra density dependence in the cooling rates that was not captured in the tables of Oppenheimer & Schaye (2013a), most notably for CII, NII, SII and FeII. This led to the cooling rates from these species being overestimated by up to an order of magnitude at the highest densities that we consider here ($n_{\text{H}} \sim 10^4$ cm⁻³, much higher

⁵These updated tables can be found on the website: <http://noneq.strw.leidenuniv.nl>

⁶<http://physics.nist.gov/asd>

Process	References ^a
Cooling Processes	
H excitation	1
He excitation	1
He ⁺ excitation	1
H collisional ionisation	1
He collisional ionisation	1
He ⁺ collisional ionisation	1
H ⁺ recombination	1
He ⁺ recombination ^b	1
He ⁺⁺ recombination	1
Grain-surface recombination	2, 3
Inverse Compton Cooling from the CMB	2, 4
Bremsstrahlung	1
Metal line cooling	1, 2
H ₂ rovibrational cooling	5
H ₂ collisional dissociation	2, 6
CO rovibrational cooling	7, 8, 9
H ₂ O rovibrational cooling	7, 8, 9
OH rotational cooling	10
Heating Processes	
Photoheating	11, 12
Cosmic ray heating ^c	2, 13
Dust photoelectric effect	14
H ₂ photodissociation	2, 15
H ₂ UV pumping	2, 16
H ₂ formation; gas phase	2, 17, 18
H ₂ formation; dust grains	2, 10

^a 1 - Oppenheimer & Schaye (2013a); 2 - Glover & Jappsen (2007); 3 - Wolfire et al. (2003); 4 - Cen (1992); 5 - Glover & Abel (2008); 6 - Mac Low & Shull (1986); 7 - Glover et al. (2010); 8 - Neufeld & Kaufman (1993); 9 - Neufeld et al. (1995); 10 - Hollenbach & McKee (1979); 11 - Verner & Yakovlev (1995); 12 - Verner et al. (1996); 13 - Goldsmith & Langer (1978); 14 - Wolfire et al. (1995); 15 - Black & Dalgarno (1977); 16 - Burton et al. (1990); 17 - Launay et al. (1991); 18 - Karpas et al. (1979)

^bradiative plus dielectronic

^cAssuming 20 eV deposited as heat into the gas per primary ionisation (Goldsmith & Langer 1978)

Table 2.1: Summary of included thermal processes.

than those considered by Oppenheimer & Schaye 2013a) compared to those calculated by CLOUDY. For these four species we therefore used the CHIANTI database version 7.1⁷ (Dere et al 1997; Landi et al 2013) to calculate line emissivities and hence cooling rates per ion, which we tabulate as functions of temperature in 80

⁷<http://www.chiantidatabase.org/chianti.html>

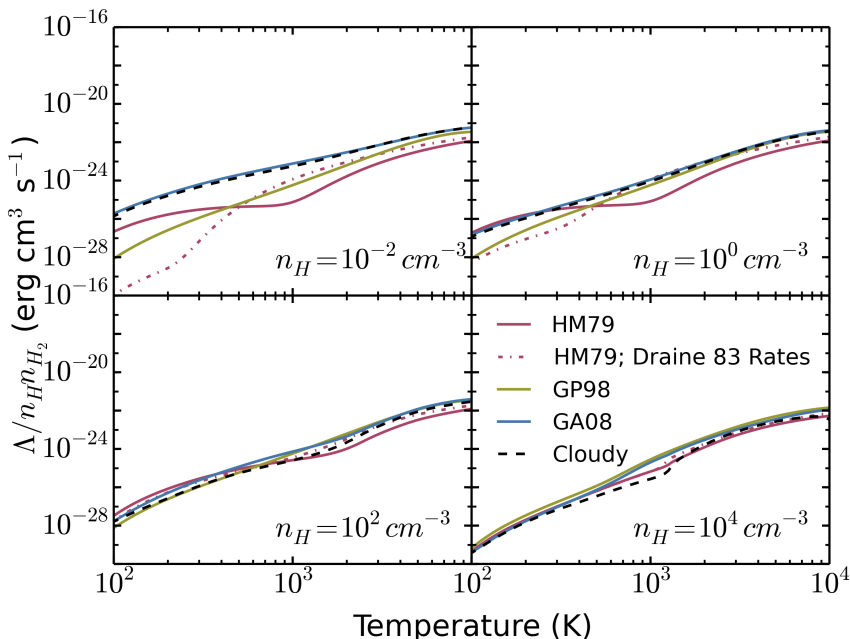


Figure 2.2: Comparison of various approximations for the H_2 cooling rate: Hollenbach & McKee (1979) (*HM79*; solid red curve), Hollenbach & McKee (1979) with the collisional excitation rates from Draine et al. (1983) (*dot-dashed red curve*), Galli & Palla (1998) (*GP98*; solid yellow curve) and Glover & Abel (2008) (*GA08*; solid blue curve). These are compared to the H_2 cooling rates calculated by *CLOUDY* (*dashed black curve*), which follows the level populations of several thousand rovibrational levels. The rovibrational cooling rate per H_2 molecule is plotted as a function of temperature, calculated in the absence of UV at various densities. We see that overall the GA08 cooling function gives the best match to the *CLOUDY* cooling rates, so we shall use the GA08 cooling rates in our model.

bins from 10 K to 10^5 K and electron density in 130 bins from 10^{-8} cm^{-3} to 10^5 cm^{-3} .

2.3.2 H_2 rovibrational cooling

Cooling from molecular hydrogen can become important in the ISM, particularly in primordial and low-metallicity gas. The primary mechanism by which H_2 cools the gas is transitions between its rotationally and vibrationally excited energy levels. To treat this properly, we would need to solve for the populations of these levels and hence obtain the rate at which they radiate away energy, but this can become computationally expensive due to the large number of levels involved. A number of studies have looked at this problem and have suggested analytic fits to the H_2 rovibrational cooling function. We have considered the analytic fits proposed by Hollenbach & McKee (1979), Galli & Palla (1998) and Glover & Abel (2008), which we compare to the cooling rates predicted by *CLOUDY* using its ‘big H_2 ’ model to accurately follow all of the rotational and vibrational energy levels

of the H₂ molecule. We also considered using the Hollenbach & McKee (1979) cooling function but using the collisional rates from Draine et al. (1983). These cooling functions typically express the H₂ cooling in terms of temperature and the densities of HI and H₂, although Glover & Abel (2008) also include its dependence upon the densities of HII, HeI and electrons, which arises from the collisional excitation of molecular hydrogen by these species. When calculating these cooling rates we have used the abundances calculated by CLOUDY to compute the collisional excitation rates, so that any discrepancies are due to differences in the analytic fits to the cooling function rather than to differences in the solution of the chemical model. These comparisons are shown in figure 2.2.

We see that the cooling function from Glover & Abel (2008) shows the closest agreement with the cooling rates computed by CLOUDY, so we shall use this in our model. For the low density limit of the cooling function we use equation 40 from Glover & Abel (2008) with the fitting coefficients listed in their table 8, for a fixed ratio of ortho- to para-H₂ of 3:1. This is then combined with the local thermodynamic equilibrium (LTE) cooling rate using their equation 39 to obtain the final H₂ cooling function. We calculate the LTE cooling rate using the radiative de-excitation rates of the rovibrational transitions in the ground electronic state taken from Wolniewicz et al. (1998).

2.3.3 CO, H₂O and OH cooling

We include cooling from CO and H₂O molecules using the same prescriptions as Glover et al. (2010) (see their section 2.3.2). Glover et al. (2010) base these prescriptions on the cooling rates calculated by Neufeld & Kaufman (1993) and Neufeld et al. (1995) but extend their treatment to account for collisions with electrons and atomic hydrogen, in addition to molecular hydrogen. Following Glover et al. (2010), we make use of the tabulated fit parameters given in Neufeld & Kaufman (1993) and Neufeld et al. (1995), which are given as functions of temperature and the effective column density per unit velocity, \tilde{N}_m . If the gas flow has no special symmetry and if the large velocity gradient approximation is valid, then (Neufeld & Kaufman 1993):

$$\tilde{N}_m = \frac{n_m}{|\underline{\nabla} \cdot \underline{v}|}, \quad (2.13)$$

where n_m is the number density of species m and $\underline{\nabla} \cdot \underline{v}$ is the divergence of the velocity field. For static gas this is equivalent to:

$$\tilde{N}_m = \frac{N_m}{\sigma}, \quad (2.14)$$

where N_m is the column density of species m and σ is the thermal velocity dispersion:

$$\sigma = \sqrt{\frac{3k_B T}{\mu m_p}}. \quad (2.15)$$

We use the static gas case in this work. However, when we use this in a hydrodynamic simulation, we could drop this assumption and calculate \tilde{N}_m directly from

equation 2.13. We also include rotational cooling from the OH molecule using the ‘universal’ cooling function for molecules with dipole moments from Hollenbach & McKee (1979) (their equations 6.21 and 6.22), using the molecular cooling parameters for OH summarised in their table 3. This function gives the cooling rate from OH in terms of the temperature and density along with the OH column density and dust extinction of the gas cell.

2.3.4 Photoheating

We include the photoheating of HI, HeI, HeII and all metal atoms and ions in our model. The optically thin photoheating rate per unit volume from the photoionisation of species i is $n_i \mathcal{E}_{i,\text{thin}}$, where:

$$\mathcal{E}_{i,\text{thin}} = \int_{\nu_{0,i}}^{\infty} \frac{4\pi J_\nu \sigma_{\nu,i}}{h\nu} (h\nu - h\nu_{0,i}) d\nu. \quad (2.16)$$

We can express this as:

$$\mathcal{E}_{i,\text{thin}} = \Gamma_{i,\text{thin}} \langle \epsilon_{i,\text{thin}} \rangle, \quad (2.17)$$

where $\Gamma_{i,\text{thin}}$ is the photoionisation rate of species i , given by equation 2.4, and $\epsilon_{i,\text{thin}}$ is the average excess energy of ionising photons:

$$\langle \epsilon_{i,\text{thin}} \rangle = \frac{\int_{\nu_{0,i}}^{\infty} \frac{4\pi J_\nu \sigma_{\nu,i}}{h\nu} (h\nu - h\nu_{0,i}) d\nu}{\int_{\nu_{0,i}}^{\infty} \frac{4\pi J_\nu \sigma_{\nu,i}}{h\nu} d\nu}. \quad (2.18)$$

For each species $\langle \epsilon_{i,\text{thin}} \rangle$ is calculated for the given incident UV spectrum J_ν , using the frequency dependent cross sections from Verner & Yakovlev (1995) and Verner et al. (1996), and is then provided to our model as an input parameter.

Note that Glover & Jappsen (2007) include an efficiency factor in equation 2.16 for the fraction of the excess photon energy that is converted into heat (as calculated using the results of e.g. Shull & van Steenberg 1985 or Dalgarno et al. 1999). This factor accounts for the fact that the electrons released by photoionisation reactions can cause secondary ionisations/excitations of HI and HeI. The energy used in these secondary reactions will subsequently be radiated away and thus does not contribute to heating the gas. However, as explained in section 2.2.2, we do not need to include the effects of secondary ionisation, as they only enhance the primary photoionisation rate by less than 0.1% for the UV radiation fields that we consider here and are thus unimportant. We therefore take this efficiency factor to be equal to 1 in equation 2.16.

The above equations are applicable to the optically thin regime. In paper II we will consider the effect of shielding on the photoheating rates.

2.3.5 Photoelectric heating

Another potentially important source of heating is photoelectric emission from dust grains. When a UV photon is absorbed by a dust grain it can release an

electron, and the excess energy absorbed by the electron is quickly thermalised, thereby heating the gas. The photoelectric heating rate is given by (Bakes & Tielens 1994; Wolfire et al. 1995):

$$\Gamma = 1.0 \times 10^{-24} \epsilon G_0 n_{\text{H}_{\text{tot}}} Z/Z_{\odot} \text{ erg cm}^{-3} \text{ s}^{-1}, \quad (2.19)$$

where G_0 is the UV radiation field in units of the Habing (1968) field (see equation 2.8), $n_{\text{H}_{\text{tot}}}$ is the total hydrogen number density, Z is the metallicity, and the heating efficiency ϵ is given by the following analytic fit for gas temperatures up to 10^4 K:

$$\epsilon = \frac{4.9 \times 10^{-2}}{1.0 + ((G_0 T^{0.5}/n_e)/(1925 \text{ K}^{0.5} \text{ cm}^3))^{0.73}} + \frac{3.7 \times 10^{-2} (T/10^4 \text{ K})^{0.7}}{1.0 + ((G_0 T^{0.5}/n_e)/(5000 \text{ K}^{0.5} \text{ cm}^3))}. \quad (2.20)$$

2.4 Equilibrium chemistry and cooling in the ISM

While our chemical model is primarily focussed on the non-equilibrium evolution of chemistry and gas cooling in the ISM, it is important that we confirm the validity of our model by comparing its results in chemical equilibrium with those from existing codes, in particular to test whether we have missed any important reactions in our chemical network. We therefore calculated the equilibrium ionisation balance and cooling rates from our model as a function of temperature from 10 K to 2×10^4 K. We are primarily interested in the temperature range $10^2 \leq T \leq 10^4$ K, corresponding to the transition from a warm to a cold phase in the ISM, but we also look at how our model behaves outside this regime. Abundances and cooling rates were calculated at a range of fixed densities relevant to the diffuse ISM, from 10^{-2} cm^{-3} to 10^4 cm^{-3} , for various metallicities and using four different assumptions for the UV radiation field: the interstellar radiation field (ISRF) of Black (1987), both by itself and also multiplied by a factor of 10; the extragalactic UV background (UVB) of Haardt & Madau (2001) and in the absence of UV radiation (i.e. fully shielded gas). The calculations were started from fully neutral and atomic initial conditions and evolved until they reached chemical equilibrium. The examples including a UV radiation field were assumed to be optically thin, i.e. with no intervening column density to shield the gas. We will consider the effect of shielding in paper II. We used the default solar metal abundances from CLOUDY (as used by e.g. Wiersma et al. 2009; Oppenheimer & Schaye 2013a), and we used a hydrogen cosmic ray ionisation rate of $\zeta_{\text{HI}} = 2.5 \times 10^{-17} \text{ s}^{-1}$ (Williams et al. 1998).

We compared the predicted equilibrium ionisation fractions and cooling rates from our model to those calculated using version 13.01 of CLOUDY (Ferland et al. 2013). In most of the CLOUDY runs the dust temperature was calculated self-consistently assuming thermal balance. However, in the absence of a UV radiation

field we found it necessary to fix the dust temperature in CLOUDY at 10 K, as used in our model, to prevent unrealistically low dust temperatures. This problem arose because our CLOUDY calculations considered an optically thin parcel of gas in which the dust is also optically thin to its own infrared radiation, so in the absence of UV radiation there is very little heating of the dust grains. We generally find that our network agrees well with CLOUDY, as we shall demonstrate in the next section. We also use these results to identify which are the most important coolants in the ISM in the various physical regimes explored here. More plots of our results from these tests can be found on our website ⁸.

2.4.1 Dominant coolants

In figure 2.3 we show the equilibrium ionisation fractions (left panels) and cooling functions (right panels) as a function of temperature at a density $n_{\text{H}} = 1 \text{ cm}^{-3}$ for the four different UV radiation fields we consider here. We show temperatures ranging from 10 K to 2×10^4 K, but have greyed out the region $T < 100$ K as this lies outside the range of temperatures that we are primarily interested in.

The top row was calculated in the presence of the Black (1987) ISRF multiplied by a factor of 10, which represents the UV radiation field one might find within a strongly star-forming galaxy. The dominant coolants in this case are, going from high to low temperatures, OIII, SIII, SiII and CII, while strong photoheating, primarily from hydrogen, balances the cooling at a thermal equilibrium temperature $T_{\text{eq}} \sim 5000$ K.

The second row shows the results for the Black (1987) ISRF, which is more typical of the local solar neighbourhood. FeII contributes significantly to the cooling here, while the more highly ionised species (e.g. OIII and SIII) become less important. Despite the weaker photoheating, the equilibrium temperature is still close to 5000 K, as the metal line cooling is also lower.

The results in the third row were calculated in the presence of the Haardt & Madau (2001) extragalactic UV background at redshift zero, in which the flux of hydrogen-ionising photons is approximately three orders of magnitude lower than the Black (1987) field. In this example we find that the cooling is now dominated by FeII, SiII and CII, and the lower photoheating rate now balances the metal line cooling at $T_{\text{eq}} \sim 800$ K.

Finally, in the bottom row of figure 2.3 we show the equilibrium state of gas in the absence of UV radiation. The dominant coolant here is molecular hydrogen, although there is still a significant contribution from some metal species, most notably SiII, OI and CI. Without UV radiation to provide photoheating, the main source of heating comes from cosmic rays, resulting in an equilibrium temperature $T_{\text{eq}} \sim 100$ K.

In table 2.2 we summarise the species that contribute at least 5% to the total equilibrium cooling rate in the temperature range $10^2 \text{ K} \leq T \leq 10^4 \text{ K}$ for solar metallicity and a density $n_{\text{H}} = 1 \text{ cm}^{-3}$, in the presence of the four UV radiation fields considered in figure 2.3. For each species we give the minimum and maximum temperatures, T_{min} and T_{max} , for which that species contributes at least 5%

⁸<http://noneqism.strw.leidenuniv.nl>

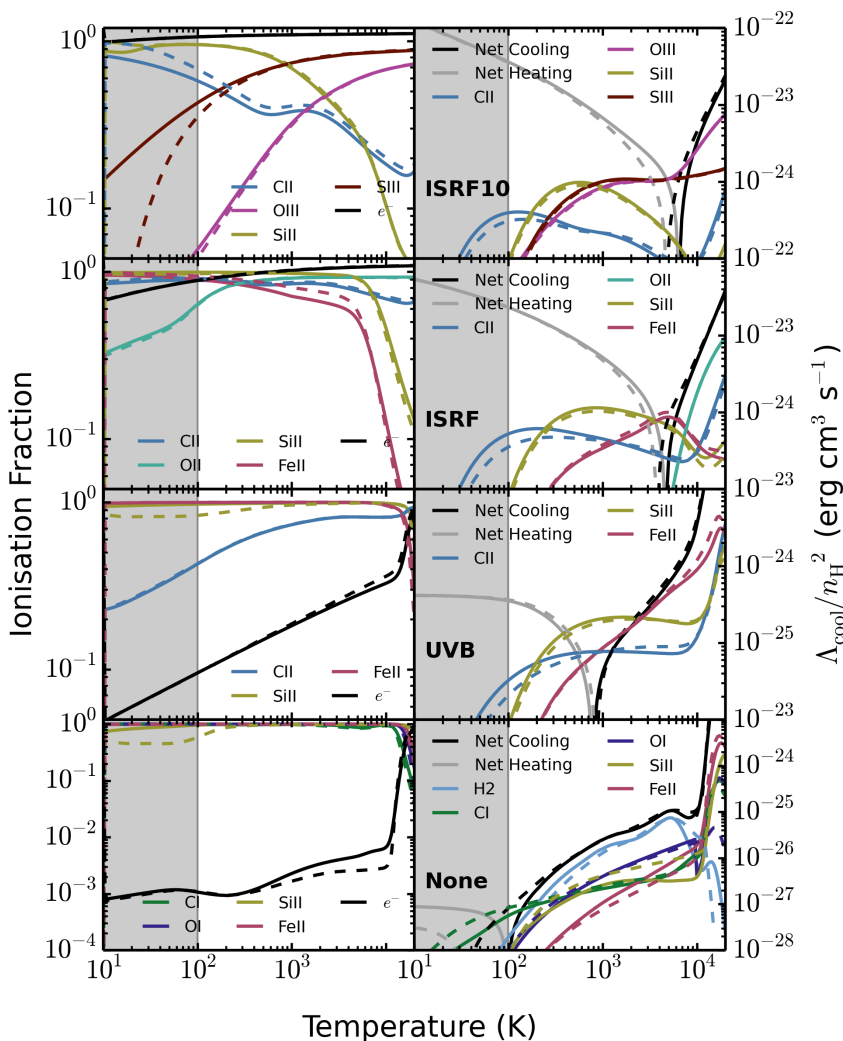


Figure 2.3: Comparison of the equilibrium ionisation fractions (*left*) and cooling functions (*right*) predicted by our model (*solid lines*) and CLOUDY (*dashed lines*), plotted against temperature. These were calculated at solar metallicity and a density $n_{\text{H}} = 1 \text{ cm}^{-3}$ for four different UV radiation fields: the Black (1987) interstellar radiation field (ISRF) multiplied by a factor 10 (*ISRF10*; *top*), the Black (1987) ISRF (*ISRF*; *second row*), the redshift zero Haardt & Madau (2001) extragalactic UV background (*UVB*; *third row*) and in the absence of UV radiation (*None*; *bottom*). In each row we show only those species that contribute at least 20 per cent to the cooling rate anywhere in the temperature range $10^2 \text{ K} < T < 10^4 \text{ K}$. The panels in the right column show the cooling rates from individual species along with the net cooling rate (total cooling minus heating). The shaded grey region highlights temperatures below 100 K that are outside the range of temperatures that we are primarily interested in, but we include this regime here for completeness.

2.4 Equilibrium chemistry & cooling in the ISM

Species	$\log T_{\min}^a$	$\log T_{\max}^b$	$\log T_{\text{peak}}^c$	Peak ^d
ISRF10				
CII	2.0	3.1	2.0	44.3%
HII	2.0	4.0	2.0	17.9%
NII	2.0	2.5	2.0	15.8%
SiII	2.0	3.7	2.5	32.9%
SIII	2.1	4.0	3.3	27.2%
OII	3.9	4.0	4.0	7.5%
OIII	2.0	4.0	4.0	35.7%
ISRF				
CII	2.0	3.9	2.0	61.8%
NII	2.0	4.0	2.0	13.4%
SiII	2.0	4.0	2.7	42.4%
FeII	2.4	4.0	3.7	23.9%
HII	2.0	4.0	3.7	15.7%
SIII	2.5	4.0	3.7	14.1%
OII	3.8	4.0	4.0	22.4%
SII	3.8	4.0	4.0	9.2%
UVB				
CII	2.0	3.9	2.0	72.5%
SiII	2.0	4.0	2.7	54.9%
FeII	2.3	4.0	3.7	47.7%
CaII	3.8	4.0	3.9	7.7%
SII	3.7	4.0	3.9	12.5%
HI	3.9	4.0	4.0	18.5%
MgII	3.9	4.0	4.0	8.4%
None				
CI	2.0	4.0	2.0	60.6%
SiII	2.0	3.5	2.3	15.4%
H ₂	2.0	4.0	3.7	70.2%
OI	2.0	4.0	3.9	30.7%
FeII	3.2	4.0	4.0	19.0%
HI	3.9	4.0	4.0	16.9%

^aMinimum temperature at which the species contributes at least 5% to the total equilibrium cooling rate.

^bMaximum temperature at which the species contributes at least 5% to the total equilibrium cooling rate.

^cTemperature at which the relative contribution of the species to the total equilibrium cooling rate is highest.

^dRelative contribution of the species to the total equilibrium cooling rate at T_{peak} .

Table 2.2: Summary of species that contribute at least 5% to the total equilibrium cooling rate in the temperature range $10^2 \text{ K} \leq T \leq 10^4 \text{ K}$ at solar metallicity and a density $n_{\text{H}} = 1 \text{ cm}^{-3}$, in the presence of four different UV radiation fields: the Black (1987) interstellar radiation field (ISRF) multiplied by a factor 10 (*ISRF10*), the Black (1987) ISRF (*ISRF*), the redshift zero Haardt & Madau (2001) extragalactic UV background (*UVB*) and in the absence of UV radiation (*None*). The four sections in the table correspond to the four rows of figure 2.3.

to the total equilibrium cooling rate, the temperature at which the relative contribution of that species to the total equilibrium cooling rate is highest, T_{peak} , and the relative contribution of that species at T_{peak} . More tables of dominant coolants for different metallicities and densities, and extending to higher temperatures up to 10^9 K , can be found on our website.

Bertone et al. (2013) have also investigated the dominant cooling channels in the Universe, although they focus on diffuse gas on cosmological scales, typically with lower densities ($n_{\text{H,tot}} < 0.1 \text{ cm}^{-3}$) than we have considered. The species that they found most important at these lower densities, in the presence of the Haardt & Madau (2001) extragalactic UV background, were OIII, CII, CIII, SiII, SiIII, FeII and SIII.

Comparing our equilibrium abundances and cooling functions (solid lines) to CLOUDY (dashed lines) in figure 2.3, we find that they are in good agreement. Below 100 K the agreement between our model and CLOUDY tends to be poorer for all UV radiation fields, but most noticeably in the absence of UV. This is partly because we include fewer molecular species in our network than CLOUDY does. However, we see in figure 2.3 that many species are still in good agreement at these low temperatures.

Figure 2.3 only shows our results for a density $n_{\text{H}} = 1 \text{ cm}^{-3}$, but we also considered densities in the range $10^{-2} \leq n_{\text{H}} \leq 10^4 \text{ cm}^{-3}$. At lower densities photoionisations and cosmic ray ionisations become relatively more important, as they scale linearly with density while two body collisional processes scale with the density squared. In the presence of a strong UV radiation field, higher ionisation species such as SiIV and FeVI contribute significantly to the cooling function in these cases, although heating is also relatively stronger. Conversely, at higher densities the importance of the UV radiation and cosmic rays becomes relatively weaker, with the cooling dominated by low ionisation state species such as OI, SiII and FeII, along with molecular hydrogen. More plots comparing the ionisation fractions and cooling functions from our model and from CLOUDY can be found on our website.

2.4.2 Molecular abundances

In this section we test the accuracy of our molecular network by comparing the equilibrium abundances of H_2 and CO calculated using our model to those from CLOUDY. In figure 2.4 we plot the molecular fraction of H_2 as a function of temperature in the presence of the extragalactic UV background of Haardt & Madau (2001) (top four panels) and in the absence of UV radiation (bottom four panels) for three different metallicities (different colours) and for four different densities (different panels).

In the presence of the Haardt & Madau (2001) UV background our molecular fractions at solar and 10% solar metallicity match those from CLOUDY well. However, we tend to predict somewhat smaller molecular fractions in primordial gas than CLOUDY. This is due to uncertainties in the reaction rate of the associative detachment of H^- , which is the primary formation mechanism of H_2 at these densities when there is no dust present. Glover et al. (2006) have demonstrated how uncertainties in this reaction rate can lead to significant uncertainties in the abundance of molecular hydrogen. We have used the rate from Bruhns et al. (2010), as given in the UMIST database, which was measured over a temperature range $30 \text{ K} < T < 3000 \text{ K}$ and is in much better agreement with theoretical calculations than earlier experimental measurements such as Schmeltekopf et al. (1967), Fehsenfeld et al. (1973) and Martinez Jr. et al. (2009). However, CLOUDY uses the

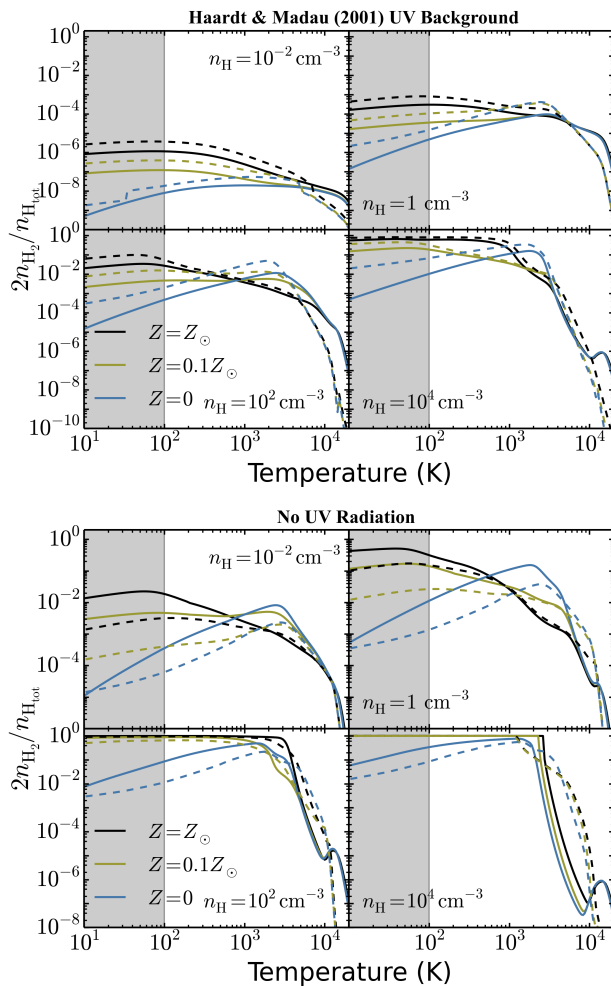


Figure 2.4: Equilibrium molecular fractions of H_2 predicted by our chemical model (*solid lines*) and CLOUDY (*dashed lines*). These were calculated in the presence of the redshift zero Haardt & Madau (2001) extragalactic UV background (*top four panels*) and in the absence of UV radiation (*bottom four panels*) at solar metallicity and densities $10^{-2} \text{ cm}^{-3} \leq n_{\text{H}} \leq 10^4 \text{ cm}^{-3}$. The shaded grey region highlights temperatures below 100 K that are outside the range of temperatures that we are primarily interested in, but we include this regime here for completeness. In the presence of the UV background the greatest discrepancies are found in primordial gas (*blue curves*), and are mainly due to uncertainties in the formation rate of H_2 via H^- . In the absence of UV we tend to find higher molecular hydrogen abundances than CLOUDY, primarily because we use a lower cosmic ray dissociation rate of H_2 . See section 2.4.2 for a more detailed discussion.

rate coefficients from Launay et al. (1991).

In the absence of UV radiation our molecular fractions follow similar trends

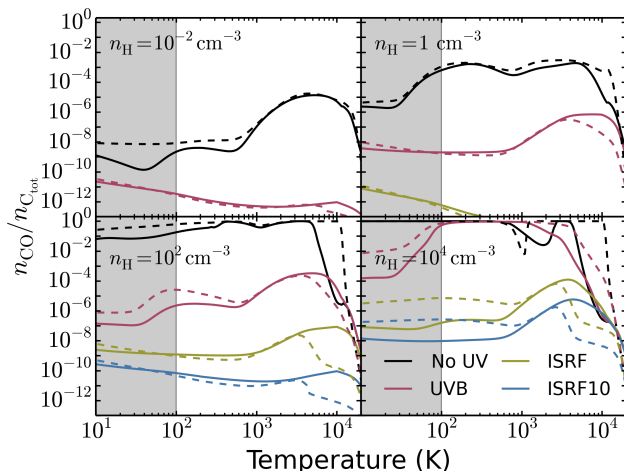


Figure 2.5: Equilibrium molecular fractions of CO predicted by our chemical model (*solid lines*) and CLOUDY (*dashed lines*). These were calculated at solar metallicity and for densities $10^{-2} \text{ cm}^{-3} \leq n_{\text{H}} \leq 10^4 \text{ cm}^{-3}$ in the absence of UV (*black, No UV*), in the presence of the redshift zero Haardt & Madau (2001) extragalactic UV background (*red, UVB*), the Black (1987) interstellar radiation field (*yellow, ISRF*) and ten times this interstellar radiation field (*blue, ISRF10*). The shaded grey region highlights temperatures below 100 K that are outside the range of temperatures that we are primarily interested in, but we include this regime here for completeness. The agreement with CLOUDY is good except in gas with both high density and high temperature, which is a combination that will be rare in nature.

with temperature as those from CLOUDY, although we generally tend to produce higher H_2 abundances for $T \lesssim 10^3$ K. This is primarily due to different dissociation rates of H_2 by cosmic rays used in CLOUDY compared to our model. In particular, CLOUDY includes the cosmic ray induced photodissociation of H_2 , which is an order of magnitude higher than the cosmic ray dissociation that we include in our model based on the rates in the UMIST database.

We find similar trends in the presence of stronger UV radiation fields, although the H_2 abundances are small in these examples, so we do not show them here.

In figure 2.5 we show the molecular fraction of CO as a function of temperature at solar metallicity for four different densities (different panels) and four different UV radiation fields (different colours). We see that in the presence of the two strongest UV radiation fields considered here the CO fraction (i.e. the fraction of carbon that is in CO) remains low ($< 10^{-4}$) even at the highest density shown in figure 2.5 ($n_{\text{H,tot}} = 10^4 \text{ cm}^{-3}$). In the presence of the Haardt & Madau (2001) extragalactic UV background the CO fraction reaches unity at $n_{\text{H,tot}} \sim 10^4 \text{ cm}^{-3}$ for temperatures $10^2 \text{ K} \lesssim T \lesssim 10^3 \text{ K}$, while in the absence of UV the CO fraction is close to one at these temperatures down to even lower densities, $n_{\text{H,tot}} \sim 10^2 \text{ cm}^{-3}$.

The CO fractions predicted by our model agree well with CLOUDY, except at a density $n_{\text{H}} \sim 10^4 \text{ cm}^{-3}$ and temperatures above a few thousand Kelvin where we predict a lower CO abundance than CLOUDY. However, since it is unlikely that gas

at such high densities would maintain temperatures of a few thousand Kelvin, this is not a problem for us.

2.4.3 Impact of cosmic rays on ionisation balance and cooling

Once the gas becomes shielded from the UV radiation field, its ionisation balance is typically dominated by cosmic ray ionisation at low temperatures. However, the cosmic ray ionisation rate in the ISM is highly uncertain. By modelling the chemistry of 23 low mass molecular cores to reproduce observed molecular ion abundances, Williams et al. (1998) infer a cosmic ray ionisation rate for H_2 of $\zeta_{\text{H}_2} = 5 \times 10^{-17} \text{s}^{-1}$, corresponding to an H I ionisation rate from cosmic rays of $\zeta_{\text{H I}} = 2.5 \times 10^{-17} \text{s}^{-1}$ (this is the default value that we use in our models). However, other authors have measured very different values for the galactic cosmic ray background. For example, Indriolo et al. (2007) use observations of H_3^+ absorption along twenty galactic sight lines to obtain a cosmic ray ionisation rate $\zeta_{\text{H I}} = 2 \times 10^{-16} \text{s}^{-1}$, while McCall et al. (2003) derive an even higher value of $\zeta_{\text{H I}} = 1.2 \times 10^{-15} \text{s}^{-1}$ based on laboratory measurements and H_3^+ observations towards ζ Persei. Furthermore, the cosmic ray ionisation rate may also depend on the galactic environment, for example Suchkov et al. (1993) estimate a much higher density of cosmic rays in the starburst galaxy M82.

Figure 2.6 shows the impact of increasing or decreasing our default cosmic ray ionisation rate by a factor of ten on the ionisation balance and cooling function of fully shielded gas at solar metallicity and a density $n_{\text{H}} = 1 \text{ cm}^{-3}$. In the left panels we see that the ionisation fractions of singly ionised helium, carbon and oxygen as well as hydrogen, and hence the electron abundance, change dramatically as we vary the cosmic ray ionisation rate, confirming that, for our default value and higher, cosmic rays do indeed dominate the ionisation balance in this fully shielded regime. In the right hand panels we see that the cooling function is also significantly affected, as cosmic rays are the primary source of heating in fully shielded gas at these temperatures and densities, so increasing the cosmic ray ionisation rate by a factor of ten above our default value increases the thermal equilibrium temperature from around 100 K to 300 K. Furthermore, when we decrease it by a factor of ten below our default value, we find that the cooling rate from molecular hydrogen increases and more strongly dominates the cooling function.

2.5 Cooling in non-equilibrium interstellar gas

The cooling functions presented in the previous section were calculated in chemical equilibrium. We now investigate what impact non-equilibrium chemistry can have on the cooling rates of interstellar gas. We consider solar metallicity gas that is cooling either isochorically or isobarically in the presence of the Haardt & Madau (2001) extragalactic UV background for different densities. Isochoric cooling is relevant to applications in hydrodynamic simulations, in which cooling over individual hydrodynamic timesteps is typically done at fixed density. Isochoric cooling is also relevant for rapidly cooling gas where the cooling time is shorter

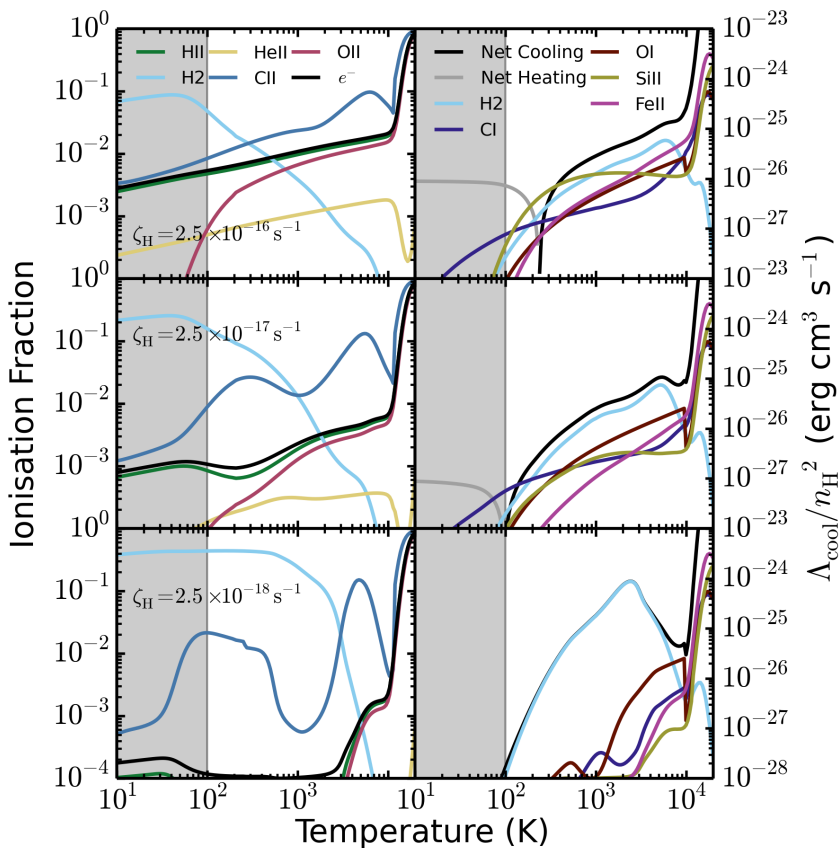


Figure 2.6: Comparison of the equilibrium ionisation fractions (*left*) and cooling functions (*right*) for three different values of the cosmic ray ionisation rate of hydrogen: $2.5 \times 10^{-16} \text{ s}^{-1}$ (*top row*), $2.5 \times 10^{-17} \text{ s}^{-1}$ (*middle row*) and $2.5 \times 10^{-18} \text{ s}^{-1}$ (*bottom row*). These were calculated using our chemical model at solar metallicity and a density $n_{\text{H}} = 1 \text{ cm}^{-3}$ in the absence of UV radiation. The shaded grey region highlights temperatures below 100 K that are outside the range of temperatures that we are primarily interested in, but we include this regime here for completeness. The cosmic ray ionisation rate, which is uncertain and may vary with environment, has a significant effect on the abundances and cooling of self shielded gas.

than the dynamical or sound crossing times for self gravitating or externally confined gas respectively. Isobaric cooling is relevant more generally in interstellar gas as the different phases of the ISM are usually in pressure equilibrium, so a parcel of gas that is not subject to heating events such as shocks or stellar feedback would tend to cool at constant pressure.

We start these calculations from chemical equilibrium and consider two different initial temperatures. Starting from $T = 10^4 \text{ K}$ corresponds to gas that is cooling from the warm phase of the ISM to the cold phase, while starting from $T = 10^6 \text{ K}$ corresponds to gas that has been strongly heated, for example by a supernova

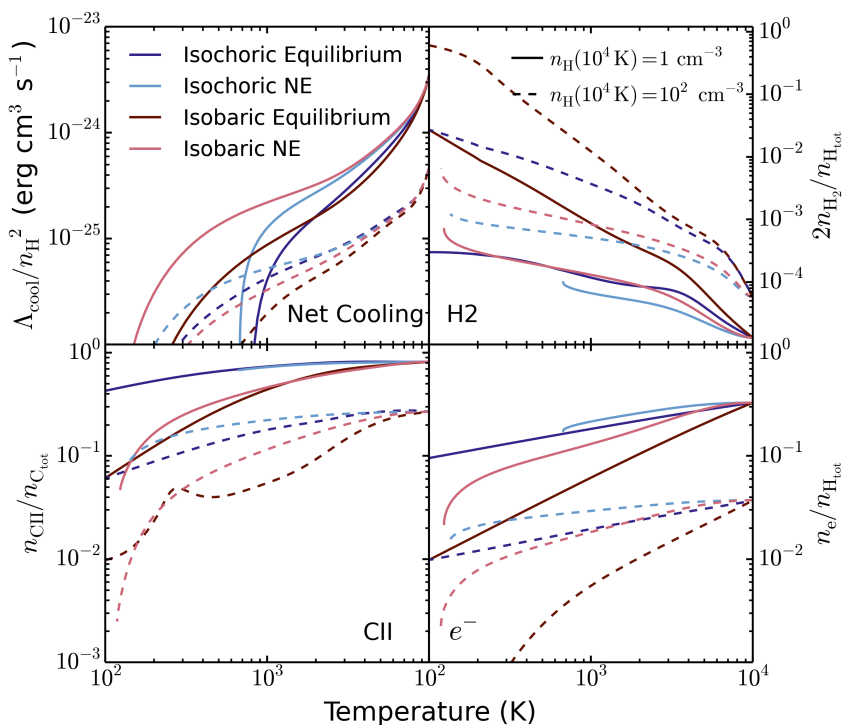


Figure 2.7: Non-equilibrium cooling functions (*top left panel*) and abundances of H_2 (*top right*), CII (*bottom left*) and electrons (*bottom right*) in gas cooling isochorically or isobarically from 10^4 K, compared to their values in chemical equilibrium. These were calculated using our chemical model in the presence of the redshift zero Haardt & Madau (2001) extragalactic UV background at solar metallicity and densities at $T = 10^4$ K of $n_{\text{H}}(10^4 \text{ K}) = 1 \text{ cm}^{-3}$ (*solid lines*) and $n_{\text{H}}(10^4 \text{ K}) = 10^2 \text{ cm}^{-3}$ (*dashed lines*).

event, and is subsequently cooling back towards the cold phase of the ISM. We compare the resulting net radiative cooling rates of the gas with the equilibrium cooling functions in sections 2.5.1 and 2.5.2 below.

2.5.1 Cooling from $T = 10^4$ K

The non-equilibrium cooling functions starting from $T = 10^4$ K are compared with their corresponding equilibrium cooling functions in the top left panel of figure 2.7, while the remaining panels compare the abundances of H_2 , CII and electrons. We see that the non-equilibrium gas tends to have higher net cooling rates than in equilibrium. This is because the electron density is decreasing as the gas cools, but it takes a finite time for the electrons to recombine with ions. Thus, if the recombination time is long compared to the cooling time, there will be a recombination lag that results in a higher electron density at a given temperature than we would expect in equilibrium, which is what we see in the bottom right

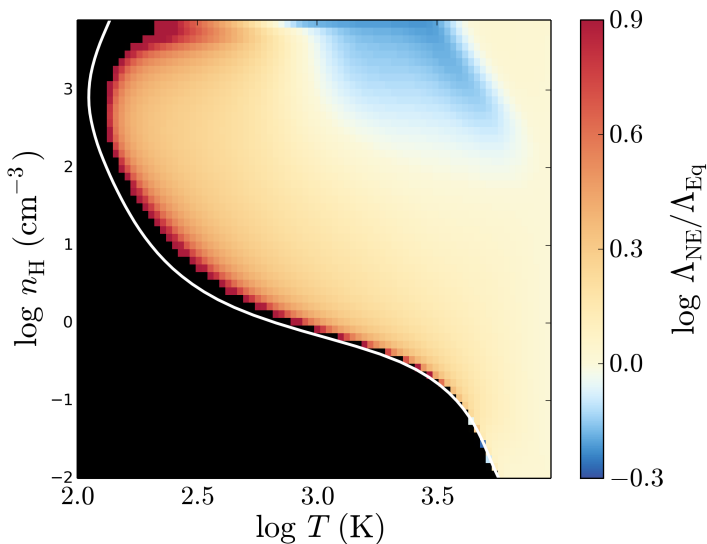


Figure 2.8: The ratio of the non-equilibrium cooling rate of gas cooling isochorically from chemical equilibrium at 10^4 K, Λ_{NE} , to the cooling rate in chemical equilibrium, Λ_{Eq} , plotted against temperature and density. These were calculated for a solar metallicity gas in the presence of the redshift zero Haardt & Madau (2001) extragalactic UV background. Blue regions indicate where non-equilibrium effects suppress the cooling rate, while red and yellow regions indicate where they enhance the cooling rate. The black region indicates where there is net heating in chemical equilibrium. The white curve shows the minimum temperature to which the isochorically cooling gas is able to cool to before there is net heating in the non-equilibrium cooling function. This is generally below the thermal equilibrium temperature. The non-equilibrium and equilibrium rates differ by up to an order of magnitude.

panel of figure 2.7. This recombination lag enhances the radiative cooling rate, which is typically driven by electron-ion collisions. Furthermore, the photoheating rate depends on the neutral fraction, so the recombination lag will also suppress the photoheating of the gas.

One exception to the above trend can be seen in isochorically cooling gas at a density $n_{\text{H}} = 10^2 \text{ cm}^{-3}$ (the blue dashed curves in figure 2.7). In this example the cooling rate around a temperature $T \sim 4000$ K is slightly lower than in equilibrium. At this temperature the contribution to the equilibrium net cooling rate from molecular hydrogen is comparable to that from SiII and FeII, the other dominant coolants. However, the formation time for molecular hydrogen is long compared to the cooling time-scale here, which results in a lower H_2 abundance, as can be seen in the top right panel. Hence its contribution to the cooling rate is suppressed in the non-equilibrium cooling function.

The non-equilibrium cooling functions are generally able to cool to lower temperatures than their corresponding equilibrium cooling functions. For example, in the isochoric cooling functions at a density $n_{\text{H}} = 1 \text{ cm}^{-3}$ (blue solid curves in the

top left panel of figure 2.7), the equilibrium net cooling rate becomes negative (net heating) at $T \sim 850$ K, whereas the isochorically cooling gas cools to $T \sim 700$ K. Thus non-equilibrium effects enable an isochorically or isobarically cooling gas to cool below the thermal equilibrium temperature, before heating back up towards its final thermal and chemical equilibrium. In figure 2.7 we only plot the non-equilibrium rates and abundances down to the temperature at which the gas begins to heat up again.

Furthermore, for some species, such as CII, the abundances in the examples presented here tend to remain close to equilibrium. For other species, such as H_2 , the abundances in isochorically or isobarically cooling gas can differ by up to an order of magnitude from their equilibrium values.

To illustrate the density dependence of the non-equilibrium effects on the cooling rate, we show in figure 2.8 the ratio of the non-equilibrium cooling rate of gas cooling isochorically from chemical equilibrium at 10^4 K to the cooling rate in chemical equilibrium, plotted against temperature and density. These were calculated for solar metallicity in the presence of the redshift zero Haardt & Madau (2001) extragalactic UV background (more examples can be found on our website). Blue regions in this plot indicate where the non-equilibrium effects suppress the cooling rate, while red and yellow regions indicate where they enhance the cooling rate. The black region shows where the equilibrium net cooling rate is negative (i.e. there is net heating). The white curve shows the minimum temperature to which the isochorically cooling gas is able to cool before there is net heating in the non-equilibrium cooling function. We see that the gas is generally able to cool below the thermal equilibrium temperature.

For most densities in figure 2.8, the enhancement of the cooling rate in non-equilibrium compared to the equilibrium cooling rate increases smoothly from the initial temperature of 10^4 K down to the thermal equilibrium temperature. This enhancement can reach up to a factor ~ 10 . However, at high densities ($n_H \gtrsim 10^2 \text{ cm}^{-3}$), the cooling rate in non-equilibrium is suppressed at temperatures around a few thousand Kelvin. This corresponds to the region where molecular hydrogen dominates the cooling rate. This figure highlights in which regions of the density-temperature plane these two opposing non-equilibrium effects are important.

2.5.2 Cooling from $T = 10^6$ K

In the top left panel of figure 2.9 we compare the non-equilibrium cooling functions starting from $T = 10^6$ K to their corresponding equilibrium cooling functions, while the abundances of H_2 , CII and electrons are shown in the remaining panels. At high temperatures ($> 10^4$ K) we find that non-equilibrium effects tend to decrease the net cooling rates. This agrees with what Oppenheimer & Schaye (2013a) found for gas typical of the intergalactic medium, and is caused by the recombination lag allowing species in higher ionisation states to persist down to lower temperatures. The electronic transitions in these high ionisation states are more energetic compared to those in the lower ionisation states, and thus they are more difficult to excite at these lower temperatures. Hence the cooling rates

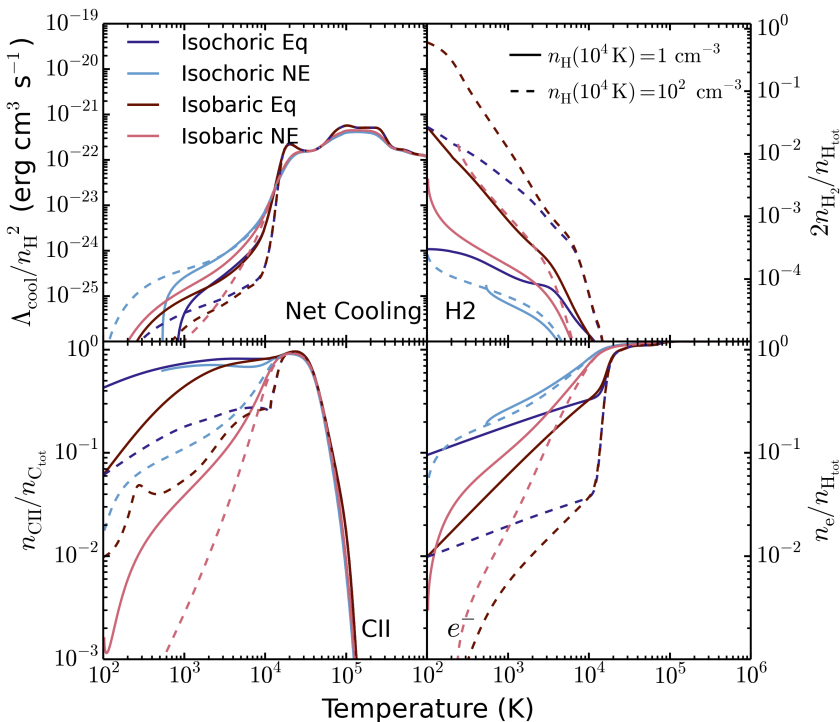


Figure 2.9: As figure 2.7, but for gas cooling from 10^6 K. Note that for the isobaric cooling curves, the densities given in the legend are valid at $T = 10^4$ K.

from these more highly ionised species are smaller, and thus the net cooling rate is suppressed with respect to the cooling rate in chemical equilibrium.

Once the gas temperature drops below 10^4 K, the non-equilibrium cooling rates generally become higher than the equilibrium cooling functions, similar to the trends we saw in figure 2.7. The most significant differences that we see compared to the previous figure are for gas at a density $n_{\text{H}} = 10^2 \text{ cm}^{-3}$. In this example the isochoric non-equilibrium cooling curve in figure 2.9 shows significantly higher cooling rates than in figure 2.7. This is because recombination lags induced as the gas cooled from 10^6 K to 10^4 K still persist and thus the electron density is even higher, as can be seen in the bottom right panel of figure 2.9, which further enhances the metal line cooling. The isobarically cooling gas at $n_{\text{H}} = 10^2 \text{ cm}^{-3}$ also shows an enhanced net cooling rate just below 10^4 K compared to figure 2.7, for the same reason. However, below $T \sim 2000$ K the cooling rate drops below the corresponding isobaric equilibrium cooling function. This is because the cooling is dominated by H_2 here, which is suppressed in the non-equilibrium cooling curve due to the long formation time-scale of molecular hydrogen, as can be seen from the top right panel.

In the bottom left panel of figure 2.9, the non-equilibrium abundances of CII remain very close to their equilibrium values down to the peak at $T \sim 2 \times 10^4$ K.

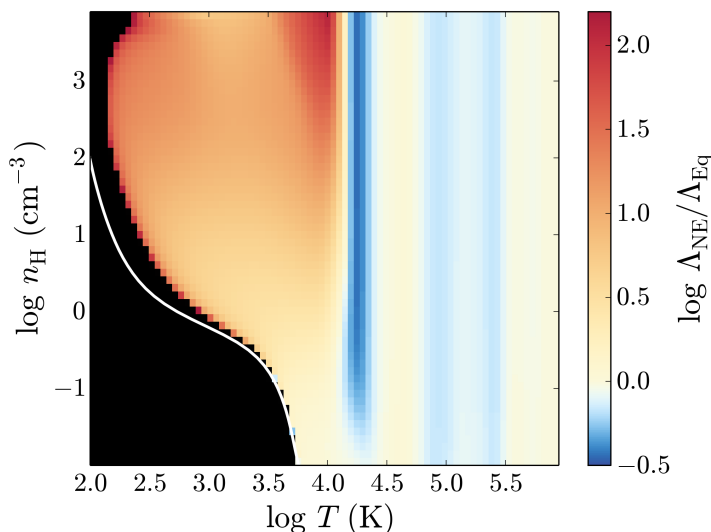


Figure 2.10: As figure 2.8, but for gas cooling isochorically from 10^6 K. The non-equilibrium rate above 10^4 K is generally suppressed compared to the equilibrium cooling rate, whereas below 10^4 K the enhancement of the cooling rate in non-equilibrium can exceed two orders of magnitude and is thus even greater than we found for gas cooling from 10^4 K in figure 2.8.

However, below this temperature the CII abundance of the cooling gas tends to fall below the equilibrium abundance, by up to an order of magnitude. We saw in figure 2.7 that CII exhibited only a small recombination lag when the gas starts cooling from 10^4 K, which indicates that it has a relatively short recombination time compared to, for example, HII. Furthermore, the bottom right panel of figure 2.9 demonstrates that the electron abundance below 10^4 K is even higher in this example than in gas that starts cooling from 10^4 K, due to recombination lags of other species that persist from higher temperatures. This suggests that, as the gas cools, the CII rapidly recombines to a lower abundance than in equilibrium due to the enhanced electron abundance.

In figure 2.10 we show the ratio of the non-equilibrium cooling rate of gas cooling isochorically from chemical equilibrium at 10^6 K to the cooling rate in chemical equilibrium, plotted against temperature and density, for solar metallicity gas in the presence of the Haardt & Madau (2001) extragalactic UV background. At temperatures $T > 10^4$ K, we see that the non-equilibrium cooling rate is suppressed compared to the equilibrium cooling rate, for the reasons discussed above. This suppression becomes approximately independent of density for $n_{\text{H}} \gtrsim 0.1 \text{ cm}^{-3}$. Below 10^4 K, the non-equilibrium cooling rate is enhanced due to the higher electron abundance caused by recombination lags. This enhancement is even greater than we saw in figure 2.8 for gas that starts cooling from 10^4 K, with an increase in the non-equilibrium cooling rate of up to a factor ~ 100 compared to in equilibrium. Furthermore, this enhancement outweighs the suppression of the non-equilibrium cooling rate at $n_{\text{H}} \gtrsim 10^2 \text{ cm}^{-3}$ and temperatures around a few thousand Kelvin that

is caused by the long formation time-scale of molecular hydrogen.

2.6 Conclusions

We have presented a model to follow the non-equilibrium thermal and chemical evolution of interstellar gas that is designed to be incorporated into hydrodynamic simulations of galaxy formation. Our chemical network includes 157 species: the molecules H_2 , H_2^+ , H_3^+ , OH , H_2O , C_2 , O_2 , HCO^+ , CH , CH_2 , CH_3^+ , CO , CH^+ , CH_2^+ , OH^+ , H_2O^+ , H_3O^+ , CO^+ , HOC^+ and O_2^+ , along with electrons and all ionisations states of the 11 elements that dominate gas cooling (H, He, C, N, O, Ne, Mg, Si, S, Ca and Fe). Our model includes chemical reactions on dust grains, most importantly H_2 formation, and thermal processes involving dust, such as photoelectric heating (but not yet thermal dust emission). We also include photochemical reactions and cosmic ray ionisations, along with their associated heating rates.

While we do not include metal depletion on dust grains in our model, as the depletion factors of metals are highly uncertain, we show that the depletion factors measured by Jenkins (2009) could potentially have a large effect on the cooling function of interstellar gas (see figure 2.1).

We have compared the equilibrium ionisation balance and cooling functions predicted by our model with the photoionisation code CLOUDY for a range of densities $10^{-2} \leq n_{\text{H}} \leq 10^4 \text{ cm}^{-3}$, temperatures $10 \text{ K} \leq T \leq 2 \times 10^4 \text{ K}$, metallicities $0 \leq Z \leq Z_{\odot}$ and in the presence of four UV radiation fields: the Black (1987) interstellar radiation field, ten times this interstellar radiation field, the Haardt & Madau (2001) extragalactic UV background and finally in the absence of UV radiation. These physical parameters include the typical conditions in the diffuse ISM that we are interested in, and also extend down to colder gas. The equilibrium abundances and cooling functions predicted by our model generally agree very well with those from CLOUDY (see figures 2.3, 2.4 and 2.5), and most remaining differences are due to different choices for uncertain rates. Additional figures showing all of these comparisons can be found on our website ⁹.

In our equilibrium cooling functions we find that the cooling rate of interstellar gas is typically dominated by CII, SiII and FeII, with OI becoming important at high densities ($n_{\text{H,tot}} \gtrsim 10^2 \text{ cm}^{-3}$) and when the UV radiation field is weak (for example the redshift zero Haardt & Madau 2001 extragalactic UV background). We also find that at these high densities and low UV radiation intensities molecular hydrogen dominates the cooling function, typically peaking around 1000 – 2000 K. See table 2.2 for a summary of the dominant coolants at solar metallicity. In primordial gas, molecular hydrogen is the only significant source of cooling below $T \sim 8000 \text{ K}$ in our model.

We note that Glover & Jappsen (2007) also investigated which species contribute significantly to the cooling rate of interstellar gas in order to determine which ions to include in their chemical network. They looked at a similar range of physical parameters (although only at a metallicity of $0.1Z_{\odot}$). We generally agree with their conclusions, although they found that FeII only contributed at most

⁹<http://noneqism.strw.leidenuniv.nl>

$\sim 10\% - 20\%$ to the cooling rate, whereas we find that it is one of the most important coolants in several cases (see for example figure 2.3). However, Glover & Jappsen (2007) used the elemental abundance ratios from Sembach et al. (2000), which are based on observations of the warm neutral medium and therefore include the effects of depletion of metals onto dust grains. Since iron is strongly affected by depletion onto dust grains (see table 2 of Sembach et al. 2000), and we do not include this depletion in our model, this likely explains why FeII cooling is much more important in our model than in Glover & Jappsen (2007).

We also calculate the non-equilibrium abundances and cooling functions of gas that is cooling isochorically or isobarically. We find that non-equilibrium chemistry tends to increase the cooling rates below 10^4 K compared to the cooling rates in chemical (including ionisation) equilibrium, due to a recombination lag that results in a higher electron density at a given temperature (see figures 2.7 and 2.8). We find enhancements in the cooling rate of up to an order of magnitude for gas that starts cooling from 10^4 K. This enables the gas to cool below its thermal equilibrium temperature, before subsequently heating back up to thermal and chemical equilibrium.

The abundance of molecular hydrogen in isochorically or isobarically cooling gas is lower than in equilibrium, by up to an order of magnitude, due to its relatively long formation time-scale compared to the cooling time. This can reduce the cooling rate if H_2 dominates the equilibrium cooling function, i.e. for high density ($n_{\text{H,tot}} \gtrsim 10^2 \text{ cm}^{-3}$) gas at temperatures around a few thousand Kelvin.

Non-equilibrium effects above 10^4 K generally suppress the cooling rates as higher ionisation species persist to lower temperatures. Such species have lower cooling rates as their electronic transitions are more energetic and thus are more difficult to excite at these lower temperatures. Furthermore, if we consider gas that starts cooling from a temperature 10^6 K, the resulting recombination lag results in a higher electron density once it reaches 10^4 K compared to equilibrium. Thus the enhancement of the net cooling rate below 10^4 K due to non-equilibrium effects will be greater if the gas starts cooling from $T \gg 10^4$ K than if we start in equilibrium at $\sim 10^4$ K. For gas cooling from 10^6 K, we find enhancements of up to two orders of magnitude (see figure 2.10).

Throughout this paper we have focussed on photoionised gas in the optically thin regime, although we also considered a case without any UV radiation. However, gas that is in the cold phase of the ISM, in particular molecular clouds, will become shielded from the UV radiation field, both by dust and by the gas itself, and hence the radiation field will vary with the depth into the cloud. In paper II we shall describe the methods that we use to calculate the attenuated photochemical rates in shielded gas and present the resulting chemistry and cooling properties under such conditions.

Acknowledgments

We thank Andreas Pawlik and Ewine van Dishoeck for useful discussions. We gratefully acknowledge support from Marie Curie Training Network CosmoComp

(PITN-GA-2009- 238356) and from the European Research Council under the European Union's Seventh Framework Programme (FP7/2007-2013) / ERC Grant agreement 278594-GasAroundGalaxies.

2.7 Appendix A: Dust temperature

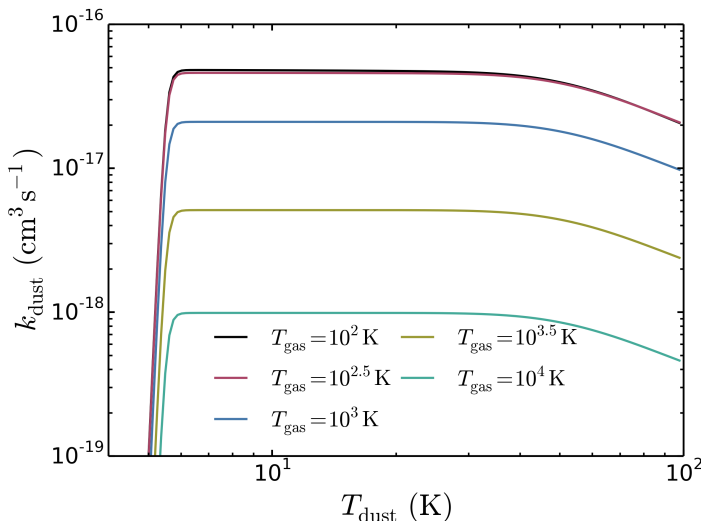


Figure 2.11: Rate coefficient for the formation of molecular hydrogen on dust grains, calculated from equation 2.12, plotted against dust temperature for different gas temperatures.

The rate of formation of molecular hydrogen on dust grains depends on the temperature of the dust as well as the gas, so we need to make an assumption about the grain temperature. Glover & Clark (2012) calculate the dust temperature by assuming that it is in thermal equilibrium and hence solving the thermal balance equation (their equation A2), but this adds to the computational cost of the model. To investigate the impact that dust temperature has on the molecular hydrogen abundance in our model we plot in figure 2.11 the rate coefficient k_{dust} (obtained by dividing equation 2.12 by n_{HI}) as a function of the dust temperature for different gas temperatures in the regime relevant to the diffuse ISM (10^2 K to 10^4 K). Below $T_{\text{dust}} \approx 6$ K the rate falls very rapidly, but we would not expect to find such low dust temperatures in the diffuse ISM. At higher dust temperatures the rate of molecular hydrogen formation on dust grains remains fairly constant up to 50 K, at which point it begins to decrease again, falling by a factor of just over 2 by $T_{\text{dust}} = 100$ K. In figure 2.12 we compare the range of dust temperatures calculated by CLOUDY using ten grain size bins (from 0.005 to 0.25 μm , assuming the power-law size distribution of Mathis et al. 1977) as a function of the gas temperature, in the presence of different radiation fields. These were calculated for carbonaceous grains, but we found that the temperatures of silicate grains are

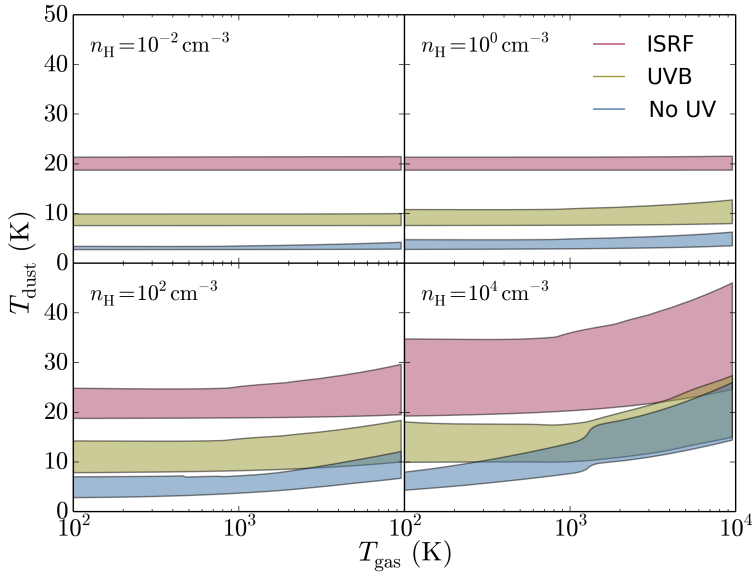


Figure 2.12: The range of (carbonaceous) dust grain temperatures calculated by CLOUDY across the 10 grain size bins, plotted against gas temperature in the presence of the Black (1987) interstellar radiation field (*red*), the redshift zero Haardt & Madau (2001) extragalactic UV background (*yellow*) and in the absence of UV radiation (*blue*).

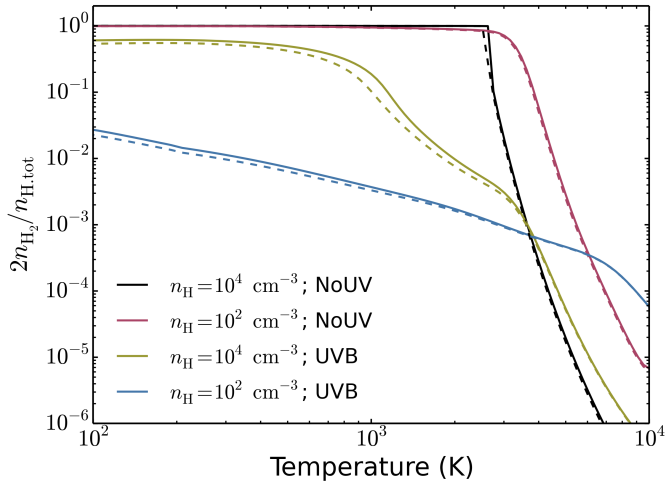


Figure 2.13: Equilibrium molecular hydrogen fractions as a function of gas temperature, calculated from our model using a constant dust temperature $T_{\text{dust}} = 10 \text{ K}$ (*solid lines*) and $T_{\text{dust}} = 50 \text{ K}$ (*dashed lines*), either in the presence of the redshift zero Haardt & Madau (2001) extragalactic UV background (*UVB*) or in the absence of UV (*NoUV*).

similar. Even in the presence of the interstellar radiation field of Black (1987) the highest dust temperatures in CLOUDY only just reach 50 K, and even this temperature is only reached for gas temperatures near 10^4 K, where molecular hydrogen becomes unimportant. We therefore would not expect the rate of molecular hydrogen formation on dust grains to be significantly affected by variations in the dust temperature in the range of physical conditions that we are interested in here, i.e. those relevant to the diffuse ISM.

To confirm the insensitivity to the dust temperature, we compare the molecular hydrogen fractions calculated using our model assuming different fixed dust temperatures. These are shown in figure 2.13. We find that the change in molecular hydrogen fraction as we increase the dust temperature from 10 K to 50 K is indeed negligible. We therefore choose to fix the dust temperature at a constant 10 K in our model.

2.8 Appendix B: Chemical reactions

Reaction No. ^a	Reaction	Ref ^b	Reaction No. ^a	Reaction	Ref ^b
1	$H + e^- \rightarrow H^- + \gamma$	1	26	$He^+ + H \rightarrow He + H^+$	17
2	$H^- + H \rightarrow H_2 + e^-$	2	27	$He + H^+ \rightarrow He^+ + H$	18
3	$H + H^+ \rightarrow H_2^+ + \gamma$	3	51	$H^- + \gamma \rightarrow H + e^-$	19, 20
4	$H + H_2^+ \rightarrow H_2 + H^+$	4	52	$H_2^+ + \gamma \rightarrow H + H^+$	21
5	$H^- + H^+ \rightarrow H + H$	5	53	$H_2 + \gamma \rightarrow H + H$	This work
6	$H_2^+ + e^- \rightarrow H + H$	6	54	$H_2 + \gamma \rightarrow H_2^+ + e^-$	22, 23
7	$H_2 + H^+ \rightarrow H_2^+ + H$	7	60	$H + H \xrightarrow{dust} H_2$	24
8	$H_2 + e^- \rightarrow H + H + e^-$	8	61	$H^+ + e^- \xrightarrow{dust} H$	25
9	$H_2 + H \rightarrow H + H + H$	9, 10	63	$He^+ + e^- \xrightarrow{dust} He$	25
10	$H_2 + H_2 \rightarrow H_2 + H + H$	11	67	$H + cr \rightarrow H^+ + e^-$	26, 27
11	$H + e^- \rightarrow H^+ + e^- + e^-$	12	69	$He + cr \rightarrow He^+ + e^-$	27, 28
13 ^c	$H^+ + e^- \rightarrow H + \gamma$	13	70	$H_2 + cr \rightarrow H_2^+ + e^-$	28
15	$H^- + e^- \rightarrow H + e^- + e^-$	12	83	$H_2^+ + H^- \rightarrow H + H + H$	29
16	$H^- + H \rightarrow H + H + e^-$	12	84	$H_2 + e^- \rightarrow H^- + H$	30
17	$H^- + H^+ \rightarrow H_2^+ + e^-$	14	85	$H_2 + He^+ \rightarrow He + H + H^+$	31
24	$He + e^- \rightarrow He^+ + e^- + e^-$	12	86	$H_2 + He^+ \rightarrow H_2^+ + He$	31
25 ^c	$He^+ + e^- \rightarrow He + \gamma$	15, 16	87	$H_2^+ + H^- \rightarrow H_2 + H$	29

^aThe reaction numbers match those used in the code.

^b1 - Wishart (1979); 2 - Bruhns et al. (2010); 3 - Ramaker & Peek (1976); 4 - Karpas et al. (1979); 5 - Moseley et al. (1970); 6 - Schneider et al. (1994); 7 - Savin et al. (2004); 8 - Trevisan & Tennyson (2002); 9 - Mac Low & Shull (1986); 10 - Lepp & Shull (1983); 11 - Martin et al. (1998); 12 - Janev et al. (1987); 13 - Ferland et al. (1992); 14 - Poulaert et al. (1978); 15 - Hummer & Storey (1998); 16 - Aldrovandi & Péquignot (1973); 17 - Zygelman et al. (1989); 18 - Kimura et al. (1993); 19 - de Jong (1972); 20 - Shapiro & Kang (1987); 21 - van Dishoeck (1988); 22 - Yan et al. (1998); 23 - Wilms et al. (2000); 24 - Cazaux & Tielens (2002); 25 - Weingartner & Draine (2001b); 26 - Williams et al. (1998); 27 - Furlanetto & Stoever (2010); 28 - Le Teuff et al. (2000); 29 - Dalgarno & Lepp (1987); 30 - Schulz & Asundi (1967); 31 - Barlow (1984); 32 - Dove et al. (1987); 33 - Linder et al. (1995); 34 - Kim et al. (1975); 35 - Petuchowski et al. (1989); 36 - Data from McCall et al. (2004), fit by Woodall et al. (2007); 37 - Geppert et al. (2005); 38 - Prasad & Huntress (1980); 39 - Nelson & Langer (1999); 40 - Sidhu et al. (1992); 41 - Gerlich & Horning (1992); 42 - Dalgarno et al. (1990); 43 - Singh et al. (1999); 44 - Smith et al. (2002); 45 - Wagner-Redeker et al. (1985); 46 - Dean et al. (1991); 47 - Harding et al. (1993); 48 - Smith et al. (2004); 49 - Baulch et al. (1992); 50 - Murrell & Rodriguez (1986); 51 - Warnatz (1984); 52 - Frank (1986); 53 - Data from Frank & Just (1984) and Frank et al. (1988), fit by Le Teuff et al. (2000); 54 - Mitchell & Deveau (1983); 55 - Fairbairn (1969); 56 - Glover et al. (2010); 57 - Natarajan & Roth (1987); 58 - Tsang & Hampson (1986); 59 - Oldenberg et al. (1992); 60 - Carty et al. (2006); 61 - Cohen & Westberg (1979); 62 - Azatyan et al. (1975); 63 - Adams et al. (1984); 64 - McEwan et al. (1999); 65 - Viggiano et al. (1980); 66 - Smith & Adams (1977a,b); 67 - Fehsenfeld (1976); 68 - Smith et al. (1978); 69 - Adams et al. (1980); 70 - Milligan & McEwan (2000); 71 - Dubernet et al. (1992); 72 - Jones et al. (1981); 73 - Raksit & Warneck (1980); 74 - Kim et al. (1974); 75 - Anicich et al. (1976); 76 - Adams et al. (1978); 77 - Smith et al. (1992); 78 - Mauclaire et al. (1978a,b); 79 - Adams & Smith (1976a,b); 80 - Federer et al. (1984); 81 - Peart & Hayton (1994); 82 - Mitchell (1990); 83 - Larson et al. (1998); 84 - Rosén et al. (2000); 85 - Jensen et al. (2000); 86 - Alge et al. (1983); 87 - Rosén et al. (1998); 88 - Stancil & Dalgarno (1998); 89 - Andreazza & Singh (1997); 90 - Barinovs & van Hemert (2006); 91 - Herbst (1985); 92 - Field et al. (1980); 93 - Orel (1987); 94 - Abel et al. (2002); 95 - Cohen & Westberg (1983); 96 - Walkauskas & Kaufman (1975); 97 - Data from Fairbairn (1969) and Slack (1976), fit by Le Teuff et al. (2000); 98 - MacGregor & Berry (1973); 99 - van Dishoeck (1987); 100 - van Dishoeck et al. (2006); 101 - van Dishoeck & Dalgarno (1984); 102 - Lee (1984); 103 - Sternberg & Dalgarno (1995); 104 - Visser et al. (2009); 105 - Gredel et al. (1989); 106 - Maloney et al. (1996); 107 - Tielens & Hollenbach (1985); 108 - Oppenheimer & Schaye (2013a); 109 - Verner & Yakovlev (1995); 110 - Verner et al. (1996); 111 - Kaastra & Mewe (1993); 112 - Lotz (1967); 113 - Langer (1978); 114 - Scott et al. (1997)

^cWe switch from the case A to case B recombination rates for hydrogen and helium when $\tau_{HI} > 1$ and $\tau_{HeI} > 1$ respectively.

Table 2.3: Summary of chemical reactions.

88	$H_2 + He \rightarrow H + H + He$	32	168	$CO + H_3^+ \rightarrow HOC^+ + H_2$	34
97	$H_3^+ + H_2 \rightarrow H_3^+ + H$	33	169	$HCO^+ + C \rightarrow CO + CH^+$	28
100	$CO + H_3^+ \rightarrow HCO^+ + H_2$	34	170	$HCO^+ + H_2O \rightarrow CO + H_3O^+$	76
101	$He^+ + CO \rightarrow C^+ + O + He$	35	171	$CH + H^+ \rightarrow CH^+ + H$	28
106	$H_3^+ + e^- \rightarrow H_2 + H$	36	172	$CH_2 + H^+ \rightarrow CH_2^+ + H$	28
107	$HCO^+ + e^- \rightarrow CO + H$	37	173	$CH_2 + He^+ \rightarrow C^+ + He + H_2$	28
108	$H_3^+ + Fe \rightarrow Fe^+ + H_2 + H$	38	174	$C_2 + He^+ \rightarrow C^+ + C + He$	28
111	$HCO^+ + \gamma \rightarrow CO + H^+$	39	175	$OH + H^+ \rightarrow OH^+ + H$	28
112	$H_3^+ + H \rightarrow H_2^+ + H_2$	40	176	$OH + He^+ \rightarrow O^+ + He + H$	28
113	$CO + He^+ \rightarrow C + O^+ + He$	35	177	$H_2O + H^+ \rightarrow H_2O^+ + H$	77
114	$H_3^+ + e^- \rightarrow H + H + H$	36	178	$H_2O + He^+ \rightarrow OH + He + H^+$	78
115	$H_2 + H^+ \rightarrow H_3^+ + \gamma$	41	179	$H_2O + He^+ \rightarrow OH^+ + He + H$	78
116	$C + O \rightarrow CO + \gamma$	42, 43	180	$H_2O + He^+ \rightarrow H_2O^+ + He$	78
117	$OH + H \rightarrow O + H + H$	28	181	$O_2 + H^+ \rightarrow O_2^+ + H$	77
118	$HOC^+ + H_2 \rightarrow HCO^+ + H_2$	44	182	$O_2 + He^+ \rightarrow O_2^+ + He$	79
119	$HOC^+ + CO \rightarrow HCO^+ + CO$	45	183	$O_2 + He^+ \rightarrow O^+ + O + He$	79
120	$C + H_2 \rightarrow CH + H$	46	184	$O_2^+ + C \rightarrow O_2 + C^+$	28
121	$CH + H \rightarrow C + H_2$	47	185	$CO^+ + H \rightarrow CO + H^+$	80
122	$CH + H_2 \rightarrow CH_2 + H$	28	186	$C^- + H^+ \rightarrow C + H$	81
123	$CH + C \rightarrow C_2 + H$	48	187	$O^- + H^+ \rightarrow O + H$	28
124	$CH + O \rightarrow CO + H$	49, 50	188	$He^+ + H^- \rightarrow He + H$	81
125	$CH_2 + H \rightarrow CH + H_2$	51	189	$CH^+ + e^- \rightarrow C + H$	82
126	$CH_2 + O \rightarrow CO + H + H$	52	190	$CH_2^+ + e^- \rightarrow CH + H$	83
127	$CH_2 + O \rightarrow CO + H_2$	53	191	$CH_2^+ + e^- \rightarrow C + H + H$	83
128	$C_2 + O \rightarrow CO + C$	54, 55, 56	192	$CH_2^+ + e^- \rightarrow C + H_2$	83
129	$O + H_2 \rightarrow OH + H$	57	193	$CH_3^+ + e^- \rightarrow CH_2 + H$	82
130	$OH + H \rightarrow O + H_2$	58	194	$CH_3^+ + e^- \rightarrow CH + H_2$	82
131	$OH + H_2 \rightarrow H_2O + H$	59	195	$CH_3^+ + e^- \rightarrow CH + H + H$	28
132	$OH + C \rightarrow CO + H$	48	196	$OH^+ + e^- \rightarrow O + H$	82
133	$OH + O \rightarrow O_2 + H$	28, 56, 60	197	$H_2O^+ + e^- \rightarrow O + H + H$	84
134	$OH + OH \rightarrow H_2O + O$	48	198	$H_2O^+ + e^- \rightarrow O + H_2$	84
135	$H_2O + H \rightarrow H_2 + OH$	61	199	$H_2O^+ + e^- \rightarrow OH + H$	84
136	$O_2 + H \rightarrow OH + O$	28	200	$H_3O^+ + e^- \rightarrow H + H_2O$	85
137	$O_2 + H_2 \rightarrow OH + OH$	62	201	$H_3O^+ + e^- \rightarrow OH + H_2$	85
138	$O_2 + C \rightarrow CO + O$	28, 48	202	$H_3O^+ + e^- \rightarrow OH + H + H$	85
139	$CO + H \rightarrow C + OH$	28	203	$H_3O^+ + e^- \rightarrow O + H + H_2$	85
140	$C + H_3^+ \rightarrow CH^+ + H$	28	204	$O_2^+ + e^- \rightarrow O + O$	86
141	$C + H_3^+ \rightarrow CH^+ + H_2$	28	205	$CO^+ + e^- \rightarrow C + O$	87
142	$C^+ + H_2 \rightarrow CH^+ + H$	63	206	$HCO^+ + e^- \rightarrow OH + C$	37
143	$CH^+ + H \rightarrow C^+ + H_2$	64	207	$HOC^+ + e^- \rightarrow CO + H$	28
144	$CH^+ + H_2 \rightarrow CH_2^+ + H$	64	208	$H^- + C \rightarrow CH + e^-$	28
145	$CH^+ + O \rightarrow CO^+ + H$	65	209	$H^- + O \rightarrow OH + e^-$	28
146	$CH_2 + H^+ \rightarrow CH^+ + H_2$	28	210	$H^- + OH \rightarrow H_2O + e^-$	28
147	$CH_2^+ + H \rightarrow CH^+ + H_2$	28	211	$C^- + H \rightarrow CH + e^-$	28
148	$CH_2^+ + H_2 \rightarrow CH_3^+ + H$	66	212	$C^- + H_2 \rightarrow CH_2 + e^-$	28
149	$CH_2^+ + O \rightarrow HCO^+ + H$	28	213	$C^- + O \rightarrow CO + e^-$	28
150	$CH_2^+ + H \rightarrow CH_2^+ + H_2$	28	214	$O^- + H \rightarrow OH + e^-$	28
151	$CH_3^+ + O \rightarrow HCO^+ + H_2$	67	215	$O^- + H_2 \rightarrow H_2O + e^-$	28
152	$C_2 + O^+ \rightarrow CO^+ + C$	28	216	$O^- + C \rightarrow CO + e^-$	28
153	$O^+ + H_2 \rightarrow OH^+ + H$	68, 69	217	$C + e^- \rightarrow C^- + \gamma$	88
154	$O + H_3^+ \rightarrow OH^+ + H$	28	218	$C + H \rightarrow CH + \gamma$	38
155	$O + H_3^+ \rightarrow OH^+ + H_2$	70	219	$C + H_2 \rightarrow CH_2 + \gamma$	38
156	$OH + H_3^+ \rightarrow H_2O^+ + H_2$	28	220	$C + C \rightarrow C_2 + \gamma$	89
157	$OH + C^+ \rightarrow CO^+ + H$	71	221	$C^+ + H \rightarrow CH^+ + \gamma$	90
283	$OH + C^+ \rightarrow CO + H^+$	71	222	$C^+ + H_2 \rightarrow CH_2^+ + \gamma$	91
158	$OH^+ + H_2 \rightarrow H_2O^+ + H$	72	223	$C^+ + O \rightarrow CO^+ + \gamma$	42
159	$H_2O^+ + H_2 \rightarrow H_3O^+ + H$	73	224	$O + e^- \rightarrow O^- + \gamma$	28
160	$H_2O + H_3^+ \rightarrow H_3O^+ + H_2$	74	225	$O + H \rightarrow OH + \gamma$	28
161	$H_2O + C^+ \rightarrow HCO^+ + H$	75	226	$O + O \rightarrow O_2 + \gamma$	38
162	$H_2O + C^+ \rightarrow HOC^+ + H$	75	227	$OH + H \rightarrow H_2O + \gamma$	92
163	$H_3O^+ + C \rightarrow HCO^+ + H_2$	28	228	$H + H + H \rightarrow H_2 + H$	93, 94
164	$O_2 + C^+ \rightarrow CO^+ + O$	66	229	$H + H + H_2 \rightarrow H_2 + H_2$	95
165	$O_2 + C^+ \rightarrow CO + O^+$	66	230	$H + H + He \rightarrow H_2 + He$	96
166	$O_2 + CH_2^+ \rightarrow HCO^+ + OH$	66	231	$C + C + He \rightarrow C_2 + He$	56, 97
167	$O_2^+ + C \rightarrow CO^+ + O$	28	232	$C + O + He \rightarrow CO + He$	35, 49

Table 2.3: Continued.

233	$C^+ + O + He \rightarrow CO^+ + He$	35	273	$CH^+ + \gamma_{cr} \rightarrow C^+ + H$	105
234	$C + O^+ + He \rightarrow CO^+ + He$	35	274	$CH_2 + \gamma_{cr} \rightarrow CH_2^+ + e^-$	28
235	$O + H + He \rightarrow OH + He$	58	275	$CH_2 + \gamma_{cr} \rightarrow CH + H$	28
236	$OH + H + He \rightarrow H_2O + He$	49	276	$C_2 + \gamma_{cr} \rightarrow C + C$	105
237	$O + O + He \rightarrow O_2 + He$	51	277	$OH + \gamma_{cr} \rightarrow O + H$	105
238	$O + CH \rightarrow HCO^+ + e^-$	98	278	$H_2O + \gamma_{cr} \rightarrow OH + H$	105
239	$H_3^+ + \gamma \rightarrow H_2 + H^+$	99	279	$O_2 + \gamma_{cr} \rightarrow O + O$	105
240	$H_3^+ + \gamma \rightarrow H_2^+ + H$	99	280	$O_2 + \gamma_{cr} \rightarrow O_2^+ + e^-$	105
241	$C^- + \gamma \rightarrow C + e^-$	28	281	$CO + \gamma_{cr} \rightarrow C + O$	106
242	$CH + \gamma \rightarrow C + H$	100	303	$CO^+ + H_2 \rightarrow HCO^+ + H$	114
243	$CH + \gamma \rightarrow CH^+ + e^-$	21	304	$CO^+ + H_2 \rightarrow HOC^+ + H$	114
244	$CH^+ + \gamma \rightarrow C + H^+$	100	44	$C^+ + Si \rightarrow C + Si^+$	38
245	$CH_2 + \gamma \rightarrow CH + H$	100	79	$Fe + C^+ \rightarrow Fe^+ + C$	38
246	$CH_2 + \gamma \rightarrow CH_2^+ + e^-$	28	80	$Fe + Si^+ \rightarrow Fe^+ + Si$	107
247	$CH_2^+ + \gamma \rightarrow CH^+ + H$	100	294	$C^+ + Mg \rightarrow C + Mg^+$	38
248	$CH_2^+ + \gamma \rightarrow CH_2^+ + H$	28	295	$N^+ + Mg \rightarrow N + Mg^+$	38
249	$CH_3^+ + \gamma \rightarrow CH_2^+ + H_2$	28	296	$Si^+ + Mg \rightarrow Si + Mg^+$	38
250	$C_2 + \gamma \rightarrow C + C$	100	297	$S^+ + Mg \rightarrow S + Mg^+$	38
251	$O^- + \gamma \rightarrow O + e^-$	28	64	$C^+ + e^- \xrightarrow{dust} C$	25
252	$OH + \gamma \rightarrow O + H$	101	65	$O^+ + e^- \xrightarrow{dust} O$	25
253	$OH + \gamma \rightarrow OH^+ + e^-$	28	66	$Si^+ + e^- \xrightarrow{dust} Si$	25
254	$OH^+ + \gamma \rightarrow O + H^+$	100	77	$Fe^+ + e^- \xrightarrow{dust} Fe$	25
255	$H_2O + \gamma \rightarrow OH + H$	102	290	$Mg^+ + e^- \xrightarrow{dust} Mg$	25
256	$H_2O + \gamma \rightarrow H_2O^+ + e^-$	21	291	$S^+ + e^- \xrightarrow{dust} S$	25
257	$H_2O^+ + \gamma \rightarrow H_2^+ + O$	103	292	$Ca^+ + e^- \xrightarrow{dust} Ca$	25
258	$H_2O^+ + \gamma \rightarrow H^+ + OH$	103	293	$Ca^{++} + e^- \xrightarrow{dust} Ca^+$	25
259	$H_2O^+ + \gamma \rightarrow O^+ + H_2$	103	298	$He^+ + e^- \rightarrow He^{++} + e^- + e^-$	108
260	$H_2O^+ + \gamma \rightarrow OH^+ + H$	103	299	$He^+ + \gamma \rightarrow He^{++} + e^-$	108
261	$H_3O^+ + \gamma \rightarrow H^+ + H_2O$	103	300	$He^{++} + e^- \rightarrow He^+$	108
262	$H_3O^+ + \gamma \rightarrow H_2^+ + OH$	103	301	$He^{++} + H \rightarrow He^+ + H^+$	108
263	$H_3O^+ + \gamma \rightarrow H_2O^+ + H$	103	302	$He^+ + cr \rightarrow He^{++} + e^-$	112, 113
264	$H_3O^+ + \gamma \rightarrow OH^+ + H_2$	103	Collision ^{ab}	$A^{+i} + e^- \rightarrow A^{+i+1} + e^- + e^-$	108
265	$O_2 + \gamma \rightarrow O_2^+ + e^-$	100	Recomb. ^c	$A^{+i+1} + e^- \rightarrow A^{+i} + \gamma$	108
266	$O_2 + \gamma \rightarrow O + O$	100	PhotoIon	$A^{+i} + \gamma \rightarrow A^{+i+1} + e^-$	109, 110
267	$CO + \gamma \rightarrow C + O$	104	Auger	$A^{+i} + \gamma \rightarrow A^{+i+n} + ne^-$	109, 110, 11
268	$H_2 + cr \rightarrow H^+ + H + e^-$	28	CTHion	$A^{+i} + H^+ \rightarrow A^{+i+1} + H$	108
269	$H_2 + cr \rightarrow H^+ + H^-$	28	CTHrec	$A^{+i+1} + H \rightarrow A^{+i} + H^+$	108
89	$H_2 + cr \rightarrow H + H$	28	CTHeion	$A^{+i} + He^+ \rightarrow A^{+i+1} + He$	108
270	$CO + cr \rightarrow CO^+ + e^-$	28	CTHerec	$A^{+i+1} + He \rightarrow A^{+i} + He^+$	108
272	$CH + \gamma_{cr} \rightarrow C + H$	105	CosmicRays	$A^{+i} + cr \rightarrow A^{+i+1} + e^-$	28, 112, 113

^aElements A include C, N, O, Ne, Mg, Si, S, Ca & Fe.

^bIonisation states i run from 0 to $Z - 1$.

^cRadiative and dielectronic

Table 2.3: Continued.

References

- Abel T., Anninos P., Zhang Y., Norman M. L., 1997, *NewA*, 2, 181
 Abel T., Bryan G. L., Norman M. L., 2002, *Sci.*, 295, 93
 Adams N. G., Smith D., 1976a, *Int. J. Mass Spectrom. Ion Phys.*, 21, 349
 Adams N. G., Smith D., 1976b, *J. Phys. B*, 9, 1439
 Adams N. G., Smith D., Grief D., 1978, *Int. J. Mass Spectrom. Ion Phys.*, 26, 405
 Adams N. G., Smith D., Paulson J. F., 1980, *J. Chem. Phys.*, 72, 288
 Adams N. G., Smith D., Millar T. J., 1984, *MNRAS*, 211, 857
 Aldrovandi S. M. V., Péquignot D., 1973, *A&A*, 25, 137
 Alge E., Adams N. G., Smith D., 1983, *J. Phys. B*, 16, 1433
 Andreazza C. M., Singh P. D., 1997, *MNRAS*, 287, 287

- Anicich V. G., Huntress W. T., Futrell J. H., 1976, *Chem. Phys. Lett.*, 40, 233
Azatyan V. V., Aleksandrov E. N., Troshin A. F., 1975, *Kinet. Cat.*, 16, 306
Bakes E. L. O., Tielens A. G. G. M., 1994, *ApJ*, 427, 822
Barinovs G., van Hemert M. C., 2006, *ApJ*, 636, 923
Barlow S. G., 1984, PhD thesis, Univ. Colorado
Baulch D. L. et al., 1992, *J. Phys. Chem. Ref. Data*, 21, 411
Bertone S., Aguirre A., Schaye J., 2013, *MNRAS*, 430, 3292
Black J. H., Dalgarno A., 1977, *ApJS*, 34, 405
Black J. H., 1987, *ASSL*, 134, 731
Bruhns H., Kreckel H., Miller K. A., Urbain X., Savin D. W., 2010, *Phys. Rev. A*, 82, 042708
Burton M. G., Hollenbach D. J., Tielens A. G. G. M., 1990, *ApJ*, 365, 620
Carty D., Goddard A., Köhler S. P. K., Sims I. R., Smith I. W. M., 2006, *J. Phys. Chem. A*, 110, 3101
Cazaux S., Tielens A. G. G. M., 2002, *ApJ*, 575, L29
Cen R., 1992, *ApJS*, 78, 341
Cohen N., Westberg K. R., 1979, *J. Phys. Chem.*, 83, 46
Cohen N., Westberg K. R., 1983, *J. Phys. Chem. Ref. Data*, 12, 531
Cox D. P., Tucker W. H., 1969, *ApJ*, 157, 1157
Dalgarno A., Lepp S., 1987, in Vardya M. S., Tarafdar S. P., eds., *Astrochemistry*. Reidel, Dordrecht, p. 109
Dalgarno A., Du M. L., You J. H., 1990, *ApJ*, 349, 675
Dalgarno A., Yan M., Liu W., 1999, *ApJS*, 125, 237
Dean A. J., Davidson D. F., Hanson R. K., 1991, *J. Phys. Chem.*, 95, 183
de Jong T., 1972, *A&A*, 20, 263
Dere K. P., Landi E., Mason H. E., Monsignori Fossi B. C., Young P. R., 1997, *A&AS*, 125, 149
De Rijcke S., Schroyen J., Vandenbroucke B., Jachowicz N., Decroos J., Cloet-Osselaer A., Koleva M., 2013 *MNRAS*, 433, 3005
Dove J. E., Rusk A. C. M., Cribb P. H., Martin P. G., 1987, *ApJ*, 318, 379
Draine B. T., 1978, *ApJS*, 36, 595
Draine B. T., Roberge W. G., Dalgarno A., 1983, *ApJ*, 264, 485
Dubernet M. L., Gargaud M., McCarroll R., 1992, *A&A*, 259, 373
Dunseath K. M., Fon W. C., Burke V. M., Reid R. H. G., Noble C. J., 1997, *J. Phys. B.*, 30, 277
Fairbairn A. R., 1969, *Proc. R. Soc. A*, 312, 207
Federer W., Villinger H., Howorka F., Lindinger W., Tosi P., Bassi D., Ferguson E., 1984, *Phys. Rev. Lett.*, 52, 2084
Fehsenfeld F. C., Howard C. J., Ferguson E. E., 1973, *J. Chem. Phys.*, 58, 5841
Fehsenfeld F. C., 1976, *ApJ*, 209, 638
Ferland G. J., Peterson B. M., Horne K., Welsh W. F., Nahar S. N., 1992, *ApJ*, 387, 95
Ferland G. J., Korista K.T., Verner D.A., Ferguson J.W., Kingdon J.B., Verner E.M., 1998, *PASP*, 110, 761
Ferland G. J., Porter R. L., van Hoof P. A. M., Williams R. J. R., Abel N. P., Lykins M. L., Shaw G., Henney W. J., Stancil P. C., 2013, *RMxAA*, 49, 137

- Field D., Adams N. G., Smith D., 1980, MNRAS, 192, 1
- Flower D. R., Le Bourlot J., Pineau des Forêts G., Roueff E., 2000, MNRAS, 314, 753
- Frank P., Just Th., 1984, Proc. Int. Symp. Shock Tubes Waves, 14, 706
- Frank P., 1986, Proc. Int. Symp. Rarefied Gas Dyn., 2, 422
- Frank P., Bhaskaran K. A., Just Th., 1988, Symp. Int. Combust. Proc., 21, 885
- Furlanetto S. R., Stoeber S. J., 2010, MNRAS, 404, 1869
- Galli D., Palla F., 1998, A&A, 335, 403
- Geppert W. D. et al., 2005, J. Phys. Conf. Ser., 4, 26
- Gerlich D., Horning S., 1992, Chem. Rev., 92, 1509
- Glover S. C. O., Savin D. W., Jappsen A.-K., 2006, ApJ, 640, 553
- Glover S. C. O., Jappsen A.-K., 2007, ApJ, 666, 1
- Glover S. C. O., Abel T., 2008, MNRAS, 388, 1627
- Glover S. C. O., Federrath C., Mac Low M.-M., Klessen R. S., 2010, MNRAS, 404, 2
- Glover S. C. O., Clark P. C., 2012, MNRAS, 421, 116
- Gnat O., Sternberg A., 2007, ApJS, 168, 213
- Gnedin N. Y., Hollon N., 2012, ApJS, 202, 13
- Goldsmith P., Langer W. D., 1978, ApJ, 222, 881
- Grassi T., Krstic P., Merlin E., Buonomo U., Piovan L., Chiosi C., 2011, A&A, 533, A123
- Grassi T., Bovino S., Gianturco F. A., Baiocchi P., Merlin E., 2012, MNRAS, 425, 1332
- Grassi T., Bovino S., Schleicher D. R. G., Prieto J., Seifried D., Simoncini E., Gianturco F. A., 2014, MNRAS, 439, 2386
- Gredel R., Lepp S., Dalgarno A., Herbst E., 1989, ApJ, 347, 289
- Haardt F., Madau P., 2001, in Neumann D. M., Tran J. T. V., eds, XX1st Moriond Astrophys. Meeting, Clusters of Galaxies and the High Redshift Universe Observed in X-rays Editions Frontieres, Paris, 64
- Habing H. J., 1968, Bull. Astron. Inst. Netherlands, 19, 421
- Harding L. B., Guadagnini R., Schatz G. C., 1993, J. Phys. Chem., 97, 5472
- Herbst E., 1985, ApJ, 291, 226
- Hollenbach D., McKee C. F., 1979, ApJS, 41, 555
- Hummer D. G., Storey P. J., 1998, MNRAS, 297, 1073
- Indriolo N., Geballe T. R., Oka T., McCall B. J., 2007, ApJ, 671, 1736
- Janev R. K., Langer W. D., Evans K., Post D. E., 1987, Elementary Processes in Hydrogen-Helium Plasmas (Berlin: Springer)
- Jappsen A.-K., Glover S. C. O., Klessen R. S., Mac Low M.-M., 2007, ApJ, 660, 1332
- Jenkins E. B., 2009, ApJ, 700, 1299
- Jensen M. J., Bilodeau R. C., Safvan C. P., Seiersen K., Andersen L. H., Pedersen H. B., Heber O., 2000, ApJ, 543, 764
- Jones J. D. C., Birkinshaw K., Twiddy N. D., 1981, Chem. Phys. Lett., 77, 484
- Kaastra J. S., Mewe R., 1993, A&AS, 97, 443
- Kafatos M., 1973, ApJ, 182, 433
- Karpas Z., Anicich V., Huntress W. T., 1979, J. Chem. Phys. 70, 2877

- Kim J. K., Theard L. P., Huntress W. T., 1974, *Int. J. Mass Spectrom. Ion Phys.*, 15, 223
- Kim J. K., Theard L. P., Huntress W. T., 1975, *Chem. Phys. Lett.*, 32, 610
- Kimura M., Lane N. F., Dalgarno A., Dixson R. G., 1993, *ApJ*, 405, 801
- Krumholz M. R., Leroy A. K., McKee, C. F., 2011, *ApJ*, 731, 25
- Krumholz M. R., 2012, *ApJ*, 759, 9
- Landi E., Young P. R., Dere K. P., Del Zanna G., Mason H. E., 2013, *ApJS*, 763, 86
- Langer W. D., 1978, *ApJ*, 225, 860
- Larson Å. et al., 1998, *ApJ*, 505, 459
- Launay J. M., Le Dourneuf M., Zeippen C. J., 1991, *A&A*, 252, 842
- Lee L. C., 1984, *ApJ*, 282, 172
- Lepp S., Shull J. M., 1983, *ApJ*, 270, 578
- Lepp S., Shull J. M., 1984, *ApJ*, 280, 465
- Le Teuff Y. H., Millar T. J., Marwick A. J., 2000, *A&AS*, 146, 157
- Linder F., Janev R. K., Botero J., 1995, in Janev R. J., ed., *Atomic and Molecular Processes in Fusion Edge Plasmas*. Plenum Press, New York, p. 397
- Lotz W., 1967, *ApJS*, 14, 207
- MacGregor M., Berry R. S., 1973, *J. Phys. B*, 6, 181
- Mac Low M.-M., Shull J. M., 1986, *ApJ*, 302, 585
- Maio U., Dolag K., Ciardi B., Tornatore L., 2007, *MNRAS*, 379, 963
- Maloney P. R., Hollenbach D. J., Tielens A. G. G. M., 1996, *ApJ*, 466, 561
- Martin P. G., Keogh W. J., Mandy M. E., 1998, *ApJ*, 499, 793
- Martinez O. Jr., Yang Z., Bettles N. B., Snow T. P., Bierbaum V. M., 2009, *ApJ*, 705, 172
- Mathis J. S., Rumpl W., Nordsieck K. H., 1977, *ApJ*, 217, 425
- Mauclaire G., Derai R., Marx R., 1978a, *Int. J. Mass Spectrom. Ion Phys.*, 26, 284
- Mauclaire G., Derai R., Marx R., 1978b, *Dyn. Mass Spectrom.*, 5, 139
- McCall B. J. et al., 2003, *Nature*, 422, 500
- McCall B. J. et al., 2004, *Phys. Rev. A*, 70, 052716
- McEwan M. J., Scott G. B. I., Adams N. G., Babcock L. M., Terzieva R., Herbst E., 1999, *ApJ*, 513, 287
- Milligan D. B., McEwan M. J., 2000, *Chem. Phys. Lett.*, 319, 482
- Mitchell G. F., Deveau T. J., 1983, *ApJ*, 266, 646
- Mitchell J. B. A., 1990, *Phys. Rep.*, 186, 215
- Moseley J., Aberth W., Peterson J. R., 1970, *Phys. Rev. Lett.*, 24, 435
- Murrell J. N., Rodriguez J. A., 1986, *J. Mol. Struct. Theochem.*, 139, 267
- Natarajan K., Roth P., 1987, *Combust. Flame*, 70, 267
- Nelson R. P., Langer W. D., 1999, *ApJ*, 524, 923
- Neufeld D. A., Kaufman M. J., 1993, *ApJ*, 418, 263
- Neufeld D. A., Lepp S., Melnick G. J., 1995, *ApJS*, 100, 132
- Oldenborg R. C., Loge G. W., Harradine D. M., Winn K. R., 1992, *J. Phys. Chem.*, 96, 8426
- Omukai K., Tsuribe T., Schneider R., Ferrara A., 2005, *ApJ*, 626, 627
- Oppenheimer B. D., Schaye J., 2013a, *MNRAS*, 434, 1043
- Oppenheimer B. D., Schaye J., 2013b, *MNRAS*, 434, 1063
- Orel A. E., 1987, *J. Chem. Phys.*, 87, 314

- Peart B., Hayton D. A., 1994, *J. Phys. B*, 27, 2551
- Peebles P. J. E., Dicke R. H., 1968, *ApJ*, 154, 891
- Péquignot D., Aldrovandi S. M. V., 1976, *A&A*, 50, 141
- Petuchowski S. J., Dwek E., Allen J. E. Jr., Nuth J. A. III, 1989, *ApJ*, 342, 406
- Poulaert G., Brouillard F., Claeys W., McGowan J. W., van Wassenhove G., 1978, *J. Phys. B*, 11, L671
- Prasad S. S., Huntress W. T. Jr., *ApJS*, 43, 1
- Puy D., Akecian G., Le Bourlot J., Leorat J., Pineau Des Forêts G., 1993, *A&A*, 267, 337
- Rahmati A., Pawlik A. H., Raičević M., Schaye J., 2013, *MNRAS*, 430, 2427
- Raksit A. B., Warneck P., 1980, *J. Chem. Soc. Faraday Trans.*, 76, 1084
- Ramaker D. E., Peek J. M., 1976, *Phys. Rev. A*, 13, 58
- Röllig M. et al. 2007, *A&A*, 467, 187
- Rosén S. et al., 1998, *Phys. Rev.*, 57, 4462
- Rosén S. et al., 2000, *Faraday Discuss.*, 115, 295
- Santoro F., Shull, J. M., 2006, *ApJ*, 643, 26
- Saslaw W. C., Zipoy D., 1967, *Nature*, 216, 976
- Savin D. W., Krstić P. S., Haiman Z., Stancil P. C., 2004, *ApJ*, 606, L167 (erratum 607, L147)
- Schaye J., Dalla Vecchia C., Booth C. M., Wiersma R. P. C., Theuns T., Haas M. R., Bertone S., Duffy A. R., McCarthy I. G., van de Voort F., 2010, *MNRAS*, 402, 1536
- Schmeltekopf A. L., Fehsenfeld F. C., Ferguson E. E., 1967, *ApJ*, 148, L155
- Schneider I. F., Dulieu O., Giusti-Suzor A., Roueff E., 1994, *ApJ*, 424, 983 (erratum 486, 580)
- Schulz G. J., Asundi R. K., 1967, *Phys. Rev.*, 158, 25
- Scott G. B. I., Fairley D. A., Freeman C. G., McEwan M. J., Spanel P., Smith D., 1997, *J. Chem. Phys.*, 106, 3982
- Sembach K. R., Howk J. C., Ryans R. S. I., Keenan F. P., 2000, *ApJ*, 528, 310
- Shapiro P. R., Kang H., 1987, *ApJ*, 318, 32
- Shaw G., Ferland G. J., Abel N. P., Stancil P. C., van Hoof P. A. M., 2005, *ApJ*, 624, 794
- Shull J. M., van Steenberg M. E., 1985, *ApJ*, 298, 268
- Sidhu K. S., Miller S., Tennyson J., 1992, *A&A*, 255, 453
- Silk J., 1970, *ApL*, 5, 283
- Singh P. D., Sanzovo G. C., Borin A. C., Ornellas F. R., 1999, *MNRAS*, 303, 235
- Slack M. W., 1976, *J. Chem. Phys.*, 64, 228
- Smith B., Sigurdsson S., Abel T., 2008, *MNRAS*, 385, 1443
- Smith D., Adams N. G., 1977a, *Int. J. Mass Spectrom. Ion Phys.*, 23, 123
- Smith D., Adams N. G., 1977b, *Chem. Phys. Lett.*, 47, 383
- Smith D., Adams N. G., Miller T. M., 1978, *J. Chem. Phys.*, 69, 308
- Smith D., Spanel P., Mayhew C. A., 1992, *Int. J. Mass Spectrom. Ion Proc.*, 117, 457
- Smith I. W. M., Herbst E., Chang Q., 2004, *MNRAS*, 350, 323
- Smith M. A., Schlemmer S., von Richthofen J., Gerlich D., 2002, *ApJ*, 578, L87
- Spitzer L., 1978, *Physical Processes in the Interstellar Medium* (New York: Wiley)

- Stancil P. C., Dalgarno A., 1998, *Faraday Discuss.*, 109, 61
Sternberg A., Dalgarno A., 1995, *ApJS*, 99, 565
Suchkov A., Allen R. J., Heckman T. M., 1993, *ApJ*, 413, 542
Sutherland R. S., Dopita M. A., 1993, *ApJS*, 88, 253
Tielens A. G. G. M., Hollenbach D., 1985, *ApJ*, 291, 722
Trevisan C. S., Tennyson J., 2002, *Plasma Phys. Control. Fusion*, 44, 1263
Tsang W., Hampson R. F., 1986, *J. Phys. Chem. Ref. Data*, 15, 1087
Tupper P. F., 2002, *Bit Numerical Mathematics*, 42, 447
van Dishoeck E. F., Dalgarno A., 1984, *ApJ*, 277, 576
van Dishoeck E. F., 1987, in Vardya M. S., Tarafdar S. P., eds., *IAU Symp. Vol. 120, Astrochemistry*. Reidel, Dordrecht, p. 51
van Dishoeck E. F., 1988, in Millar T. J., Williams D. A., eds., *Rate Coefficients in Astrochemistry*. Kluwer, Dordrecht, p. 49
van Dishoeck E. F., Jonkheid B., van Hemert M. C., 2006, *Faraday Discuss.*, 133, 231
Vasiliev E. O., 2013, *MNRAS*, 431, 638
Verner D. A., Yakovlev D. G., 1995, *A&AS*, 109, 125
Verner D. A., Ferland G. J., Korista K. T., Yakovlev D. G., 1996, *ApJ*, 465, 487
Viggiano A. A., Howorka F., Albritton D. L., Fehsenfeld F. C., Adams N. G., Smith D., 1980, *ApJ*, 236, 492
Visser R., van Dishoeck E. F., Black J. H., 2009, *A&A*, 503, 323
Vogelsberger M., Genel S., Sijacki D., Torrey P., Springel V., Hernquist L., 2013, *MNRAS*, 436, 3031
Wagner-Redeker W., Kemper P. R., Jarrold M. F., Bowers M. T., 1985, *J. Chem. Phys.*, 83, 1121
Walkauskas L. P., Kaufman F., 1975, *Symp. Int. Combust. Proc.*, 15, 691
Warnatz J., 1984, in Gardiner W. C. Jr., ed., *Combustion Chemistry*. Springer-Verlag, NY, p. 197
Weingartner J. C., Draine B. T., 2001a, *ApJ*, 548, 296
Weingartner J. C., Draine B. T., 2001b, *ApJ*, 563, 842
Wiebe D., Semenov D., Henning T., 2003, *A&A*, 399, 197
Wiersma R. P. C., Schaye J., Smith B. D., 2009, *MNRAS*, 393, 99
Williams J. P., Bergin E. A., Caselli P., Myers P. C., Plume, R., 1998, *ApJ*, 503, 689
Wilms J., Allen A., McCray R., 2000, *ApJ*, 542, 914
Wishart A. W., 1979, *MNRAS*, 187, 59P
Wolfire M. G., Hollenbach D., McKee C. F., Tielens A. G. G. M., Bakes E. L. O., 1995, *ApJ*, 443, 152
Wolfire M. G., McKee C. F., Hollenbach D., Tielens A. G. G. M., 2003, *ApJ*, 587, 278
Wolniewicz L., Simbotin I., Dalgarno A., 1998, *ApJS*, 115, 293
Woodall J., Agúndez M., Markwick-Kemper A. J., Millar T. J., 2007, *A&A*, 466, 1197
Yan M., Sadeghpour H. R., Dalgarno A., 1998, *ApJ*, 496, 1044
Zygelman B., Dalgarno A., Kimura M., Lane N. F., 1989, *Phys. Rev. A*, 40, 2340

NON-EQUILIBRIUM CHEMISTRY AND COOLING IN THE DIFFUSE INTERSTELLAR MEDIUM - II. SHIELDED GAS

We extend the non-equilibrium model for the chemical and thermal evolution of diffuse interstellar gas presented in Richings et al. (2014) to account for shielding from the UV radiation field. We attenuate the photochemical rates by dust and by gas, including absorption by H I , H_2 , He I , He II and CO where appropriate. We then use this model to investigate the dominant cooling and heating processes in interstellar gas as it becomes shielded from the UV radiation. We consider a one-dimensional plane-parallel slab of gas irradiated by the interstellar radiation field, either at constant density and temperature or in thermal and pressure equilibrium. The dominant thermal processes tend to form three distinct regions in the clouds. At low column densities cooling is dominated by ionised metals such as Si III , Fe II , Fe III and C II , which are balanced by photoheating, primarily from H I . Once the hydrogen-ionising radiation becomes attenuated by neutral hydrogen, photoelectric dust heating dominates, while C II becomes dominant for cooling. Finally, dust shielding triggers the formation of CO and suppresses photoelectric heating. The dominant coolants in this fully shielded region are H_2 and CO . The column density of the H I-H_2 transition predicted by our model is lower at higher density (or at higher pressure for gas clouds in pressure equilibrium) and at higher metallicity, in agreement with previous PDR models. We also compare the H I-H_2 transition in our model to two prescriptions for molecular hydrogen formation that have been implemented in hydrodynamic simulations.

Alexander J. Richings, Joop Schaye and Benjamin D. Oppenheimer
Monthly Notices of the Royal Astronomical Society
Volume 442, Issue 3, pp. 2780-2796 (2014)

3.1 Introduction

The thermal evolution of gas is an important component of hydrodynamic simulations of galaxy formation as it determines how quickly the gas can cool and collapse to form dense structures, and ultimately stars. The star formation in such simulations can be limited to the cold phase of the interstellar medium (ISM) if we have sufficient resolution to resolve the Jeans mass ($M_J \propto \rho^{-1/2} T^{3/2}$) in the cold gas. It is desirable to include a multi-phase treatment of the ISM, as this will produce a more realistic description of the distribution of star formation within the galaxy, along with the resulting impact of stellar feedback on the ISM and the galaxy as a whole (e.g. Ceverino & Klypin 2009; Governato et al. 2010; Halle & Combes 2013; Hopkins et al. 2014). Therefore, it is important that we correctly follow the thermal evolution of gas between the warm ($T \sim 10^4$ K) and cold ($T \lesssim 100$ K) phases of the ISM in these simulations.

The radiative cooling rate depends on the chemical abundances in the gas, including the ionisation balance, and hence on its chemical evolution. However, following the full non-equilibrium chemistry of the ISM within a hydrodynamic simulation can be computationally expensive, as it requires us to integrate a system of stiff differential equations that involves hundreds of species and thousands of reactions. Therefore, many existing cosmological hydrodynamic simulations use tabulated cooling rates assuming chemical (including ionisation) equilibrium, meaning that the abundances of individual ions and molecules have reached an equilibrium or steady state. For example, the cosmological simulations that were run as part of the Overwhelmingly Large Simulations project (OWLS; Schaye et al. 2010) use the pre-computed cooling functions of Wiersma et al. (2009), which were calculated using CLOUDY¹ (Ferland et al. 1998, 2013) as a function of temperature, density and abundances of individual elements assuming ionisation equilibrium in the presence of the Haardt & Madau (2001) extragalactic UV background. However, this assumption of ionisation equilibrium may not remain valid if the cooling or dynamical time-scale becomes short compared to the chemical time-scale (e.g. Kafatos 1973; Gnat & Sternberg 2007; Oppenheimer & Schaye 2013a; Vasiliev 2013) or if the UV radiation field is varying in time (e.g. Oppenheimer & Schaye 2013b).

In the first paper of this series (Richings et al. 2014; hereafter paper I) we presented a chemical network to follow the non-equilibrium thermal and chemical evolution of interstellar gas. Using this model we investigated the chemistry and cooling properties of optically thin interstellar gas in the ISM and identified the dominant coolants for gas exposed to various UV radiation fields. We also looked at the impact that non-equilibrium chemistry can have on the cooling rates and chemical abundances of such gas.

In this paper we extend our thermochemical model to account for gas that is shielded from the incident UV radiation field by some known column density. We focus on physical conditions with densities $10^{-2} \text{ cm}^{-3} \lesssim n_{\text{H,tot}} \lesssim 10^4 \text{ cm}^{-3}$ and temperatures of $10^2 \text{ K} \lesssim T \lesssim 10^4 \text{ K}$. This is most relevant to gas that is cooling

¹<http://nublado.org/>

from the warm phase to the cold phase of the ISM. We apply our model to a one-dimensional plane-parallel slab of gas that is irradiated by the Black (1987) interstellar radiation field to investigate how the chemistry and cooling properties of the gas change as it becomes shielded from the UV radiation, both by dust and by the gas itself. The spectral shape of the radiation field will change with the depth into the cloud as high energy photons are able to penetrate deeper. Hence, the major coolants and heating processes will vary with column density. Such one-dimensional models are commonly used to model photodissociation regions (PDRs) and diffuse and dense clouds (e.g. Tielens & Hollenbach 1985; van Dishoeck & Black 1986, 1988; Le Petit et al. 2006; Visser et al. 2009; Wolfire et al. 2010).

It has been suggested recently that the star formation rate of galaxies may be more strongly correlated to the molecular gas content than to atomic hydrogen (Wong & Blitz 2002; Schaye 2004; Kennicutt et al. 2007; Leroy et al. 2008; Bigiel et al. 2008, 2010), although the more fundamental and physically relevant correlation may be with the cold gas content (Schaye 2004; Krumholz et al. 2011; Glover & Clark 2012). Motivated by this link between molecular hydrogen and star formation, a number of studies have implemented simple methods to follow the abundance of H_2 in numerical simulations of galaxies (e.g. Pelupessy et al. 2006; Gnedin et al. 2009; McKee & Krumholz 2010; Christensen et al. 2012). We compare the H_2 fractions predicted by some of these methods to those calculated using our model to investigate the physical processes that determine the HI-H_2 transition and to explore in which physical regimes these various prescriptions remain valid.

This paper is organised as follows. In section 3.2 we summarise the thermochemical model presented in paper I, and in section 3.3 we describe how the photochemical rates are attenuated by dust and gas. We look at the photoionisation rates in section 3.3.1, the photodissociation of molecular species in section 3.3.2 and the photoheating rates in section 3.3.3. In section 3.4 we apply this model to a one-dimensional plane-parallel slab of gas to investigate the chemistry and cooling properties of the gas as it becomes shielded from the UV radiation field, and we compare these results with `CLOUDY`. In section 3.5 we compare the time-dependent molecular H_2 fractions predicted by our model with two prescriptions for H_2 formation taken from the literature that have been implemented in hydrodynamic simulations. Finally, we discuss our results and conclusions in section 3.6.

3.2 Thermochemical Model

In this section we give a brief overview of the chemical and thermal processes that are included in our model. These are described in more detail in paper I.

We follow the evolution of 157 chemical species, including 20 molecules (H_2 , H_2^+ , H_3^+ , OH , H_2O , C_2 , O_2 , HCO^+ , CH , CH_2 , CH_3^+ , CO , CH^+ , CH_2^+ , OH^+ , H_2O^+ , H_3O^+ , CO^+ , HOC^+ and O_2^+) along with electrons and all ionisation states of the 11 elements that dominate the cooling rate (H, He, C, N, O, Ne, Si, Mg, S, Ca and Fe). The rate equations of these species and the equation for the temperature

evolution give us a system of 158 differential equations that we integrate from the initial conditions with CVODE (a part of the SUNDIALS² suite of non-linear differential/algebraic equation solvers), using the backward difference formula method and Newton iteration.

3.2.1 Chemistry

Our chemical network contains 907 reactions, including:

Collisional reactions. We include the collisional ionisation, radiative and di-electronic recombination and charge transfer reactions of all ionisation states of the 11 elements in our network. The rate coefficients of these reactions were tabulated as a function of temperature by Oppenheimer & Schaye (2013a) using CLOUDY (they use version 10.00, but they have since produced updated versions of these tables using version 13.01 of CLOUDY³). We also include reactions for the formation and destruction of molecular hydrogen taken from Glover & Jappsen (2007); Glover & Abel (2008) and others, and the CO network from Glover et al. (2010) with some small modifications (see section 2.5 of paper I).

Photochemical reactions. We compute the optically thin photoionisation rates using the grey approximation cross sections of each atom and ion species for a given UV spectrum, which we calculate using the frequency dependent cross sections from Verner & Yakovlev (1995) and Verner et al. (1996). We also include Auger ionisation, where photoionisation of inner shell electrons can lead to the ejection of multiple electrons by a single photon. For these we use the electron vacancy distribution probabilities from Kaastra & Mewe (1993). We assume that the optically thin photodissociation rate of molecular hydrogen scales linearly with the number density of photons in the energy band $12.24 \text{ eV} < h\nu < 13.51 \text{ eV}$, normalised to the photodissociation rate in the presence of the Black (1987) interstellar radiation field calculated by CLOUDY (see section 2.2.2 of paper I). For the remaining molecular species, we use the photoionisation and photodissociation rates given by van Dishoeck et al. (2006) and Visser et al. (2009) where available, or Glover et al. (2010) otherwise. In paper I we only considered optically thin gas. In section 3.3 we describe how we modify these optically thin rates for shielded gas.

Cosmic ray ionisation. The primary ionisation rate of H I due to cosmic rays, ζ_{HI} , is a free parameter in our model. We use a default value of $\zeta_{\text{HI}} = 2.5 \times 10^{-17} \text{ s}^{-1}$ (Williams et al. 1998), although recent observations suggest that this could be an order of magnitude larger (e.g. Indriolo & McCall 2012). In paper I we consider the impact that increasing or decreasing our default value of ζ_{HI} by a factor of ten can have on the abundances in fully shielded gas (see figure 6 in paper I).

²<https://computation.llnl.gov/casc/sundials/main.html>

³These updated tables are available on the website: <http://noneq.strw.leidenuniv.nl>

The cosmic ray ionisation rates of the other species are then scaled linearly with ζ_{HI} . The ratio of the ionisation rate of each species with respect to HI is assumed to be equal to the ratio of these ionisation rates given in the UMIST database⁴ (Le Teuff et al. 2000) where available. For species that do not appear in this database, we calculate their cosmic ray ionisation rate with respect to ζ_{HI} using Lotz (1967), Silk (1970) and Langer (1978). For the molecular species, we use the cosmic ray ionisation and dissociation rates from table B3 of Glover et al. (2010), again scaled with ζ_{HI} .

Dust grain reactions. The formation rate of molecular hydrogen on dust grains is calculated using equation 18 from Cazaux & Tielens (2002). We take a constant dust temperature $T_{\text{dust}} = 10$ K, which we find has a negligible impact on our results, and we assume that the abundance of dust scales linearly with metallicity. We also include a small number of recombination reactions on dust grains, taken from Weingartner & Draine (2001a).

3.2.2 Thermal processes

For a complete list of cooling and heating processes in our model, see table 1 of paper I. Below we summarise some of the cooling and heating mechanisms that are most important in the diffuse ISM.

Metal-line cooling. Oppenheimer & Schaye (2013a) tabulate the radiative cooling rates of all ionisation states of the 11 elements in our chemical network as a function of temperature, calculated using CLOUDY (as for the rate coefficients, they use version 10.00, but they have since produced updated versions of these tables using version 13.01 of CLOUDY³). We use these cooling rates for most metal species in our model. However, these rates assume that the radiative cooling is dominated by electron-ion collisions. For a small number of species this assumption can break down at low temperatures ($T \lesssim 10^3$ K). We therefore found it necessary to calculate the cooling rates of OI and CI as a function of temperature and of HI, HII and electron densities, using the same method as Glover & Jappsen (2007). This enables us to follow the radiative cooling rates of these species in regimes that are dominated by collisions with HI or HII, as well as when electron-ion collisions dominate. We also tabulated the cooling rates of CII, NII, SII and FEII as functions of temperature and electron density using version 7.1 of the CHIANTI database⁵ (Dere et al 1997; Landi et al 2013).

H₂ rovibrational cooling. We use the H₂ cooling function from Glover & Abel (2008), assuming an ortho- to para- ratio of 3:1. This includes collisional excitation of the rovibrational levels of molecular hydrogen by HI, HII, H₂, HeI and electrons.

Photoheating. We calculate the average excess energy of ionising photons for each species, given the incident UV spectrum, using the frequency dependent

⁴<http://www.udfa.net>

⁵<http://www.chiantidatabase.org/chianti.html>

cross sections from Verner & Yakovlev (1995) and Verner et al. (1996). We then multiply these by the corresponding photoionisation rate to obtain the photoheating rate for each species. See section 3.3.3 for a description of how we modify these optically thin photoheating rates for shielded gas.

Photoelectric heating. The absorption of UV photons by dust grains can release electrons, and the excess energy that is absorbed by the electrons is quickly thermalised, which heats the gas. We calculate the photoelectric heating rate from dust grains using equations 1 and 2 from Wolfire et al. (1995).

3.3 Shielding processes

In paper I we considered only optically thin gas. However, for shielded gas we need to consider how both the intensity and the shape of the UV spectrum change as the radiation field becomes attenuated by both dust and the gas itself. The photochemical rates presented in paper I involve integrals over photon frequency, but these are expensive to compute. For the optically thin rates we use the grey approximation to obtain the average cross section of each species, weighted by the frequency dependent radiation field, so that these integrals do not need to be re-evaluated at every timestep in the chemistry solver. However, this approximation becomes invalid if the shape of the UV spectrum is no longer invariant.

In the following sections we describe how we modify the optically thin rates of photoionisation, photodissociation and photoheating for gas that is shielded by a known column density. To implement these methods in a hydrodynamic simulation, we would need to estimate this column density for each gas particle/cell. This is typically done by assuming that shielding occurs locally over some characteristic length scale L , so that the column density N_i of a gas cell with density n_i can be estimated from local quantities as:

$$N_i = n_i L. \quad (3.1)$$

If the macroscopic velocity gradient dv/dr is large with respect to local variations in the thermal line broadening, for example in turbulent molecular clouds, we can use the Sobolev length (Sobolev 1957), which gives the length scale over which the Doppler shift of a line due to the velocity gradient is equal to the thermal width of the line:

$$L_{\text{Sob}} = \frac{v_{\text{th}}}{|dv/dr|}, \quad (3.2)$$

where v_{th} is the thermal velocity. This method is applicable to the shielding of individual lines, for example in the self-shielding of molecular hydrogen. Gnedin et al. (2009) use a Sobolev-like approximation to estimate the column density using the density gradient rather than the velocity gradient:

$$L_{\text{Sob},\rho} = \frac{\rho}{|\nabla\rho|}. \quad (3.3)$$

By integrating column densities along random lines of sight in their cosmological simulations, in which they are able to resolve individual giant molecular complexes, Gnedin et al. (2009) confirm that this approximation reproduces the true column density with a scatter of a factor ~ 2 in the range $3 \times 10^{20} \text{ cm}^{-2} < N_{\text{HI}} + 2N_{\text{H}_2} < 3 \times 10^{23} \text{ cm}^{-2}$ (see their figure 1).

An alternative approach is to assume that shielding occurs locally on scales of the Jeans length, L_{Jeans} (Schaye 2001a,b; Rahmati et al. 2013). For example, Hopkins et al. (2014) integrate the density out to L_{Jeans} for each particle to obtain its shielding column density, which they use to attenuate the UV background.

Wolcott-Green et al. (2011) use these three methods to estimate the self-shielding of molecular hydrogen and compare them to their calculations of the radiative transfer of Lyman Werner radiation through simulated haloes at redshift $z \sim 10$. They find that using the Sobolev length (equation 3.2) is the most accurate method based only on local properties, compared to their radiative transfer calculations.

Our chemical model could also be coupled to a full 3D radiative transfer simulation, in which the shielding of the UV radiation is computed by the radiative transfer solver rather than using the methods that we describe below. However, to include the impact of shielding on the shape of the UV spectrum, we require multiple frequency bins, as the spectral shape is assumed to remain constant within individual frequency bins. Such a calculation is likely to be computationally expensive. In a future work we shall compare our methods described below, with different approximations for the column density, to radiative transfer calculations to investigate in which physical conditions these various approximations can be applied in hydrodynamic simulations.

3.3.1 Photoionisation

The incident UV radiation field is attenuated by both dust and gas. The factor by which dust reduces the photoionisation rate of a species can be written as:

$$S_d^i = \exp(-\gamma_d^i A_v) = \exp\left(-4.0 \times 10^{-22} \gamma_d^i N_{\text{H}_{\text{tot}}} Z/Z_\odot\right), \quad (3.4)$$

where we can express this factor in terms of the visual extinction A_v or the total intervening hydrogen column density $N_{\text{H}_{\text{tot}}} = N_{\text{HI}} + N_{\text{HII}} + 2N_{\text{H}_2}$. Following Krumholz et al. (2011), we use $A_v/N_{\text{H}_{\text{tot}}} = 4.0 \times 10^{-22} Z/Z_\odot \text{ mag cm}^2$, which is intermediate between the values from the models of Weingartner & Draine (2001b) for the Milky Way (with a visual extinction to reddening ratio $R_v = 3.1$ or 5.5), the Large Magellanic Cloud and the Small Magellanic Cloud, and assumes that the dust content of the gas scales linearly with its metallicity. The factor γ_d^i is a constant that is different for each species and depends on the range of photon energies that ionise that species. This factor accounts for the fact that the absorbing cross section of dust grains varies with photon energy, so the effective dust column density depends on which energy range we are interested in. We use the values for γ_d^i calculated for the Draine (1978) interstellar radiation field from table 3 of van Dishoeck et al. (2006) where available, or from table B2 of Glover et al. (2010) otherwise. Since CaI and CaII were not included in either reference, we

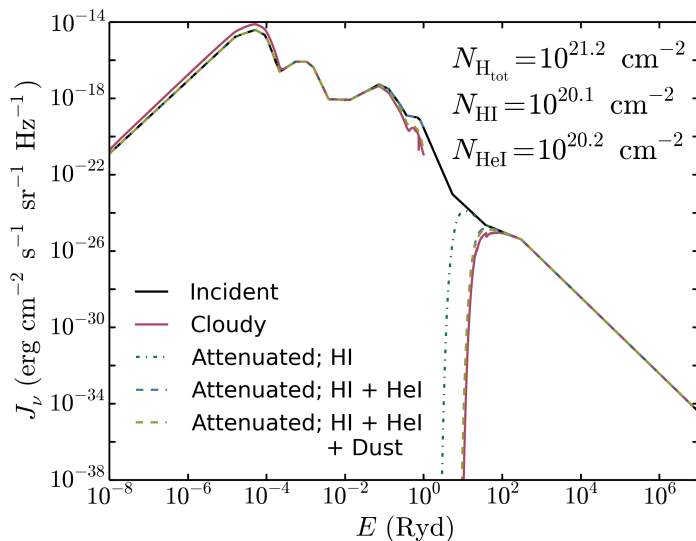


Figure 3.1: The effect of dust and gas shielding on the radiation spectrum. The incident spectrum of the Black (1987) interstellar radiation field is shown by the black curve, and the coloured curves show the resulting spectrum after it has passed through a total hydrogen column density $N_{\text{H,tot}} = 1.6 \times 10^{21} \text{ cm}^{-2}$ at solar metallicity, as calculated by CLOUDY, and the spectrum attenuated only by HI, by HI and HeI, and by HI, HeI and dust.

simply use the value of γ_d^i from species that have similar ionisation energies (MgI and Cl respectively).

While dust is the dominant source of absorption of UV radiation below 13.6 eV, above this limit UV radiation is strongly absorbed by neutral hydrogen, since photons at these energies are able to ionise hydrogen, which has a much higher cross sectional area σ_{H} ($\sim 10^{-17} \text{ cm}^2$ at 1 Ryd) than the dust. Neutral helium can also significantly attenuate the UV radiation at energies above 24.6 eV.

To illustrate how different components impact the spectrum at different energies, we show in figure 3.1 the Black (1987) interstellar radiation field and the resulting spectrum after it has passed through a total hydrogen column density $N_{\text{H,tot}} = 1.6 \times 10^{21} \text{ cm}^{-2}$ at solar metallicity, including an HI column density $N_{\text{HI}} = 1.2 \times 10^{20} \text{ cm}^{-2}$ and a HeI column density $N_{\text{HeI}} = 1.6 \times 10^{20} \text{ cm}^{-2}$, as calculated by CLOUDY. We then compare these to a spectrum attenuated by only HI, by HI and HeI, and by HI, HeI and dust, calculated using the frequency dependent cross sections of Verner et al. (1996) and the dust opacities from Martin & Whittet (1990). We see that at energies just below 1 Ryd the UV radiation is suppressed by dust absorption, while the strong break above 1 Ryd is caused by neutral hydrogen. Comparing the green curve to the blue and yellow curves, we also see that absorption by neutral helium is important at higher energies, from a few Rydbergs up to 100 Ryd, while dust absorption is relatively unimportant at these higher energies. Note that the attenuated spectrum calculated by CLOUDY (the red curve) includes thermal emission from dust grains, which is why it is slightly higher than

the incident spectrum at low energies $E < 10^{-4}$ Ryd.

Throughout this paper we use the Black (1987) interstellar radiation field, which consists of the background radiation field from IR to UV of Mathis et al. (1983), the soft X-ray background from Bregman & Harrington (1985) and a blackbody with a temperature of 2.7 K. However, several of the photoionisation and photodissociation rates that we use for molecular species were calculated using the Draine (1978) interstellar radiation field (e.g. van Dishoeck et al. 2006; Visser et al. 2009). We normalise these rates by the radiation field strength in the energy band $6 \text{ eV} < h\nu < 13.6 \text{ eV}$, but the shape of these UV spectra are different. This will introduce an additional uncertainty in our results.

While the column densities considered in the above example are typical of cold, atomic interstellar gas, there are certain regimes in which we also need to include the attenuation by additional species. For example, once the gas becomes molecular, the H_2 column density can be greater than the neutral hydrogen column density. Furthermore, at the high temperatures and low densities that are typical of the circumgalactic medium (for example $T \sim 10^5 \text{ K}$, $n_{\text{H, tot}} \sim 10^{-4} \text{ cm}^{-3}$), helium is singly ionised and shielding of radiation above 54.4 eV by HeII can be important. Therefore, to calculate the shielded photoionisation rates of species with ionisation energies above 13.6 eV, we need to account for the attenuation by four species: HI, H_2 , HeI and HeII. For an incident spectrum with intensity J_ν per unit solid angle per unit frequency, the photoionisation rate of species i , $\Gamma_{i, \text{thick}}$, is then given by:

$$\Gamma_{i, \text{thick}} = \int_{\nu_{0,i}}^{\infty} \frac{4\pi J_\nu}{h\nu} \exp(-N_{\text{HI}}\sigma_{\nu, \text{HI}} - N_{\text{H}_2}\sigma_{\nu, \text{H}_2} - N_{\text{HeI}}\sigma_{\nu, \text{HeI}} - N_{\text{HeII}}\sigma_{\nu, \text{HeII}})\sigma_{\nu,i} d\nu, \quad (3.5)$$

where $\sigma_{\nu,i}$ and $\nu_{0,i}$ are respectively the frequency dependent cross section and the ionisation threshold frequency of species i .

Calculating these integrals at every timestep in the chemistry solver would be too computationally expensive, so instead we need to pre-compute them and tabulate the results. However, this would require us to tabulate the optically thick rates in four dimensions, one for each of the attenuating column densities, for every species. Such tables would require too much memory to be feasible. To reduce the size of the tables, we note that the H_2 cross section can be approximated as:

$$\sigma_{\nu, \text{H}_2} \approx \begin{cases} 3.00\sigma_{\nu, \text{HI}} & h\nu > 15.4 \text{ eV} = h\nu_{0, \text{H}_2} \\ 0 & \text{otherwise.} \end{cases} \quad (3.6)$$

Similarly, the HeII cross section can be approximated as:

$$\sigma_{\nu, \text{HeII}} \approx \begin{cases} 0.75\sigma_{\nu, \text{HeI}} & h\nu > 54.4 \text{ eV} = h\nu_{0, \text{HeII}} \\ 0 & \text{otherwise.} \end{cases} \quad (3.7)$$

We use the H_2 cross section from Yan et al. (1998) and Wilms et al. (2000), and the HI, HeI and HeII cross sections from Verner & Yakovlev (1995) and Verner et al. (1996).

Using these approximations, we can divide the shielded photoionisation rates into three integrals as follows:

$$\begin{aligned}
 \Gamma_{i,\text{thick}} &= \int_{\nu_{0,i}}^{\nu_{0,\text{H}_2}} \frac{4\pi J_\nu}{h\nu} \exp(-N_{\text{HI}}\sigma_{\nu,\text{HI}})\sigma_{\nu,i}d\nu + \\
 &\int_{\nu_{0,\text{H}_2}}^{\nu_{0,\text{HeII}}} \frac{4\pi J_\nu}{h\nu} \exp(-N_{\text{H}}^{\text{eff}}\sigma_{\nu,\text{HI}} - N_{\text{HeI}}\sigma_{\nu,\text{HeI}})\sigma_{\nu,i}d\nu + \\
 &\int_{\nu_{0,\text{HeII}}}^{\infty} \frac{4\pi J_\nu}{h\nu} \exp(-N_{\text{H}}^{\text{eff}}\sigma_{\nu,\text{HI}} - N_{\text{He}}^{\text{eff}}\sigma_{\nu,\text{HeI}})\sigma_{\nu,i}d\nu \\
 &= \Gamma_{i,\text{thin}}(S_{\text{gas},1}^i(N_{\text{HI}}) + S_{\text{gas},2}^i(N_{\text{H}}^{\text{eff}}, N_{\text{HeI}}) \\
 &+ S_{\text{gas},3}^i(N_{\text{H}}^{\text{eff}}, N_{\text{He}}^{\text{eff}})), \tag{3.8}
 \end{aligned}$$

where the effective hydrogen and helium column densities are:

$$N_{\text{H}}^{\text{eff}} = N_{\text{HI}} + 3.00N_{\text{H}_2} \tag{3.9}$$

$$N_{\text{He}}^{\text{eff}} = N_{\text{HeI}} + 0.75N_{\text{HeII}}. \tag{3.10}$$

These effective column densities also account for the attenuation by H_2 and HeII respectively. Note that equation 3.8 is valid for species with an ionisation threshold frequency $\nu_{0,i} < \nu_{0,\text{H}_2}$. If $\nu_{0,i} \geq \nu_{0,\text{H}_2}$, the first integral will be zero. Similarly, the second integral in equation 3.8 will also be zero if $\nu_{0,i} \geq \nu_{0,\text{HeII}}$.

By using these approximations, we only need to create tables of $S_{\text{gas},\{1,2,3\}}^i$ in up to two dimensions, which greatly reduces the memory that they require. This approach is not exact, but we find that it introduces errors in $\Gamma_{i,\text{thick}}$ of at most a few tens of per cent, and typically much less than this. In Appendix A we show the relative errors in the photoionisation rates of each species that are introduced by these approximations. For each species i we use equation 3.8 to tabulate the integrals $S_{\text{gas},1}^i(N_{\text{HI}})$, $S_{\text{gas},2}^i(N_{\text{H}}^{\text{eff}}, N_{\text{HeI}})$ and $S_{\text{gas},3}^i(N_{\text{H}}^{\text{eff}}, N_{\text{He}}^{\text{eff}})$ as a function of the given column densities from 10^{15} to 10^{24} cm^{-2} in intervals of 0.1 dex. Added together, these integrals give the ratio of the optically thick to the optically thin photoionisation rate of species i , $S_{\text{gas}}^i(N_{\text{HI}}, N_{\text{H}_2}, N_{\text{HeI}}, N_{\text{HeII}})$.

3.3.2 Photodissociation

The photodissociation rates of molecular species are attenuated by dust according to equation 3.4, where we take the values of γ_{d}^i calculated for the Draine (1978) interstellar radiation field from table 2 of van Dishoeck et al. (2006) where available, or from table B2 of Glover et al. (2010) otherwise. In addition to dust shielding, the absorption of Lyman Werner radiation (i.e. photon energies $11.2 \text{ eV} < h\nu < 13.6 \text{ eV}$) by molecular hydrogen allows H_2 to become self-shielded. An accurate treatment of this effect would require us to solve the radiative transfer of the Lyman Werner radiation and to follow the level populations of the rovibrational states of the H_2 molecule, which would be computationally expensive.

However, we can approximate the self-shielding of H_2 as a function of H_2 column density. For example, the following analytic fitting function from Draine & Bertoldi (1996) is commonly used in hydrodynamic simulations of galaxies and molecular clouds (e.g. Glover & Jappsen 2007; Glover et al. 2010; Gnedin et al. 2009; Christensen et al. 2012; Krumholz 2012):

$$S_{\text{self}}^{\text{H}_2} = \frac{1 - \omega_{\text{H}_2}}{(1 + x/b_5)^\alpha} + \frac{\omega_{\text{H}_2}}{(1 + x)^{1/2}} \exp(-8.5 \times 10^{-4}(1 + x)^{1/2}), \quad (3.11)$$

where $x \equiv N_{\text{H}_2}/(5 \times 10^{14} \text{cm}^{-2})$, ω_{H_2} and α are adjustable parameters (Draine & Bertoldi 1996 use $\omega_{\text{H}_2} = 0.035$ and $\alpha = 2$), $b_5 \equiv b/(10^5 \text{cm s}^{-1})$ and b is the Doppler broadening parameter. This function was introduced by Draine & Bertoldi (1996) and was motivated by their detailed radiative transfer and photodissociation calculations. The suppression factor $S_{\text{self}}^{\text{H}_2}$ initially declines rapidly (indicating increased shielding) with N_{H_2} as individual Lyman Werner lines shield themselves. However, once these lines become saturated, the shielding is determined by the wings of the lines, leading to a shallow power law dependence $\sim N_{\text{H}_2}^{-1/2}$. Finally, at high column densities the lines overlap, creating an exponential cut off in the self-shielding function.

Some authors have used equation 3.11 with different values for some of the parameters. For example, Gnedin et al. (2009) and Christensen et al. (2012) adopt a value $\omega_{\text{H}_2} = 0.2$, as this gives better agreement between their model for H_2 formation and observations of atomic and molecular gas fractions in nearby galaxies.

Wolcott-Green et al. (2011) also investigate the validity of equation 3.11 and compare it to their detailed radiative transfer calculations of Lyman Werner radiation through simulated haloes at high redshift ($z \sim 10$). They find that equation 3.11, with $\omega_{\text{H}_2} = 0.035$ and $\alpha = 2$, as used by Draine & Bertoldi (1996), underestimates the value of $S_{\text{self}}^{\text{H}_2}$ (i.e. it predicts too strong self-shielding) by up to an order of magnitude in warm gas (with $T \gtrsim 500$ K). They argue that this discrepancy arises because the assumptions made in Draine & Bertoldi (1996) are only accurate for cold gas in which only the lowest rotational states of H_2 are populated. However, they obtain better agreement with their calculations (within ~ 15 per cent) if they use equation 3.11 with $\alpha = 1.1$.

We have compared the H_2 self-shielding function of Draine & Bertoldi (1996) and the modification to this function suggested by Wolcott-Green et al. (2011), with $\alpha = 1.1$, to the ratio of the optically thick to optically thin H_2 photodissociation rates predicted by CLOUDY in primordial gas. Details of this comparison can be found in Appendix B. We find that neither function produces satisfactory agreement with CLOUDY. For example, both overestimate $S_{\text{self}}^{\text{H}_2}$ compared to CLOUDY by a factor ~ 3 at H_2 column densities $N_{\text{H}_2} \gtrsim 10^{17} \text{cm}^{-2}$ in gas with a temperature $T = 100$ K (see figure 3.7). We also find that the temperature dependence of $S_{\text{self}}^{\text{H}_2}$ predicted by CLOUDY is not accurately reproduced by the modified self-shielding function from Wolcott-Green et al. (2011). Furthermore, Wolcott-Green et al. (2011) only consider gas in which the Doppler broadening is purely thermal. However, if it is dominated by turbulence then the Doppler broadening will be independent of temperature. The H_2 self-shielding function will still depend on

temperature in this case because the level populations of the H_2 molecule, which affect the shielding, will depend on temperature.

To obtain a better fit to the H_2 self-shielding predicted by CLOUDY (with its 'big H2' model), we modified equation 3.11 as follows:

$$S_{\text{self}}^{\text{H}_2} = \frac{1 - \omega_{\text{H}_2}(T)}{(1 + x'/b_5)^{\alpha(T)}} \exp(-5 \times 10^{-7}(1 + x')) + \frac{\omega_{\text{H}_2}(T)}{(1 + x')^{1/2}} \exp(-8.5 \times 10^{-4}(1 + x')^{1/2}), \quad (3.12)$$

where $x' = N_{\text{H}_2}/N_{\text{crit}}(T)$. To reproduce the temperature dependence of $S_{\text{self}}^{\text{H}_2}$ that we see in CLOUDY, we fit the parameters $\omega_{\text{H}_2}(T)$, $\alpha(T)$ and $N_{\text{crit}}(T)$ as functions of the temperature T . We obtain the best agreement with CLOUDY using:

$$\omega_{\text{H}_2}(T) = 0.013 \left[1 + \left(\frac{T}{2700 \text{ K}} \right)^{1.3} \right]^{\frac{1}{1.3}} \exp \left[- \left(\frac{T}{3900 \text{ K}} \right)^{14.6} \right], \quad (3.13)$$

$$\alpha(T) = \begin{cases} 1.4 & T < 3000 \text{ K} \\ \left(\frac{T}{4500 \text{ K}} \right)^{-0.8} & 3000 \leq T < 4000 \text{ K} \\ 1.1 & T \geq 4000 \text{ K}, \end{cases} \quad (3.14)$$

$$\frac{N_{\text{crit}}(T)}{10^{14} \text{ cm}^{-2}} = \begin{cases} 1.3 \left[1 + \left(\frac{T}{600 \text{ K}} \right)^{0.8} \right] & T < 3000 \text{ K} \\ \left(\frac{T}{4760 \text{ K}} \right)^{-3.8} & 3000 \leq T < 4000 \text{ K} \\ 2.0 & T \geq 4000 \text{ K}. \end{cases} \quad (3.15)$$

We fit this self-shielding function to the results from CLOUDY at a density of $n_{\text{H}} = 100 \text{ cm}^{-3}$. There will also be an additional density dependence, because the level populations of the H_2 molecule will depend on density, but we do not attempt to model this density dependence here. The H_2 self-shielding factor that we obtain with equations 3.12 to 3.15 agrees with CLOUDY to within 30 per cent at 100 K for $N_{\text{H}_2} < 10^{21} \text{ cm}^{-2}$, and to within 60 per cent at 5000 K for $N_{\text{H}_2} < 10^{20} \text{ cm}^{-2}$ (see Appendix B).

Doppler broadening of the Lyman Werner lines suppresses self-shielding. In a hydrodynamic simulation there are a number of ways we can estimate b (see Glover & Jappsen (2007) for a more detailed discussion of some of the approximations that have been used in the literature). In this paper we shall include turbulence with a constant velocity dispersion of 5 km s^{-1} (unless stated otherwise), which corresponds to a turbulent Doppler broadening parameter of $b_{\text{turb}} = 7.1 \text{ km s}^{-1}$, as used by Krumholz (2012). We also include thermal Doppler broadening b_{therm} , which is related to the temperature T by:

$$b_{\text{therm}} = \sqrt{\frac{2k_{\text{B}}T}{m_{\text{H}_2}}}, \quad (3.16)$$

where m_{H_2} is the mass of an H_2 molecule. The total Doppler broadening parameter is then:

$$b = \sqrt{b_{\text{therm}}^2 + b_{\text{turb}}^2}. \quad (3.17)$$

In our model we only include shielding of H_2 by itself and by dust. However, neutral hydrogen has absorption lines in the Lyman-Werner bands, so HI can also shield H_2 . Draine & Bertoldi (1996) show the HI shielding of H_2 is unimportant in typical molecular clouds, but Wolcott-Green & Haiman (2011) demonstrate that it can be important at low metallicity. We will address this issue in future work.

CO has a dissociation energy of 11.1 eV, which is very close to the lower energy of the Lyman Werner band. Therefore, photons in the Lyman Werner band are also able to dissociate CO. CO is photodissociated via absorptions in discrete lines (dissociation via continuum absorption is negligible for CO), so it can become self-shielded once these lines are saturated, but it can also be shielded by H_2 , as its lines also lie in the Lyman Werner band. The shielding factor of CO due to H_2 and CO ($S_{\text{self},\text{H}_2}^{\text{CO}}$) has been tabulated in two dimensions as a function of N_{H_2} and N_{CO} by Visser et al. (2009) for different values of the Doppler broadening and excitation temperatures of CO and H_2 . High resolution versions of these tables can be found on their website⁶. We use their table calculated for Doppler widths of CO and H_2 of 0.3 km s^{-1} and 3.0 km s^{-1} respectively, and excitation temperatures of CO and H_2 of 50.0 K and 353.6 K respectively, with the elemental isotope ratios of Carbon and Oxygen from Wilson (1999) for the local ISM.

Additionally, dust can shield CO, where the dust shielding factor is given by equation 3.4 (with $\gamma_{\text{d}}^{\text{CO}} = 3.53$).

To summarise, the optically thick photodissociation rates of H_2 and CO are:

$$\Gamma_{\text{H}_2,\text{thick}} = \Gamma_{\text{H}_2,\text{thin}} S_{\text{d}}^{\text{H}_2}(N_{\text{H}_{\text{tot}}}, Z) S_{\text{self}}^{\text{H}_2}(N_{\text{H}_2}) \quad (3.18)$$

$$\Gamma_{\text{CO},\text{thick}} = \Gamma_{\text{CO},\text{thin}} S_{\text{d}}^{\text{CO}}(N_{\text{H}_{\text{tot}}}, Z) S_{\text{self},\text{H}_2}^{\text{CO}}(N_{\text{CO}}, N_{\text{H}_2}), \quad (3.19)$$

while the photoionisation and photodissociation rates of the remaining species are:

$$\Gamma_{i,\text{thick}} = \Gamma_i S^i, \quad (3.20)$$

where $S^i = S_{\text{d}}^i(N_{\text{H}_{\text{tot}}}, Z)$ if the ionisation energy is below 13.6 eV, or $S_{\text{gas}}^i(N_{\text{HI}}, N_{\text{H}_2}, N_{\text{HeI}}, N_{\text{HeII}})$ otherwise.

To calculate the optically thick rates, we thus need to specify the column densities of HI, HeI, HeII, H_2 , H_{tot} and CO, and the metallicity.

3.3.3 Photoheating

The photoheating rate of a species is the photoionisation rate Γ_i multiplied by the average excess energy of the ionising photons $\langle \epsilon_i \rangle$ (see equations 3.5 and 3.6 from paper I). As the gas becomes shielded, the shape of the UV spectrum changes, as more energetic photons are able to penetrate deeper into the gas, thus $\langle \epsilon_i \rangle$

⁶home.strw.leidenuniv.nl/~ewine/photo

increases. In particular, species that have an ionisation energy above 13.6 eV may be strongly affected by absorption by HI, H₂, HeI and HeII (see section 3.3.1). For UV radiation attenuated by column densities N_{HI} , N_{H_2} , N_{HeI} and N_{HeII} , the average excess energy of ionising photons for species i is:

$$\langle \epsilon_{i,\text{thick}} \rangle = \left[\int_{\nu_{0,i}}^{\infty} \frac{4\pi J_{\nu}}{h\nu} \exp(-N_{\text{HI}}\sigma_{\nu,\text{HI}} - N_{\text{H}_2}\sigma_{\nu,\text{H}_2} - N_{\text{HeI}}\sigma_{\nu,\text{HeI}} - N_{\text{HeII}}\sigma_{\nu,\text{HeII}})(h\nu - h\nu_{0,i})\sigma_{\nu,i} d\nu \right] \bigg/ \left[\int_{\nu_{0,i}}^{\infty} \frac{4\pi J_{\nu}}{h\nu} \exp(-N_{\text{HI}}\sigma_{\nu,\text{HI}} - N_{\text{H}_2}\sigma_{\nu,\text{H}_2} - N_{\text{HeI}}\sigma_{\nu,\text{HeI}} - N_{\text{HeII}}\sigma_{\nu,\text{HeII}})\sigma_{\nu,i} d\nu \right]. \quad (3.21)$$

To pre-compute these integrals, we would require four dimensional tables. However, as described in section 3.3.1, we can use the approximations in equations 3.6 and 3.7 to reduce the size of these tables. With these approximations, equation 3.21 becomes:

$$\langle \epsilon_{i,\text{thick}} \rangle = \left[\int_{\nu_{0,i}}^{\nu_{0,\text{H}_2}} \frac{4\pi J_{\nu}}{h\nu} \exp(-N_{\text{HI}}\sigma_{\nu,\text{HI}})(h\nu - h\nu_{0,i})\sigma_{\nu,i} d\nu + \int_{\nu_{0,\text{H}_2}}^{\nu_{0,\text{HeII}}} \frac{4\pi J_{\nu}}{h\nu} \exp(-N_{\text{H}}^{\text{eff}}\sigma_{\nu,\text{HI}} - N_{\text{HeI}}\sigma_{\nu,\text{HeI}})(h\nu - h\nu_{0,i})\sigma_{\nu,i} d\nu + \int_{\nu_{0,\text{HeII}}}^{\infty} \frac{4\pi J_{\nu}}{h\nu} \exp(-N_{\text{H}}^{\text{eff}}\sigma_{\nu,\text{HI}} - N_{\text{He}}^{\text{eff}}\sigma_{\nu,\text{HeI}})(h\nu - h\nu_{0,i})\sigma_{\nu,i} d\nu \right] \bigg/ \left[\int_{\nu_{0,i}}^{\nu_{0,\text{H}_2}} \frac{4\pi J_{\nu}}{h\nu} \exp(-N_{\text{HI}}\sigma_{\nu,\text{HI}})\sigma_{\nu,i} d\nu + \int_{\nu_{0,\text{H}_2}}^{\nu_{0,\text{HeII}}} \frac{4\pi J_{\nu}}{h\nu} \exp(-N_{\text{H}}^{\text{eff}}\sigma_{\nu,\text{HI}} - N_{\text{HeI}}\sigma_{\nu,\text{HeI}})\sigma_{\nu,i} d\nu + \int_{\nu_{0,\text{HeII}}}^{\infty} \frac{4\pi J_{\nu}}{h\nu} \exp(-N_{\text{H}}^{\text{eff}}\sigma_{\nu,\text{HI}} - N_{\text{He}}^{\text{eff}}\sigma_{\nu,\text{HeI}})\sigma_{\nu,i} d\nu \right], \quad (3.22)$$

where the effective hydrogen and helium column densities, $N_{\text{H}}^{\text{eff}}$ and $N_{\text{He}}^{\text{eff}}$, are given in equations 3.9 and 3.10, and account for the attenuation by H₂ and HeII respectively.

For each species with an ionisation energy above 13.6 eV, we tabulate the six integrals in equation 3.22 as a function of the given column densities from 10^{15} to 10^{24} cm⁻² in intervals of 0.1 dex.

3.4 Chemistry and cooling in shielded gas

In this section we look at gas that is illuminated by a radiation field that is attenuated by some column density. We consider a one-dimensional plane-parallel slab

of gas with solar metallicity that is illuminated from one side by the Black (1987) interstellar radiation field. Throughout this paper we use the default solar abundances assumed by CLOUDY, version 13.01 (see for example table 1 in Wiersma et al. 2009). In particular, we take the solar metallicity to be $Z_{\odot} = 0.0129$. The slab is divided into cells such that the total hydrogen column density from the illuminated face of the slab increases from 10^{14} cm^{-2} to 10^{24} cm^{-2} in increments of 0.01 dex. Using the methods described in section 3.3, we then use the resulting column densities to calculate the attenuated photoionisation, photodissociation and photoheating rates and hence to solve for the chemical and thermal evolution in each cell.

The thermochemical evolution of a cell will depend on the chemical state of all cells between it and the illuminated face of the slab, since HI, HeI, HeII, H₂ and CO contribute to the shielding of certain species. We therefore integrate the thermochemistry over a timestep that is determined such that the relative change in the column densities of HI, HeI, HeII, H₂ and CO in each cell will be below some tolerance ϵ (which we take to be 0.1), as estimated based on their change over the previous timestep. In other words, the timestep Δt is given by:

$$\Delta t = \min \left(\frac{\epsilon N_i \Delta t^{\text{prev}}}{\Delta N_i^{\text{prev}} + \psi} \right), \quad (3.23)$$

where N_i is the column density of species i and ΔN_i^{prev} is the change in N_i over the previous timestep Δt^{prev} . We take the minimum over the five species that contribute to shielding and over all gas cells. ψ is a small number that is introduced to prevent division by zero - we take $\psi = 10^{-40}$. At the end of each timestep we then update the column densities of these five species for each cell.

3.4.1 Comparison with CLOUDY

We use CLOUDY version 13.01 to calculate the abundances and the cooling and heating rates in chemical equilibrium as a function of the total hydrogen column density, $N_{\text{H,tot}}$, and compare them to the results from our model. These were calculated for a number of temperatures and densities, which were held fixed across the entire gas slab for this comparison. We add turbulence to the CLOUDY models with a Doppler broadening parameter $b_{\text{turb}} = 7.1 \text{ km s}^{-1}$, in agreement with the default value that we use.

CLOUDY has two possible models for the microphysics of molecular hydrogen. Their ‘big H2’ model follows the level populations of 1893 rovibrational states of molecular hydrogen, and the photodissociation rates from the various electronic and rovibrational transitions via the Solomon process are calculated self-consistently. However, as this is computationally expensive, CLOUDY also has a ‘small H2’ model in which the ground electronic state of molecular hydrogen is split between two vibrational states, a ground state and a single vibrationally excited state, following the approach of Tielens & Hollenbach (1985). These two states are then treated as separate species in the chemical network. The photodissociation rates of H₂ in the small H2 model are taken from Elwert et al. (2005) by default (although there are options to use alternative dissociation rates). We

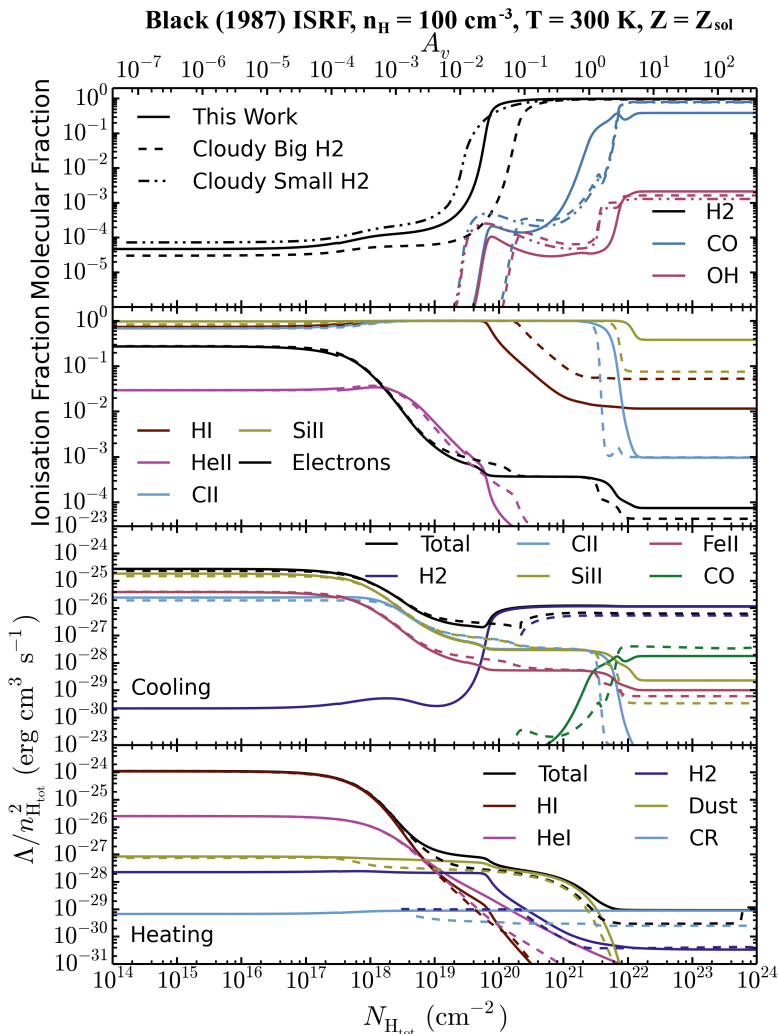


Figure 3.2: Chemistry and cooling properties of a one-dimensional plane-parallel slab of gas illuminated by the Black (1987) interstellar radiation field, plotted as a function of the total hydrogen column density into the gas cloud, assuming solar metallicity with constant density $n_{\text{H}} = 100 \text{ cm}^{-3}$ and constant temperature $T = 300 \text{ K}$. The corresponding dust extinction is marked on the top x-axis, where we have used $A_{\text{v}}/N_{\text{H,tot}} = 4 \times 10^{-22} \text{ mag cm}^2$ for a solar metallicity gas (see section 3.3.1). We compare our model (*solid lines*) to CLOUDY using its big H2 model (*dashed lines*) and its small H2 model (*dot-dot-dashed lines*; top panel only) in chemical equilibrium. **Top panel:** equilibrium molecular fractions ($2n_{\text{H}_2}/n_{\text{H,tot}}$, $n_{\text{CO}}/n_{\text{C,tot}}$ and $n_{\text{OH}}/n_{\text{O,tot}}$); **second panel:** equilibrium ionisation fractions; **third panel:** equilibrium cooling rates; **bottom panel:** equilibrium heating rates. The small discontinuity in the electron abundance at $N_{\text{H,tot}} \sim 3 \times 10^{17} \text{ cm}^{-2}$ is due to the recombination of hydrogen, which switches from case A to case B when the HI optical depth is unity.

primarily focus on the big H₂ model for this comparison, as it includes a more complete treatment of the microphysics involved, although we also show the molecular abundances from the small H₂ model to illustrate the differences between these two CLOUDY models.

The comparison with CLOUDY is shown in figure 3.2 for gas at solar metallicity with a constant density $n_{\text{H}} = 100 \text{ cm}^{-3}$ and a temperature $T = 300 \text{ K}$. More examples at other densities and temperatures can be found on our website⁷. In the top two panels we compare some of the equilibrium molecular and ionisation fractions. Compared to the big H₂ model in CLOUDY, the HI-H₂ transition occurs at a somewhat lower column density in our model, with a molecular hydrogen fraction $x_{\text{H}_2} = 0.5$ at $N_{\text{H, tot}} \approx 8.1 \times 10^{19} \text{ cm}^{-2}$, compared to $N_{\text{H, tot}} \approx 2.8 \times 10^{20} \text{ cm}^{-2}$ in CLOUDY. Below this transition the molecular hydrogen fraction tends towards a value $x_{\text{H}_2} \approx 5 \times 10^{-5}$ in our model. This fraction is sufficiently high for the H₂ to shield itself from the Lyman Werner radiation before dust shielding becomes important (with $S_{\text{d}}^{\text{H}_2} \sim 0.1$ at $A_{\text{v}} \approx 0.6$), as the self-shielding is significant at relatively low H₂ column densities (with $S_{\text{self}}^{\text{H}_2} \sim 0.1$ at $N_{\text{H}_2} \approx 6 \times 10^{15} \text{ cm}^{-2}$, as defined in equation 3.12). The H₂ fraction in the photodissociated region is $x_{\text{H}_2} \approx 3 \times 10^{-5}$ for CLOUDY's big H₂ model, which is slightly lower than in our model. This explains why the gas becomes self-shielded at a somewhat higher total column density in CLOUDY than in our model. This discrepancy occurs because we use a different photodissociation rate. As discussed in paper I, the dissociation rate of H₂ via the Solomon process depends on the level populations of the rovibrational states of H₂. This is calculated self-consistently in the big H₂ model of CLOUDY, whereas we must use an approximation to the photodissociation rate, as we do not follow the rovibrational levels of H₂. We therefore miss, for example, the dependence of the photodissociation rate on density, which affects the rovibrational level populations.

For comparison, we also show the molecular hydrogen abundance predicted by the small H₂ model of CLOUDY in the top panel of figure 3.2 (*black dot-dot-dashed line*). The HI-H₂ transition in the small H₂ model is closer to our model than the big H₂ model, with $x_{\text{H}_2} = 0.5$ at $N_{\text{H, tot}} \approx 1.1 \times 10^{20} \text{ cm}^{-2}$. However, the transition in our model is somewhat steeper than in CLOUDY's small H₂ model.

While the HI-H₂ transition in this example, with constant temperature and density, is caused by H₂ self-shielding, we would not expect temperatures as low as 300 K in the photodissociated region, nor would we expect densities as high as 100 cm^{-3} . This example therefore overestimates the importance of H₂ self-shielding. In section 3.4.3 we address this issue by considering a cloud that is in thermal and pressure equilibrium.

After the HI-H₂ transition the neutral hydrogen abundance x_{HI} tends to $x_{\text{HI}} \approx 0.01$ at $N_{\text{H, tot}} \gtrsim 10^{22} \text{ cm}^{-2}$ in our model, compared to $x_{\text{HI}} \approx 0.05$ in CLOUDY. This difference arises because the cosmic ray dissociation rate of H₂ that we use in our model, which is based on the rates in the UMIST database, is an order of magnitude lower than that used in CLOUDY.

The onset of the HI-H₂ transition leads to a rise in the CO abundance, although

⁷<http://noneqism.strw.leidenuniv.nl>

most carbon is still in CII at this transition. At higher column densities the dust is able to shield the photodissociation of CO, which becomes fully shielded at $N_{\text{H,tot}} \gtrsim 10^{22} \text{ cm}^{-2}$. This second transition also corresponds to a drop in the abundances of singly ionised metals with ionisation energies lower than 1 Ryd, such as CII and SiII, whose photoionisation rates are attenuated by dust rather than by neutral hydrogen and helium. These species become shielded at a slightly higher column density in our model than in CLOUDY (for example, CII has an ionisation fraction $x_{\text{CII}} = 0.1$ at $N_{\text{H,tot}} \approx 7 \times 10^{21} \text{ cm}^{-2}$ in our model, compared to $N_{\text{H,tot}} \approx 4 \times 10^{21} \text{ cm}^{-2}$ in CLOUDY).

Previous models of photodissociation regions have demonstrated that molecules such as H₂O will freeze out at large depths, with visual extinction $A_v \gtrsim 10$ (e.g. Hollenbach et al. 2009, 2012). However, we do not include the freeze out of molecules in our model (and we also exclude molecule freeze out in CLOUDY for comparison with our model). This will affect the gas phase chemistry, so the abundances predicted by our model in figure 3.2 are likely to be unrealistic at the highest depths shown here ($A_v \gtrsim 10$).

In the bottom two panels of figure 3.2 we show the total cooling and heating rates for this example, along with the contributions from selected individual species. Before the HI-H₂ transition the cooling is dominated by SiII, FeII and CII, with heating coming primarily from photoionisation of neutral hydrogen. After this transition the photoheating rates drop rapidly, with the main heating mechanism being photoelectric dust heating, while the total cooling rates are lower and are primarily from molecular hydrogen. Once dust shielding begins to significantly attenuate the UV radiation field below 13.6 eV at a column density $N_{\text{H,tot}} \sim 10^{21} \text{ cm}^{-2}$, the photoelectric heating rate falls sharply. For $N_{\text{H,tot}} \gtrsim 10^{22} \text{ cm}^{-2}$ the heating rates are dominated by cosmic rays. In our model this is primarily from cosmic ray ionisation heating of H₂. However, CLOUDY only includes cosmic ray heating of HI, hence the total heating rates in our model are higher than CLOUDY in this region. The most important coolants in the fully shielded gas are molecular hydrogen and CO.

We have also compared our abundances and cooling and heating rates with CLOUDY at densities of 1 cm^{-3} and 10^4 cm^{-3} , and a temperature of 100 K. These results can be found on our website. We generally find good agreement with CLOUDY, although we sometimes find that the abundances of singly ionised metals with low ionisation energies, such as SiII and FeII, are in poor agreement in fully shielded gas, once carbon becomes fully molecular. This occurs at the highest densities that we consider, although we begin to see such discrepancies in the SiII abundance in figure 3.2. In this regime the ionisation of these species is typically dominated by charge transfer reactions between metal species, the rates of which tend to be uncertain. Moreover, a significant fraction of Si is found in SiO in the CLOUDY models and, because our simplified molecular network does not include silicon molecules, we are unable to reproduce the correct silicon abundances in fully shielded gas. Since the abundances of other low ionisation energy ions such as FeII and MgII are dependent on SiII due to charge transfer reactions in this regime, these species will also be uncertain in fully shielded gas. However, the predicted abundances of molecules such as H₂ and CO are in good agreement

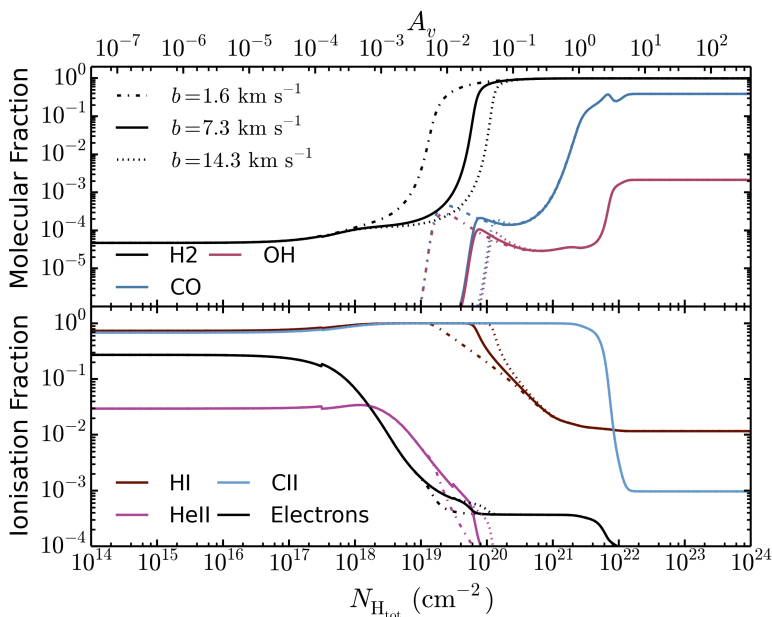


Figure 3.3: Comparison of the chemical properties of a one-dimensional plane-parallel slab of gas for three different Doppler broadening parameters, corresponding to different levels of turbulence in the gas, with $b = 1.6 \text{ km s}^{-1}$ corresponding to pure thermal broadening. **Top panel:** equilibrium molecular fractions ($2n_{\text{H}_2}/n_{\text{H,tot}}$, $n_{\text{CO}}/n_{\text{C,tot}}$ and $n_{\text{OH}}/n_{\text{O,tot}}$); **bottom panel:** equilibrium ionisation fractions. These were calculated at solar metallicity, a constant density $n_{\text{H}} = 100 \text{ cm}^{-3}$ and a constant temperature $T = 300 \text{ K}$. The strongest turbulence shown here ($b = 14.3 \text{ km s}^{-1}$) increases the column density at which the hydrogen starts to become molecular by more than an order of magnitude compared to pure thermal Doppler broadening, although its impact on the transition column density at which $x_{\text{H}_2} = 0.5$ is less significant.

with CLOUDY in this regime.

3.4.2 Importance of turbulence for H₂ self-shielding

In the previous section we found that the small H₂ abundance in the photodissociated region can be sufficient to begin attenuating the photodissociation rate of molecular hydrogen via self-shielding before dust extinction becomes significant. However, the presence of turbulence in the gas can suppress self-shielding due to Doppler broadening of the Lyman Werner lines. In this section we investigate the impact that turbulence can have on the HI-H₂ transition by repeating the above calculations for three different values of the turbulent Doppler broadening parameter: $b_{\text{turb}} = 0 \text{ km s}^{-1}$, $b_{\text{turb}} = 7.1 \text{ km s}^{-1}$ (our default value) and $b_{\text{turb}} = 14.2 \text{ km s}^{-1}$. The thermal Doppler broadening parameter at 300 K is $b_{\text{therm}} = 1.6 \text{ km s}^{-1}$, thus the total Doppler broadening parameters are $b = 1.6 \text{ km s}^{-1}$, 7.3 km s^{-1} and 14.3 km s^{-1} .

In figure 3.3 we show the molecular and ionisation fractions for these three

Doppler broadening parameters at a constant density $n_{\text{H}_{\text{tot}}} = 100 \text{ cm}^{-3}$ and a constant temperature $T = 300 \text{ K}$. We find that, while the ion fractions are hardly affected, increasing the turbulent Doppler broadening parameter from 0 to 14.2 km s^{-1} increases the column density at which the hydrogen starts to become molecular by more than an order of magnitude, as it suppresses H_2 self-shielding. However, the transition also becomes sharper for higher values of b , so the change in the column density at which half of the hydrogen is molecular is less significant, increasing from $N_{\text{H}_{\text{tot}}} \approx 3.3 \times 10^{19} \text{ cm}^{-2}$ to $N_{\text{H}_{\text{tot}}} \approx 1.4 \times 10^{20} \text{ cm}^{-2}$. The transition to molecular hydrogen is still caused by H_2 self-shielding in these examples, even for the highest value of b that we consider here.

3.4.3 Atomic to molecular transition in thermal and pressure equilibrium

The previous sections considered gas at a constant temperature of 300 K, but figure 3.2 showed that the heating and cooling rates vary strongly with the column density into the cloud. Furthermore, we assumed a constant density throughout the cloud, which is unrealistic as gas at low column densities will be strongly photoheated and will thus typically have lower densities. It would therefore be more realistic to consider a cloud that is in thermal and pressure equilibrium. To achieve this, we first ran a series of models with different constant densities that were allowed to evolve to thermal equilibrium, from which we obtained the thermal equilibrium temperature on a two-dimensional grid of density and column density. Then, for each column density bin, we used this grid to determine the density that will give the assumed pressure. Finally, we imposed this isobaric density profile on the one-dimensional plane-parallel slab of gas and evolved it until it reached thermal and chemical equilibrium. This scenario is more typical of the two-phase ISM, in which gas is photoheated to higher temperatures, with lower densities, at low column densities, and then cools to a much colder and denser phase once the ionising photons have been attenuated and molecular cooling becomes important.

In figure 3.4 we show the results for a cloud with a constant pressure $P/k_{\text{B}} = 10^3 \text{ cm}^{-3} \text{ K}$, assuming solar metallicity. The equilibrium molecular and ionisation fractions of some species are shown in the top two panels of figure 3.4 as a function of the total column density $N_{\text{H}_{\text{tot}}}$, the equilibrium gas temperature and density are shown in the middle panel, and the equilibrium cooling and heating rates are shown in the bottom two panels.

We see that gas is more strongly ionised in the photodissociated region compared to the constant temperature and density run in figure 3.2. This is due to both the higher temperature and the lower density. Furthermore, the molecular hydrogen fraction is much lower in this region, and the H_2 self-shielding is thus weaker. Hence, the HI-H_2 transition occurs at a higher column density compared to figure 3.2 ($x_{\text{H}_2} = 0.5$ at $N_{\text{H}_{\text{tot}}} \approx 1.5 \times 10^{21} \text{ cm}^{-2}$ in figure 3.4, compared to $N_{\text{H}_{\text{tot}}} \approx 8.1 \times 10^{19} \text{ cm}^{-2}$ in figure 3.2). The H_2 fraction first rises at $N_{\text{H}_{\text{tot}}} \sim 2 \times 10^{20} \text{ cm}^{-2}$ due to a corresponding rise in the HI abundance, which is required to form H_2 . The HI abundance increases because it is able to shield itself against ionising radi-

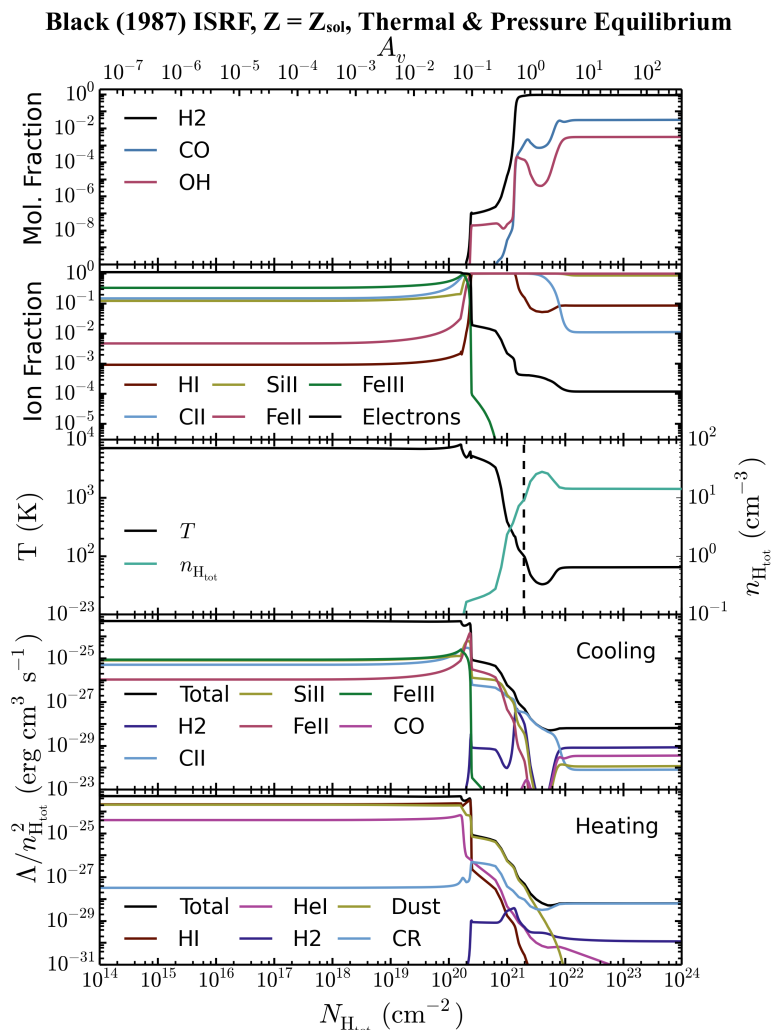


Figure 3.4: Chemistry and cooling properties of a one-dimensional plane-parallel slab of gas that is in thermal and pressure equilibrium with a pressure $P/k_B = 10^3$ cm⁻³ K, plotted as a function of the total hydrogen column density into the gas cloud, assuming solar metallicity in the presence of the Black (1987) interstellar radiation field. **Top panel:** equilibrium molecular fractions ($2n_{\text{H}_2}/n_{\text{H,tot}}$, $n_{\text{CO}}/n_{\text{C,tot}}$ and $n_{\text{OH}}/n_{\text{O,tot}}$); **second panel:** equilibrium ionisation fractions; **third panel:** equilibrium gas temperature and density; **fourth panel:** equilibrium cooling rates; **bottom panel:** equilibrium heating rates. The vertical dashed line in the third panel indicates the column density at which the gas becomes Jeans unstable. To the right of this dashed line we would expect the gas cloud to become self-gravitating, and the density profile that we have imposed assuming pressure equilibrium will underestimate the typical densities corresponding to these column densities. At low column densities, the total cooling rate in the fourth panel is dominated by OIII and SIII (not shown here).

ation above 1 Ryd (the HI column density here is $\sim 10^{17} \text{ cm}^{-2}$). However, the H_2 fraction still remains low after this initial increase ($x_{\text{H}_2} \approx 10^{-7}$). The HI- H_2 transition at $N_{\text{H}_{\text{tot}}} \approx 1.5 \times 10^{21} \text{ cm}^{-2}$ is initially triggered by the increasing density, which enhances the formation rate of H_2 on dust grains with respect to the photodissociation rate. However, H_2 self-shielding then becomes significant and is responsible for the final transition to a fully molecular gas. When we repeat this model without H_2 self-shielding, we find that the HI- H_2 transition occurs at a factor ~ 5 higher column density, with $x_{\text{H}_2} = 0.5$ at $N_{\text{H}_{\text{tot}}} \approx 7.2 \times 10^{21} \text{ cm}^{-2}$.

In figure 3.4, CO becomes fully shielded from dissociating radiation at $N_{\text{H}_{\text{tot}}} \gtrsim 10^{22} \text{ cm}^{-2}$. Like in the constant density run in figure 3.2, this transition is determined by dust shielding. However, the fraction of carbon in CO in the fully shielded region is $\lesssim 5$ per cent in figure 3.4, compared to ~ 40 per cent in figure 3.2, with most of the remaining carbon in C I (not shown in the figures). This lower abundance of CO in the isobaric run is due to the lower density, which is a factor of ~ 10 lower than the constant density run in the fully shielded region.

Observations of diffuse clouds at low column densities find abundances of CH^+ that are several orders of magnitude higher than can be explained using standard chemical models (e.g. Federman et al. 1996; Sheffer et al. 2008; Visser et al. 2009). This also leads to predicted CO abundances that are lower than observed in such regions, as CH^+ is an important formation channel for CO. Various non-thermal production mechanisms for CH^+ have been proposed to alleviate this discrepancy. For example, Federman et al. (1996) suggest that Alfvén waves that enter the cloud can produce non-thermal motions between ions and neutral species, thus increasing the rates of ion-neutral reactions.

To see what effect such suprathermal chemistry has on our chemical network, we repeated the models in figures 3.2 and 3.4 with the kinetic temperature of all ion-neutral reactions replaced by an effective temperature that is enhanced by Alfvén waves, as given by the prescription of Federman et al. (1996) with an Alfvén speed of 3.3 km s^{-1} . Following Sheffer et al. (2008) and Visser et al. (2009), we only include this enhancement of the ion-neutral reactions at low column densities, $N_{\text{H}_2} < 4 \times 10^{20} \text{ cm}^{-2}$. In the model with a constant density $n_{\text{H}_{\text{tot}}} = 100 \text{ cm}^{-3}$ and constant temperature $T = 300 \text{ K}$, we find that the CH^+ abundance is increased by up to four orders of magnitude at intermediate column densities $5 \times 10^{19} \text{ cm}^{-2} \lesssim N_{\text{H}_{\text{tot}}} \lesssim 10^{21} \text{ cm}^{-2}$, which is consistent with previous studies (e.g. Federman et al. 1996). However, the CO abundance is only enhanced by up to a factor of 6 in this same region, which is less than the enhancements in CO abundance seen in e.g. Sheffer et al. (2008), who find that the CO abundance increases by a factor ~ 100 for an Alfvén speed of 3.3 km s^{-1} . We see similar enhancements in the model with a constant pressure $P/k_B = 10^3 \text{ cm}^{-3} \text{ K}$, but only at column densities $10^{21} \text{ cm}^{-2} \lesssim N_{\text{H}_{\text{tot}}} \lesssim 3 \times 10^{21} \text{ cm}^{-2}$, as the temperature at lower column densities is much higher than in the constant density model ($T > 1000 \text{ K}$).

At low column densities the cooling rate in figure 3.4 is determined by several ionised species including SiII, FeII, FeIII and CII, along with NIII, OIII, NeIII and SiIII (not shown in figure 3.4). Heating at low column densities is primarily from dust heating and photoionisation of HI and HeI. At $N_{\text{H}_{\text{tot}}} \sim 2 \times 10^{20} \text{ cm}^{-2}$ the cooling rates from SiII and FeII peak as SiIII and FeIII recombine, creating a small dip in

the temperature profile. The photoheating rate then drops sharply as the ionising radiation above 1 Ryd becomes shielded by HI, and the total heating rate becomes dominated by the dust photoelectric effect. The thermal equilibrium temperature reaches a minimum of 30 K at $N_{\text{H}_{\text{tot}}} \sim 4 \times 10^{21} \text{ cm}^{-2}$ as the dust photoelectric heating becomes suppressed by dust shielding, leaving heating primarily from cosmic ray ionisation of H_2 . However, after this point the carbon forms CO and the cooling becomes dominated by molecules (CO and H_2). These species are less efficient at cooling than CII, so the thermal equilibrium temperature increases to 60 K. Hence, the temperature in the fully molecular region is higher than the minimum at $N_{\text{H}_{\text{tot}}} \sim 4 \times 10^{21} \text{ cm}^{-2}$.

We note that the assumption of pressure equilibrium in these examples will be unrealistic at high column densities, where the gas becomes self-gravitating. The vertical dashed line in the middle panel of figure 3.4 indicates the column density at which the size of the system, $N_{\text{H}_{\text{tot}}}/n_{\text{H}_{\text{tot}}}$, becomes larger than the local Jeans length, at $N_{\text{H}_{\text{tot}}} \approx 2 \times 10^{21} \text{ cm}^{-2}$. Thus, we would expect the fully molecular region in these examples to have a higher density than we have used here.

We also considered a gas cloud with a pressure that is a factor 100 larger than is shown in figure 3.4. This results in higher densities in the fully shielded region that are more typical of molecular clouds ($n_{\text{H}_{\text{tot}}} \sim 10^3 \text{ cm}^{-3}$), although the densities in the photodissociated region are then higher than we would expect for the warm ISM. The cumulative H_2 fractions for the two pressures are shown in figure 3.5 (see section 3.5). The top panels are at the lower pressure ($P/k_{\text{B}} = 10^3 \text{ cm}^{-3} \text{ K}$), and the bottom panels are at the higher pressure ($P/k_{\text{B}} = 10^5 \text{ cm}^{-3} \text{ K}$). In the left panels we use a metallicity $0.1Z_{\odot}$, and in the right panels we use solar metallicity. We find that in all of these examples H_2 self-shielding is again important for the final transition to fully molecular hydrogen, reducing the column density of this transition by up to two orders of magnitude compared to the same model without H_2 self-shielding.

We thus find that the effect of H_2 self-shielding can be weaker in a cloud that is in thermal and pressure equilibrium due to the lower densities at low column densities compared to a model with a constant density and temperature. However, H_2 self-shielding still determines the final transition to fully molecular hydrogen. Furthermore, H_2 self-shielding will be even more important if the pressure (and hence densities) are higher. This trend with density agrees with previous models of photodissociation regions and molecular clouds (e.g. Black & van Dishoeck 1987; Krumholz et al. 2009).

Figure 3.5 also demonstrates the dependence of the transition column density on pressure and metallicity. The HI- H_2 transition occurs at a lower column density for higher pressure and higher metallicity. Both of these trends are driven by H_2 self-shielding because the H_2 fraction in the dissociated region is higher at higher pressure (due to the increased density) and at higher metallicity (due to the increased formation of H_2 on dust grains, and also due to the increased cooling from metals, which results in a lower temperature and a higher density at a given pressure). These trends with pressure (or density) and metallicity have also been seen in previous studies of the H_2 transition in photodissociation regions (e.g. Wolfire et al. 2010).

We also see the time evolution of the molecular hydrogen fraction, starting from neutral, atomic gas, in figure 3.5. In the low pressure run at a metallicity $0.1Z_{\odot}$ (*top left panel*) the H_2 abundance in the fully shielded region takes ~ 1 Gyr to reach equilibrium. This time-scale is shorter in the high pressure runs and at higher metallicity. At the high pressure and solar metallicity (*bottom right panel*), the H_2 abundance already reaches equilibrium after ~ 1 Myr.

3.5 Comparison with published approximations for H_2 formation

The connection between gas surface density and star formation rate density is well established observationally, both averaged over galactic scales (e.g. Kennicutt 1989, 1998) and also in observations that are spatially resolved on \sim kpc scales (Wong & Blitz 2002; Heyer et al. 2004; Schuster et al. 2007), although at smaller scales, comparable to giant molecular clouds ($\lesssim 100$ pc), this relation breaks down (e.g. Onodera et al. 2010). It has emerged more recently that star formation correlates more strongly with the molecular than with the atomic or total gas content (e.g. Kennicutt et al. 2007; Leroy et al. 2008; Bigiel et al. 2008, 2010), although the more fundamental correlation may in fact be with the cold gas content (Schaye 2004; Krumholz et al. 2011; Glover & Clark 2012).

This important observational link between molecular gas and star formation has motivated several new models and prescriptions for following the H_2 fraction of gas in hydrodynamic simulations. These studies aim to use a more physical prescription for star formation and to investigate its consequence for galactic environments that are not covered by current observations, such as very low metallicity environments at high redshifts. Some of these prescriptions utilise very simple chemical models that include the formation of molecular hydrogen on dust grains and its photodissociation by Lyman Werner radiation to follow the non-equilibrium H_2 fraction (e.g. Gnedin et al. 2009; Christensen et al. 2012). Others use approximate analytic models to predict the H_2 content of a cloud from its physical parameters such as the dust optical depth and incident photodissociating radiation field (e.g. Krumholz et al. 2008, 2009; McKee & Krumholz 2010), which can then be applied to gas particles/cells in hydrodynamic simulations (e.g. Krumholz & Gnedin 2011; Halle & Combes 2013).

In this section we compare the molecular hydrogen fractions predicted by some of these models with our chemical network. We begin by introducing the molecular hydrogen models from the literature that we will compare our chemical network to, and then we present our results.

3.5.1 Gnedin09 model

Gnedin et al. (2009) present a simple prescription to follow the non-equilibrium evolution of the molecular hydrogen fraction in hydrodynamic simulations, which has been implemented in cosmological Adaptive Mesh Refinement (AMR) simulations (Gnedin & Kravtsov 2010), and was also adapted by Christensen et al.

(2012) for cosmological Smoothed Particle Hydrodynamics (SPH) simulations. This model includes the formation of H_2 on dust grains, photodissociation by Lyman Werner radiation, shielding by both dust and H_2 , and a small number of gas phase reactions that become important in the dust-free regime (we use the five gas phase reactions suggested by Christensen et al. 2012; see below). The evolution of the neutral and molecular hydrogen fractions, x_{HI} and x_{H_2} , can then be described by the following rate equations:

$$\dot{x}_{HI} = R(T)n_e x_{HII} - S_d x_{HI} \Gamma_{HI} - C_{HI} x_{HI} n_e - 2\dot{x}_{H_2}, \quad (3.24)$$

$$\dot{x}_{H_2} = R_d n_{H_{tot}} x_{HI} (x_{HI} + 2x_{H_2}) - S_d S_{self}^{H_2} \Gamma_{H_2}^{LW} + \dot{x}_{H_2}^{SP}. \quad (3.25)$$

Following Christensen et al. (2012), we have also included the collisional ionisation of HI, C_{HI} , in the above equations, even though it was omitted by Gnedin et al. (2009). $R(T)$ is the recombination rate of HII, Γ_{HI} is the photoionisation rate of HI and $\Gamma_{H_2}^{LW}$ is the photodissociation rate of H_2 by Lyman Werner radiation. For the gas phase reactions, $\dot{x}_{H_2}^{SP}$, we include the five reactions suggested by Christensen et al. (2012): the formation of H_2 via H^- and its collisional dissociation via H_2 , HI, HII and e^- , with the abundance of H^- assumed to be in chemical equilibrium, as given by equation (27) of Abel et al. (1997).

Gnedin et al. (2009) use the H_2 self-shielding factor $S_{self}^{H_2}$ from Draine & Bertoldi (1996), albeit with different parameters. They find that using $\omega_{H_2} = 0.2$ and a constant Doppler broadening parameter of $b = 1 \text{ km s}^{-1}$ in equation 3.11, along with the original value of $\alpha = 2$, produces better agreement between their model and observations. This choice of parameters results in weaker H_2 self-shielding compared to our temperature-dependent self-shielding function (equations 3.12 to 3.15) for the same value of b . However, in our fiducial model we include a turbulent Doppler broadening parameter of $b_{turb} = 7.1 \text{ km s}^{-1}$, which makes the self-shielding weaker in our model than in the Gnedin09 model at intermediate H_2 column densities ($10^{14} \text{ cm}^{-2} \lesssim N_{H_2} \lesssim 10^{16} \text{ cm}^{-2}$).

The dust shielding factor S_d is given in equation 3.4, except that Gnedin et al. (2009) use an effective dust area per hydrogen atom of $\sigma_{d,eff} = \gamma_d^{H_2} A_v / N_{H_{tot}} = 4 \times 10^{-21} \text{ cm}^2$. This is a factor of 2.7 larger than the value that we use. Also, unlike us, they use the same dust shielding factor for both H_2 and HI.

For the rate of formation of H_2 on dust grains (R_d), Gnedin et al. (2009) use a rate that was derived from observations by Wolfire et al. (2008), scaled linearly with the metallicity and multiplied by a clumping factor C_ρ that accounts for the fact that there may be structure within the gas below the resolution limit, and that molecular hydrogen will preferentially form in the higher density regions:

$$R_d = 3.5 \times 10^{-17} Z/Z_\odot C_\rho \text{ cm}^3 \text{ s}^{-1}. \quad (3.26)$$

Gnedin et al. (2009) use a clumping factor $C_\rho = 30$, but in our comparisons we consider spatially resolved, one-dimensional simulations of an illuminated slab of gas. Therefore, for these comparisons we shall take $C_\rho = 1$. For gas temperatures $10 \text{ K} < T < 10^3 \text{ K}$, the rate in equation 3.26 is within a factor ~ 2 of the value used in our model, taken from Cazaux & Tielens (2002) with a dust temperature

of 10 K. However, above 10^3 K the H_2 formation rate on dust grains in our model decreases. This temperature dependence is not included in the Gnedin09 model.

Finally, the abundances of electrons and HII can be calculated from constraint equations.

Gnedin & Kravtsov (2011) expand the Gnedin09 model to include the Helium chemistry. There are also other examples in the literature of methods that follow the non-equilibrium evolution of H_2 using simplified chemical models. For example, Bergin et al. (2004) present a model for the evolution of molecular hydrogen that includes the formation of H_2 on dust grains and its dissociation by Lyman Werner radiation and cosmic rays, although they do not include the gas phase reactions (see their equation A1). The model of Bergin et al. (2004) has been used to investigate the formation of molecular clouds in galactic discs (e.g. Dobbs & Bonnell 2008; Khoperskov et al. 2013). We only consider the Gnedin09 chemical model in this section.

3.5.2 KMT model

Krumholz et al. (2008, 2009) and McKee & Krumholz (2010) develop a simple analytic model that considers a spherical gas cloud that is immersed in an isotropic radiation field. By solving approximately the radiative transfer equation with shielding of the Lyman Werner radiation by dust and H_2 to obtain the radial dependence of the radiation field, and then balancing the photodissociation of molecular hydrogen against its formation on dust grains, they derive simple analytic estimates for the size of the fully molecular region of the cloud, and hence for its molecular fraction in chemical equilibrium.

We use equation (93) of McKee & Krumholz (2010) to calculate the mean equilibrium H_2 fraction, f_{H_2} , of a gas cloud:

$$f_{\text{H}_2} = 1 - \left(\frac{3}{4}\right) \frac{s}{1 + 0.25s}, \quad (3.27)$$

where s is given by their equation (91):

$$s = \frac{\ln(1 + 0.6\chi + 0.01\chi^2)}{0.6\tau_c}, \quad (3.28)$$

where χ and τ_c are dimensionless parameters of their model, which represent a measure of the incident Lyman Werner radiation field and the dust optical depth to the centre of the cloud respectively. They are given by their equations (9) and (86):

$$\chi = 71 \left(\frac{\sigma_{\text{d},-21}}{R_{\text{d},-16.5}} \right) \frac{G'_0}{(n_{\text{H}}/\text{cm}^{-3})}, \quad (3.29)$$

$$\tau_c = \frac{3}{4} \left(\frac{\Sigma\sigma_{\text{d}}}{\mu_{\text{H}}} \right) = \sigma_{\text{d}} N_{\text{H}_{\text{tot}}}, \quad (3.30)$$

where $\sigma_{\text{d},-21} = \sigma_{\text{d}}/10^{-21} \text{ cm}^2$, σ_{d} is the cross-sectional area of dust grains available to absorb photons (Krumholz et al. 2009 use $\sigma_{\text{d}} = 10^{-21} Z/Z_{\odot} \text{ cm}^2$), and $R_{\text{d},-16.5} =$

$R_d/10^{-16.5}\text{cm}^3\text{s}^{-1}$, where R_d is the rate coefficient for H₂ formation on dust grains. For the latter, McKee & Krumholz (2010) use an observationally determined value from Draine & Bertoldi (1996), multiplied by the metallicity: $R_{d,-16.5} = Z/Z_\odot$. Krumholz & Gnedin (2011) also boost $R_{d,-16.5}$ by the clumping factor C_ρ , whereas Krumholz (2013) multiply τ_c by the clumping factor, but we take $C_\rho = 1$. G'_0 is the number density of dissociating photons in the Lyman Werner band, normalised to the value from Draine (1978) for the Milky Way. For the Black (1987) interstellar radiation field that we consider here, $G'_0 = 0.803$. n_H is the total hydrogen number density, μ_H is the mean mass per hydrogen nucleus, Σ is the average surface density of the spherical cloud and N_{Htot} is the total hydrogen column density from the edge of the cloud to its centre.

Krumholz et al. (2009) and Krumholz (2013) demonstrate that the molecular gas content predicted by this model is in agreement with various extragalactic observations and with observations of molecular clouds within the Milky Way, for particular values of the clumping factor C_ρ and assumptions about the radiation field and/or density. For example, Krumholz et al. (2009) assume that the ratio of the radiation field to the density, G'_0/n_H , is set by the minimum density of the cold neutral medium required for the ISM to be in two-phase equilibrium. As shown in their equation 7, the ratio G'_0/n_H then depends only on metallicity under this assumption. Krumholz (2013) extends the approach of Krumholz et al. (2009) by assuming that, as $G'_0 \rightarrow 0$, the density n_H reaches a minimum floor, which is required to ensure that the thermal pressure of the ISM is able to maintain hydrostatic equilibrium in the disc. This becomes important in the molecule-poor regime. In contrast, the runs that we present below use a constant incident radiation field (the Black 1987 interstellar radiation field) and assume a density profile such that the gas pressure is constant throughout the cloud.

Krumholz & Gnedin (2011) implement this model in cosmological AMR simulations to estimate the equilibrium H₂ fraction of each gas cell. Halle & Combes (2013) also implement the KMT model in SPH simulations of isolated disc galaxies to investigate the role that the cold molecular phase of the ISM plays in star formation and as a gas reservoir in the outer disc.

3.5.3 Results

In Figure 3.5 we compare the molecular abundances from our model (*coloured solid curves*) with the simpler Gnedin09 (*coloured dashed curves*) and KMT (*black solid curves*) models described above. These were calculated using temperature and density profiles that are in thermal and pressure equilibrium. We use two different pressures, $P/k_B = 10^3\text{cm}^{-3}\text{K}$ (*top row*) and $P/k_B = 10^5\text{cm}^{-3}\text{K}$ (*bottom row*), and two metallicities, $Z = 0.1Z_\odot$ (*left column*) and Z_\odot (*right column*). The colour encodes the time evolution in our model and the Gnedin09 model, starting from fully neutral, atomic gas (KMT is an equilibrium model). In figures 3.2-3.4 we showed the abundances in each gas cell, but figure 3.5 shows the cumulative molecular fraction, i.e. the fraction of all hydrogen atoms that is in H₂ up to a given column density. This allows us to compare our results to the KMT model, in which the specified column density is measured to the centre of a spherical cloud, and

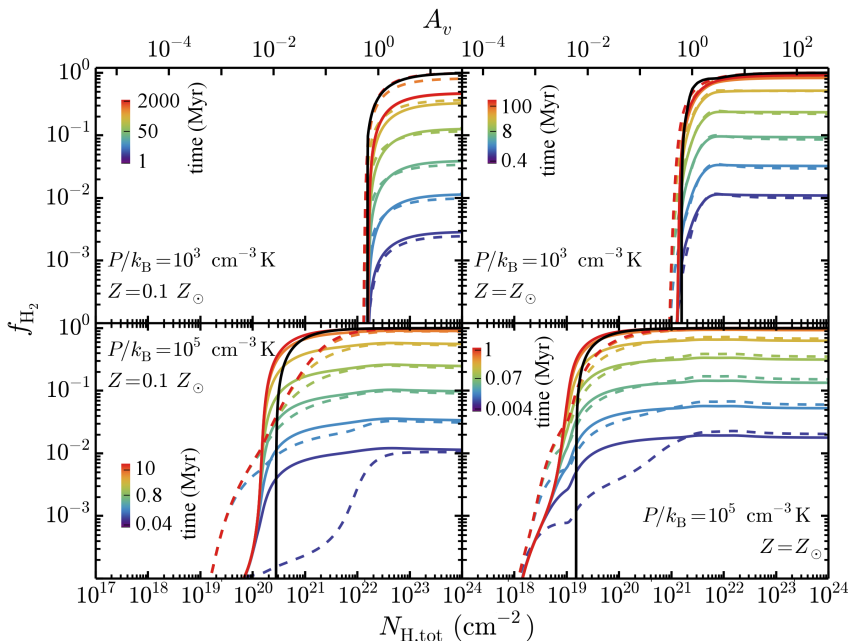


Figure 3.5: Comparison of the cumulative molecular hydrogen fraction, plotted as a function of total hydrogen column density, as predicted by our chemical model (*solid coloured curves*), the Gnedin09 model (*dashed coloured curves*) and the equilibrium KMT model (*solid black curve*). The coloured lines show the non-equilibrium evolution measured at logarithmic time intervals, as indicated by the colour bars, until the simulation reaches chemical equilibrium (red curves). Each run was calculated with a density and temperature profile in pressure and thermal equilibrium, with a pressure $P/k_B = 10^3 \text{ cm}^{-3} \text{ K}$ (*top row*) and $P/k_B = 10^5 \text{ cm}^{-3} \text{ K}$ (*bottom row*). We used a metallicity $0.1Z_\odot$ (*left column*) and Z_\odot (*right column*). At low pressure the agreement between the different models is good, except that in the low metallicity run (top left panel), cosmic ray dissociation of H_2 , which was not included in the KMT and Gnedin09 models, reduces the equilibrium H_2 fraction by a factor of two in the fully shielded region. At high pressure the differences between the models are substantial.

then the H_2 fraction, f_{H_2} , is the fraction of gas in the entire cloud that is molecular, rather than the fraction of molecular gas at that column density. However, this is still not entirely equivalent to our model as we assume a plane-parallel geometry, whereas the KMT model assumes a spherical geometry.

In the low pressure runs, the final molecular fractions predicted by our model generally agree well with both the Gnedin09 and the KMT models. The time evolution of the H_2 fraction in our model and the Gnedin09 model are also in good agreement. The largest discrepancy in the equilibrium abundance is in the fully shielded region at low metallicity (top left panel of figure 3.5), where the equilibrium H_2 fraction in our model is a factor of two lower than that predicted by the Gnedin09 and KMT models. This is due to cosmic ray dissociation of H_2 , which

lowers the H_2 abundance but is not included in the Gnedin09 or KMT models.

In the high pressure runs the $HI-H_2$ transition occurs at a slightly lower column density than in the KMT model. For example, at solar metallicity (bottom right panel of figure 3.5), we predict that $f_{H_2} = 0.5$ at $N_{H_{tot}} = 2.2 \times 10^{19} \text{ cm}^{-2}$, compared to $N_{H_{tot}} = 3.0 \times 10^{19} \text{ cm}^{-2}$ for KMT. In the Gnedin09 model, the $HI-H_2$ transition is noticeably flatter at high pressure than in our model or in the KMT model. The H_2 fraction starts to increase at a lower column density in the Gnedin09 model than in the other two models, but the column density at which $f_{H_2} = 0.5$ is higher, e.g. $N_{H_{tot}} = 5.6 \times 10^{19} \text{ cm}^{-2}$ at solar metallicity. This difference is due to the different H_2 self-shielding function that is used in the Gnedin09 model.

Krumholz & Gnedin (2011) compare the KMT and Gnedin09 models in a hydrodynamic simulation of a Milky Way progenitor galaxy. For the Gnedin09 model, they include the changes described in Gnedin & Kravtsov (2011), which adds Helium chemistry to the chemical network, and uses the simpler power-law H_2 self-shielding function given in equation 36 of Draine & Bertoldi (1996). They find that the molecular fractions predicted by the two models are in excellent agreement for metallicities $Z > 10^{-2} Z_{\odot}$, with discrepancies at lower metallicities likely due to time-dependent effects. This is consistent with what we find in the top row of figure 3.5 for the low pressure runs. In contrast, the high pressure runs in the bottom row of figure 3.5 show poor agreement between the KMT and Gnedin09 models. However, this high pressure was chosen to reproduce densities typical of molecular clouds ($n_{H_{tot}} \sim 10^3 \text{ cm}^{-2}$) in the fully shielded region, and it produces unusually high densities in the low column density region ($n_{H_{tot}} \sim 10 \text{ cm}^{-2}$). Such regions of high density and low column density were not probed by the simulation of Krumholz & Gnedin (2011), and are likely to be rare in realistic galactic environments. Therefore, the discrepancies that we see in figure 3.5 do not contradict the results of Krumholz & Gnedin (2011).

In all three models the $HI-H_2$ transition occurs at a lower column density at higher metallicity and at higher pressure. As described in section 3.4.3, these trends are driven by H_2 self-shielding, because the H_2 fraction in the photodissociated region is higher at high metallicity and at high pressure. These trends have also been seen in previous models of photodissociation regions (e.g. Wolfire et al. 2010). From the colour bars in each panel of figure 3.5, we also see that the molecular fractions reach chemical equilibrium faster at higher metallicity and higher pressure.

To confirm the impact that H_2 self-shielding has on the $HI-H_2$ transition in our model, we repeated the above calculations with H_2 self-shielding switched off. We find that the total hydrogen column density of the $HI-H_2$ transition, at which $f_{H_2} = 0.5$, increases significantly when H_2 self-shielding is omitted, for example by a factor of ~ 5 and ~ 300 in the low and high pressure runs respectively at solar metallicity. This confirms that the $HI-H_2$ transition is determined by H_2 self-shielding in all of the examples shown in figure 3.5. The importance of H_2 self-shielding for the $HI-H_2$ in photodissociation region models has previously been studied by e.g. Black & van Dishoeck (1987); Draine & Bertoldi (1996); Lee et al. (1996).

3.6 Conclusions

We have extended the thermochemical model from paper I to account for gas that becomes shielded from the incident UV radiation field. We attenuate the photoionisation, photodissociation and photoheating rates by dust and by the gas itself, including absorption by HI, H₂, HeI, HeII and CO where appropriate. For the self-shielding of H₂, we use a new temperature-dependent analytic approximation that we fit to the suppression of the H₂ photodissociation rate predicted by CLOUDY as a function of H₂ column density (see Appendix B). Using this model, we investigated the impact that shielding of both the photoionising and the photodissociating radiation has on the chemistry and the cooling properties of the gas.

We have performed a series of one-dimensional calculations of a plane-parallel slab of gas illuminated by the Black (1987) interstellar radiation field at constant density. Comparing equilibrium abundances and cooling and heating rates as a function of column density with CLOUDY, we generally find good agreement. At $n_{\text{H,tot}} = 100 \text{ cm}^{-3}$, solar metallicity and a constant temperature $T = 300 \text{ K}$, we find that the HI-H₂ transition occurs at a somewhat lower column density in our model than in CLOUDY's big H2 model, with a molecular hydrogen fraction $x_{\text{H}_2} = 0.5$ at $N_{\text{H,tot}} \approx 8.1 \times 10^{19} \text{ cm}^{-2}$ in our model, compared to $N_{\text{H,tot}} \approx 2.8 \times 10^{20} \text{ cm}^{-2}$ in CLOUDY (see figure 3.2). However, CLOUDY's small H2 model predicts an HI-H₂ transition column density that is closer to our value, with $x_{\text{H}_2} = 0.5$ at $N_{\text{H,tot}} \approx 1.1 \times 10^{20} \text{ cm}^{-2}$.

In the examples shown here, the HI-H₂ transition is determined by H₂ self-shielding in our model, as the residual molecular hydrogen fraction in the photodissociated region at low column densities is sufficient for self-shielding to become important before dust shielding. As the photodissociation rate is slightly lower in our model than in the big H2 model of CLOUDY, the H₂ fraction at low column densities is slightly higher in our model. This explains why the transition column density is somewhat lower in our model compared to the CLOUDY big H2 model. The importance of H₂ self-shielding also means that the molecular hydrogen transition is sensitive to turbulence, which can suppress self-shielding. The transition for carbon to form CO is primarily triggered by dust shielding and thus occurs at a higher column density, $N_{\text{H,tot}} \sim 10^{22} \text{ cm}^{-2}$.

We also consider gas clouds with temperature and density profiles that are in thermal and pressure equilibrium, which is more realistic for a two-phase ISM than a gas cloud with constant temperature and density throughout. The effect of H₂ self-shielding is weaker in these examples due to the lower densities in the photodissociated region (see figure 3.4). However, the HI-H₂ transition is still determined by self-shielding, which becomes more important in runs with higher pressure (and hence higher densities). This trend with density is consistent with previous studies that have looked at the importance of H₂ self-shielding for the HI-H₂ transition (e.g. Black & van Dishoeck 1987; Draine & Bertoldi 1996; Lee et al. 1996; Krumholz et al. 2009).

The HI-H₂ transition occurs at a lower total column density for higher density (or equivalently, for higher pressure if the cloud is in pressure equilibrium) and for higher metallicity (see figure 3.5), in agreement with previous models of pho-

todissociation regions (e.g. Wolfire et al. 2010). These trends are due to the H_2 self-shielding, because an increase in the density and/or metallicity will increase the H_2 fraction in the photodissociated region, and hence decrease the total column density at which the H_2 becomes self-shielded. The time evolution of the H_2 fraction is also dependent on the density (or pressure) and the metallicity. For a gas cloud with pressure $P/k_B = 10^3 \text{ cm}^{-3} \text{ K}$ and metallicity $0.1Z_\odot$, the molecular hydrogen abundance in the fully shielded region only reaches equilibrium (starting from neutral, atomic initial conditions) after $\sim 1 \text{ Gyr}$. This time-scale decreases as the pressure and/or the metallicity increase.

We compare the dominant cooling and heating processes in our low pressure example ($P/k_B = 10^3 \text{ cm}^{-3} \text{ K}$) at solar metallicity, and we find that they form three distinct regions (see figure 3.4). At low column densities, where the dissociating and ionising radiation flux is still high, cooling is primarily from ionised metals such as SiII, FeII, FeIII and CII, which are balanced by photoheating, primarily from HI. At column densities above $N_{\text{H,tot}} \sim 2 \times 10^{20} \text{ cm}^{-2}$ the hydrogen-ionising radiation above 1 Ryd becomes significantly attenuated by neutral hydrogen. This reduces the photoheating rates, making photoelectric dust heating the dominant heating mechanism, while CII starts to dominate the cooling rate above $N_{\text{H,tot}} \sim 10^{21} \text{ cm}^{-2}$. It is also in this region that hydrogen becomes fully molecular, driven initially by an increase in the HI abundance and the rising density, and ultimately by self-shielding. Finally, dust shielding attenuates the radiation flux below 1 Ryd at column densities above $N_{\text{H,tot}} \sim 10^{21} \text{ cm}^{-2}$, which strongly cuts off the dust heating rate and also allows CO to form. In this fully shielded region heating is primarily from cosmic rays, while cooling is mostly from CO and H_2 .

Finally, we compare the HI- H_2 transition predicted by our one-dimensional plane-parallel slab simulations in thermal and pressure equilibrium with two other prescriptions for molecular hydrogen formation that are already employed in hydrodynamic simulations: the simpler non-equilibrium model of Gnedin et al. (2009) (*Gnedin09*), and the analytic equilibrium model developed in Krumholz et al. (2008, 2009) and McKee & Krumholz (2010) (*KMT*) (see figure 3.5).

At low pressure ($P/k_B = 10^3 \text{ cm}^{-3} \text{ K}$) the equilibrium H_2 fractions predicted by all three models generally agree well, as does the time evolution of the H_2 fraction predicted by our model and the Gnedin09 model. However, at low metallicity ($0.1 Z_\odot$) cosmic ray dissociation of H_2 reduces the H_2 fraction in the fully shielded region by a factor of two in our model, but cosmic ray dissociation is not included in the KMT or the Gnedin09 models. At high pressure ($P/k_B = 10^5 \text{ cm}^{-3} \text{ K}$) the HI- H_2 transition predicted by our model in chemical equilibrium occurs at a slightly lower column density than in the KMT model (e.g. $f_{\text{H}_2} = 0.5$ at $N_{\text{H,tot}} = 2.2 \times 10^{19} \text{ cm}^{-2}$ at solar metallicity, compared to $N_{\text{H,tot}} = 3.0 \times 10^{19} \text{ cm}^{-2}$ in the KMT model). Furthermore, the HI- H_2 transition at this high pressure is flatter in the Gnedin09 model than in our model or the KMT model, due to the different H_2 self-shielding function that they use.

Acknowledgments

We thank Ewine van Dishoeck for useful discussions. We gratefully acknowledge support from Marie Curie Training Network CosmoComp (PITN-GA-2009-238356) and from the European Research Council under the European Union's Seventh Framework Programme (FP7/2007-2013) / ERC Grant agreement 278594-GasAroundGalaxies.

3.7 Appendix A: Shielding approximations

In section 3.3 we described how we calculate the photoionisation and photoheating rates after the radiation field has been attenuated by a total column density $N_{\text{H,tot}}$. To compute the attenuation of the radiation by gas, we include absorption by HI, H₂, HeI and HeII. However, to reduce the number of dimensions in which we tabulate the attenuated rates, H₂ and HeII absorption are included as follows. We assume that the H₂ cross section is three times the HI cross section above the H₂ ionisation energy (15.4 eV), and similarly that the HeII cross section is 0.75 times the HeI cross section above the HeII ionisation energy (54.4 eV). In this section we show the errors that these approximations introduce to the photoionisation rates.

For every species included in our chemical network, we calculate the ratio of the optically thick to optically thin photoionisation rates, S_{gas} , from the Black (1987) radiation field after it has been attenuated purely by H₂. We calculate this exactly using equation 3.5, then we calculate it with our approximation using equation 3.8. In the top panel of figure 3.6 we show contours of the relative error in S_{gas} that is introduced by our approximation for H₂ absorption, plotted against the threshold energy of each species, E_{thresh} , on the x-axis, and the exact ratio of the optically thick to optically thin rates, S_{exact} , on the y-axis. Blue contours indicate where our approximation underestimates the photoionisation rates and red contours indicate where we overestimate them.

The largest errors seen in the top panel of figure 3.6 are seen in the blue contours, which show that we underestimate the photoionisation rates of some species by up to 60% at $S_{\text{exact}} \lesssim 10^{-3}$. However, since these errors are found at low values of S_{exact} , the photoionisation rates have already been suppressed and so are unlikely to be important in the chemical network. The more significant errors in this example are shown by the red contours in the top left corner of the top panel of figure 3.6. These show that we overestimate the photoionisation rates of species with $E_{\text{thresh}} \sim 20$ eV by up to 40% at $S_{\text{exact}} \sim 10^{-1}$.

We also calculated the relative errors in the photoionisation rates when the radiation field is attenuated purely by HeII. These are shown in the bottom panel of figure 3.6. For species with $E_{\text{thresh}} < 100$ eV, the errors are below 20%. Larger errors are seen for species with higher threshold energies and mostly in the strongly shielded regime ($S_{\text{exact}} \lesssim 10^{-3}$). However, species with such high ionisation energies are unlikely to be found in shielded gas.

The errors in the optically thick photoionisation rates shown in figure 3.6 were calculated for absorption purely by H₂ or HeII. However, in practice the radiation

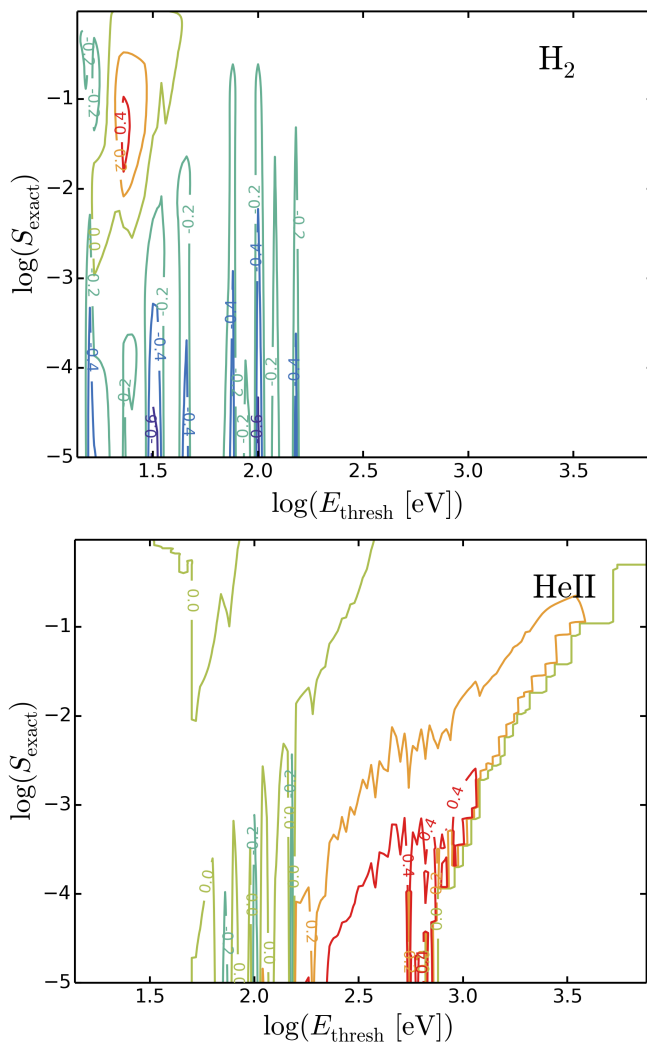


Figure 3.6: Contours of the relative errors in the ratio of optically thick to optically thin photoionisation rates of all species in our chemical network introduced by our approximations for absorption by H_2 and HeII , as given by equations 3.6, 3.7 and 3.8, in the presence of the Black (1987) interstellar radiation field. These contours are plotted against the threshold energy of each species, E_{thresh} , on the x-axis, and the exact ratio of the optically thick to optically thin rates, S_{exact} , on the y-axis. A value of $\log S_{\text{exact}} = 0$ corresponds to the optically thin limit, and a value of $\log S_{\text{exact}} = -\infty$ corresponds to the fully shielded limit. The top panel shows the errors if the radiation is absorbed purely by H_2 and the bottom panel shows if the radiation is absorbed purely by HeII . The largest errors that we see are $\sim 60\%$, but these are rare and are typically found at $S_{\text{exact}} \lesssim 10^{-3}$, where the photoionisation rate is already strongly suppressed and so the errors are less important.

will typically be absorbed by a combination of the four species that we consider in section 3.3, including HI and HeI, which we treat exactly. Therefore, figure 3.6 represents upper limits on the actual errors.

3.8 Appendix B: H₂ self-shielding function

In this section we look at the accuracy of the H₂ self-shielding function that we use, as described in section 3.3.2, by comparing it to the ratio of the optically thick to optically thin H₂ photodissociation rates predicted by CLOUDY as a function of H₂ column density. We consider a plane-parallel slab of gas with primordial abundances at a density of $n_{\text{H}} = 100 \text{ cm}^{-3}$ that is illuminated from one side by the Black (1987) interstellar radiation field.

Figure 3.7 shows the suppression factor of the H₂ photodissociation rate due to self-shielding, $S_{\text{self}}^{\text{H}_2}$, plotted against H₂ column density for five different temperatures in the range $100 \text{ K} \leq T \leq 5000 \text{ K}$ (shown in the different rows). The left panels were calculated using purely thermal Doppler broadening, while the right panels include turbulence with a Doppler broadening parameter $b_{\text{turb}} = 7.1 \text{ km s}^{-1}$. The black circles show the results from CLOUDY, while the coloured curves show different analytic approximations to the H₂ self-shielding function. The yellow dot-dashed curves show the self-shielding function from Draine & Bertoldi (1996) (DB96), as given in equation 3.11 with $\omega_{\text{H}_2} = 0.035$ and $\alpha = 2$, and the blue dotted curves show the suggested modification to this function given by Wolcott-Green et al. (2011) (WG11), with $\alpha = 1.1$. We see that, in the absence of turbulence, the WG11 function gives weaker self-shielding than the DB96 function at intermediate column densities ($10^{15} \text{ cm}^{-2} \lesssim N_{\text{H}_2} \lesssim 10^{17} \text{ cm}^{-2}$), by up to a factor ~ 6 . However, both of these functions underestimate the strength of the self-shielding in cold gas compared to CLOUDY. For example, at 100 K the value of $S_{\text{self}}^{\text{H}_2}$ predicted by CLOUDY is a factor of ~ 3 lower than the DB96 and WG11 functions at column densities $N_{\text{H}_2} \gtrsim 10^{17} \text{ cm}^{-2}$.

To improve the agreement with CLOUDY, we modified the self-shielding function of Draine & Bertoldi (1996) as shown in equation 3.12, then we fitted the parameters $\omega_{\text{H}_2}(T)$, $\alpha(T)$ and $N_{\text{crit}}(T)$ to the suppression factor $S_{\text{self}}^{\text{H}_2}$ predicted by CLOUDY as a function of H₂ column density for each temperature separately, including only thermal broadening. To reproduce the temperature dependence of $S_{\text{self}}^{\text{H}_2}$ seen in CLOUDY we then fitted analytic formulae to these three parameters as a function of temperature. These are given in equations 3.13 to 3.15.

Our best-fitting self-shielding function is shown by the red solid curves in figure 3.7. In the absence of turbulence, this function agrees with CLOUDY to within 30 per cent at $T = 100 \text{ K}$ for column densities $N_{\text{H}_2} < 10^{21} \text{ cm}^{-2}$, and to within 60 per cent at $T = 5000 \text{ K}$ for $N_{\text{H}_2} < 10^{20} \text{ cm}^{-2}$.

To highlight the temperature dependence of $S_{\text{self}}^{\text{H}_2}$, we also show our best-fitting function using the parameters $\omega_{\text{H}_2}(T)$, $\alpha(T)$ and $N_{\text{crit}}(T)$ fixed at $T = 100 \text{ K}$. These are indicated by the green dashed curves in figure 3.7. This represents the self-shielding function that we would get if we only fitted equation 3.12 at 100 K. Note that the green curves in each panel of figure 3.7 are not identical as they use the

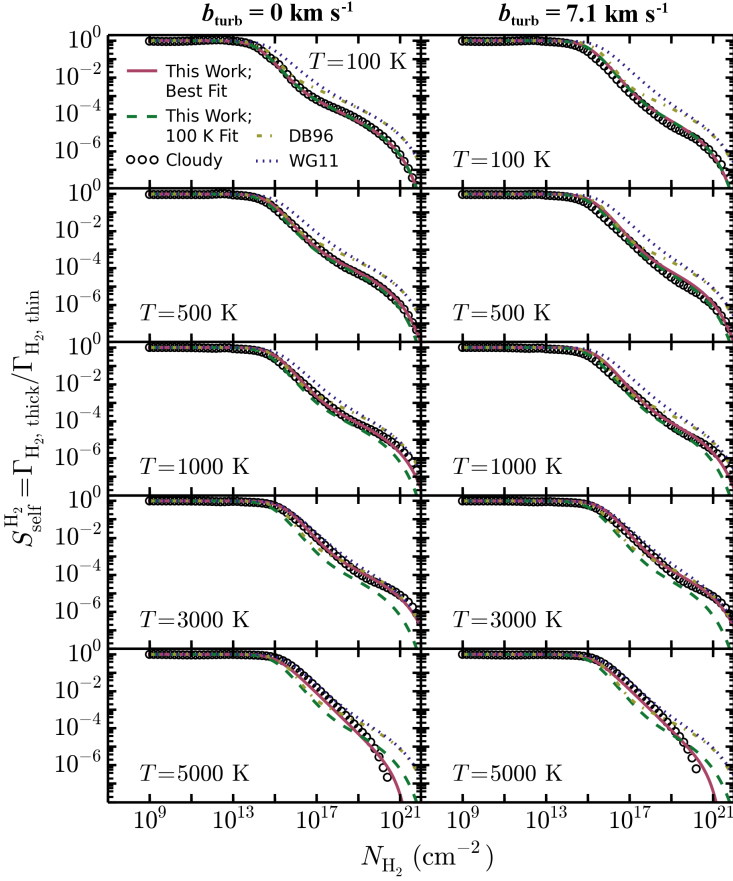


Figure 3.7: The ratio of the optically thick to optically thin H_2 photodissociation rates, $S_{\text{self}}^{H_2}$, plotted against the H_2 column density, N_{H_2} , as predicted by CLOUDY (black circles), the self-shielding function of Draine & Bertoldi (1996) (DB96; yellow dot-dashed curves), the self-shielding function of Wolcott-Green et al. (2011) (WG11; blue dotted curves), our self-shielding function fitted to CLOUDY at all temperatures (as given in equations 3.12 to 3.15; red solid curves), and our self-shielding function fitted to CLOUDY at only 100 K (green dashed curves). Each row shows gas at different temperatures in the range $100 \text{ K} \leq T \leq 5000 \text{ K}$. In the left column Doppler broadening is purely thermal, while the right column includes turbulence with a Doppler broadening parameter of $b_{\text{turb}} = 7.1 \text{ km s}^{-1}$. In the absence of turbulence, the DB96 and WG11 functions overestimate $S_{\text{self}}^{H_2}$ by up to a factor ~ 3 at low temperatures, and they do not reproduce the temperature dependence of $S_{\text{self}}^{H_2}$ that is seen in CLOUDY. Our best-fitting self-shielding function agrees with CLOUDY to within 30 per cent at 100 K for $N_{H_2} < 10^{21} \text{ cm}^{-2}$, and at 5000 K it agrees to within 60 per cent for $N_{H_2} < 10^{20} \text{ cm}^{-2}$. The agreement between our best-fitting self-shielding function and CLOUDY is poorer when turbulence is included, as it was fitted to the purely thermal Doppler broadening case. However, the DB96 and WG11 functions overestimate $S_{\text{self}}^{H_2}$ in cold gas by a larger factor when turbulence is included.

thermal Doppler broadening parameter for the given temperature.

Comparing the red and the green curves in figure 3.7, we see that the self-shielding is weaker at temperatures $500 \text{ K} \lesssim T \lesssim 3000 \text{ K}$ when we use our full temperature-dependent function (red curves), compared to the function fitted only at 100 K (green curves). This agrees with the trend seen by Wolcott-Green et al. (2011). However, at $T = 5000 \text{ K}$ the shape of the self-shielding function changes, and it becomes steeper than at lower temperatures for high column densities. This results in stronger self-shielding at $N_{\text{H}_2} \gtrsim 10^{19} \text{ cm}^{-2}$ compared to the fit at 100 K.

Our self-shielding function was fitted to the predictions from CLOUDY for gas with purely thermal Doppler broadening. To confirm that our best-fitting self-shielding function is also valid for turbulent gas, we repeated this comparison for gas that includes a turbulent Doppler broadening parameter $b_{\text{turb}} = 7.1 \text{ km s}^{-1}$. This comparison is shown in the right panels of figure 3.7.

When we include turbulence, the agreement between our best-fitting self-shielding function and CLOUDY is poorer. For example, at 100 K we overestimate $S_{\text{self}}^{\text{H}_2}$ by up to 90 per cent compared to CLOUDY for $10^{15} \text{ cm}^{-2} < N_{\text{H}_2} < 10^{20} \text{ cm}^{-2}$. However, this agreement is still much better than that between CLOUDY and the DB96 and WG11 functions. For example, in the same range of column densities the WG11 function overestimates $S_{\text{self}}^{\text{H}_2}$ by up to an order of magnitude at 100 K.

References

- Abel T., Anninos P., Zhang Y., Norman M. L., 1997, *NewA*, 2, 181
Bergin E. A., Hartmann L. W., Raymond J. C., Ballesteros-Paredes J., 2004, *ApJ*, 612, 921
Bigiel F., Leroy A., Walter F., Brinks E., de Blok W. J. G., Madore B., Thornley M. D., 2008, *AJ*, 136, 2846
Bigiel F., Walter F., Blitz L., Brinks E., de Blok W. J. G., Madore B. F., 2010, *AJ*, 140, 1194
Black J. H., 1987, *ASSL*, 134, 731
Black J. H., van Dishoeck E. F., 1987, *ApJ*, 322, 412
Bregman J. N., Harrington J. P., 1985, *ApJ*, 309, 833
Cazaux S., Tielens A. G. G. M., 2002, *ApJ*, 575, L29
Ceverino D., Klypin A., 2009, *ApJ*, 695, 292
Christensen C., Quinn T., Governato F., Stilp A., Shen S., Wadsley J., 2012, *MNRAS*, 425, 3058
Dere K. P., Landi E., Mason H. E., Monsignori Fossi B. C., Young P. R., 1997, *A&AS*, 125, 149
Dobbs C. L., Bonnell I. A., 2008, *MNRAS*, 385, 1893
Draine B. T., 1978, *ApJS*, 36, 595
Draine B. T., Bertoldi F., 1996, *ApJ*, 468, 269
Elwert T., Ferland G. J., Henney W. J., Williams R. J. R., 2005, *IAU Symposium*, 235, 132

- Federman S. R., Rawlings J. M. C., Taylor S. D., Williams D. A., 1996, *MNRAS*, 279, L41
- Ferland G. J., Korista K.T., Verner D.A., Ferguson J.W., Kingdon J.B., Verner E.M., 1998, *PASP*, 110, 761
- Ferland G. J., Porter R. L., van Hoof P. A. M., Williams R. J. R., Abel N. P., Lykins M. L., Shaw G., Henney W. J., Stancil P. C., 2013, *RMxAA*, 49, 137
- Glover S. C. O., Jappsen A.-K., 2007, *ApJ*, 666, 1
- Glover S. C. O., Abel T., 2008, *MNRAS*, 388, 1627
- Glover S. C. O., Federrath C., Mac Low M.-M., Klessen R. S., 2010, *MNRAS*, 404, 2
- Glover S. C. O., Clark P. C., 2012, *MNRAS*, 421, 9
- Gnat O., Sternberg A., 2007, *ApJS*, 168, 213
- Gnedin N. Y., Tassis K., Kravtsov A. V., 2009, *ApJ*, 697, 55 (Gnedin09)
- Gnedin N. Y., Kravtsov A. V., 2010, *ApJ*, 714, 287
- Gnedin N. Y., Kravtsov A. V., 2011, *ApJ*, 728, 88
- Governato F., Brook C., Mayer L., Brooks A., Rhee G., Wadsley J., Jonsson P., Willman B., Stinson G., Quinn T., Madau P., 2010, *Nature*, 463, 203
- Haardt F., Madau P., 2001, in Neumann D. M., Tran J. T. V., eds, *XXIst Moriond Astrophys. Meeting, Clusters of Galaxies and the High Redshift Universe Observed in X-rays Editions Frontieres*, Paris, p. 6
- Halle A., Combes F., 2013, *A&A*, 559, 55
- Heyer M. H., Corbelli E., Schneider S. E., Young J. S., 2004, *ApJ*, 602, 723
- Hollenbach D., Kaufman M. J., Bergin E. A., Melnick G. J., 2009, *ApJ*, 690, 1497
- Hollenbach D., Kaufman M. J., Neufeld D., Wolfire M., Goicoechea J. R., 2012, *ApJ*, 754, 105
- Hopkins P. F., Kereš D., Oñorbe J., Faucher-Giguère C.-A., Quataert E., Murray N., Bullock J. S., 2014, *MNRAS*, 445, 581
- Indriolo N., McCall B. J., 2012, *ApJ*, 745, 91
- Kaastra J. S., Mewe R., 1993, *A&AS*, 97, 443
- Kafatos M., 1973, *ApJ*, 182, 433
- Kennicutt R. C. Jr., 1989, *ApJ*, 344, 685
- Kennicutt R. C. Jr., 1998, *ApJ*, 498, 541
- Kennicutt R. C. Jr. et al., 2007, *ApJ*, 671, 333
- Khoperskov S. A., Vasiliev E. O., Sobolev A. M., Khoperskov A. V., 2013, *MNRAS*, 428, 2311
- Krumholz M. R., McKee C. F., Tumlinson J., 2008, *ApJ*, 689, 865 (KMT)
- Krumholz M. R., McKee C. F., Tumlinson J., 2009, *ApJ*, 693, 216
- Krumholz M. R., Leroy A. K., McKee C. F., 2011, *ApJ*, 731, 25
- Krumholz M. R., Gnedin N. Y., 2011, *ApJ*, 729, 36
- Krumholz M. R., 2012, *ApJ*, 759, 9
- Krumholz M. R., 2013, *MNRAS*, 436, 2747
- Landi E., Young P. R., Dere K. P., Del Zanna G., Mason H. E., 2013, *ApJS*, 763, 86
- Langer W. D., 1978, *ApJ*, 225, 860
- Lee H.-H., Herbst E., Pineau des Forêts G., Roueff E., Le Bourlot J., 1996, *A&A*, 311, 690
- Le Petit F., Nehmé C., Le Bourlot J., Roueff E., 2006, *ApJS*, 164, 506

- Leroy A., Walter F., Bigiel F., Brinks E., de Blok W. J. G., Madore B., 2008, *AJ*, 136, 2782
- Le Teuff Y. H., Millar T. J., Marwick A. J., 2000, *A&AS*, 146, 157
- Lotz W., 1967, *ApJS*, 14, 207
- Martin P. G., Whittet D. C. B., 1990, *ApJ*, 357, 113
- Mathis J. S., Mezger P. G., Panagia N., 1983, *A&A*, 128, 212
- McKee C. F., Krumholz M. R., 2010, *ApJ*, 709, 308
- Onodera S., Kuno N., Tosaki T., Kohno K., Nakanishi K., Sawada T., Muraoka K., Komugi S., Miura R., Kaneko H., Hirota A., Kawabe R., 2010, *ApJ*, 722, 127
- Oppenheimer B. D., Schaye J., 2013a, *MNRAS*, 434, 1043
- Oppenheimer B. D., Schaye J., 2013b, *MNRAS*, 434, 1063
- Pelupessy F. I., Papadopoulos P. P., van der Werf P., 2006, *ApJ*, 645, 1024
- Rahmati A., Pawlik A. H., Raičević M., Schaye J., 2013, *MNRAS*, 430, 2427
- Richings A. J., Schaye J., & Oppenheimer B. D., 2014, *MNRAS*, 440, 3349 (Paper I)
- Schaye J., 2001a, *ApJ*, 559, 507
- Schaye J., 2001b, *ApJ*, 562, L95
- Schaye J., 2004, *ApJ*, 609, 667
- Schaye J., Dalla Vecchia C., Booth C. M., Wiersma R. P. C., Theuns T., Haas M. R., Bertone S., Duffy A. R., McCarthy I. G., van de Voort F., 2010, *MNRAS*, 402, 1536
- Schuster K. F., Kramer C., Hitschfeld M., Garcia-Burillo S., Mookerjea B., 2007, *A&A*, 461, 143
- Sheffer Y., Rogers M., Federman S. R., Abel N. P., Gredel R., Lambert D. L., Shaw G., 2008, *ApJ*, 687, 1075
- Silk J., 1970, *ApL*, 5, 283
- Sobolev V. V., 1957, *SvA*, 1, 678
- Tielens A. G. G. M., Hollenbach D., 1985, *ApJ*, 291, 722
- van Dishoeck E. F., Black J. H., 1986, *ApJS*, 62, 109
- van Dishoeck E. F., Black J. H., 1988, *ApJ*, 334, 771
- van Dishoeck E. F., Jonkheid B., van Hemert M. C., 2006, *Faraday Discuss.*, 133, 231
- Vasiliev E. O., 2013, *MNRAS*, 431, 638
- Verner D. A., Yakovlev D. G., 1995, *A&AS*, 109, 125
- Verner D. A., Ferland G. J., Korista K. T., Yakovlev D. G., 1996, *ApJ*, 465, 487
- Visser R., van Dishoeck E. F., Black J. H., 2009, *A&A*, 503, 323
- Weingartner J. C., Draine B. T., 2001a, *ApJ*, 563, 842
- Weingartner J. C., Draine B. T., 2001b, *ApJ*, 548, 296
- Wiersma R. P. C., Schaye J., Smith B. D., 2009, *MNRAS*, 393, 99
- Williams J. P., Bergin E. A., Caselli P., Myers P. C., Plume R., 1998, *ApJ*, 503, 689
- Wilms J., Allen A., McCray R., 2000, *ApJ*, 542, 914
- Wilson T. L., 1999, *Rep. Prog. Phys.*, 62, 143
- Wolcott-Green J., Haiman Z., 2011, *MNRAS*, 412, 2603
- Wolcott-Green J., Haiman Z., Bryan G. L., 2011, *MNRAS*, 418, 838
- Wolfire M. G., Hollenbach D., McKee C. F., Tielens A. G. G. M., Bakes E. L. O., 1995, *ApJ*, 443, 152

- Wolfire M. G., Tielens A. G. G. M., Hollenbach D. J., Kaufman M. J., 2008, *ApJ*, 680, 384
Wolfire M. G., Hollenbach D., McKee C. F., *ApJ*, 716, 1191
Wong T., Blitz L., 2002, *ApJ*, 569, 157
Yan M., Sadeghpour H. R., Dalgarno A., 1998, *ApJ*, 496, 1044

THE EFFECTS OF METALLICITY, UV RADIATION AND NON-EQUILIBRIUM CHEMISTRY IN HIGH-RESOLUTION SIMULATIONS OF GALAXIES

We present a series of hydrodynamic simulations of isolated galaxies with stellar mass of $10^9 M_{\odot}$. The models use a resolution of $750 M_{\odot}$ per particle and include a treatment for the full non-equilibrium chemical evolution of ions and molecules (157 species in total), along with gas cooling rates computed self-consistently using the non-equilibrium abundances. We compare these to simulations evolved using cooling rates calculated assuming chemical (including ionisation) equilibrium, and we consider a wide range of metallicities and UV radiation fields, including a local prescription for self-shielding by gas and dust. We find higher star formation rates and stronger outflows at higher metallicity and for weaker radiation fields, as gas can more easily cool to a cold (few hundred Kelvin) star forming phase under such conditions. Contrary to variations in the metallicity and the radiation field, non-equilibrium chemistry generally has no strong effect on the total star formation rates or outflow properties. However, it is important for modelling molecular outflows. For example, the mass of H_2 outflowing with velocities $> 50 \text{ km s}^{-1}$ is enhanced by a factor ~ 20 in non-equilibrium. We also compute the observable line emission from CII and CO. Both are stronger at higher metallicity, while CII and CO emission are higher for stronger and weaker radiation fields respectively. We find that CII is generally unaffected by non-equilibrium chemistry. However, emission from CO varies by a factor of $\sim 2 - 4$. This has implications for the mean X_{CO} conversion factor between CO emission and H_2 column density, which we find is lowered by up to a factor ~ 2.3 in non-equilibrium, and for the fraction of CO-dark molecular gas.

Alexander J. Richings and Joop Schaye
Monthly Notices of the Royal Astronomical Society
Submitted (2015), *arXiv:1506.08829*

4.1 Introduction

Hydrodynamic simulations of galaxy formation typically model gas cooling by tabulating the cooling rate as a function of gas properties such as the density and temperature, under certain assumptions. For example, the simplest approach, as used in some of the first cosmological hydrodynamic simulations (e.g. Katz et al. 1992), is to assume that the gas has primordial abundances and is in collisional ionisation equilibrium (CIE). Sutherland & Dopita (1993) also included the effects of metal-line cooling, computing cooling curves in CIE for a range of metallicities.

Another effect that can be important for gas cooling is the presence of a photoionising UV radiation field, which can change the ionisation balance and heat the gas. Efstathiou (1992) showed that an extragalactic UV background (UVB) can suppress the cooling rate in a primordial plasma, thereby inhibiting the formation of dwarf galaxies. Katz et al. (1996) implemented primordial radiative cooling in the presence of a UVB in cosmological hydrodynamic simulations.

Wiersma et al. (2009) considered the impact that a photoionising UVB has on cooling rates in the presence of metals. They showed that photoionisation can suppress the cooling rate by up to an order of magnitude at temperatures and densities typical of the intergalactic medium (e.g. $10^4 \text{ K} \lesssim T \lesssim 10^6 \text{ K}$, $\rho/\langle\rho\rangle \lesssim 100$). They also showed that variations in relative abundances from their solar values can change the cooling rate by a factor of a few. Wiersma et al. (2009) tabulated the cooling rate from 11 elements separately in the presence of the redshift-dependent UVB of Haardt & Madau (2001), and these tables have been used in several cosmological hydrodynamic simulations (e.g. Crain et al. 2009; Schaye et al. 2010, 2015; Hopkins et al. 2014).

The effects of metal cooling and UV radiation are particularly important below 10^4 K , as cooling from atomic hydrogen becomes inefficient at such temperatures. In primordial gas, the only major coolants are H_2 and HD (e.g. Saslaw & Zipoy 1967; Flower et al. 2000; Glover & Abel 2008). However, these molecules can easily be dissociated by Lyman-Werner radiation (11.2 eV – 13.6 eV). If metals are present, efficient cooling can continue down to $T \lesssim 100 \text{ K}$ via fine-structure line emission (e.g. Glover & Jappsen 2007; Richings et al. 2014a). Conversely, the presence of UV radiation will hinder cooling to such low temperatures, as it heats the gas via photoionisation and photoelectric heating from dust grains, the latter of which also depends on metallicity. Metallicity and UV radiation therefore influence the transition from the warm ($\sim 10^4 \text{ K}$) to the cold ($\sim 10^2 \text{ K}$) gas phase.

Wolfire et al. (2003) investigated the warm-to-cold transition by calculating the minimum pressure, and hence the minimum density, at which a cold phase can exist in pressure equilibrium with a warm phase, as a function of UV intensity, metallicity, dust abundance and ionisation rate from cosmic rays and Extreme UV (EUV)/X-ray radiation (see their equations 33-35). This minimum density increases with decreasing metallicity and increasing UV intensity (see also Glover & Clark 2014).

Schaye (2004) demonstrated that the critical surface density above which a cold ISM phase can form in a galactic disc increases with decreasing metallicity and increasing UV intensity (see his equation 23). He additionally showed that

the formation of a cold phase can trigger gravitational instabilities, due to the lower velocity dispersion in cold gas. Metallicity and UV radiation can thus affect the star forming properties of galaxies, in particular the threshold surface density below which star formation is unable to proceed. The transition from atomic to molecular hydrogen also depends on metallicity and UV radiation (e.g. Schaye 2001; Krumholz et al. 2008; Gnedin & Kravtsov 2011; Sternberg et al. 2014).

Many of the above approaches assume that the gas is in chemical (including ionisation) equilibrium, or in other words, that the abundances of individual ions and molecules have reached an equilibrium or steady state. However, this assumption may not be valid if the dynamical or cooling time-scale of the gas is short compared to the chemical time-scale (e.g. Kafatos 1973; Sutherland & Dopita 1993; Gnat & Sternberg 2007; Oppenheimer & Schaye 2013a; Vasiliev 2013), or if the UV radiation field is varying on time-scales shorter than the chemical time-scale (e.g. Oppenheimer & Schaye 2013b).

Non-equilibrium chemistry has been shown to affect cooling rates in certain idealised scenarios. For example, in collisionally ionised gas that is cooling either isobarically or isochorically, the cooling rate computed self-consistently from non-equilibrium abundances is suppressed at temperatures $T > 10^4$ K compared to gas in CIE (e.g. Sutherland & Dopita 1993; Gnat & Sternberg 2007). Oppenheimer & Schaye (2013a) investigated non-equilibrium ionisation and cooling in the presence of a photoionising radiation field, and they showed that the UVB reduces the non-equilibrium effects, although the cooling rates at $T > 10^4$ K are still suppressed with respect to chemical equilibrium. Richings et al. (2014a) showed that, at temperatures below 10^4 K, the direction of the non-equilibrium effects is reversed and the cooling rates are enhanced, due to an increase in the electron abundance compared to equilibrium.

These studies considered special cases of a plasma that is cooling at constant density or pressure. Walch et al. (2011) compared equilibrium and non-equilibrium chemistry and cooling in high-resolution simulations of a turbulent medium, in a box 500 pc across. They found that non-equilibrium chemistry did have a noticeable, albeit fairly small, effect on the gas temperature in their simulations. Vasiliev (2013) applied a treatment for non-equilibrium cooling to simulations of a supernova remnant, and showed that the evolution of the supernova remnant is sensitive to non-equilibrium effects. However, it remains to be seen whether such non-equilibrium effects will be relevant on galactic scales.

In this paper we investigate the effects of metallicity, UV radiation and non-equilibrium chemistry on galaxy formation. We run a series of hydrodynamic simulations of isolated galaxies with stellar and total halo masses of 10^9 and $10^{11} M_{\odot}$, respectively. The simulations use a resolution of $750 M_{\odot}$ per particle and a gravitational force softening of 3.1 pc, which is sufficient to resolve the warm-to-cold transition. We consider a range of metallicities, $0.01 Z_{\odot} \leq Z \leq Z_{\odot}$, and a range of UV radiation fields that span nearly three orders of magnitude in HI photoionisation rate: the local interstellar radiation field (ISRF) of Black (1987), ten per cent of the Black (1987) ISRF and the redshift zero extragalactic UV background (UVB) of Haardt & Madau (2001). We include a local prescription for self-shielding by gas and dust, and we also consider a model without self-shielding for comparison.

We first run these simulations with the temperature and chemical abundances of the gas evolved using the non-equilibrium chemical model of Richings et al. (2014a,b), which follows the ionisation states of 11 elements that are important for the gas cooling rate, along with the abundances of 20 molecular species, including H_2 and CO. We then compare these to simulations evolved using cooling rates tabulated in chemical equilibrium.

In addition to the dynamical impact on the galaxy due to the effects on the cooling rate, non-equilibrium chemistry can also affect observable diagnostics of individual chemical species, e.g. in the presence of a fluctuating UV field (Oppenheimer & Schaye 2013b), or in the presence of supersonic turbulence (Gray et al. 2015). To investigate how non-equilibrium chemistry can affect observable emission on galactic scales, we perform radiative transfer calculations in post-processing to compute line emission from CII and CO. We then compare the intensity of line emission computed from non-equilibrium abundances to that computed assuming chemical equilibrium.

The remainder of this paper is organised as follows. In section 4.2 we describe the hydrodynamic methods and subgrid physics models used in our simulations. We present our simulations in section 4.3, where we discuss the initial conditions (4.3.1), morphologies and star formation rates (4.3.2), outflow properties (4.3.3), and the phase structure of the ISM (4.3.4). We compute the observable line emission from CII and CO in section 4.4, and we summarise our main results in section 4.5.

4.2 Subgrid Physics Models

Our simulations were run using a modified version of the tree/Smoothed Particle Hydrodynamics (SPH) code GADGET3 (last described in Springel 2005). The hydrodynamic equations were solved using the set of numerical methods known as ANARCHY, which includes many of the latest improvements to the standard SPH implementation. In particular, ANARCHY uses the pressure-entropy formulation of SPH, derived by Hopkins (2013); the artificial viscosity switch of Cullen & Dehnen (2010); a switch for artificial conduction, similar to that used in Price (2008); the time-step limiters of Durier & Dalla Vecchia (2012); and the C^2 Wendland (1995) kernel. ANARCHY will be described in more detail in Dalla Vecchia (in preparation); see also Appendix A of Schaye et al. (2015) for a description of the implementation of ANARCHY in the cosmological simulations that were run for the EAGLE project, which is identical to the ANARCHY implementation that we use here.

We use prescriptions to model physical processes that are unresolved in our simulations, including the chemical evolution of ions and molecules, radiative cooling, star formation and stellar feedback. These subgrid models are summarised below.

UV field	G_0^a	$\Gamma_{\text{HI}} (\text{s}^{-1})^b$	$\Gamma_{\text{HeI}} (\text{s}^{-1})^c$	$\Gamma_{\text{HeII}} (\text{s}^{-1})^d$
ISRF	1.2	4.4×10^{-11}	3.7×10^{-12}	1.7×10^{-14}
lowISRF	0.12	4.4×10^{-12}	3.7×10^{-13}	1.7×10^{-15}
UVB	0.014	8.4×10^{-14}	2.0×10^{-14}	1.5×10^{-16}

^aRadiation field strength in the energy range 6.0–13.6 eV, in units of the Habing (1968) field.

^bUnattenuated HI photoionisation rate.

^cUnattenuated HeI photoionisation rate.

^dUnattenuated HeII photoionisation rate.

Table 4.1: Properties of the UV radiation fields considered in this paper.

4.2.1 Chemistry and radiative cooling

We use the chemical model of Richings et al. (2014a,b) to evolve the chemical abundances of 157 species, including all ionisation states of the 11 elements that are most important for cooling¹ and 20 molecular species². The gas temperature is evolved using radiative cooling and heating rates calculated from the non-equilibrium abundances. This gives us a set of 158 differential equations (157 chemical rate equations and the energy equation), which we integrate over each hydrodynamic timestep for each gas particle. We integrate these differential equations using the backward difference formula method and Newton iteration in CVODE (from the SUNDIALS³ suite of non-linear differential/algebraic equation solvers), using a relative tolerance of 10^{-4} and an absolute tolerance of 10^{-10} .

We summarise the main chemical and thermal processes that are included in our model below.

Chemical processes

We include collisional ionisation, radiative and di-electronic recombinations and charge transfer reactions. The formation of molecular hydrogen occurs on dust grains, using equation 18 of Cazaux & Tielens (2002) with a dust temperature $T_{\text{dust}} = 10$ K, as well as via gas phase reactions. We also include cosmic ray ionisations, assuming a primary ionisation rate of atomic hydrogen due to cosmic rays of $\zeta_{\text{HI}} = 2.5 \times 10^{-17} \text{s}^{-1}$ (Williams et al. 1998). The primary ionisation rates of other species due to cosmic rays are then scaled to this value using the ratios in the UMIST database⁴ (McElroy et al. 2013) where available, or using the equations from Lotz (1967), Silk (1970) and Langer (1978) otherwise. We include secondary ionisations of HI and HeI from cosmic rays using the tables of Furlanetto & Stoeber (2010), assuming a typical mean primary electron energy of $E = 35$ eV.

We include photoionisation of atoms and ions, including Auger ionisation, using optically thin cross sections calculated in the grey approximation for a given

¹H, He, C, N, O, Ne, Mg, Si, S, Ca & Fe.

²H₂, H₂⁺, H₃⁺, OH, H₂O, C₂, O₂, HCO⁺, CH, CH₂, CH₃⁺, CO, CH⁺, CH₂⁺, OH⁺, H₂O⁺, H₃O⁺, CO⁺, HOC⁺, O₃⁺.

³<https://computation.llnl.gov/casc/sundials/main.html>

⁴<http://www.udfa.net/>

UV spectrum. We consider three UV spectra in this paper: the local ISRF of Black (1987), ten per cent of the Black (1987) ISRF and the redshift zero extragalactic UVB of Haardt & Madau (2001). The properties of these radiation fields are summarised in Table 4.1. We then attenuate the optically thin rates by the gas and dust, as a function of the column densities of H I, H₂, He I, He II and dust, as described in Richings et al. (2014b). To calculate these column densities, we assume that each gas particle is shielded locally. The total hydrogen column density, $N_{\text{H}_{\text{tot}}}$, is then:

$$N_{\text{H}_{\text{tot}}} = n_{\text{H}_{\text{tot}}} L, \quad (4.1)$$

where $n_{\text{H}_{\text{tot}}}$ is the hydrogen number density of the gas particle and L is the shielding length, i.e. the length scale over which the gas particle is able to shield itself. We use a Sobolev-like approximation to estimate the shielding length based on the gradient of the density, ρ :

$$L = L_{\text{Sob},\rho} = \frac{\rho}{|2\nabla\rho|}. \quad (4.2)$$

Gnedin et al. (2009) use this approximation in cosmological simulations to follow the formation of molecular hydrogen. They show that this approximation accurately reproduces the true column densities in their simulations, as measured along random lines of sight, with a scatter of a factor of 2 in the range $3 \times 10^{20} \text{ cm}^{-2} < N_{\text{HI}} + 2N_{\text{H}_2} < 3 \times 10^{23} \text{ cm}^{-2}$.

The column density of species i is then:

$$N_i = x_i N_{\text{H}_{\text{tot}}}, \quad (4.3)$$

where $x_i = n_i/n_{\text{H}_{\text{tot}}}$ is the abundance of species i .

The photodissociation rates of molecular species are also attenuated using the shielding length given in equation 4.2. The attenuation of the photodissociation rate of species i due to dust is given by:

$$S_{\text{d}}^i(N_{\text{H}_{\text{tot}}}, Z) = \exp(-\gamma_{\text{d}}^i A_{\text{v}}), \quad (4.4)$$

where $S_{\text{d}}^i(N_{\text{H}_{\text{tot}}}, Z)$ is the shielding factor (i.e. the ratio of the optically thick to optically thin photodissociation rates) due to dust, $A_{\text{v}} = 4.0 \times 10^{-22} N_{\text{H}_{\text{tot}}} Z/Z_{\odot}$ mag is the visual dust extinction, Z is the metallicity and the factors γ_{d}^i are taken from table 2 of van Dishoeck et al. (2006) where available, or from table B2 of Glover et al. (2010) otherwise.

In addition to dust shielding, molecular hydrogen can also be self-shielded. We use the temperature-dependent self-shielding function given in equations 3.12 to 3.15 of Richings et al. (2014b), which gives the shielding factor of H₂ as a function of the molecular hydrogen column density, N_{H_2} , gas temperature, T , and Doppler broadening parameter, b . The Doppler broadening parameter includes thermal broadening and broadening due to turbulence. In our simulations, we assume a constant turbulent broadening parameter $b_{\text{turb}} = 7.1 \text{ km s}^{-1}$, as used by e.g. Krumholz (2012), as this is typical for observed molecular clouds.

CO can also be self-shielded and shielded by H₂. We use the tables of the shielding factor of CO as a function of CO and H₂ column densities given by Visser et al. (2009).

A full list of the chemical reactions that are included in our model can be found in table B1 of Richings et al. (2014a).

Thermal processes

We use the non-equilibrium abundances from the chemical network to calculate the net cooling rate of the gas. We include cooling from the collisional excitation and ionisation of H and He, fine-structure line emission from metals, recombination cooling and bremsstrahlung radiation. We use the H₂ cooling function from Glover & Abel (2008) for rovibrational cooling from H₂, and we include cooling from CO, H₂O and OH. The photoheating rate is attenuated by gas and dust, as described by Richings et al. (2014b), using column densities calculated from equations 4.1 and 4.2 above. We also include photoelectric heating on dust grains (Bakes & Tielens 1994; Wolfire et al. 1995), cosmic ray heating (Goldsmith & Langer 1978; Glover & Jappsen 2007), and heating from the photodissociation of H₂ (Black & Dalgarno 1977), UV pumping of H₂ (Burton et al. 1990), and the formation of H₂ on dust grains (Hollenbach & McKee 1979) and in the gas phase (Karpas et al. 1979; Launay et al. 1991).

Equilibrium cooling tables

One aim of this paper is to compare simulations run using the full non-equilibrium chemical model described above to simulations evolved with cooling rates that are calculated assuming chemical equilibrium. We therefore used our chemical model to create tables of the cooling and heating rates and the mean molecular weight in chemical equilibrium as a function of gas temperature, hydrogen number density and total hydrogen column density. Note that the simulations in this paper were run at fixed metallicity, so we do not need to include an additional dimension for metallicity in the cooling tables. These tables were then used to evolve the gas temperature in the equilibrium cooling runs. By computing equilibrium cooling rates using the same chemical model as used for the non-equilibrium runs, we ensure that any differences are due to non-equilibrium effects, and not simply due to the use of different chemical rates in the models.

4.2.2 Star formation

We allow a gas particle to form stars if its temperature, T , and hydrogen number density, $n_{\text{H}_{\text{tot}}}$, satisfy the following criteria:

$$T < T_{\text{thresh}} = 1000 \text{ K}, \quad (4.5)$$

$$n_{\text{H}_{\text{tot}}} > n_{\text{H}_{\text{tot}},\text{thresh}} = 1.0 \text{ cm}^{-3}. \quad (4.6)$$

Gas particles that satisfy these criteria form stars at a rate given by:

$$\dot{\rho}_* = \epsilon_{\text{SF}} \frac{\rho_{\text{gas}}}{t_{\text{ff}}}, \quad (4.7)$$

where $\dot{\rho}_*$ is the star formation rate per unit volume, ρ_{gas} is the gas density and $t_{\text{ff}} = \sqrt{3\pi/(32G\rho)}$ is the free fall time. We use a star formation efficiency per free fall time of $\epsilon_{\text{SF}} = 0.005$. This is slightly lower than the value of $\epsilon_{\text{SF}} \sim 0.015$ that is typically observed in the Milky Way and nearby galaxies (Krumholz et al. 2012). We calibrated this parameter, along with the density and temperature thresholds and the parameters for the stellar feedback model described in the next section, to reproduce the observed Kennicutt-Schmidt relation in nearby galaxies (see Fig. 4.3).

In a timestep Δt , star forming gas particles are stochastically turned into star particles with a probability p given by:

$$p = \min\left(\frac{\dot{\rho}_* \Delta t}{\rho_{\text{gas}}}, 1\right). \quad (4.8)$$

4.2.3 Stellar feedback

Each star particle represents a stellar population, rather than an individual star. We assume that the stellar population initially follows the Chabrier (2003) Initial Mass Function (IMF) with masses in the range $0.1 - 100 M_{\odot}$. We then calculate how many type II supernovae will explode in each timestep for each star particle, using the metallicity-dependent stellar lifetimes of Portinari et al. (1998) and assuming that all stars with a mass greater than $6 M_{\odot}$ will end their lives in a supernova (stars with masses of $6 - 8 M_{\odot}$ explode as electron capture supernovae in models with convective overshoot, e.g. Chiosi et al. 1992).

The energetic feedback from supernovae is implemented using the stochastic thermal feedback prescription of Dalla Vecchia & Schaye (2012), except that we distribute the total available energy from type II supernovae from a single star particle in time according to the stellar lifetimes of the massive stars, rather than combine it into a single supernova event. For each star particle that has a non-zero number of supernovae, N_{SNII} , in timestep Δt , we stochastically select gas particles from the $N_{\text{ngb}} = 48$ neighbours to be heated by $\Delta T = 10^{7.5}$ K. Note that N_{ngb} is smaller than the number of neighbours that we use to compute the SPH kernel ($N_{\text{ngb}}^{\text{SPH}} = 100$). This reduces the computational cost of the neighbour-finding routine for star particles, and has little impact on the accuracy of the stellar feedback. The probability p of selecting a given gas particle to be heated is:

$$p = \min\left(\frac{2 E_{\text{SNII}} N_{\text{SNII}} \mu m_{\text{p}}}{3 k_{\text{B}} \Delta T \sum_{i=1}^{N_{\text{ngb}}} m_i}, 1\right), \quad (4.9)$$

where $E_{\text{SNII}} = 10^{51}$ erg is the energy injected per supernova, μ is the mean molecular mass of the gas particle, m_{p} is the mass of a proton and m_i is the mass of the i^{th} neighbouring gas particle.

By imposing a minimum heating temperature ΔT , we ensure that the cooling time of the heated gas is long enough to avoid artificial radiative losses that

would otherwise make the feedback scheme ineffective. However, note that, at the resolution that we use in our simulations (750 M_\odot per particle), we require approximately 10 supernovae to heat a single gas particle to $10^{7.5}$ K. We therefore do not resolve individual supernovae, as each feedback event is equivalent to several supernovae exploding simultaneously.

While we include the energetic feedback from supernovae, we do not include the chemical enrichment from supernovae or from stellar mass loss. This allows us to follow model galaxies at a fixed metallicity, which eases the interpretation of our numerical experiments.

4.2.4 Jeans limiter

To ensure that we always resolve the Jeans mass, M_J , and the Jeans length, L_J , we impose a minimum floor on the pressure that enters the hydrodynamic equations. This is similar to the approach used by e.g. Robertson & Kravtsov (2008); Schaye & Dalla Vecchia (2008); Hopkins et al. (2011).

There are two criteria that we can consider to determine the pressure floor. Firstly, we can require that the Jeans mass be resolved by at least a factor $N_{J,m}$ times the mass within the SPH kernel. The Jeans mass is given by:

$$M_J = \frac{\pi^{5/2} c_s^3}{6G^{3/2} \rho^{1/2}}, \quad (4.10)$$

where $c_s = \sqrt{\gamma P/\rho}$ is the sound speed, $\gamma = 5/3$ is the ratio of specific heats, P is the thermal gas pressure and ρ is the gas density.

If each gas particle has mass m_{gas} , and we use $N_{\text{ngb}}^{\text{SPH}}$ neighbours in the SPH kernel, then the mass within the kernel is:

$$M_k = N_{\text{ngb}}^{\text{SPH}} m_{\text{gas}}. \quad (4.11)$$

From equations 4.10 and 4.11, we find that the minimum pressure that we require is:

$$P_{\text{floor},m} = \left(\frac{36}{\pi^5}\right)^{1/3} \frac{G}{\gamma} (N_{J,m} N_{\text{ngb}}^{\text{SPH}} m_{\text{gas}})^{2/3} \rho^{4/3}. \quad (4.12)$$

Secondly, we can require that the Jeans length be resolved by at least a factor $N_{J,1}$ times the SPH smoothing length, h_{sml} . Using equation 4.10, the Jeans length is:

$$L_J = \frac{\pi^{1/2} c_s}{G^{1/2} \rho^{1/2}}. \quad (4.13)$$

Hence the minimum pressure that we require is:

$$P_{\text{floor},1} = \frac{G}{\pi\gamma} N_{J,1}^2 h_{\text{sml}}^2 \rho^2. \quad (4.14)$$

Since the smoothing length is defined such that the number of SPH neighbours, $N_{\text{ngb}}^{\text{SPH}}$, is constant, we can express h_{sml} in terms of the kernel mass as:

$$h_{\text{sml}} = \left(\frac{3N_{\text{ngb}}^{\text{SPH}} m_{\text{gas}}}{4\pi\rho} \right)^{1/3}. \quad (4.15)$$

By combining equations 4.12, 4.14 and 4.15, we see that these two criteria are equivalent if:

$$N_{\text{J},1} = 2N_{\text{J},\text{m}}^{1/3}. \quad (4.16)$$

We set the pressure floor in our simulations such that we resolve M_{J} by at least $N_{\text{J},\text{m}} = 4$ kernel masses, and thus we resolve L_{J} by at least $N_{\text{J},1} = 3.2$ smoothing lengths.

Note that, while we impose this floor on the pressure that enters the hydrodynamic equations, the temperature is still allowed to cool below this limit. This means that the thermal pressure will effectively be decoupled from the hydrodynamic equations once this floor is reached. For the resolution of our simulations, the pressure floor that we use corresponds to the thermal pressure at a temperature of 240 K at the star formation threshold density $n_{\text{H}_{\text{tot}},\text{thresh}} = 1.0 \text{ cm}^{-3}$. We implement the Jeans limiter as a pressure floor rather than a temperature floor (as was used in Schaye & Dalla Vecchia 2008) so that the thermal and chemical state of the gas will evolve towards a realistic equilibrium for the given density, although we miss small-scale, high-density structures that are unresolved in the simulation.

4.3 Simulations

We ran a suite of SPH simulations of isolated galaxies with a range of metallicities and UV radiation fields, using a resolution of $750 M_{\odot}$ per gas particle, with 100 SPH neighbours, and a gravitational softening length of 3.1 pc. Each simulation was evolved for 1 Gyr. We ran each simulation twice: once using the full non-equilibrium chemical model summarised in section 4.2.1, and once using tabulated cooling rates calculated assuming chemical equilibrium, as described in section 4.2.1. In this section, we describe the initial conditions, and we compare the morphologies, star formation rates, outflow properties and ISM phases in our simulated galaxies. For each of these, we focus on the effects of metallicity, radiation field and non-equilibrium chemistry.

4.3.1 Initial conditions

The initial conditions that we use are based on the model of Springel et al. (2005), and were generated using a modified version of a code that was kindly provided to us by Volker Springel. Each galaxy consists of an exponential disc of gas and stars with a radial scale length of 2.0 kpc, and a central stellar bulge with a Hernquist (1990) density profile, embedded within a dark matter halo. The stellar disc and bulge are represented by collisionless particles with the same mass as the gas particles ($750 M_{\odot}$ per particle). The main difference between our initial conditions

Model	M_{200} (M_{\odot})	c_{200}	$M_{*,\text{init}}$ (M_{\odot})	$M_{\text{gas,init}}$ (M_{\odot})	$f_{\text{d, gas}}$	m_{baryon} (M_{\odot})	ϵ_{soft} (pc)	Z (Z_{\odot})	UV Field ^a	Shielding
ref	10^{11}	8.0	1.4×10^9	4.8×10^8	0.3	750	3.1	0.1	ISRF	yes
lowZ	10^{11}	8.0	1.4×10^9	4.8×10^8	0.3	750	3.1	0.01	ISRF	yes
hiZ	10^{11}	8.0	1.4×10^9	4.8×10^8	0.3	750	3.1	1.0	ISRF	yes
lowISRF	10^{11}	8.0	1.4×10^9	4.8×10^8	0.3	750	3.1	0.1	lowISRF	yes
UVB	10^{11}	8.0	1.4×10^9	4.8×10^8	0.3	750	3.1	0.1	UVB	yes
UVBthin	10^{11}	8.0	1.4×10^9	4.8×10^8	0.3	750	3.1	0.1	UVB	no

^aSee Table 4.1

Table 4.2: Parameters and properties of the galaxies in the suite of simulations used in this paper: total mass M_{200} within the radius $R_{200,\text{crit}}$ enclosing a mean density of 200 times the critical density of the Universe at redshift zero, concentration c_{200} of the dark matter halo, initial stellar mass $M_{*,\text{init}}$, initial gas mass $M_{\text{gas,init}}$, disc gas mass fraction $f_{\text{d, gas}}$, mass per gas or star particle m_{baryon} , gravitational softening length ϵ_{soft} , gas metallicity Z , UV radiation field and whether we include self-shielding.

and the model of Springel et al. (2005) is that we represent the dark matter halo using a static potential, rather than with live dark matter particles. Using a static potential speeds up the calculation without affecting the results.

The gas is initially isothermal, with a temperature of 10^4 K, and the chemical abundances are initially in chemical equilibrium. The stellar disc is set up with a vertical distribution that follows an isothermal profile with a scale height of ten per cent of the radial scale length of the disc, while the vertical structure of the gaseous disc is set to be in hydrostatic equilibrium using an iterative procedure.

The total mass of each galaxy within $R_{200,\text{crit}}$ (i.e. the radius enclosing a sphere with a mean density of 200 times the critical density of the Universe at redshift zero) is $M_{200} = 10^{11} M_{\odot}$, and the initial stellar mass is $M_* = 1.4 \times 10^9 M_{\odot}$. These masses are consistent with the stellar mass-halo mass relation obtained from abundance matching by Moster et al. (2013) and corrected for baryonic effects using the prescription of Sawala et al. (2015).

A fraction $f_{*,\text{B}} = 0.2$ of the stellar mass is in the bulge, with the remainder in the disc. We use a disc gas mass fraction $f_{\text{d, gas}} = 0.3$, which gives an initial gas mass of $M_{\text{gas}} = 1.8 \times 10^8 M_{\odot}$. The dark matter density profile that we use to calculate the static dark matter potential follows a Hernquist (1990) profile that has been scaled to match the inner regions of a Navarro et al. (1996) (NFW) profile with a concentration $c_{200} = 8.0$, which agrees with the redshift zero mass-concentration relation of Duffy et al. (2008).

In our reference model (ref), we use a fixed metallicity of $0.1 Z_{\odot}$, and for the UV radiation field we use the ISRF of Black (1987), along with the self-shielding prescription described in section 4.2.1. We also consider two additional metallicities ($0.01 Z_{\odot}$ and Z_{\odot}), and three additional radiation fields (ten per cent of the Black (1987) ISRF and the redshift zero UVB of Haardt & Madau (2001), both with self-shielding, and the redshift zero Haardt & Madau (2001) UVB without self-shielding). The parameters and properties of the galaxies in our suite of simulations are summarised in Table 4.2. We summarise the properties of the different radiation fields used in our simulations in Table 4.1.

Throughout this paper we assume that the dust-to-gas ratio scales linearly with

metallicity, or in other words, that the dust-to-metals ratio is constant. However, there is observational evidence that the dust-to-metals ratio decreases at low metallicity, below $\approx 0.3 Z_{\odot}$ (e.g. Rémy-Ruyer et al. 2014). Therefore, it is possible that our runs at $0.01 Z_{\odot}$ and $0.1 Z_{\odot}$ overestimate the total dust abundance. This would affect the formation rate of H_2 , shielding of the radiation field, and photoelectric heating from dust grains.

4.3.2 Morphology and star formation

Maps of the gas surface density after 500 Myr from the simulations run with the full non-equilibrium chemical model are shown in Fig. 4.1 for different metallicities (top row) and different UV radiation fields (bottom row), and maps of the gas temperature after 500 Myr are shown in Fig. 4.2. Each pair of panels in these figures shows projections looking at the disc face-on (top) and edge-on (bottom).

Comparing the three different metallicities, we see that the morphology of the gas is very different in these three runs. In the simulation with the lowest metallicity (one per cent solar; top left pair of panels in Figs. 4.1 and 4.2), star formation only occurs at the centre of the disc. However, at higher metallicities, star formation becomes more vigorous and extends to larger radii. This leads to more supernovae, which create more bubbles of hot gas in the disc (as seen in Fig. 4.2), and drive more gas out of the disc in vertical fountains and outflows (as seen in the edge-on views).

These trends with metallicity occur because, at higher metallicities, there is more metal-line cooling, which allows the gas to cool down to a cold ISM phase (with temperatures of a few hundred Kelvin) at lower densities. Gas needs to cool down to the cold ISM phase before it can form stars. Therefore, in the runs at higher metallicity, star formation can proceed in lower-density gas, and hence at lower gas surface densities. Our models all start with the same gas density profile. Hence, if star formation extends to lower gas surface densities, then it will extend to larger radii.

Additionally, the increase in metal-line cooling at higher metallicities means that gas can more easily undergo gravitational collapse to higher densities. These two effects (star formation at lower densities and more gas collapsing to higher densities) lead to an increase in the total star formation rate, and hence more stellar feedback in the disc.

Furthermore, the fact that the Jeans scale is smaller at lower temperatures also contributes to the more fragmented appearance of the gas disc at high metallicities.

However, it is important to note that these runs at different metallicities all use the same radiation field. In reality, the lower star formation rate that we find at lower metallicity will also result in a weaker radiation field. As we show below, this will tend to increase the star formation rate and thus will lessen the differences in star formation rate at different metallicities.

The bottom rows of Figs. 4.1 and 4.2 show runs at ten per cent solar metallicity with different UV radiation fields: ten per cent of the Black (1987) ISRF ('low-ISRF') and the redshift zero extragalactic UVB of Haardt & Madau (2001) ('UVB'),

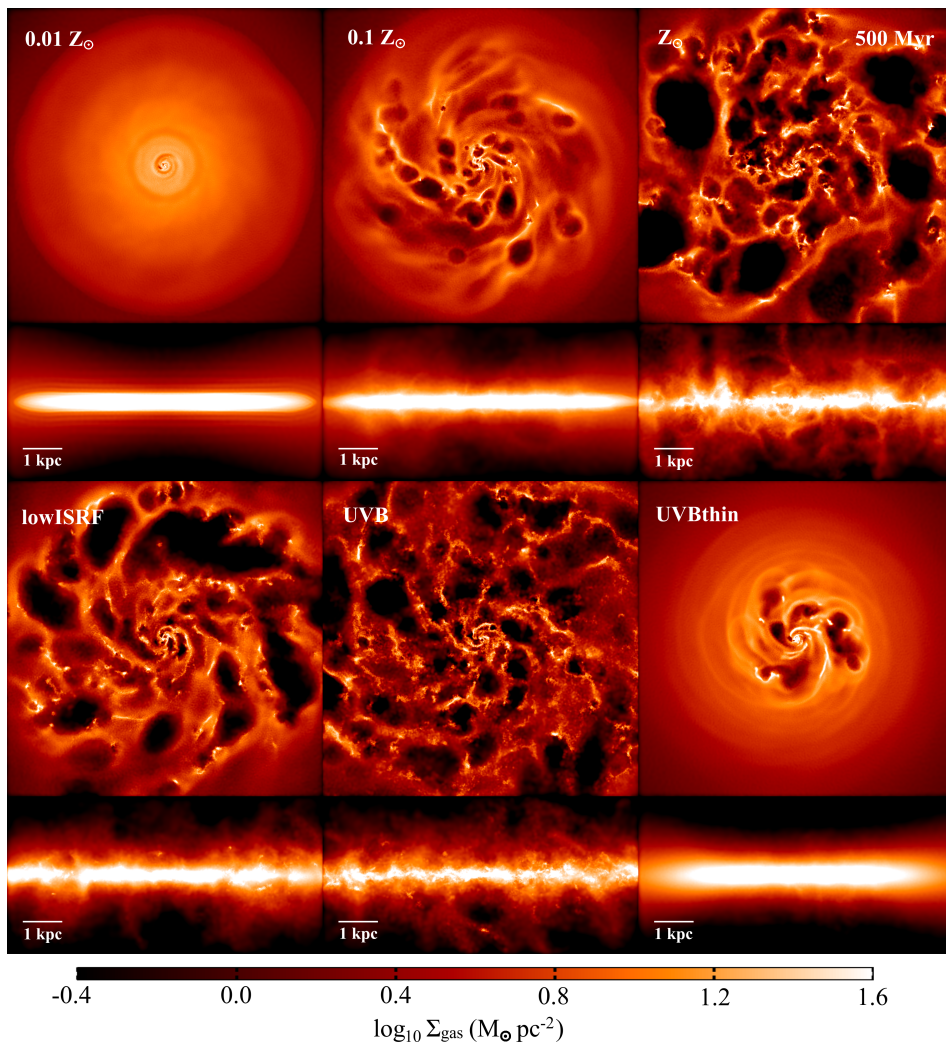


Figure 4.1: Maps of the total gas surface density after 500 Myr in the simulations run with the full non-equilibrium chemical model. The simulations in the top row were run with the Black (1987) ISRF at different metallicities: 0.01 Z_{\odot} (*lowZ*; *left*), 0.1 Z_{\odot} (*ref*; *centre*) and Z_{\odot} (*hiZ*; *right*). The simulations in the bottom row were run at a metallicity of 0.1 Z_{\odot} with different UV radiation fields: ten per cent of the Black (1987) ISRF (*lowISRF*; *left*), the Haardt & Madau (2001) UVB at redshift zero (*UVB*; *centre*) and the Haardt & Madau (2001) UVB without self-shielding (*UVBthin*; *right*). Each pair of panels shows projections looking at the disc face-on (*top*) and edge-on (*bottom*). The face-on projections are 8 kpc across, and the edge-on projections cover 4 kpc in the vertical direction.

both run with self-shielding, and the redshift zero Haardt & Madau (2001) UVB without self-shielding (*UVBthin*). See Table 4.1 for the properties of these ra-

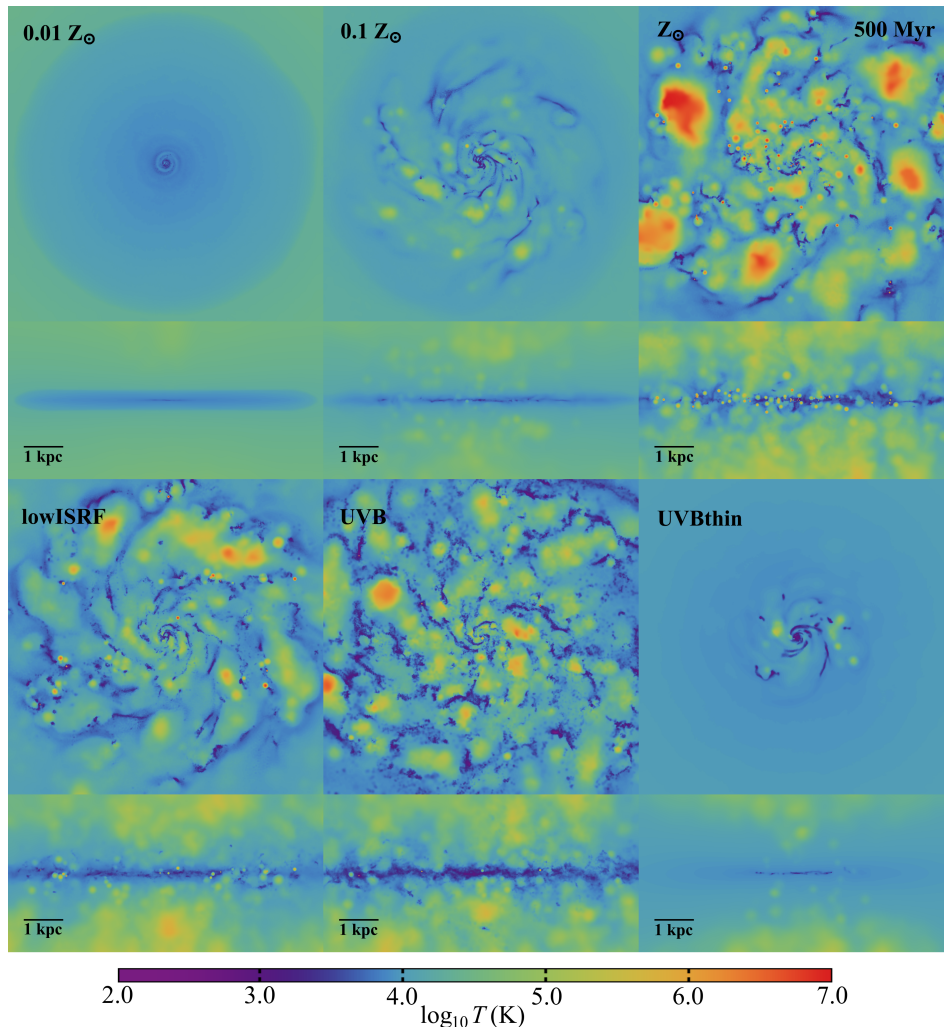


Figure 4.2: As Fig. 4.1, but for the gas temperature. Except for $Z = 0.01 Z_{\odot}$, hot bubbles of gas driven by supernovae disrupt the otherwise smooth density distribution in the disc and drive vertical outflows of gas.

diation fields. As we decrease the strength of the UV radiation field (from the reference run in the top centre panels of Figs. 4.1 and 4.2, to ‘lowISRF’ to ‘UVB’), the gas disc becomes more fragmented. A lower radiation field reduces the heating rate from photoionisation and photoelectric dust heating, which allows the gas to cool to the cold, star forming ISM phase (with temperatures of a few hundred Kelvin) at lower densities. This increases the star formation rate, leading to more stellar feedback, and it decreases the Jeans scale in this gas. Hence the gas becomes more fragmented, similar to the effect of increasing the metallicity.

In the run without self-shielding (‘UVBthin’; bottom right pair of panels in

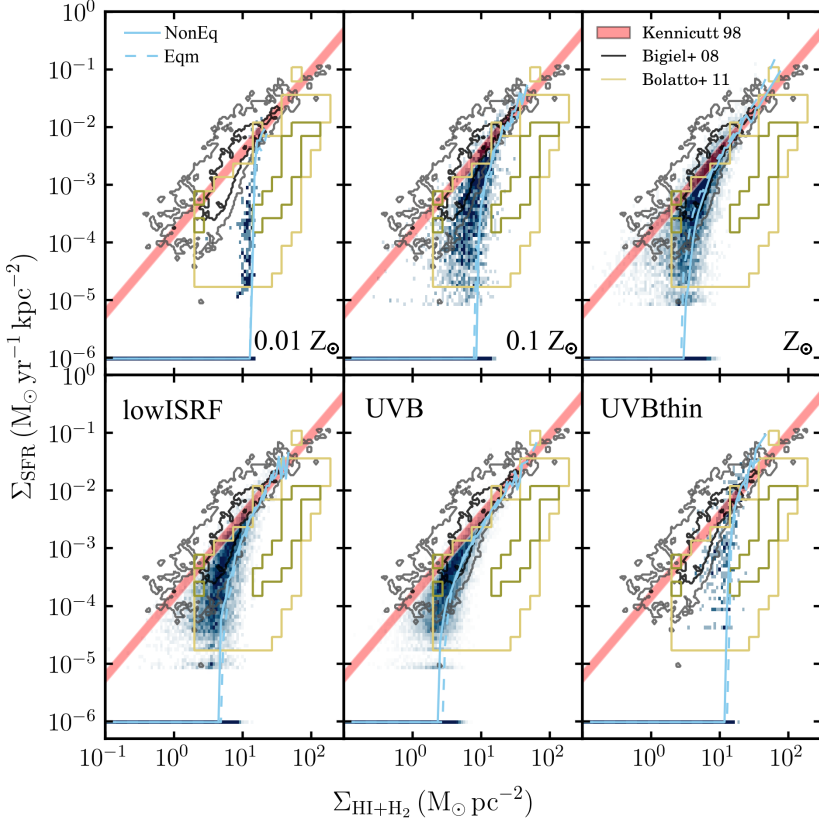


Figure 4.3: The star formation rate surface density, Σ_{SFR} , versus surface density of neutral (atomic plus molecular) hydrogen, $\Sigma_{\text{HI}+\text{H}_2}$, i.e. the Kennicutt-Schmidt relation. The intensity of the blue-green colour corresponds to two-dimensional histograms of Σ_{SFR} and $\Sigma_{\text{HI}+\text{H}_2}$ measured in the simulations run with the full non-equilibrium chemical model at different metallicities (*top row*) and for different radiation fields (*bottom row*; see Table 4.1). We measure Σ_{SFR} and $\Sigma_{\text{HI}+\text{H}_2}$ on a grid of cells, each 100 pc across, that span a square region 8 kpc across aligned such that the disc is viewed face on. We combine measurements from all snapshot outputs from 100 Myr to 1000 Myr, at intervals of 100 Myr. We set all cells to have a minimum Σ_{SFR} of $10^{-6} \text{ M}_{\odot} \text{ yr}^{-1} \text{ kpc}^{-2}$, so that they are visible in these plots. The cyan curves show the median value of Σ_{SFR} in bins of $\Sigma_{\text{HI}+\text{H}_2}$, from simulations evolved with the full non-equilibrium chemical model (*solid*) and those run with cooling rates in chemical equilibrium (*dashed*). The contours show the observed Kennicutt-Schmidt relation from various samples. The red shaded region shows the best-fit power-law relation of Kennicutt (1998) (their equation 4), with the width of this region indicating the uncertainty in the normalisation. The black and grey contours are taken from Bigiel et al. (2008) (the centre-right panel of their fig. 8), measured in sub-kpc regions of nearby galaxies. Finally, the yellow contours are taken from Bolatto et al. (2011) (from their fig. 6), measured in the Small Magellanic Cloud. We use their data at a resolution of 200 pc, rather than their full resolution data, as this is closer to the spatial scale that we use for the measurements of Σ_{SFR} and $\Sigma_{\text{HI}+\text{H}_2}$ in the simulations (100 pc). We have renormalised Σ_{SFR} from the observations for a Chabrier (2003) IMF, as used in our simulations.

Figs. 4.1 and 4.2), the gas is heated by photoionisation of HI even at high densities, where it would otherwise become shielded from ionising radiation. This means that in this run gas can only cool below 1000 K and form stars at high densities ($n_{\text{H,tot}} \gtrsim 10 \text{ cm}^{-3}$). Furthermore, the high-density gas remains much warmer than in the corresponding run with self-shielding ('UVB'), so the Jeans scale in this gas is larger. Hence the gas morphology is smoother when we do not include self-shielding.

The simulations in Figs. 4.1 and 4.2 were run with the full non-equilibrium chemical model. In the simulations evolved with cooling rates in chemical equilibrium, we find very similar morphologies to those seen in Figs. 4.1 and 4.2.

The trends of star formation rate with metallicity and radiation field can be understood more clearly in plots of the star formation rate surface density, Σ_{SFR} , versus gas surface density of neutral (atomic and molecular) hydrogen, $\Sigma_{\text{HI+H}_2}$, i.e. the Kennicutt-Schmidt relation (Kennicutt 1998). These are shown in Fig. 4.3 for different metallicities (top row) and different radiation fields (bottom row). The intensity of the blue-green colour indicates the mass-weighted distribution of gas as a function of Σ_{SFR} and $\Sigma_{\text{HI+H}_2}$ in simulations evolved with the full non-equilibrium chemical model. We measure these on a grid of cells, each 100 pc across, that span a square region 8 kpc across centred on the disc and are aligned such that the disc is viewed face on. In each simulation we have combined measurements of Σ_{SFR} and $\Sigma_{\text{HI+H}_2}$ from all snapshot outputs from 100 Myr to 1000 Myr, at intervals of 100 Myr. The cyan curves in Fig. 4.3 show the median value of Σ_{SFR} in bins of $\Sigma_{\text{HI+H}_2}$ for simulations evolved with the full non-equilibrium model ('NonEq'; solid curves) and with cooling rates in chemical equilibrium ('Eqm'; dashed curves), and the contours show the observed Kennicutt-Schmidt relations in various samples of galaxies, as indicated in the legend.

At high gas surface densities, Σ_{SFR} tends towards a power-law relation, with a slope similar to (albeit slightly larger than) that measured by Kennicutt (1998) (the red region in Fig. 4.3). At low gas surface densities, the star formation rate drops below this power-law relation, and is cut off below a threshold gas surface density, $\Sigma_{\text{HI+H}_2}^{\text{thresh}}$.

In the top right panel of Fig. 4.3, we see that the simulation at solar metallicity agrees fairly well with the relation measured for nearby galaxies by Bigiel et al. (2008) (black and grey contours). Note that we calibrated the parameters of our star formation and stellar feedback models to match the normalisation of the observed relation. The threshold $\Sigma_{\text{HI+H}_2}^{\text{thresh}}$ below which star formation is cut off increases with decreasing metallicity, as predicted by Schaye (2004). If we define $\Sigma_{\text{HI+H}_2}^{\text{thresh}}$ as the surface density at which the median Σ_{SFR} is 1 dex below the power-law relation of Kennicutt (1998), we find $\Sigma_{\text{HI+H}_2}^{\text{thresh}} \propto Z^{-0.3}$. This agrees well with the metallicity dependence derived by Schaye (2004) for the column density at which the cold ISM phase forms (see his equation 23).

In the lowest-metallicity simulation, in the top left panel of Fig. 4.3, the gas surface densities do not extend much above $\Sigma_{\text{HI+H}_2}^{\text{thresh}}$, so we cannot see whether the relation turns over and follows a power-law relation at higher gas surface densities.

Comparing runs at ten per cent solar metallicity for different radiation fields

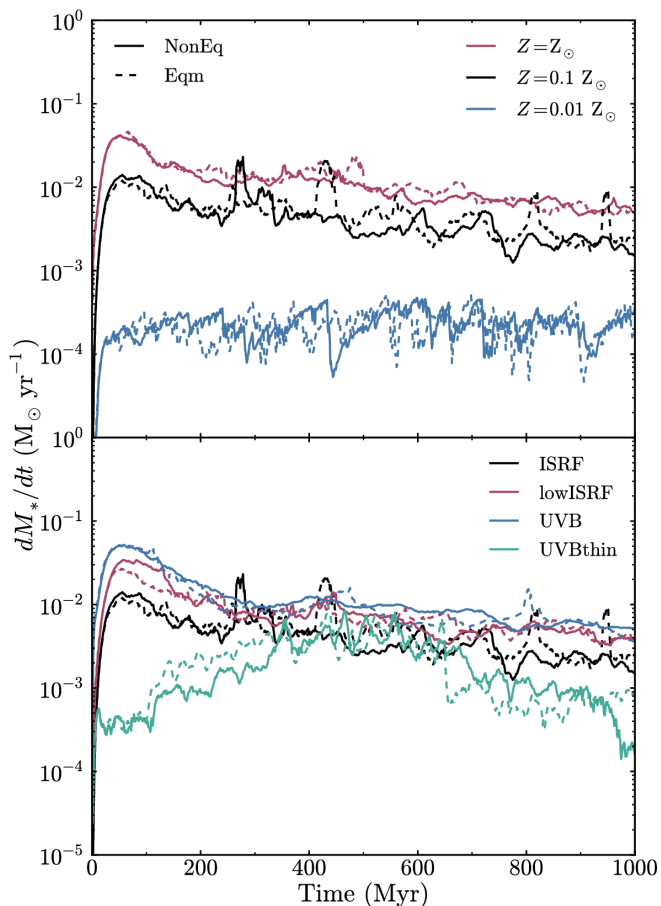


Figure 4.4: Star formation histories of simulations run with the full non-equilibrium chemical model (*solid curves*) and run with cooling rates in chemical equilibrium (*dashed curves*) at different metallicities (*top panel*) and for different radiation fields (*bottom panel*; see *Table 4.1*). The black curves in the two panels are from the same simulation. We find higher star formation rates in the simulations at higher metallicity and, to a lesser extent, in the presence of a weaker UV radiation field.

(top centre, bottom left and bottom centre panels of Fig. 4.3), we see that, as we decrease the strength of the UV radiation field, the threshold gas surface density, $\Sigma_{\text{HI+H}_2}^{\text{thresh}}$, below which star formation is cut off decreases, as predicted by Schaye (2004). This is similar to the effect of increasing the metallicity that we see in the top row. We find $\Sigma_{\text{HI+H}_2}^{\text{thresh}} \propto G_0^{0.3}$, in good agreement with the dependence on UV intensity derived by Schaye (2004) for the column density at which the cold ISM phase forms (his equation 23).

The bottom right panel shows that, when we do not include self-shielding, $\Sigma_{\text{HI+H}_2}^{\text{thresh}}$ increases. Furthermore, at gas surface densities above $\Sigma_{\text{HI+H}_2}^{\text{thresh}}$, the star for-

mation rate continues to rise steeply, and lies above the observed relation of Kennicutt (1998). However, since we calibrated the parameters of our star formation and stellar feedback models to reproduce the observed Kennicutt-Schmidt relation in simulations that included self-shielding, this could possibly be remedied by re-calibrating these parameters.

The star formation histories are shown in Fig. 4.4 for different metallicities (top panel) and different radiation fields (bottom panel). The solid and dashed curves show simulations evolved with the full non-equilibrium chemical model and with cooling rates in chemical equilibrium respectively. The star formation rate initially rises rapidly as gas cools from its initial temperature of 10^4 K to form a cold, star-forming ISM phase. Once stellar feedback takes effect (after ~ 50 Myr), the star formation rate levels off and then steadily declines over the course of the simulation, as gas is either consumed by star formation or driven out of the disc in outflows.

The star formation rate increases with metallicity and is about two orders of magnitude higher for solar metallicity than for $0.01 Z_{\odot}$. As we decrease the strength of the radiation field, the total star formation rate increases, by a factor of ~ 3 for the radiation fields that we consider here. This is similar to the trend that we see when we increase the metallicity from $0.01 Z_{\odot}$ to Z_{\odot} , although the size of the effect is smaller than when we vary the metallicity over this range.

In the run without self-shielding, the total star formation rate is typically lower, by up to an order of magnitude, than in the corresponding run with self-shielding, although they are similar (to within a factor of two) between 400 and 600 Myr.

Comparing the solid and dashed curves in Figs. 4.3 and 4.4, we see that non-equilibrium cooling has no noticeable systematic effect on the simulated Kennicutt-Schmidt relation or on the total star formation rate of the simulated galaxy. However, this conclusion may be dependent on the resolution of our simulations. In particular, our star formation prescription allows gas to form stars at densities $n_{\text{H}} > 1.0 \text{ cm}^{-3}$ and temperatures $T < 1000$ K. In other words, gas in our models becomes star forming once it transitions from the Warm Neutral Medium (WNM) to the Cold Neutral Medium (CNM). It is possible that there are still important non-equilibrium effects on smaller scales than we resolve that could affect the star formation rate.

4.3.3 Outflows

Stellar feedback drives gas out of the disc in our simulations. To measure the radial mass outflow rates and velocities, we consider a spherical shell of radius $0.2R_{200,\text{crit}} = 19$ kpc and thickness $\Delta r = R_{200,\text{crit}}/150 = 0.64$ kpc, centred on the origin (which is defined as the centre of the static dark matter potential). The net mass outflow rate, dM_{net}/dt , is then given by:

$$\frac{dM_{\text{net}}}{dt} = \frac{1}{\Delta r} \sum_{i=1}^{N^{\text{shell}}} m_i \frac{\mathbf{v}_i \cdot \mathbf{r}_i}{|\mathbf{r}_i|}, \quad (4.17)$$

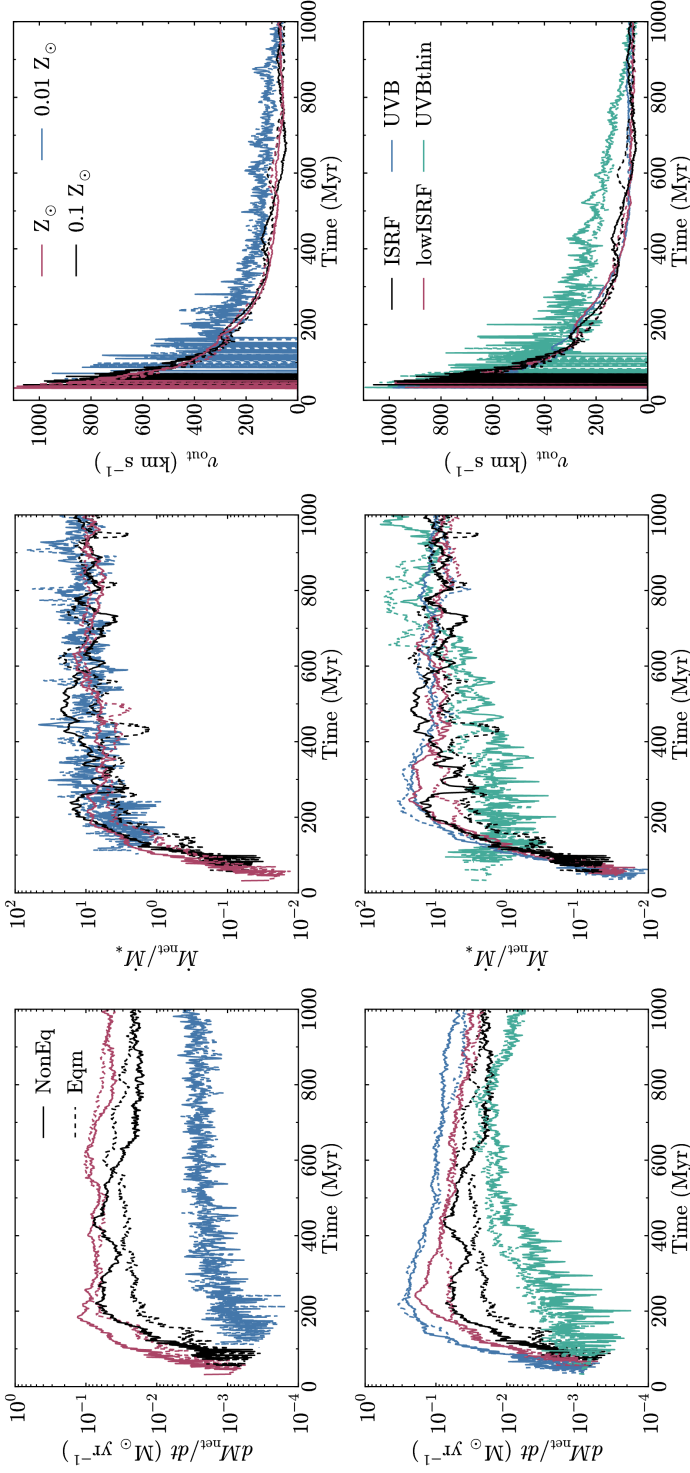


Figure 4.5: Evolution of the net mass outflow rate (*left panels*), mass loading factor (*centre panels*) and mass-weighted mean radial outflow velocity (*right panels*) measured through a thin spherical shell of radius $0.2R_{200,\text{crit}} = 19$ kpc and thickness 0.64 kpc. We show simulations evolved using the full non-equilibrium chemical model (*solid curves*) or using cooling rates in chemical equilibrium (*dashed curves*) at different metallicities (*top row*) and for different radiation fields (*bottom row*; see *Table 4.1*). The mass outflow rate increases with increasing metallicity and decreasing radiation field, although the mass loading factor at late times is ~ 10 , regardless of metallicity or radiation field.

where m_i , \mathbf{v}_i and \mathbf{r}_i are the mass, velocity and position of the i^{th} particle respectively, and we sum over the N^{shell} gas particles in the shell. We also calculate the mass-weighted mean radial velocity, v_{out} , of the outflowing particles as:

$$v_{\text{out}} = \langle v \rangle_+ = \frac{\sum_{i=1}^{N^{\text{shell}}} m_i (\mathbf{v}_i \cdot \mathbf{r}_i / |\mathbf{r}_i|)_+}{\sum_{i=1}^{N^{\text{shell}}} m_i}, \quad (4.18)$$

where the subscript ‘+’ indicates that we only consider particles with $\mathbf{v}_i \cdot \mathbf{r}_i > 0$, i.e. that are moving radially outward.

We could split the net outflow rate in equation 4.17 into separate outflow and inflow rates, using particles that are moving radially outward or inward respectively. However, we find that the inflow rates at this radius are negligible in our simulations.

We measure the mass outflow rates and mean outflow velocities from each simulation in snapshots output at 1 Myr intervals, using equations 4.17 and 4.18. These are shown in Fig. 4.5 for the simulations with different metallicities (top row), and in the presence of different UV radiation fields (bottom row). Solid and dashed curves are from simulations run with the full non-equilibrium chemical model and cooling rates in chemical equilibrium respectively.

We see that the mass outflow rates (left panels) generally increase during the first 200 Myr, as there is a delay between the onset of star formation and the first supernovae, and it takes a finite time for the gas to reach the radius of 19 kpc where we measure the outflows (~ 10 Myr for gas travelling at 200 km s^{-1}). In the simulations without self-shielding (green curves in the bottom row), this initial increase is more gentle and extends over a longer period of time (~ 500 Myr). We saw in Fig. 4.4 that the star formation rates in the simulations without self-shielding also increase more gently over this period. After the initial rise, the mass outflow rates fluctuate around an approximately steady or gently declining value.

The outflow rates tend to be larger in simulations at higher metallicity or in the presence of a weaker UV radiation field, due to the larger star formation rates that we find in these cases (see Fig. 4.4). In the centre panels of Fig. 4.5 we show the evolution of the ratio between the mass outflow rate and the star formation rate, i.e. the mass loading factor. After 200 Myr, the mass loading factor tends towards a value of ~ 10 , independent of the metallicity or strength of the UV radiation field. An exception to this trend is seen in the simulations that do not include self-shielding (green curves in the bottom row), which show a steady rise in the mass loading factor from ~ 1 at 200 Myr to ~ 30 at the end of the simulation, albeit with large fluctuations on timescales of a few Myr.

One caveat is that we do not include a gaseous halo in the initial conditions. In a realistic galaxy, the outflowing gas may be slowed down as it interacts with an existing gaseous halo, which could decrease the mass loading factor at $R_{200,\text{crit}}$. Alternatively, it may sweep up more material from the halo, which could increase the mass loading factor.

In the right panels of Fig. 4.5, we show the evolution of the mean radial velocity of outflowing gas. Initially, we find very large outflow velocities ($v_{\text{out}} \sim 1000 \text{ km s}^{-1}$), because the fastest particles ejected from the disc are the first to

reach the radius at which we measure the outflows. The mean outflow velocity subsequently decreases as the slower particles reach this radius, and tends towards a value of $\sim 65 \text{ km s}^{-1}$ by the end of the simulation.

Comparing solid and dashed curves in Fig.4.5, we see that the outflows are generally not strongly affected by the use of equilibrium cooling rates. In the runs at solar and ten per cent solar metallicity in the presence of the Black (1987) ISRF (red and black curves respectively in the top row of Fig. 4.5), the mass outflow rates (left panels) rise more gently in the first 200 Myr in the simulations run with equilibrium cooling rates (dashed curves), compared to the corresponding runs evolved with non-equilibrium cooling rates (solid curves). However, this difference becomes less pronounced in the presence of a weaker UV radiation field (red and blue curves in the bottom row of Fig. 4.5). Also, the mass loading factors (centre panels) and outflow velocities (right panels) are similar whether we use non-equilibrium or equilibrium cooling.

We also considered how the mass loading factor, $\beta = \dot{M}_{\text{out}}/\dot{M}_*$, depends on gas surface density in our simulations. To do this, we measured vertical outflows close to the disc, at a vertical height of 1 kpc above and below the mid-plane of the disc. We positioned two thin sheets of thickness $\Delta z = 50 \text{ pc}$ parallel to the disc (in the $x - y$ plane) at a vertical distance $|z| = 1 \text{ kpc}$. Each sheet covered a square region 8 kpc across centred on the galaxy centre, which corresponds to the region shown in the face-on views in Figs. 4.1 and 4.2. The vertical mass outflow rate through these two sheets is given by:

$$\frac{dM_{\text{out}}}{dt} = \frac{1}{\Delta z} \sum_{i=1}^{N_{+}^{\text{sheet}}} m_i |v_{z,i}|_{+}, \quad (4.19)$$

where $v_{z,i}$ is the z -component of the velocity of the i^{th} particle, the subscript ‘+’ indicates that we only include particles with $\mathbf{z} \cdot \mathbf{v} > 0$ (i.e. that are moving vertically away from the mid-plane), and we sum over the N_{+}^{sheet} gas particles with $\mathbf{z} \cdot \mathbf{v} > 0$ in the two sheets.

To compare the mass loading factor at a vertical height of 1 kpc to the gas surface density within the disc, we divided the two thin sheets into a grid of cells, each 100 pc across. We then measured the mass outflow rates through the two sheets in each cell, along with the star formation rate and gas surface density in the disc within the cell.

In Fig. 4.6 we plot the mass loading factor as a function of gas surface density for different metallicities (top row) and different UV radiation fields (bottom row). We measured the mass loading factors and gas surface densities in all snapshot outputs from each simulation, at intervals of 1 Myr, and we show the median mass loading factor (solid curves) and the range between the tenth and ninetieth percentiles (shaded regions) in bins of gas surface density. Simulations run with the full non-equilibrium and equilibrium chemical models are shown in black and red respectively.

The mass loading factor decreases with increasing gas surface density, following approximately a power-law, with $\beta \propto \Sigma_{\text{gas}}^{-2}$. At constant gas surface density, the mass loading factor increases with decreasing metallicity and increasing UV

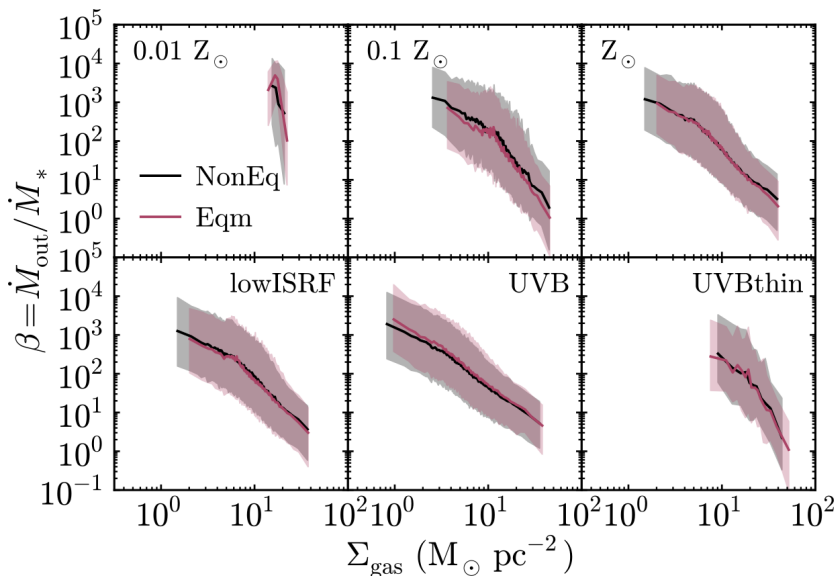


Figure 4.6: Mass loading factor, $\beta = \dot{M}_{\text{out}}/\dot{M}_*$, plotted against gas surface density, Σ_{gas} , measured in regions of the disc 100 pc across at a vertical distance $|z|$ of 1 kpc above and below the mid-plane of the disc. We show simulations at different metallicities (*top row*) and for different radiation fields (*bottom row*; see Table 4.1), evolved using the full non-equilibrium chemical model (*black*) or using cooling rates in chemical equilibrium (*red*). The solid curves show the median mass loading factor in bins of Σ_{gas} , and the shaded regions indicate the range between the tenth and ninetieth percentiles in each bin. The mass loading factor decreases with increasing Σ_{gas} , and this relation is unaffected by using equilibrium cooling.

radiation field. The mass loading factors in the different panels of Fig. 4.6 suggest a scaling of $\beta \propto Z^{-0.5}$ and $\beta \propto G_0^{0.3}$, although these scalings are highly uncertain, as we only consider a small number of different metallicities and radiation fields.

Comparing black and red curves in Fig. 4.6, we see that we recover the same relation between mass loading factor and gas surface density, regardless of whether we use non-equilibrium cooling rates or cooling rates in chemical equilibrium.

Hopkins et al. (2012) explored the dependence of β on galaxy properties in their SPH simulations of isolated galaxies. They found:

$$\beta = 10(V_C(R)/100 \text{ km s}^{-1})^{-1}(\Sigma_{\text{gas}}(R)/10 M_\odot \text{ pc}^{-2})^{-0.5} \quad (4.20)$$

(their equation 8), where V_C is the circular velocity at radius R . This has a much weaker dependence on Σ_{gas} , with a power-law slope of -0.5 , compared to ~ -2 from our simulations. This different scaling with Σ_{gas} may be due to the different prescription for stellar feedback that was used by Hopkins et al. (2012).

The relation between β and Σ_{gas} has also been explored by Creasey et al. (2013). They used high-resolution mesh simulations of supernova-driven galactic winds in a 1 kpc column through a galactic disc, but they did not include radiative

cooling below 10^4 K. They showed that β increases with decreasing Σ_{gas} , and with increasing gas fraction, f_{gas} . They fit a power-law dependence of β on Σ_{gas} and f_{gas} in their simulations, and they found $\beta = 13\Sigma_{\text{gas}}^{-1.15} f_{\text{gas}}^{0.16}$ (see equations 39-42 of Creasey et al. 2013). This power-law scaling with Σ_{gas} is intermediate between our value and the relation of Hopkins et al. (2012).

We find much larger mass loading factors than Creasey et al. (2013) at a given gas surface density. For example, at $\Sigma_{\text{gas}} = 10 M_{\odot} \text{pc}^{-2}$, we typically find a median mass loading factor of ~ 100 at $|z| = 1$ kpc, whereas, for a gas fraction $f_{\text{gas}} = 0.3$, the best-fit relation of Creasey et al. (2013) gives a mass loading factor of 0.8. For comparison, the relation of Hopkins et al. (2012) gives $\beta = 20$, where $V_C \sim 50 \text{ km s}^{-1}$ in our simulations. Creasey et al. (2013) measured the outflows from their simulation volume closer to the mid-plane, at $|z| = 500$ pc. However, when we consider outflows at $|z| = 500$ pc in our simulations, we still find a mass loading factor ~ 100 at $\Sigma_{\text{gas}} = 10 M_{\odot} \text{pc}^{-2}$, and a slope ~ -2 .

There are several differences between our simulations and those of Creasey et al. (2013) that could explain these discrepancies. Most importantly, Creasey et al. (2013) did not include radiative cooling below 10^4 K, whereas gas in our simulations can cool to 10 K. The presence of a cold phase in the ISM is likely to affect how outflowing gas escapes the disc. Creasey et al. (2013) also did not include rotation of the disc, or self-gravity of the gas. However, they did use a slightly higher resolution (1.6 pc) than we have in our simulations (we use a gravitational softening length of 3.1 pc for gas particles). Creasey et al. (2013) also injected energy from individual supernovae, whereas our stellar feedback model requires that we inject energy from several supernovae simultaneously in a single feedback event, to prevent artificial radiative losses (see section 4.2.3).

Chemistry of outflowing gas

We have seen that the mass outflow rates and velocities are generally not strongly affected by non-equilibrium cooling. However, we might expect the abundances in outflowing gas to be out of equilibrium, since this gas is highly dynamic. This would be important for comparing with observations of particular chemical species in outflows. For example, molecular outflows have been observed in extragalactic systems, including starbursting galaxies and Active Galactic Nuclei (AGN). These have been observed in emission and absorption from a number of molecules, including CO, H_2 , OH and HCO^+ (e.g. Baan et al. 1989; Walter et al. 2002; Leon et al. 2007; Sakamoto et al. 2009; Sturm et al. 2011; Emonts et al. 2014; Geach et al. 2014).

To investigate whether the molecular abundances are out of equilibrium in outflowing gas, we measured the total mass of H_2 in particles with a vertical velocity (perpendicular to the plane of the disc) greater than some velocity v_z , i.e. $M_{\text{H}_2}(> v_z)$. We include only particles moving away from the mid-plane of the disc (i.e. that are outflowing), with $\mathbf{z} \cdot \mathbf{v} > 0$.

In Fig. 4.7 we plot $M_{\text{H}_2}(> v_z)$ as a function of v_z , averaged over ten snapshot outputs for each simulation at intervals of 100 Myr. We show different metallicities and different radiation fields in the top and bottom panels respectively. The solid

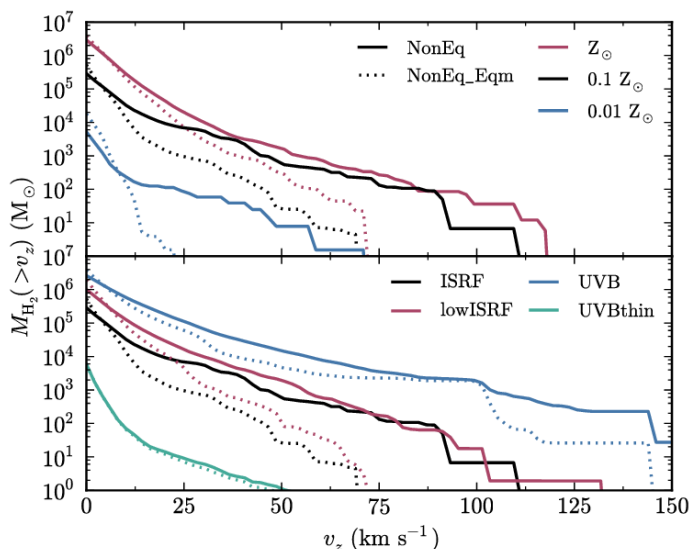


Figure 4.7: Mass of molecular hydrogen in particles moving away from the mid-plane of the disc with a vertical velocity $> v_z$, plotted as a function of v_z , for different metallicities (*top panel*) and for different radiation fields (*bottom panel*; see Table 4.1). We calculate the H_2 masses from simulations run using the full chemical model using non-equilibrium abundances (*solid curves*) and from the same simulations but with abundances set to chemical equilibrium in post-processing (*dotted curves*). We average these curves over ten snapshots for each simulation, at intervals of 100 Myr. The mass of H_2 in outflowing gas ($\geq 50 \text{ km s}^{-1}$) is generally much higher in non-equilibrium, e.g. by a factor of ~ 20 in the ISRF run.

curves in each panel show the H_2 mass computed from the simulations evolved with the full chemical model using non-equilibrium H_2 abundances, while the dotted curves are calculated from the same non-equilibrium simulations, but using abundances that are set to equilibrium in post-processing. The latter we label as ‘NonEq_Eqm’, to distinguish them from the ‘Eqm’ simulations that were evolved with cooling rates in chemical equilibrium (not shown).

At low v_z (below 5 km s^{-1}) the non-equilibrium H_2 masses are generally slightly lower than in equilibrium. The H_2 mass at low v_z is dominated by molecular clouds in the disc and, as we will see in section 4.3.4, H_2 is underabundant in gas that is starting to become molecular. However, at larger v_z , where we include only gas that is outflowing, we find much larger H_2 masses when we use non-equilibrium abundances than when we assume chemical equilibrium. This gas was previously in molecular clouds, but has not yet had enough time for the H_2 to be destroyed and reach the new chemical equilibrium state since being ejected. For example, in the simulation at $0.1 Z_\odot$ in the presence of the Black (1987) ISRF (black curves), we find $600 M_\odot$ of molecular hydrogen outflowing at $> 50 \text{ km s}^{-1}$, compared to only $30 M_\odot$ if we assume chemical equilibrium. Thus, non-equilibrium chemistry enhances the mass of outflowing H_2 by a factor ~ 20 in this example. We see

such differences in all runs with the Black (1987) ISRF and ten per cent of the Black (1987) ISRF, but the differences due to non-equilibrium abundances are much smaller in the presence of the Haardt & Madau (2001) UVB (blue curves in the bottom panel). Also, in the simulation without self-shielding (green curves in the bottom panel), the non-equilibrium and equilibrium H_2 masses are almost identical, and are much lower (by more than two orders of magnitude) than in the corresponding run with self-shielding, because gas does not become shielded from the dissociating radiation in this run.

Fig. 4.7 therefore demonstrates that non-equilibrium chemistry can be very important for modelling molecular outflows, as the molecules in gas that is ejected from the galaxy are not instantly destroyed, but instead take time to evolve to a new chemical equilibrium.

4.3.4 Phase structure of the ISM

Fig. 4.8 shows two-dimensional histograms of the gas temperature and density for simulations with different metallicities (top row) and radiation fields (bottom row), evolved with the full non-equilibrium chemical model. In each panel we stack snapshot outputs taken at intervals of 100 Myr to show the time-averaged distribution of gas. The colour scale indicates the mass fraction of gas in each pixel, so we see the mass-weighted distribution, rather than the volume-weighted distribution.

Comparing different metallicities (top row), we see that increasing the metallicity allows more gas to cool to lower temperatures and higher densities. Reducing the strength of the radiation field (top centre, bottom left and bottom centre panels) also increases the amount of cold gas in the simulation, due to the reduced photoionisation heating and photoelectric dust heating. Note that, in the star formation prescription that we use, gas particles are allowed to form stars if they have a density $n_{\text{H}} > 1.0 \text{ cm}^{-3}$ and a temperature $T < 10^3 \text{ K}$, i.e. if they lie in the bottom right region delineated by the vertical and horizontal dotted lines in each panel. We thus see that there is more star forming gas in the galaxies at higher metallicity or in the presence of a weaker UV radiation field. This explains the higher star formation rates that we saw in section 4.3.2, and hence the stronger supernova-driven galactic winds that we saw in section 4.3.3, at higher metallicity and lower radiation field strength.

At densities $10^{-2} \text{ cm}^{-3} \lesssim n_{\text{H}} \lesssim 10^0 \text{ cm}^{-3}$, the gas at low metallicity follows two distinct tracks in the temperature-density plane, which become less distinct at higher metallicity. We find that the high-temperature track consists of strongly ionised gas, which experiences strong photoheating, while the low-temperature track consists of neutral gas that has become shielded from hydrogen-ionising radiation (see, for example, the first and third rows of Fig. 4.10, which show temperature-density diagrams with a colour scale indicating the electron abundance). At high metallicities, metal cooling reduces the thermal equilibrium temperature of the ionised gas and thus brings the two tracks closer together. We also see that the distinction between these two tracks is less clear in the presence of a weaker UV radiation field, and that they coincide if we neglect self-shielding.

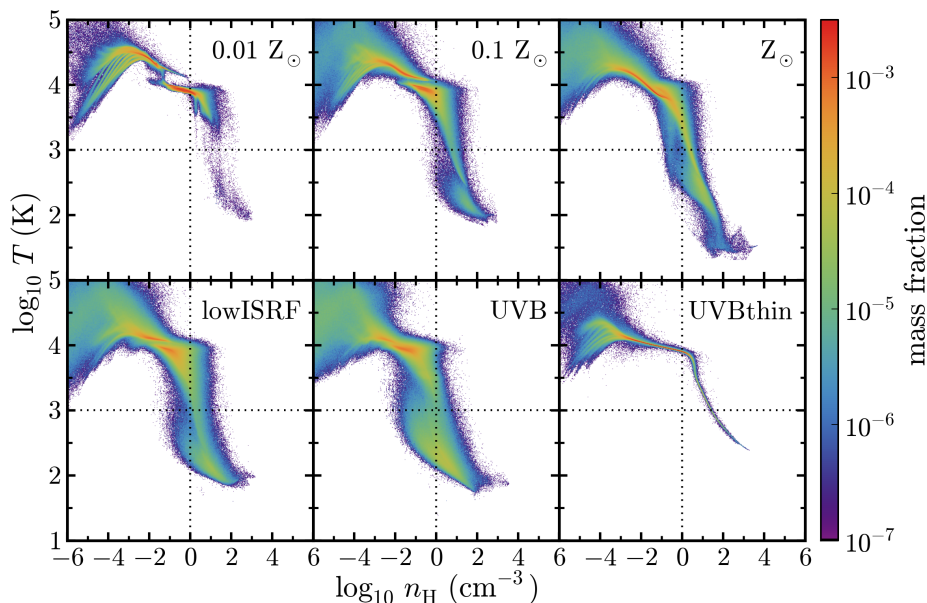


Figure 4.8: The distribution of gas in the temperature-density plane from simulations at different metallicities (*top row*) and for different radiation fields (*bottom row*; see Table 4.1). These simulations were run using the full non-equilibrium chemical model. In each panel we combine snapshot outputs taken at intervals of 100 Myr. The colour scale indicates the mass fraction of gas in each pixel. The dotted horizontal and vertical lines indicate the temperature and density thresholds, respectively, of our star formation prescription. Thus gas in the bottom right region of each panel is allowed to form stars. We find more cold, star forming gas in the simulations run at higher metallicity and in the presence of a weaker UV radiation field.

In the bottom right panel of Fig. 4.8, we see that there is much less scatter in the gas temperature and density when we do not include self-shielding of gas from the radiation field, with most of the gas at densities $n_{\text{H}} > 10^{-1} \text{ cm}^{-3}$ following a very narrow region in the temperature-density plane. When we include self-shielding, gas particles at a particular density and temperature can exhibit a wide range of different shielding column densities, which explains the larger scatter that we see in the temperature-density plane when self-shielding is included.

In the simulations evolved with equilibrium cooling rates, we generally find similar distributions to those in Fig. 4.8 for the simulations evolved with the full non-equilibrium chemical model. However, there are some regions in this plane that appear different. To quantify these differences, we show the one-dimensional probability density functions (pdfs) of gas density in Fig. 4.9 for simulations with different metallicities (*top panel*) and different radiation fields (*bottom panel*). Solid and dashed curves correspond to the full non-equilibrium chemical model and cooling rates in chemical equilibrium respectively. We show here the density

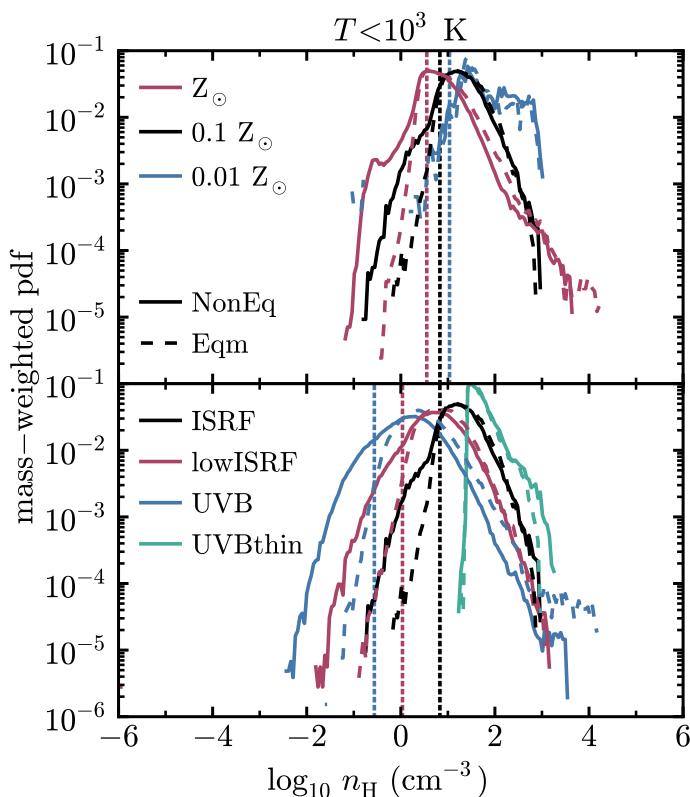


Figure 4.9: One-dimensional mass-weighted density pdf of cold gas ($T < 10^3$ K) from simulations evolved using the full non-equilibrium chemical model (*solid curves*) and using cooling rates in chemical equilibrium (*dashed curves*) at different metallicities (*top panel*) and for different UV radiation fields (*bottom panel*; see Table 4.1). The vertical dotted lines show the minimum density of the cold neutral medium predicted by the model of Wolfire et al. (2003), as a function of metallicity and radiation field.

distributions for cold gas, with $T < 10^3$ K, which corresponds to the temperature threshold below which gas particles can form stars in our star formation prescription. This temperature is indicated by the dotted horizontal lines in Fig. 4.8.

At metallicities $Z \geq 0.1 Z_\odot$, we see that the density distribution in the top panel of Fig. 4.9 extends to lower densities, by ~ 0.5 dex, when the galaxy is evolved using the full non-equilibrium chemical model. We also see this effect when we consider weaker UV radiation fields at $0.1 Z_\odot$, shown by the red and blue curves in the bottom panel.

For comparison, the vertical dotted lines show the minimum density of the cold neutral medium (CNM) predicted by the model of Wolfire et al. (2003), if the CNM is in pressure equilibrium with the warm neutral medium (WNM). To determine this minimum density, Wolfire et al. (2003) calculate the thermal equi-

librium temperature of the gas as a function of density, assuming that photoelectric heating from dust grains is balanced by radiative cooling from CII and OI. Using this temperature-density relation, they determine the minimum pressure at which two stable ISM phases can exist in pressure equilibrium. This minimum pressure corresponds to the minimum density of the CNM, which is given by their equation 35:

$$n_{\min} \approx 31 \frac{G'_0(Z'_d/Z'_g)}{1 + 3.1(G'_0 Z'_d / \zeta'_t)^{0.365}} \text{ cm}^{-3}, \quad (4.21)$$

where G_0 is the strength of the UV radiation field in units of the Habing (1968) field, Z_d is the abundance of dust and polycyclic aromatic hydrocarbons (PAHs), Z_g is the gas phase metallicity, and ζ_t is the ionisation rate from cosmic rays and EUV/X-ray radiation. Primes indicate that these values have been normalised to their values in the local solar neighbourhood, for which Wolfire et al. (2003) take $G_0 = 1.7$ and $\zeta_t = 10^{-16} \text{ s}^{-1}$.

At solar metallicity, the minimum CNM density predicted by Wolfire et al. (2003) coincides with the peak of the density distribution from our simulations, below which the distribution declines rapidly. Since this low-density tail is more extended in the simulations run with the full non-equilibrium chemical model, we find more cold gas below the minimum density of the Wolfire et al. (2003) model in this case than when we evolve the galaxy with equilibrium cooling rates. For example, at $Z = Z_\odot$, 27.9 per cent of the cold gas mass has a density $n < n_{\min}$ when we use non-equilibrium cooling rates, compared to 17.9 per cent when we use cooling rates in chemical equilibrium.

Note that, in the Wolfire et al. (2003) model, the CNM has a maximum temperature of 243 K, whereas we consider cold gas with $T < 10^3 \text{ K}$, since this corresponds to the temperature threshold that we use in our star formation prescription. If we consider the density distribution of gas with $T < 243 \text{ K}$ in our simulations, we find that 2.4 per cent of the gas mass has a density $n < n_{\min}$ in the non-equilibrium run at solar metallicity, compared to 0.6 per cent in the equilibrium run. Thus our simulations are not in conflict with the predictions of Wolfire et al. (2003). We continue to use n_{\min} as a convenient metallicity- and radiation field-dependent reference point in our comparisons below.

At lower metallicities, the peak of the density distribution of cold gas moves to higher densities. The minimum density predicted by Wolfire et al. (2003) also increases as the metallicity decreases, although it does not increase as quickly as in our simulations. We thus find less cold gas with $n < n_{\min}$ at lower metallicity. For example, at $Z = 0.1 Z_\odot$, 14.2 per cent of the cold ($T < 10^3 \text{ K}$) gas mass has $n < n_{\min}$ when we use non-equilibrium cooling, compared to 6.5 per cent when we use cooling rates in chemical equilibrium.

In the presence of a weaker UV radiation field (i.e. lower G_0), the density distribution of cold gas moves to lower densities in our simulations, as does the minimum CNM density predicted by Wolfire et al. (2003). We also see that the differences between non-equilibrium and equilibrium cooling become more pronounced in the presence of weaker UV radiation fields. For example, in the simulations run in the presence of the Haardt & Madau (2001) UVB (blue curves in the

bottom panel of Fig. 4.9), 13.2 per cent of the cold gas mass in the simulation run with non-equilibrium cooling has a density below n_{\min} predicted by equation 4.21, compared to 0.8 per cent in the corresponding simulation evolved using cooling rates in chemical equilibrium.

To understand why non-equilibrium cooling causes these differences in the temperature-density distribution, it is useful to explore in which regions of the temperature-density plane the chemical abundances are out of equilibrium. In Fig. 4.10 we show temperature-density diagrams with a colour scale indicating the mass-weighted mean electron abundance (first and third rows) and the mass-weighted mean ratio between the non-equilibrium electron abundance and the abundance of electrons in chemical equilibrium (second and fourth rows). Red and blue in the second and fourth rows indicate that the electron abundance is enhanced and reduced respectively, with respect to equilibrium. The top two rows and bottom two rows of Fig. 4.10 show variations in metallicity and radiation field respectively.

At metallicities $Z \leq 0.1 Z_{\odot}$ the electron abundance is close to equilibrium throughout most of the simulation. In the centre panel of the second row of Fig. 4.10 the electron abundance at densities $n_{\text{H}} \sim 10^2 \text{ cm}^{-3}$ is enhanced by a factor of a few compared to equilibrium, and cold gas (with $T < 10^3 \text{ K}$) at densities $n_{\text{H}} \sim 1 \text{ cm}^{-3}$ shows electron abundances that are reduced by $\sim 20 - 40$ per cent below equilibrium. The narrow region between the warm ionised and warm neutral phases at $T \sim 10^4 \text{ K}$ also shows electron abundances that are out of equilibrium, by up to an order of magnitude.

Similar trends are also seen in the presence of a weaker radiation field, in the left and centre panels of the bottom row of Fig. 4.10. When we neglect self-shielding, in the right panels of the bottom two rows of Fig. 4.10, the electron abundance is everywhere consistent with chemical equilibrium.

At solar metallicity, in the right panels of the top two rows of Fig. 4.10, there is also a region at $n_{\text{H}} \sim 0.1 \text{ cm}^{-3}$ that extends from $T \sim 250 \text{ K}$ to $T \sim 4000 \text{ K}$ where the electron abundance is enhanced by about an order of magnitude. We find that there is no gas in this region of the temperature-density plane in the simulation evolved with cooling rates in chemical equilibrium. In the non-equilibrium simulation, the enhanced electron abundance increases the collisional excitation rate of ions (such as CII) by electrons and thus increases the radiative cooling rate, allowing it to cool below the thermal equilibrium temperature corresponding to chemical equilibrium.

In Fig. 4.11 we similarly show temperature-density diagrams with a colour scale indicating the non-equilibrium H_2 abundance (first and third rows) and the ratio between the non-equilibrium and equilibrium H_2 abundances (second and fourth rows), for different metallicities (top two rows) and different radiation fields (bottom two rows).

At metallicities $Z \geq 0.1 Z_{\odot}$, in the centre and right panels of the second row of Fig. 4.11, and at lower radiation field strengths, in the left and centre panels of the bottom row of Fig. 4.11, we see that gas with $T < 10^3 \text{ K}$ and $n_{\text{H}} \sim 1 \text{ cm}^{-3}$ has a very strongly enhanced H_2 abundance, by up to six orders of magnitude. We find that these gas particles were previously in molecular clouds, with densities

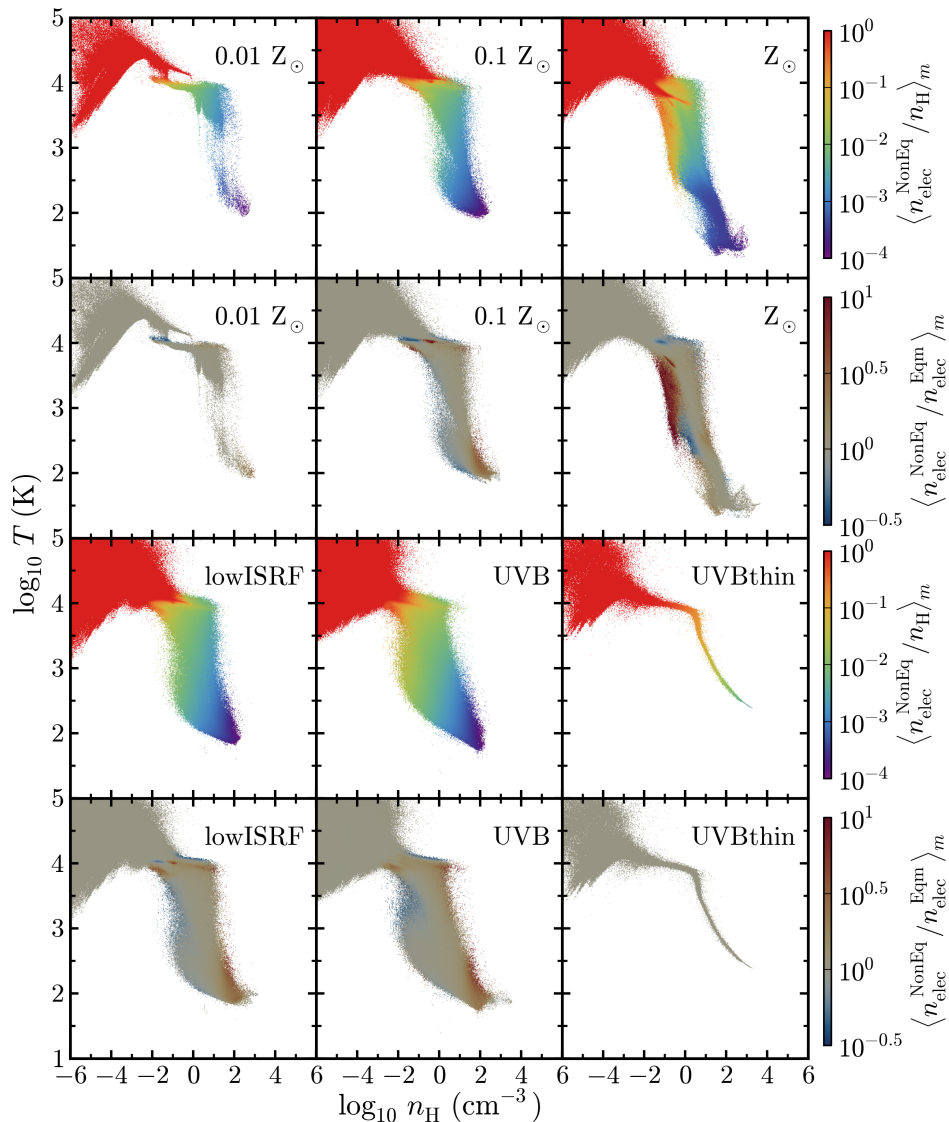


Figure 4.10: Temperature-density diagrams from simulations run with the full non-equilibrium chemical model at different metallicities (*top two rows*) and for different radiation fields (*bottom two rows*; see Table 4.1). The colour scale indicates the mass-weighted mean non-equilibrium electron abundance (*first and third rows*) and the mass-weighted mean ratio between the non-equilibrium electron abundance and the electron abundance in equilibrium (*second and fourth rows*). We have averaged over snapshot outputs taken at intervals of 100 Myr. Red regions in the second and fourth rows show where electrons are enhanced with respect to equilibrium, and blue regions show where it is suppressed.

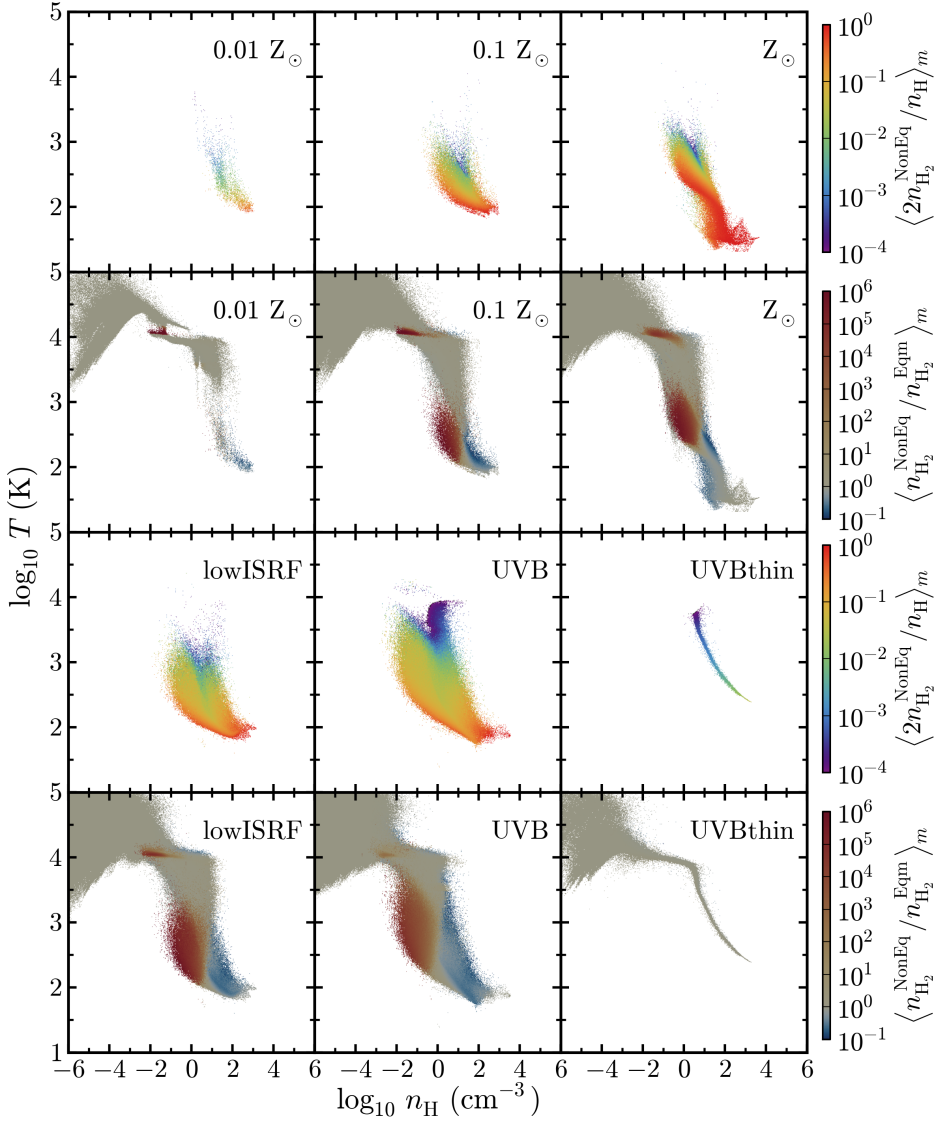


Figure 4.11: As Fig. 4.10, but with the colour scale now indicating the mass-weighted mean non-equilibrium H_2 abundance (*first and third rows*) and the mass-weighted mean ratio between the non-equilibrium H_2 abundance and the H_2 abundance in equilibrium (*second and fourth rows*). We see that the H_2 abundance at $T < 10^3$ K and $n_{\text{H}} \sim 1 \text{ cm}^{-3}$ is strongly enhanced, by up to six orders of magnitude, at $Z \geq 0.1 Z_{\odot}$. The resulting increase in H_2 cooling in this region explains why we see more cold gas at low densities in the one-dimensional density pdfs in Fig. 4.9 when we use non-equilibrium cooling compared to equilibrium cooling.

$\sim 10 - 100$ times their current value in the previous ~ 5 Myr. These molecular clouds then became disrupted or destroyed, and the gas moved to lower densities. However, since it takes a finite time for the molecular hydrogen to be destroyed and reach a new equilibrium, they retain a high molecular fraction, resulting in a strong overabundance of H_2 with respect to equilibrium.

Similar non-equilibrium effects in the H_2 fraction were also found by Dobbs et al. (2008) in their simulations of spiral galaxies. However, it is possible that this enhancement in the H_2 abundance is sensitive to the resolution of our simulations. For example, this low-density gas may in reality be clumpy on scales smaller than we resolve, which would make it less well shielded from the photodissociating radiation than in our simulations.

This region of enhanced H_2 in the temperature-density plane corresponds to the extended low-density tail that we saw in the density distributions of cold ($T < 10^3$ K) gas in Fig. 4.9. The enhanced H_2 abundance increases the cooling rate from H_2 , which allows this low-density gas to cool to lower temperatures. The enhanced H_2 abundances in outflowing gas that we saw in Fig. 4.7 also correspond primarily to this region of the temperature-density plane.

At higher densities, we also see blue regions in the second row of Fig. 4.11 at all metallicities, and in the left and centre panels of the bottom row, where the H_2 abundance is reduced below its equilibrium value by up to an order of magnitude. We find that these gas particles were previously at lower densities and higher temperatures, and are now starting to become molecular.

Pelupessy & Papadopoulos (2009) also explored non-equilibrium H_2 chemistry in their hydrodynamic simulations of isolated galaxies, with metallicities up to Z_\odot . They found H_2 fractions that were often far out of equilibrium in their simulations, in agreement with our results. In contrast, Krumholz & Gnedin (2011) compared the time-dependent H_2 model from Gnedin & Kravtsov (2011) to the equilibrium H_2 model of Krumholz et al. (2008, 2009) and McKee & Krumholz (2010), implemented in cosmological simulations, and they found good agreement between these two models at metallicities $\gtrsim 0.01 Z_\odot$. They therefore concluded that their equilibrium treatment of H_2 is sufficient above one per cent solar metallicity. However, their simulations used a lower resolution than we use. For example, the maximum resolution in their zoom-in cosmological simulations was 65 pc, whereas our simulations use a gravitational softening length of 3.1 pc. This difference in resolution may explain why we find non-equilibrium chemistry to be more important than Krumholz & Gnedin (2011).

4.4 Observable Line Emission

To investigate the effects of metallicity, radiation field and non-equilibrium chemistry on observable diagnostics, we computed line emission maps for CII and CO. We used the publicly available Monte-Carlo radiative transfer code RADMC-3D⁵ (version 0.38) to compute the line emission from these species by post-processing the output from our simulations. RADMC-3D includes thermal emission from dust

⁵<http://www.ita.uni-heidelberg.de/~dullemond/software/radmc-3d/>

and line emission from user-specified species and transitions. We also include anisotropic scattering of continuum and line emission by dust grains, although in the current version of RADMC-3D scattering of line emission does not include the corresponding doppler shift due to the relative motion of the dust, it only changes the direction of the radiation.

We include two populations of dust grains, graphite and silicate, using opacities from the calculations of Martin & Whittet (1990), who used the power-law grain size distribution of Mathis et al. (1977). We use a dust-to-gas mass ratio of $2.4 \times 10^{-3} Z/Z_{\odot}$ and $4.0 \times 10^{-3} Z/Z_{\odot}$ for the graphite and silicate grains respectively, which we take from the ‘ISM’ grain abundances used in the photoionisation code CLOUDY⁶ version 13.01 (Ferland et al. 2013).

The line emission from a given species depends on its level populations. However, unless we assume that these level populations are in Local Thermodynamic Equilibrium (LTE), they will also depend on the radiation field, including the emission lines themselves. A full, self-consistent non-LTE treatment can therefore be computationally expensive, as line emission from one gas cell can influence the level populations of its neighbours. Nevertheless, non-LTE effects can be important. Duarte-Cabral et al. (2015) created synthetic maps of CO emission from their hydrodynamic simulations of spiral galaxies, and they compared maps created with and without assuming LTE. They found that, while the morphology of the CO emission was unaffected, the CO line intensity was generally overestimated when assuming LTE.

RADMC-3D includes a number of approximate methods to include non-LTE effects. We use the Large Velocity Gradient (LVG) method, which is also known as the Sobolev approximation (Sobolev 1957). This method assumes that, after propagating for some distance, an emission line will be sufficiently Doppler shifted, due to motions of the gas, to propagate freely. We can thus calculate an escape probability for emitted photons based on the velocity gradient, which allows us to calculate the level populations from local quantities. A full description of the LVG method as implemented in RADMC-3D can be found in Shetty et al. (2011).

With the LVG method, the non-LTE line emission from species i depends on the density of i and the species j that can collisionally excite it, along with the gas temperature, gas velocity and the radiation field. Apart from the radiation field, we compute these quantities, and the densities of graphite and silicate grains, on a $4.0 \text{ kpc} \times 4.0 \text{ kpc} \times 4.0 \text{ kpc}$ Cartesian grid with a resolution of 10 pc per cell. We calculate these quantities from the SPH particles in the snapshot outputs using SPH interpolation with the same Wendland C2 kernel with 100 SPH neighbours as was used in the simulations. We then compute the line and thermal dust emission, viewing the disc face-on, in 80 wavelength bins centred on the line and covering a velocity range of $\pm 40 \text{ km s}^{-1}$. Finally, we repeat this without the emission line to create a map of the thermal dust emission only, and we subtract this from the full map to obtain the continuum-subtracted line emission.

It is important to note that the CII and CO emission presented in this section may be affected by the resolution of our simulations. In particular, both CII and CO

⁶<http://nublado.org/>

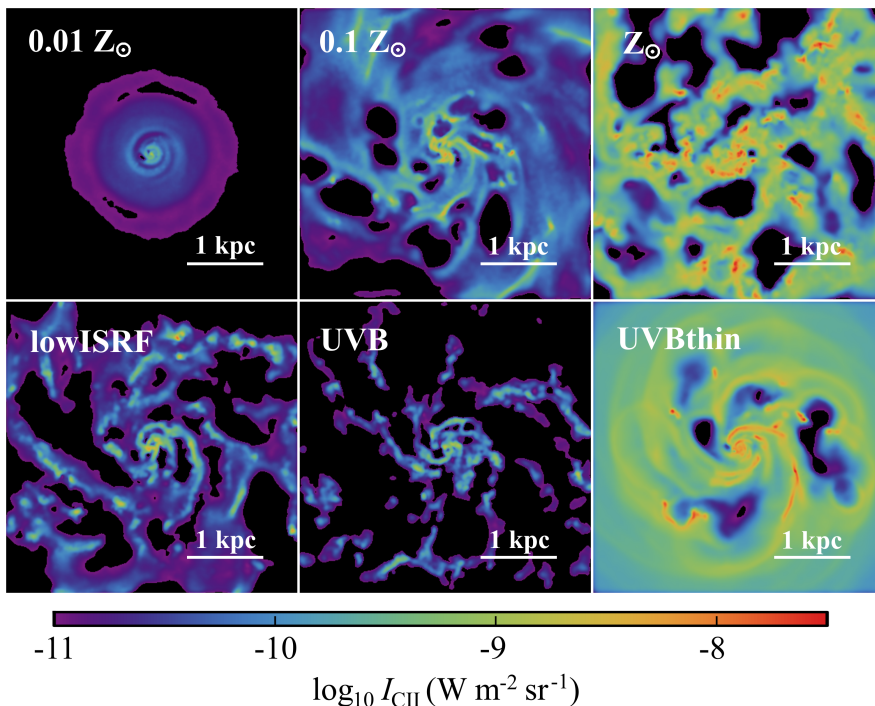


Figure 4.12: CII $158\mu\text{m}$ line emission from simulations evolved with the full non-equilibrium chemical model at different metallicities (*top row*) and for different radiation fields (*bottom row*; see Table 4.1). Each map shows the central region of the galaxy, 4.0 kpc across, at 500 Myr, viewing the disc face on. CII emission increases with increasing metallicity and increasing radiation field.

have a critical density of $\sim 10^3 \text{ cm}^{-3}$. However, we saw in Fig. 4.8 that structures with such high densities are not well resolved in our simulations. Therefore, we might underestimate the CII and CO emission from dense, unresolved structures. Additionally, high-resolution simulations of dense clouds find that most CO is concentrated in compact ($\sim 1 \text{ pc}$), high density ($\sim 10^3 \text{ cm}^{-3}$) clumps and filaments (e.g. Glover & Clark 2012).

4.4.1 CII fine-structure line emission

The CII fine-structure line at $158\mu\text{m}$ is an important coolant in neutral, atomic gas (e.g. Richings et al. 2014a). This line is therefore commonly used as an observational tracer of the cooling properties and physical conditions of the neutral phases of the ISM (e.g. Malhotra et al. 2001; Brauher et al. 2008; Gracía-Carpio et al. 2011; Kennicutt et al. 2011; Beirão et al. 2012; Croxall et al. 2012).

We calculate the emission from the CII $158\mu\text{m}$ line using RADMC-3D, as de-

scribed above, with atomic data for the CII ion taken from the LAMDA database⁷ (Schöier et al. 2005). These include excitation rates from collisions with ortho- and para-H₂ (Lique et al. 2013; Wiesenfeld & Goldsmith 2014), for which we assume an ortho-to-para ratio of 3:1, neutral HI (Barinova et al. 2005), and electrons (Wilson & Bell 2002).

Fig. 4.12 shows CII line emission maps of the central region of each galaxy, 4.0 kpc across, at 500 Myr, viewing the disc face on. The top row shows variations in metallicity, while the bottom row shows different UV radiation fields. These maps were computed from simulations evolved with the full chemical model, using the non-equilibrium abundances of CII and the collision species (H₂, HI and electrons).

Comparing the galaxies at different metallicities Z , we see that the total CII line emission increases approximately linearly with Z . We might have expected such a linear relationship as increasing Z will increase the amount of carbon in the gas. However, this simple picture is complicated by the fact that the densities and temperatures of the neutral gas are also affected by the metallicity, as we saw in Fig. 4.8, which will affect the emissivities per CII ion. A better way to explain this trend of CII emission with metallicity is to note that, if the neutral gas is in thermal equilibrium, the cooling rate of the gas (which comes primarily from CII and OI line emission) will balance the heating rate (which is mainly from photoelectric heating from dust grains). The photoelectric heating rate (Bakes & Tielens 1994; Wolfire et al. 1995) scales with the abundance of dust grains, which we assume scales linearly with Z . Therefore, at higher metallicity, the photoelectric heating rate increases, and thus we need more CII emission to achieve thermal balance.

We also see very different morphologies of CII emission at different metallicities. At $Z \geq 0.1 Z_{\odot}$, we see CII emission from dense clumps that are loosely arranged into spiral arms. In contrast, at $Z = 0.01 Z_{\odot}$ we see an almost undisturbed disc, with CII emission peaking in the centre. This reflects the different morphologies of the total gas distribution that we saw in Fig. 4.1, which are due to the disruption of the disc by stellar feedback and the ability of the gas to cool to lower temperatures and higher densities at higher metallicities, as discussed in section 4.3.2.

Comparing galaxies with different UV radiation fields at ten per cent solar metallicity (top centre, bottom left and bottom centre panels of Fig. 4.12), we see that the total CII emission increases as the strength of the radiation field increases. This can also be understood as the photoelectric heating rate is higher in the presence of a stronger UV field, and thus more CII emission is needed to balance the heating rate. However, the photoelectric heating rate does not increase linearly with radiation field strength, because dust grains become positively charged in the presence of a strong UV field, which reduces the photoelectric heating efficiency.

In the run without self-shielding (bottom right panel), we find much stronger CII emission, by nearly an order of magnitude compared to the corresponding simulation that includes self-shielding (bottom centre panel). This is because the dense gas is much warmer when self-shielding is ignored. For example, at $n_{\text{H}} =$

⁷<http://home.strw.leidenuniv.nl/~moldata/>

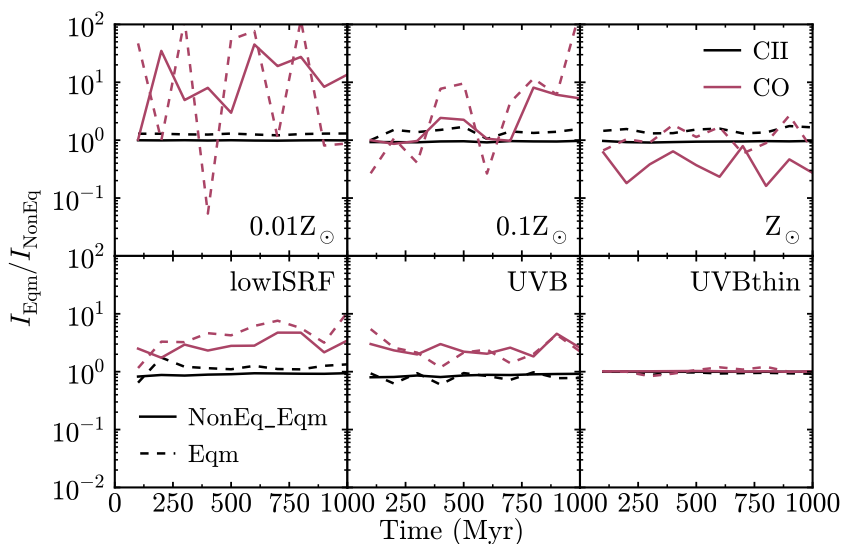


Figure 4.13: Ratio of average line intensity assuming equilibrium abundances, I_{Eqm} , to that using non-equilibrium abundances, I_{NonEq} , plotted against time, for different metallicities (top row) and different UV radiation fields (bottom row; see Table 4.1). We calculated I_{Eqm} from simulations evolved with the full non-equilibrium chemical model with abundances set to equilibrium in post-processing (*NonEq_Eqm*; solid curves), and from simulations evolved in chemical equilibrium (*Eqm*; dashed curves). We show the CII 158 μm line (black curves) and the CO $J = 1 - 0$ line (red curves).

100 cm^{-3} , $T \sim 500 \text{ K}$ when self-shielding is not included, compared to $T \sim 50 - 100 \text{ K}$ when it is included (see Fig. 4.8). Another way to see this is that, without self-shielding, the hydrogen-ionising radiation persists in the dense gas, so we have additional heating from photoionisation of hydrogen. We therefore need more CII emission to achieve thermal balance.

One caveat to note here is that, since we use a uniform UV radiation field, and we do not model local sources of radiation such as young stars, our simulations do not include HII regions and PDRs. However, these are often strong sources of CII emission. Therefore, it is possible that we are underestimating the CII emission.

We saw in section 4.3.4 that evolving a galaxy using cooling rates in non-equilibrium can affect the distribution of gas densities and temperatures, compared to using cooling rates in chemical equilibrium. We also found that some chemical species (particularly the free electrons and H_2) can be far out of equilibrium at certain densities and temperatures. These two effects could potentially have an impact on the observable line emission from individual species.

To investigate the impact of non-equilibrium chemistry on the line emission maps, we also computed these from equilibrium abundances in two ways. Firstly, we used the simulations evolved with the full non-equilibrium chemical model and set the chemical abundances of each gas particle to chemical equilibrium (*'NonEq_Eqm'*). This shows how non-equilibrium abundances affect the line emis-

sion. Secondly, we used the simulations that were evolved using cooling rates in chemical equilibrium ('Eqm'). This shows how the different distributions of gas density and temperature, due to using non-equilibrium cooling, affect the line emission.

Fig. 4.13 shows the ratio of the average line intensity assuming equilibrium abundances to that using non-equilibrium abundances, plotted against time. Solid and dashed curves show 'NonEq_Eqm' and 'Eqm' respectively. CII line emission is shown by the black curves, while the red curves show CO line emission, which we will discuss in section 4.4.2. The top row shows simulations run at different metallicities, and the bottom row shows for different UV radiation fields.

The black solid curves, for CII 'NonEq_Eqm', are all very close to unity in all panels. This tells us that the abundances of CII and those species that collisionally excite it are close to equilibrium in CII-emitting gas for the non-equilibrium runs. The black dashed curves, from the simulations evolved in chemical equilibrium, also remain close to unity, except in runs at ten per cent solar and solar metallicity in the presence of the Black (1987) ISRF (top centre and top right panels), where the equilibrium emission is ~ 50 per cent higher.

4.4.2 CO line emission

Molecular hydrogen is difficult to observe directly in cold, molecular gas, because the lowest rovibrational levels of the H_2 molecule are difficult to excite at the temperatures typical of molecular clouds (~ 10 K). For example, the lowest rotational transition in the ground vibrational state, $0-0S(0)$, has an excitation energy $E/k_B = 510$ K. However, one of the next most abundant molecules after H_2 is CO, which can be observed at much lower temperatures than H_2 . For example, the lowest rotational transition of CO, $J = 1-0$, has an excitation energy of 5.53 K. CO emission is therefore commonly used to map cold molecular gas (e.g. Helfer et al. 2003; Kuno et al. 2007; Bolatto et al. 2008; Leroy et al. 2009). However, to determine the H_2 content from CO emission alone, we need to know the conversion factor, X_{CO} , between CO emission and H_2 column density (see Bolatto et al. 2013 for a recent review). The X_{CO} factor is commonly defined as:

$$X_{\text{CO}} = \frac{N_{\text{H}_2}}{I_{\text{CO}}} \text{ cm}^{-2} (\text{K km s}^{-1})^{-1}, \quad (4.22)$$

where N_{H_2} is the H_2 column density and I_{CO} is the velocity-integrated intensity of the CO $J = 1-0$ line.

In this section we present the emission from the CO $J = 1-0$ line, at a wavelength of 2.6 mm, in our simulations, computed using RADMC-3D. We use molecular CO data from the LAMDA database, including collisional excitation by ortho- and para- H_2 (Yang et al. 2010), for which we assume an ortho-to-para ratio of 3:1.

We show velocity-integrated line emission maps for the $J = 1-0$ line in Fig. 4.14 for different metallicities (top row) and different radiation fields (bottom row). In the galaxy with the lowest metallicity ($0.01 Z_{\odot}$; top left panel of Fig. 4.14), and in the run without self-shielding (bottom right panel), the CO intensity is very low, and would not be detectable. For comparison, for the CO observations of Local

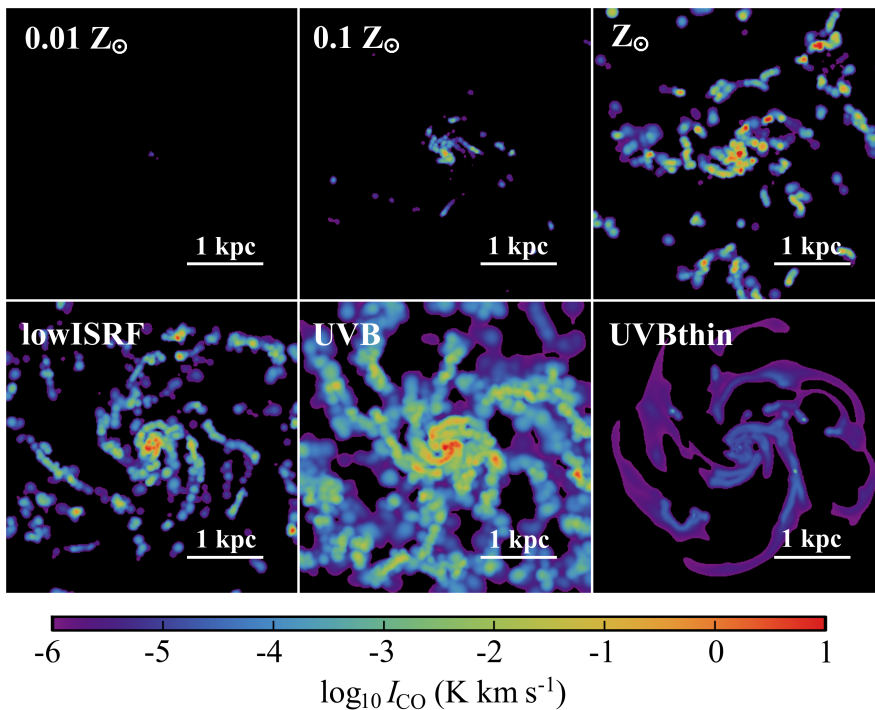


Figure 4.14: As Fig. 4.12, but for CO $J = 1 - 0$ line emission at 2.6 mm. CO emission increases with increasing metallicity and decreasing UV radiation field.

Group galaxies in Leroy et al. (2011), the 3σ CO intensity threshold for the Small Magellanic Cloud is 0.25 K km s^{-1} .

We see very weak CO emission in the lowest-metallicity run because there is less carbon and oxygen available to form CO. Additionally, there is less dust shielding at lower metallicity, which is needed to prevent the destruction of CO by photodissociation. Similarly, in the simulations run without self-shielding, we see little CO emission because photodestruction of CO is always efficient.

In the remaining galaxies, we see that the CO emission is concentrated in dense clumps along the spiral arms. Comparing panels in the top row, the CO intensity increases with increasing metallicity, while in the bottom left and bottom centre panels, the CO intensity increases with decreasing radiation field strength.

The ratio of the average CO line intensity assuming equilibrium to that using non-equilibrium abundances is shown by the red curves in Fig. 4.13. Non-equilibrium chemistry has a greater effect on line emission from CO than for CII. For example, in the simulations run in the presence of ten per cent of the Black (1987) ISRF at ten per cent solar metallicity (lowISRF, bottom left panel), the average CO line intensity computed in equilibrium is higher by a factor of ~ 4 than in non-equilibrium. We also see very large relative differences between equilib-

rium and non-equilibrium CO emission at the lowest metallicity ($0.01 Z_{\odot}$; top left panel), although we saw in Fig. 4.14 that the CO emission is very weak in this run, and would not be detectable in typical CO surveys.

These non-equilibrium trends in CO emission are not always in the same direction. For example, at solar metallicity (top right panel of Fig. 4.13), the average CO line intensity calculated by setting the abundances to equilibrium in post-processing ('NonEq_Eqm', solid red curve) is lower than in non-equilibrium by a factor of ~ 2 . This is opposite to the trend that we saw in the lowISRF run. We find that there are two competing non-equilibrium effects that act on the CO abundance, and hence on the CO intensity. Firstly, gas that is forming into molecular clouds takes a finite time to form CO. Such gas is underabundant in CO with respect to equilibrium. Secondly, when an existing molecular cloud is disrupted or destroyed, it takes a finite time for the CO in this gas to be destroyed. Hence, CO is overabundant in such gas.

Therefore, the effect of non-equilibrium chemistry on CO emission is not a simple one, as there are two competing effects, which depend crucially on the thermal history of the gas. Thus, non-equilibrium abundances can either increase or decrease the CO intensity.

In Fig. 4.15 we plot the H_2 column density of each pixel versus the velocity-integrated intensity of the CO $J = 1 - 0$ line. Each pixel in the emission line maps is 10 pc across, and the maps cover the central 4 kpc of the disc. We include ten snapshot outputs from each simulation, taken at intervals of 100 Myr. Many of the pixels have very low CO intensities that would be undetectable in a realistic survey of CO emission in extragalactic sources. We therefore only include pixels with a CO intensity $I_{CO} > 0.25 \text{ K km s}^{-1}$, which corresponds to the 3σ intensity threshold used by Leroy et al. (2011) for the Small Magellanic Cloud.

We show the $N_{H_2} - I_{CO}$ relation from simulations run with the full non-equilibrium chemical model for different metallicities in the top row, and for different UV radiation fields in the bottom row. We do not include the simulations run at one per cent solar metallicity or run without self-shielding, as these do not show detectable CO emission. The black line in each panel shows the linear relation between N_{H_2} and I_{CO} using the mean X_{CO} factor measured in the simulation, averaged over pixels with $I_{CO} > 0.25 \text{ K km s}^{-1}$.

In Fig. 4.15, we see that the mean X_{CO} factor increases with increasing radiation field strength, G_0 . For comparison, measurements of the X_{CO} factor in molecular clouds in the Milky Way, using various different methods (Virial mass, CO isotopologues, dust extinction or emission, diffuse gamma-ray emission), find $X_{CO,20} = X_{CO}/(10^{20} \text{ cm}^{-2} (\text{K km s}^{-1})^{-1}) \sim 2 - 4$ (e.g. Bolatto et al. 2013 and references therein). This trend with G_0 may arise because, in our simulations with different radiation fields (at $0.1 Z_{\odot}$), the dust extinction only extends up to $A_v \sim 1$. CO is therefore not fully shielded from photodissociation by dust in these simulations, whereas the molecular hydrogen can still become fully shielded, by self-shielding. Therefore, as G_0 increases, the CO intensity is suppressed more than the H_2 column density, and thus X_{CO} increases.

In Fig. 4.15, there is almost no dependence of X_{CO} on metallicity. This lack of dependence on metallicity may seem surprising, as observations find that X_{CO}

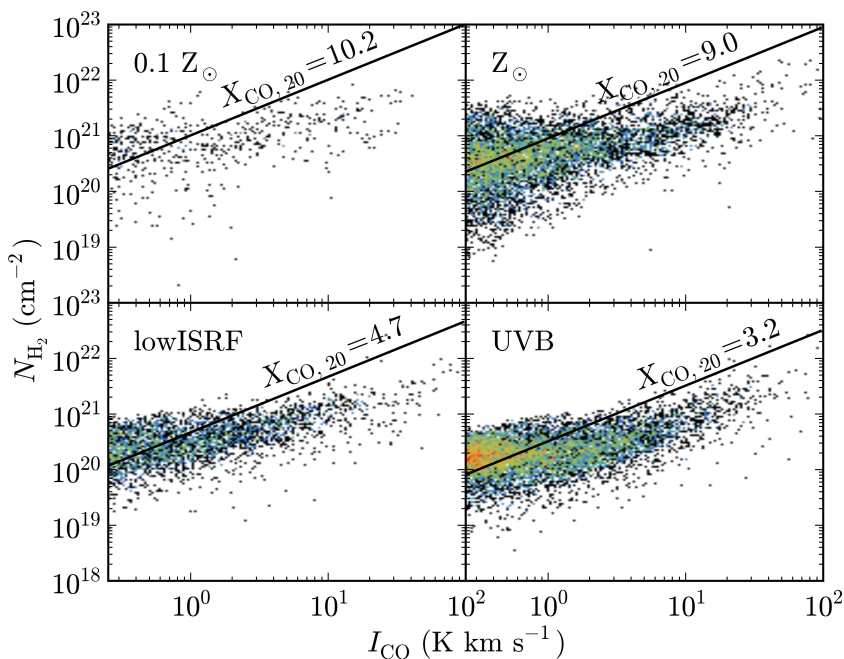


Figure 4.15: Relation between H_2 column density, N_{H_2} , and velocity-integrated intensity of the CO $J = 1 - 0$ line, I_{CO} , measured in pixels 10 pc across that span the central 4 kpc of the galaxy, viewing the disc face-on. We show simulations run with the full non-equilibrium chemical model at different metallicities (*top row*) and for different radiation fields (*bottom row*; see Table 4.1). We include ten snapshots from each simulation, taken at intervals of 100 Myr. Black lines show the linear $N_{\text{H}_2} - I_{\text{CO}}$ relation obtained using the mean X_{CO} factor from the given simulation, averaged over pixels with $I_{\text{CO}} > 0.25 \text{ K km s}^{-1}$. We express this mean conversion factor as $X_{\text{CO},20} = X_{\text{CO}} / (10^{20} \text{ cm}^{-2} (\text{K km s}^{-1})^{-1})$.

decreases with increasing metallicity (e.g. Israel 1997; Leroy et al. 2011). However, this apparent discrepancy is likely because our simulations at ten per cent solar metallicity only probe regions with dust extinctions $A_v \lesssim 1$, while the solar metallicity runs extend up to $A_v \sim 10$.

To understand the trends of the X_{CO} factor at different A_v , we can look at the model of Feldmann et al. (2012). They construct a model for X_{CO} as a function of metallicity, Z , radiation field, U , and dust extinction, A_v . They use H_2 and CO abundances from small-scale MHD simulations of the turbulent ISM from Glover & Mac Low (2011), which included a treatment for the non-equilibrium chemistry of H_2 and CO, although Feldmann et al. (2012) assume photodissociation equilibrium to determine the dependence of the CO abundance on U , as most of the simulations of Glover & Mac Low (2011) were run for only one radiation field. Feldmann et al. (2012) compute the CO line emission based on an escape probability formalism, assuming that the level populations of the CO molecule are in LTE and using an assumption for the CO line width (either a constant line width

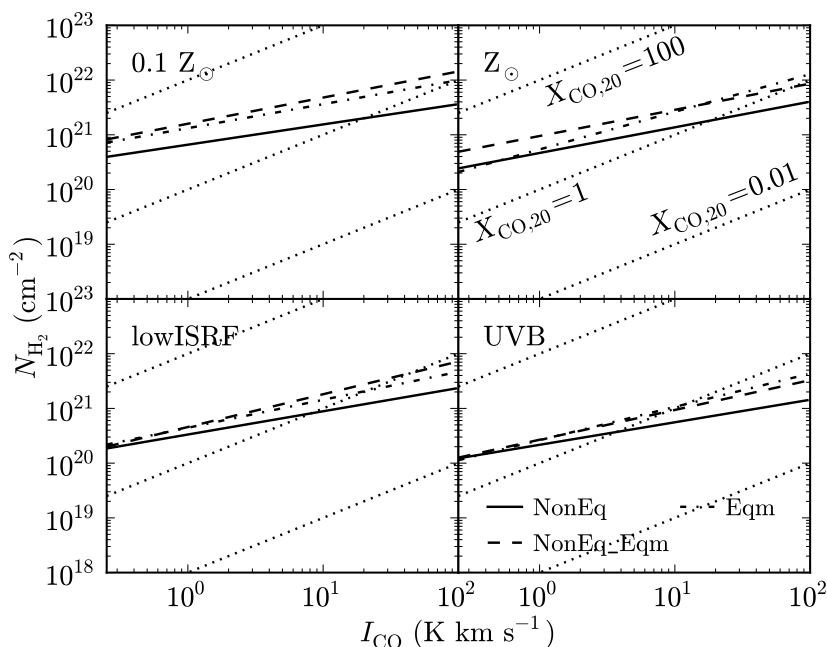


Figure 4.16: Best-fit power law relation between H_2 column density, N_{H_2} , and velocity-integrated intensity of the $\text{CO } J = 1 - 0$ line, I_{CO} , at different metallicities (*top row*) and for different radiation fields (*bottom row*; see Table 4.1). We use maps of N_{H_2} and I_{CO} computed from simulations evolved with the full non-equilibrium chemical model using non-equilibrium abundances (*NonEq*; solid curves) and with abundances set to equilibrium in post-processing (*NonEq_Eqm*; dashed curves), and from simulations evolved in chemical equilibrium (*Eqm*; dot-dashed curves). Dotted curves indicate lines of constant X_{CO} , as indicated in the top right panel. Each relation was fit to pixels with $I_{\text{CO}} > 0.25 \text{ K km s}^{-1}$.

or a virial scaling).

Feldmann et al. (2012) show the dependence of X_{CO} on A_v in their model for various Z and U (see their fig. 2). They show that X_{CO} reaches a minimum at $A_v \sim 2 - 10$, which approximately corresponds to where the CO line becomes optically thick. At A_v below this minimum (where the CO line is optically thin), they show that, at fixed A_v , X_{CO} increases with U (in agreement with our simulations), but is independent of Z .

In our simulations at solar metallicity, we probe regions up to $A_v \sim 10$. However, all our simulations at lower metallicities only extend up to $A_v \sim 1$. Therefore, it is likely that we do not recover the observed trends of X_{CO} with metallicity because we do not cover a range of metallicities in the optically thick regime.

The X_{CO} conversion factor between CO intensity and H_2 column density, as defined in equation 4.22, may also be affected by non-equilibrium chemistry, which affects both the CO emission (as seen in Fig. 4.13) and the abundance of H_2 (as seen in Fig. 4.11). Fig. 4.16 compares the best-fit power-law relation between

Simulation	$X_{\text{CO}}/10^{20}\text{cm}^{-2}(\text{K km s}^{-1})^{-1}$		
	NonEq	NonEq_Eqm	Eqm
ref	10.2	23.9	23.0
hiZ	9.0	23.4	13.6
lowISRF	4.7	5.9	6.6
UVB	3.2	3.5	3.3

Table 4.3: Mean X_{CO} factor, averaged over pixels with a velocity-integrated CO line intensity $I_{\text{CO}} > 0.25 \text{ K km s}^{-1}$.

N_{H_2} and I_{CO} from the non-equilibrium simulations (‘NonEq’; solid curves) to those from the same simulations with abundances set to equilibrium in post-processing (‘NonEq_Eqm’; dashed curves), and from simulations evolved in chemical equilibrium (‘Eqm’; dot-dashed curves). Dotted curves indicate lines of constant X_{CO} . The top and bottom rows show different metallicities and UV radiation fields respectively. Each curve was fit to pixels with $I_{\text{CO}} > 0.25 \text{ K km s}^{-1}$.

The best-fit relations in Fig. 4.16 have power-law slopes of $\sim 0.4 - 0.6$. This is flatter than the linear relation that we would expect for a constant X_{CO} factor, and indicates that X_{CO} decreases as I_{CO} increases.

The $N_{\text{H}_2} - I_{\text{CO}}$ relations calculated using non-equilibrium abundances (solid curves) are lower than those calculated in equilibrium. Table 4.3 summarises the mean X_{CO} factors from each simulation, averaged over pixels with $I_{\text{CO}} > 0.25 \text{ K km s}^{-1}$.

In the presence of the Black (1987) ISRF (ref and hiZ), we find that the mean X_{CO} factor decreases by a factor ~ 2.3 when we use non-equilibrium abundances. At lower radiation field strengths (lowISRF and UVB), the effect of non-equilibrium chemistry on the mean X_{CO} factor is much smaller (e.g. 10 per cent in the UVB runs). Nevertheless, we saw in Fig. 4.13 that the mean CO intensity for weaker radiation fields is lower, by a factor of ~ 4 , when we use non-equilibrium abundances than in equilibrium. We also find fewer pixels with I_{CO} above the detection threshold of 0.25 K km s^{-1} when we use non-equilibrium abundances in these examples.

If we find fewer pixels with detectable CO emission when we use non-equilibrium abundances, we might also expect this to have an impact on the fraction of CO-dark molecular gas, i.e. molecular hydrogen that is not traced by CO emission (e.g. Tielens & Hollenbach 1985; van Dishoeck & Black 1988; Wolfire et al. 2010; Smith et al. 2014). In the two simulations run with the lowest radiation fields (lowISRF and UVB), we find that the mass of H_2 in pixels with $I_{\text{CO}} < 0.25 \text{ K km s}^{-1}$ is almost unaffected by non-equilibrium abundances. For example, in the lowISRF run, we find $M_{\text{H}_2}(I_{\text{CO}} < 0.25 \text{ K km s}^{-1}) = 1.0 \times 10^7 M_{\odot}$ using non-equilibrium abundances, compared to $1.1 \times 10^7 M_{\odot}$ when we set the abundances to equilibrium. However, the total mass of H_2 in all pixels is a factor $\sim 1.5 - 2$ lower using non-equilibrium abundances. We thus find that the fraction of H_2 that is CO-dark is ~ 80 per cent in these two simulations when we use non-equilibrium abundances, compared to ~ 50 per cent in equilibrium.

4.5 Conclusions

We have run a series of hydrodynamic simulations of isolated galaxies with a virial mass $M_{200,\text{crit}} = 10^{11} M_{\odot}$ and stellar mass $10^9 M_{\odot}$. The models use a resolution of $750 M_{\odot}$ per gas particle and a gravitational force resolution of 3.1 pc, and were run with a modified version of the SPH code GADGET3. We included a treatment for the full non-equilibrium chemical evolution of ions and molecules (157 species in total), along with gas cooling rates computed self-consistently from these non-equilibrium abundances (Richings et al. 2014a,b), and we compared these to simulations evolved using cooling rates in chemical equilibrium.

Our simulations were run at a fixed metallicity and in the presence of a uniform UV radiation field, with a local prescription for self-shielding by gas and dust. We covered a wide range of metallicities ($0.01 Z_{\odot}$, $0.1 Z_{\odot}$ and Z_{\odot}), and different UV radiation fields that span nearly three orders of magnitude in H I photoionisation rate (the Black (1987) ISRF, ten per cent of the Black (1987) ISRF, and the redshift zero UVB of Haardt & Madau (2001); see Table 4.1), and we also repeated the runs with the Haardt & Madau (2001) UVB without self-shielding.

Our goal was to investigate the effects of metallicity, radiation field and non-equilibrium chemistry, which have all been demonstrated to affect gas cooling rates, in simulations of galaxy evolution. There are two aspects to the impact of these effects. Firstly, how the changes in gas cooling rates affect the evolution of the galaxy, and secondly, how observable tracers of individual chemical species are affected.

Our main results are as follows:

- (i) In simulations at higher metallicity, and for weaker UV radiation fields, gas can more easily cool to a cold ($T \sim 100$ K), star forming ISM phase, due to increased metal-line cooling and reduced UV heating respectively. We thus find higher star formation rates in these cases, by two orders of magnitude and a factor ~ 3 for the different metallicities and different radiation fields, respectively, that we consider here (Fig. 4.4). In particular, the gas surface density threshold below which star formation is cut off decreases with increasing metallicity and decreasing UV radiation field (Fig. 4.3), as predicted by Schaye (2004).
- (ii) We find higher mass outflow rates at higher metallicity (by two orders of magnitude) and for weaker radiation fields (by a factor ~ 3), due to the higher star formation rates (Fig. 4.5). However, the average mass loading factor (i.e. the ratio of outflow to star formation rates), measured at $0.2R_{200,\text{crit}} = 19$ kpc, is ~ 10 , regardless of metallicity or radiation field.
- (iii) The mass loading factor, β , measured 1 kpc above and below the disc decreases with increasing gas surface density, Σ_{gas} , following approximately a power-law, $\beta \propto \Sigma_{\text{gas}}^{-2}$ (Fig. 4.6). At fixed Σ_{gas} , the mass loading factor increases with decreasing metallicity and increasing radiation field strength.
- (iv) Non-equilibrium cooling does not strongly affect the total star formation rate of the galaxy (Fig. 4.4). The initial rise in mass outflow rate in the first

~ 200 Myr of the simulation is sometimes more gradual when we use equilibrium cooling, compared to the non-equilibrium runs (Fig. 4.5). However, apart from this initial difference, non-equilibrium cooling does not strongly affect the outflow properties.

- (v) Non-equilibrium chemistry does have a large effect on the chemical make-up of outflowing gas (Fig. 4.7). For example, in our reference run (black curves in Fig. 4.7), we find on average $600 M_{\odot}$ of H_2 outflowing with a vertical velocity of $> 50 \text{ km s}^{-1}$ if we use non-equilibrium abundances, compared to $30 M_{\odot}$ if we assume chemical equilibrium. Non-equilibrium chemistry therefore enhances the mass of outflowing H_2 by a factor ~ 20 in this example. This has important implications for modelling molecular outflows in hydrodynamic simulations of galaxies.
- (vi) We investigated where in the temperature-density plane molecular hydrogen is out of equilibrium (Fig. 4.11). H_2 can be enhanced, by up to six orders of magnitude, in gas that was previously in molecular clouds at higher densities but has since been disrupted. We also find regions, around $n_H \sim 10\text{--}100 \text{ cm}^{-3}$, where H_2 is underabundant, by up to an order of magnitude. This is due to gas that is starting to form molecular clouds, but has not yet had enough time to fully form H_2 .
- (vii) Using the publicly available Monte-Carlo radiative transfer code `RADMC-3D`⁸, we performed radiative transfer calculations on our simulations in post-processing to compute the line emission from CII and CO. CII emission from the $158 \mu\text{m}$ line is stronger at higher metallicity and for stronger radiation fields (Fig. 4.12), while CO emission from the $J = 1 - 0$ line is stronger at higher metallicity and for weaker radiation fields (Fig. 4.14).
- (viii) CII emission is generally unaffected by non-equilibrium chemistry, whereas CO emission is affected by a factor of $\sim 2 - 4$ (Fig. 4.13). However, the CO emission can be either higher or lower in non-equilibrium, since, similarly to H_2 , the CO abundance can be either enhanced or suppressed. This also affects the mean X_{CO} conversion factor between CO line intensity and H_2 column density (equation 4.22) that we measure in the simulations, by up to a factor ~ 2.3 (Table. 4.3).
- (ix) Non-equilibrium chemistry also affects the fraction of CO-dark molecular gas (e.g. Tielens & Hollenbach 1985; van Dishoeck & Black 1988; Wolfire et al. 2010; Smith et al. 2014), i.e. the fraction of molecular hydrogen that is not traced by observable CO emission. For example, in our ‘lowISRF’ run, we find ~ 80 per cent of the H_2 mass in the central 4 kpc of the disc lies in pixels with $I_{CO} < 0.25 \text{ K km s}^{-1}$ if we use non-equilibrium abundances, compared to ~ 50 per cent if we assume chemical equilibrium.

To summarise, we have demonstrated that metallicity and UV radiation affect the global properties of galaxies, such as their star formation rates, and the observ-

⁸<http://www.ita.uni-heidelberg.de/~dullemond/software/radmc-3d/>

able signatures of individual chemical species. In contrast, non-equilibrium chemistry and cooling generally do not strongly affect the global properties of galaxies, although they do affect the observable diagnostics, particularly in molecular gas.

However, there are several important caveats that we need to highlight that may mean that we have underestimated the importance of non-equilibrium chemistry in these simulations. Firstly, we simulate isolated galaxies that do not include cosmological processes such as galaxy mergers and accretion of gas onto the galaxy. We might expect that such processes could enhance the non-equilibrium effects. For example, during and immediately after a merger, the ISM will evolve rapidly as it re-distributes its gas in the temperature-density plane. This could potentially drive chemical abundances further out of equilibrium. To investigate the importance of such processes for the chemistry, we could repeat this study using cosmological zoomed simulations of individual galaxy haloes.

Secondly, turbulence in the ISM can also drive chemical abundances out of equilibrium. For example, Gray et al. (2015) recently presented a series of high-resolution simulations of the turbulent ISM. They showed that the steady-state ion abundances at the end of their simulations can be out of equilibrium by several orders of magnitude at high Mach numbers. If, as expected, we do not fully resolve such small-scale turbulence in our simulations, then we are likely to underestimate the importance of non-equilibrium chemistry.

Thirdly, chemical abundances can also be driven out of equilibrium by a fluctuating radiation field. For example, Oppenheimer & Schaye (2013b) demonstrated that the abundances of metal ions in the circumgalactic medium can be affected by the presence of an AGN even after the AGN has turned off, as it takes a long time for the ions to recombine. In our simulations, we apply a local prescription for self-shielding of the radiation field by gas and dust, which does vary with position and time. However, we apply the self-shielding to a constant, uniform radiation field. In reality, the UV radiation from young stars will fluctuate as new stars are born, existing stars age and gas particles move in relation to the stars. This may drive additional non-equilibrium effects that we do not capture in our current simulations.

Furthermore, since we have shown that UV radiation affects the global properties of galaxies, the inclusion of a fluctuating radiation field will also influence the galaxy directly, in addition to any non-equilibrium effects that it may drive. Likewise, it will also be important to include fluctuations in metallicity due to chemical enrichment from stars, which are not included in the fixed-metallicity models that we present here.

Acknowledgments

We are very grateful to Volker Springel for sharing GADGET3 and his initial conditions code, and to Claudio Dalla Vecchia for allowing us to use ANARCHY. We thank everyone who has contributed to the development of the EAGLE code, which our simulations were partly based on, and we thank Rob Crain and Benjamin Oppenheimer for useful discussions. We gratefully acknowledge support from the

European Research Council under the European Union's Seventh Framework Programme (FP7/2007-2013) / ERC Grant agreement 278594-GasAroundGalaxies. This work used the DiRAC Data Centric system at Durham University, operated by the Institute for Computational Cosmology on behalf of the STFC DiRAC HPC Facility (www.dirac.ac.uk). This equipment was funded by BIS National E-infrastructure capital grant ST/K00042X/1, STFC capital grant ST/H008519/1, and STFC DiRAC Operations grant ST/K003267/1 and Durham University. DiRAC is part of the National E-Infrastructure. This work also used computer resources provided by the Gauss Centre for Supercomputing/Leibniz Supercomputing Centre under grant: pr83le. We further acknowledge PRACE for awarding us access to resource Supermuc based in Germany at LRZ Garching (proposal number 2013091919).

References

- Baan W. A., Haschick A. D., Henkel C., 1989, *ApJ*, 346, 680
Bakes E. L. O., Tielens A. G. G. M., 1994, *ApJ*, 427, 822
Barinova G., van Hemert M. C., Krems R., Dalgarno A., 2005, *ApJ*, 620, 537
Beirão P. et al., 2012, *ApJ*, 751, 144
Black J. H., Dalgarno A., 1977, *ApJS*, 34, 405
Bigiel F., Leroy A., Walter F., Brinks E., de Blok W. J. G., Madore B., Thornley M. D., 2008, *AJ*, 136, 2846
Black J. H., 1987, *ASSL*, 134, 731
Bolatto A. D., Leroy A. K., Rosolowsky E., Walter F., Blitz L., 2008, *ApJ*, 686, 948
Bolatto A. D. et al., 2011, *ApJ*, 741, 12
Bolatto A. D., Wolfire M., Leroy A. K., 2013, *ARA&A*, 51, 207
Brauhar J. R., Dale D. A., Helou G., 2008, *ApJS*, 178, 280
Burton M. G., Hollenbach D. J., Tielens A. G. G. M., 1990, *ApJ*, 365, 620
Cazaux S., Tielens A. G. G. M., 2002, *ApJ*, 575, L29
Chabrier G., 2003, *PASP*, 115, 763
Chiosi C., Bertelli G., Bressan A., 1992, *ARA&A*, 30, 235
Crain R. A. et al., 2009, *MNRAS*, 399, 1773
Creasey P., Theuns T., Bower R. G., 2013, *MNRAS*, 429, 1922
Croxall K. V. et al., 2012, *ApJ*, 747, 81
Cullen L., Dehnen W., 2010, *MNRAS*, 408, 669
Dalla Vecchia C., Schaye J., 2012, *MNRAS*, 426, 140
Dobbs C. L., Glover S. C. O., Clark P. C., Klessen R. S., 2008, *MNRAS*, 389, 1097
Duarte-Cabral A., Acreman D. M., Dobbs C. L., Mottram J. C., Gibson S. J., Brunt C. M., Douglas K. A., 2015, *MNRAS*, 447, 2144
Duffy A. R., Schaye J., Kay S. T., Dalla Vecchia C., 2008, *MNRAS*, 390, 64
Durier F., Dalla Vecchia C., 2012, *MNRAS*, 419, 465
Efstathiou G., 1992, *MNRAS*, 256, 43
Emonts B. H. C. et al., 2014, *A&A*, 572, 40
Feldmann R., Gnedin N. Y., Kravtsov A. V., 2012, *ApJ*, 747, 124
Ferland G. J. et al., 2013, *RMxAA*, 49, 137

- Flower D. R., Le Bourlot J., Pineau des Forêts G., Roueff E., 2000, *MNRAS*, 314, 753
- Furlanetto S. R., Stoever S. J., 2010, *MNRAS*, 404, 1869
- Geach J. E. et al., 2014, *Nature*, 516, 68
- Glover S. C. O., Jappsen A.-K., 2007, *ApJ*, 666, 1
- Glover S. C. O., Abel T., 2008, *MNRAS*, 388, 1627
- Glover S. C. O., Federrath C., Mac Low M.-M., Klessen R. S., 2010, *MNRAS*, 404, 2
- Glover S. C. O., Mac Low M.-M., 2011, *MNRAS*, 412, 337
- Glover S. C. O., Clark P. C., 2012, *MNRAS*, 426, 377
- Glover S. C. O., Clark P. C., 2014, *MNRAS*, 437, 9
- Gnat O., Sternberg A., 2007, *ApJS*, 168, 213
- Gnedin N. Y., Tassis K., Kravtsov A. V., 2009, *ApJ*, 697, 55
- Gnedin N. Y., Kravtsov A. V., 2011, *ApJ*, 728, 88
- Goldsmith P., Langer W. D., 1978, *ApJ*, 222, 881
- Gracia-Carpio J. et al., 2011, *ApJ*, 728, L7
- Gray W. J., Scannapieco E., Kasen D., 2015, *ApJ*, 801, 107
- Haardt F., Madau P., 2001, in Neumann D. M., Tran J. T. V., eds, *XXIst Moriond Astrophys. Meeting, Clusters of Galaxies and the High Redshift Universe Observed in X-rays Editions Frontieres*, Paris, 64
- Habing H. J., 1968, *Bull. Astron. Inst. Netherlands*, 19, 421
- Helfer T. T., Thornley M. D., Regan M. W., Wong T., Sheth K., Vogel S. N., Blitz L., Bock D. C.-J., 2003, *ApJS*, 145, 259
- Hernquist L., 1990, *ApJ*, 356, 359
- Hollenbach D., McKee C. F., 1979, *ApJS*, 41, 555
- Hopkins P. F., Quataert E., Murray N., 2011, *MNRAS*, 417, 950
- Hopkins P. F., Quataert E., Murray N., 2012, *MNRAS*, 421, 3522
- Hopkins P. F., 2013, *MNRAS*, 428, 2840
- Hopkins P. F., Kereš D., Oñorbe J., Faucher-Giguère C.-A., Quataert E., Murray N., Bullock J. S., 2014, *MNRAS*, 445, 581
- Israel F. P., 1997, *A&A*, 328, 471
- Jaquet R., Staemmler V., Smith M. D., Flower D. R., 1992, *J. Phys. B*, 25, 285
- Kafatos M., 1973, *ApJ*, 182, 433
- Karpas Z., Anicich V., Huntress W. T., 1979, *J. Chem. Phys.* 70, 2877
- Katz N., Hernquist L., Weinberg D. H., 1992, *ApJ*, 399, L109
- Katz N., Weinberg D. H., Hernquist L., 1996, *ApJS*, 105, 19
- Kennicutt R. C., Jr., 1998, *ApJ*, 498, 541
- Kennicutt R. C., Jr. et al., 2011, *PASP*, 123, 1347
- Krumholz M. R., McKee C. F., Tumlinson J., 2008, *ApJ*, 689, 865
- Krumholz M. R., McKee C. F., Tumlinson J., 2009, *ApJ*, 693, 216
- Krumholz M. R., Gnedin N. Y., 2011, *ApJ*, 729, 36
- Krumholz M. R., 2012, *ApJ*, 759, 9
- Krumholz M. R., Dekel A., McKee C. F., 2012, *ApJ*, 745, 69
- Kuno N. et al., 2007, *PASJ*, 59, 117
- Langer W. D., 1978, *ApJ*, 225, 860
- Launay J. M., Le Dourneuf M., Zeppen C. J., 1991, *A&A*, 252, 842

- Leon S. et al., 2007, *A&A*, 473, 747
Leroy A. K. et al., 2009, *AJ*, 137, 4670
Leroy A. K. et al., 2011, *ApJ*, 737, 12
Lique F., Werfelli G., Halvick P., Stoecklin T., Faure A., Wiesenfeld L., Dagdigian P. J., 2013, *JChPh*, 138, 204314
Lotz W., 1967, *ApJS*, 14, 207
Malhotra S. et al., 2001, *ApJ*, 561, 766
Martin P. G., Whittet D. C. B., 1990, *ApJ*, 357, 113
Mathis J. S., Rumpl W., Nordsieck K. H., 1977, *ApJ*, 217, 425
McElroy D., Walsh C., Markwick A. J., Cordiner M. A., Smith K., Millar T. J., 2013, *A&A*, 550, 36
McKee C. F., Krumholz M. R., 2010, *ApJ*, 709, 308
Moster B. P., Naab T., White S. D. M., 2013, *MNRAS*, 428, 3121
Navarro J. F., Frenk C. S., White S. D. M., 1996, *ApJ*, 462, 563
Oppenheimer B. D., Schaye J., 2013a, *MNRAS*, 434, 1043
Oppenheimer B. D., Schaye J., 2013b, *MNRAS*, 434, 1063
Pelupessy F. I., Papadopoulos P. P., 2009, *ApJ*, 707, 954
Portinari L., Chiosi C., Bressan A., 1998, *A&A*, 334, 505
Price D. J., 2008, *J. Comput. Phys.*, 227, 10040
Rémy-Ruyer A. et al., 2014, *A&A*, 563, 31
Richings A. J., Schaye J., Oppenheimer B. D., 2014a, *MNRAS*, 440, 3349
Richings A. J., Schaye J., Oppenheimer B. D., 2014b, *MNRAS*, 442, 2780
Robertson B. E., Kravtsov A. V., 2008, *ApJ*, 680, 1083
Sakamoto K. et al., 2009, *ApJ*, 700, L104
Saslaw W. C., Zipoy D., 1967, *Nature*, 216, 976
Sawala T. et al., 2015, *MNRAS*, 448, 2941
Schaye J., 2001, *ApJ*, 562, L95
Schaye J., 2004, *ApJ*, 609, 667
Schaye J., Dalla Vecchia C., 2008, *MNRAS*, 383, 1210
Schaye J. et al., 2010, *MNRAS*, 402, 1536
Schaye J. et al., 2015, *MNRAS*, 446, 521
Schöier F. L., van der Tak F. F. S., van Dishoeck E. F., Black J. H., 2005, *A&A*, 432, 369
Shetty R., Glover S. C., Dullemond C. P., Klessen R. S., 2011, *MNRAS*, 412, 1686
Silk J., 1970, *ApL*, 5, 283
Smith R. J., Glover S. C. O., Clark P. C., Klessen R. S., Springel V., 2014, *MNRAS*, 441, 1628
Sobolev V. V., 1957, *SvA*, 1, 678
Springel V., 2005, *MNRAS*, 364, 1105
Springel V., Di Matteo T., Hernquist L., 2005, *MNRAS*, 361, 776
Sternberg A., Le Petit F., Roueff E., Le Bourlot J., 2014, *ApJ*, 790, 10
Sturm E. et al., 2011, *ApJ*, 733, L16
Sutherland R. S., Dopita M. A., 1993, *ApJS*, 88, 253
Tielens A. G. G. M., Hollenbach D., 1985, *ApJ*, 291, 722
van Dishoeck E. F., Black J. H., 1988, *ApJ*, 334, 771
van Dishoeck E. F., Jonkheid B., van Hemert M. C., 2006, *Faraday Discuss.*, 133,

231

- Vasiliev E. O., 2013, MNRAS, 431, 638
Visser R., van Dishoeck E. F., Black J. H., 2009, A&A, 503, 323
Walch S., Wünsch R., Burkert A., Glover S., Whitworth A., 2011, ApJ, 733, 47
Walter F., Weiss A., Scoville N., 2002, ApJ, 580, L21
Wendland H., 1995, Adv. Comput. Math. 4, 389
Wiersma R. P. C., Schaye J., Smith B. D., 2009, MNRAS, 393, 99
Wiesenfeld L., Goldsmith P. F., 2014, ApJ, 780, 183
Williams J. P., Bergin E. A., Caselli P., Myers P. C., Plume, R., 1998, ApJ, 503, 689
Wilson N. J., Bell K. L., 2002, MNRAS, 337, 1027
Wolfire M. G., Hollenbach D., McKee C. F., Tielens A. G. G. M., Bakes E. L. O., 1995, ApJ, 443, 152
Wolfire M. G., McKee C. F., Hollenbach D., Tielens A. G. G. M., 2003, ApJ, 587, 278
Wolfire M. G., Hollenbach D., McKee C. F., 2010, ApJ, 716, 1191
Yang B., Stancil P. C., Balakrishnan N., Forrey R. C., 2010, ApJ, 718, 1062

CHEMICAL EVOLUTION OF GIANT MOLECULAR CLOUDS IN SIMULATIONS OF GALAXIES

We present an analysis of Giant Molecular Clouds (GMCs) identified in hydrodynamic simulations of isolated disc galaxies, with a particular focus on the evolution of molecular abundances and the implications for CO emission and the X_{CO} conversion factor in individual clouds. We define clouds either as regions above a density threshold $n_{\text{H},\text{min}} = 10 \text{ cm}^{-3}$, or using an observationally motivated velocity-integrated CO line intensity threshold of 0.25 K km s^{-1} . Our simulations include a non-equilibrium treatment for the chemistry of 157 species, including 20 molecules. We find cloud lifetimes up to $\approx 40 \text{ Myr}$, with a median of 13 Myr , in agreement with observations. At ten per cent solar metallicity, young clouds ($\lesssim 10 - 15 \text{ Myr}$) tend to be underabundant in H_2 and CO compared to chemical equilibrium, by factors of ≈ 3 and $1 - 2$ orders of magnitude, respectively. At solar metallicity, GMCs reach chemical equilibrium faster (within $\approx 1 \text{ Myr}$), due to a higher formation rate of H_2 on dust grains. We also compute CO $J = 1 - 0$ line emission from our simulated GMCs in post-processing. We find that the mean CO intensity, I_{CO} , is strongly suppressed at low dust extinction, A_v , and possibly saturates towards high A_v , in agreement with observations. Our simulated $I_{\text{CO}} - A_v$ relation shifts towards higher A_v for higher metallicities and, to a lesser extent, for stronger UV radiation fields. At ten per cent solar metallicity, we find weaker CO emission in young clouds ($\lesssim 10 - 15 \text{ Myr}$), consistent with the underabundance of CO in such clouds. This is reflected in the median X_{CO} factor, which decreases by an order of magnitude from 0 to 15 Myr, albeit with a large scatter.

Alexander J. Richings and Joop Schaye
To be submitted

5.1 Introduction

Molecular hydrogen is the main constituent of Giant Molecular Clouds (GMCs), making up most of their mass. However, cold H_2 is difficult to observe in emission, as the lowest rotational transition of the H_2 molecule has an excitation energy of $E/k_B = 510$ K (Dabrowski 1984). It is therefore difficult to excite H_2 at the cold temperatures typical of GMCs (~ 10 K).

CO is typically the next most abundant molecule in GMCs. It is also much easier to excite the rotational and vibrational levels of the CO molecule at low temperatures. For example, the lowest rotational transition of CO ($J = 1 - 0$) has an excitation energy of $E/k_B = 5.53$ K. CO emission is therefore commonly used as a tracer of molecular gas in GMCs (e.g. Solomon et al. 1987; Dame et al. 2001; Heyer et al. 2001). The velocity-integrated CO intensity, I_{CO} , is then converted to an H_2 column density, N_{H_2} , using a conversion factor X_{CO} , defined as:

$$X_{\text{CO}} = \frac{N_{\text{H}_2}}{I_{\text{CO}}} \text{ cm}^{-2} (\text{K km s}^{-1})^{-1}. \quad (5.1)$$

To accurately determine the molecular content of a GMC in this way, we therefore require a detailed understanding of the X_{CO} factor, including how it depends on the physical conditions in the GMC, such as its metallicity and the radiation field.

There have been many studies, both observational and theoretical, to determine the X_{CO} factor (see Bolatto et al. 2013 for a recent review). Observational studies use various methods to determine the total molecular content, which can then be compared to the CO emission to determine the X_{CO} factor. For example, virial techniques assume that the GMC is in virial equilibrium, which allows one to measure the total mass of a GMC from its size and velocity dispersion, which is assumed to be the molecular mass (e.g. Scoville et al. 1987; Solomon et al. 1987). Other studies estimate the dust content of GMCs, either by mapping the extinction towards background stars (e.g. Frerking et al. 1982; Lombardi et al. 2006; Pineda et al. 2008), or by measuring dust emission in the far-infrared (e.g. Dame et al. 2001; Planck Collaboration XIX 2011). This can then be converted into a total gas column density, assuming a dust-to-gas ratio. Diffuse gamma-ray emission arising from interactions between cosmic rays and nucleons can also be used to estimate the total gas column density (e.g. Strong & Mattox 1996; Abdo et al. 2010; Ackermann et al. 2012).

Some theoretical studies of the X_{CO} factor use models of photodissociation regions (PDRs), where a cloud of gas is illuminated from one side by an external UV radiation field. Tielens & Hollenbach (1985) use PDR models to determine the chemical and temperature structure of such clouds for various gas densities and radiation fields. van Dishoeck & Black (1988) and Visser et al. (2009) focus on the chemistry and photodissociation of CO in PDR models, and they use these models to determine how the CO column density varies with dust extinction. Sternberg et al. (2014) recently presented a detailed study of the H I -to- H_2 transition in clouds, using both analytic theory and numerical PDR models. These PDR models assume that the abundances of molecules and atoms are in chemical equilibrium, or a ‘steady state’, and that the clouds have a constant density profile.

These PDR models can then be used to study how the X_{CO} factor depends on the physical conditions. For example, Bell et al. (2006) use PDR models to explore how X_{CO} varies in different environments. They find that, at low dust extinction, A_v , X_{CO} decreases with increasing A_v , until it reaches a minimum and subsequently increases with A_v once the CO line becomes optically thick. They show that the $X_{\text{CO}} - A_v$ profile depends on cloud properties, including gas density, radiation field strength, metallicity and turbulent velocity dispersion.

Other theoretical studies of the X_{CO} factor use hydrodynamic simulations of a turbulent interstellar medium (ISM) to study the environmental dependence of the X_{CO} factor, which account for more realistic cloud geometries (e.g. Glover & Mac Low 2011; Shetty et al. 2011a,b; Clark & Glover 2015). Narayanan et al. (2011, 2012) combine hydrodynamic simulations of isolated and merging galaxies, using a subgrid model for cold gas below 10^4 K, with radiative transfer calculations of dust and molecular line emission to explore how galaxy mergers and the galactic environment affect the X_{CO} factor. Feldmann et al. (2012) combine the results of sub-parsec resolution simulations from Glover & Mac Low (2011) with gas distributions from the cosmological simulations of Gnedin & Kravtsov (2011) to model the X_{CO} factor, finding a metallicity dependence of X_{CO} (averaged over kpc scales) of $X_{\text{CO}} \propto Z^{-\gamma}$, where $\gamma \approx 0.5 - 0.8$.

Theoretical models of X_{CO} need to determine the abundances of CO and H_2 under various conditions. The simplest approach is to assume that these abundances are in chemical equilibrium (e.g. Narayanan et al. 2011, 2012). However, this assumption may not be valid if the formation time-scale of molecules is comparable to the lifetimes of GMCs, particularly in young clouds. Observational estimates have suggested a wide range of GMC lifetimes, from a few Myr (e.g. Elmegreen 2000), to $\approx 20 - 40$ Myr (e.g. Bash et al. 1977; Kawamura et al. 2009; Murray 2011; Miura et al. 2012), to hundreds of Myr (e.g. Scoville et al. 1979).

Bell et al. (2006) include time-dependent chemistry of H_2 and CO in their PDR models, with metallicities $0.01 \leq Z/Z_\odot \leq 1.0$, and they consider various cloud ages. They find significant evolution in the X_{CO} factor at times $\lesssim 1$ Myr, with less evolution for cloud ages 1 – 10 Myr, and no notable evolution beyond 10 Myr, even though it takes up to 100 Myr for the chemical abundances to reach steady-state in their models. Glover & Mac Low (2011) and Shetty et al. (2011a,b) also include time-dependent chemistry in their simulations of a turbulent ISM, with metallicities $0.03 \leq Z/Z_\odot \leq 1.0$ and $0.1 \leq Z/Z_\odot \leq 1.0$, respectively. However, since they include only a region of the ISM in their simulations, and not an entire galaxy, they may be missing some aspects of the evolution of GMCs in a galactic environment. Indeed, Dobbs & Pringle (2013) explore GMC evolution in simulations of isolated disc galaxies, with solar metallicity, and they find complex evolutionary histories. GMCs in their simulations often form by assembling from smaller clouds and ambient ISM material, or by breaking off from larger clouds, while they are dispersed by stellar feedback and shear, or are accreted onto larger clouds. It would therefore be useful to explore the chemical evolution of GMCs within a realistic galactic environment.

In this paper we investigate how the molecular abundances of GMCs evolve, and under what conditions these abundances are out of chemical equilibrium. We

consider the effects of cloud age, metallicity and the radiation field. We can then determine how the conditions affect the X_{CO} factor. We study clouds of dense gas ($n_{\text{H}} > 10 \text{ cm}^{-3}$) in the high-resolution Smoothed Particle Hydrodynamics (SPH) simulations of isolated disc galaxies presented in Richings & Schaye (2015), hereafter Paper I. These simulations include a treatment for the non-equilibrium chemistry of 157 species, including 20 different molecules (Richings et al. 2014a,b). We also run radiative transfer calculations on these simulations in post-processing to determine the $^{12}\text{CO } J = 1 - 0$ line emission¹ from individual GMCs, and hence compute their X_{CO} factors.

The remainder of this paper is organised as follows. In section 5.2 we summarise the simulations and initial conditions from paper I. In section 5.3 we describe the methods that we use to analyse GMCs in these simulations, including how we identify clouds, how we link clouds in previous and subsequent snapshots to identify their progenitors and descendants, and how we create maps of CO emission from individual clouds in post-processing. In section 5.4 we investigate the scaling relations of these clouds and compare them to observations. In section 5.5 we look at the H_2 and CO abundances of our simulated GMCs as a function of cloud age to explore their chemical evolution. In section 5.6 we use the CO $J = 1 - 0$ line emission from simulated clouds to investigate the X_{CO} factor, and we summarise our main results in section 5.7. Finally, in Appendix A we explore how our results are affected by the pressure floor that we impose in our simulations to ensure that the Jeans mass is always well-resolved.

5.2 Simulations

We study GMCs in the suite of hydrodynamic simulations of isolated disc galaxies that were first presented in paper I. The details of how these simulations were run, along with properties of the galaxies such as their star formation histories, outflow rates and velocities, can be found in paper I. Here we summarise the main features of these simulations.

The simulations were run using a modified version of the tree/SPH code GADGET3, last described in Springel (2005). The hydrodynamics solver has been replaced with the suite of hydrodynamical methods collectively known as ANARCHY, which incorporates many of the latest improvements on ‘classical’ SPH methods, including the pressure-entropy formulation of SPH, as derived by Hopkins (2013); a switch for artificial conduction, similar to the one used by Price (2008); a switch for artificial viscosity, from Cullen & Dehnen (2010); the time-step limiters from Durier & Dalla Vecchia (2012); and the C^2 Wendland (1995) kernel, for which we use 100 neighbours. ANARCHY will be described in more detail in Dalla Vecchia (in preparation); see also Appendix A of Schaye et al. (2015) for a full description of our version of ANARCHY.

¹For the remainder of this paper, we will use ‘CO’ to refer to ^{12}CO , unless stated otherwise.

5.2.1 Chemistry and subgrid models

We follow the chemical evolution of the abundances of ions and molecules in the gas using the chemical model of Richings et al. (2014a,b). This model includes all ionisation states of the 11 elements that contribute most to the cooling rate², along with 20 molecular species³, most importantly H₂ and CO. This gives us a chemical network of 157 species in total. The chemical species evolve via collisional ionisation, radiative and di-electronic recombination, charge transfer reactions, photoionisation (including Auger ionisation), cosmic ray ionisation (parameterised by an HI cosmic ray ionisation rate of $2.5 \times 10^{-17} \text{ s}^{-1}$; Williams et al. 1998), and various molecular reactions, including the formation of H₂ on dust grains (Cazaux & Tielens 2002) and in the gas phase.

The photoionisation, photoheating and photoelectric dust heating rates are computed assuming a constant, uniform UV radiation field, either the local interstellar radiation field (ISRF) of Black (1987), or ten per cent of this ISRF. We also use a self-shielding prescription to account for the attenuation of photochemical rates by dust and gas (Richings et al. 2014b). This prescription includes self-shielding of H₂ and CO, and shielding of CO by H₂. We assume that the shielding occurs locally, which allows us to express the column density of each particle as the density, ρ , multiplied by a local shielding length, L . For the shielding length, we use a local Sobolev-like approximation, $L = \rho/|2\nabla\rho|$ (e.g. Gnedin et al. 2009).

From the chemical network we obtain a system of 158 differential equations (157 chemical rate equations and the thermal equation for the temperature evolution), which we integrate for each gas particle over each hydrodynamic time-step using the implicit differential equation solver CVODE, from the SUNDIALS⁴ suite. This enables us to follow the non-equilibrium evolution of ion and molecule abundances, and also to evolve the temperature using cooling rates computed from these abundances, without needing to assume chemical equilibrium.

Gas particles are allowed to form stars if their hydrogen number density, n_{H} , exceeds a threshold of 1 cm^{-3} and their temperature is below 1000 K. If a particle meets these criteria, it forms stars at a rate per unit volume given by the gas density over the local free fall time, multiplied by an efficiency factor ϵ_{SF} , which we take to be 0.005. Gas particles are then stochastically converted into star particles according to a probability that is determined from the particle's star formation rate and the hydrodynamic time-step. The value of the efficiency, ϵ_{SF} (and the value of the heating temperature, ΔT , used in the stellar feedback model; see below) were chosen to reproduce the observed Kennicutt-Schmidt relation (see fig. 3 in paper I).

We include feedback from star formation using a thermal supernova prescription similar to that of Dalla Vecchia & Schaye (2012), with some modifications. As each star particle is treated as a simple stellar population (rather than an individual star), we can calculate the number of supernovae that explode from each star particle in a given time-step, using the stellar lifetimes of Portinari et al. (1998)

²H, He, C, N, O, Ne, Mg, Si, S, Ca, Fe

³H₂, H₂⁺, H₃⁺, OH, H₂O, C₂, O₂, HCO⁺, CH, CH₂, CH₃⁺, CO, CH⁺, CH₂⁺, OH⁺, H₂O⁺, H₃O⁺, CO⁺, HOC⁺, O₂⁺

⁴<https://computation.llnl.gov/casc/sundials/main.html>

and assuming a Chabrier (2003) initial mass function (IMF). When supernovae explode, their energy is injected into the gas thermally by stochastically selecting neighbouring gas particles to be heated by $\Delta T = 10^{7.5}$ K. By imposing a minimum heating temperature, we ensure that we minimise artificial radiative losses due to our finite resolution, which would otherwise make the stellar feedback unrealistically inefficient. The difference between our stellar feedback model and that of Dalla Vecchia & Schaye (2012) is that we distribute the total available supernova energy from each star particle over time, according to the lifetimes of massive stars, rather than injecting it all at 30 Myr after the birth of the star particle.

To ensure that the Jeans mass is always resolved, we impose a density-dependent pressure floor, P_{floor} , in the hydrodynamic equations, such that the Jeans mass will always be at least a factor $N_{\text{J,m}}$ times the mass within the SPH kernel. This is similar to the methods used by e.g. Robertson & Kravtsov (2008); Schaye & Dalla Vecchia (2008); Hopkins et al. (2011). The pressure floor is given by equation 2.12 of paper I:

$$P_{\text{floor, m}} = \left(\frac{36}{\pi^5}\right)^{1/3} \frac{G}{\gamma} (N_{\text{J, m}} N_{\text{ngb}}^{\text{SPH}} m_{\text{gas}})^{2/3} \rho^{4/3}, \quad (5.2)$$

where $\gamma = 5/3$ is the ratio of specific heats, $N_{\text{ngb}}^{\text{SPH}}$ is the number of SPH neighbours, m_{gas} is the mass per SPH particle, and ρ is the gas density. We use a conservative fiducial value of $N_{\text{J, m}} = 4$ in our simulations, but see Appendix A for the effects of lowering this pressure floor. We impose this Jeans limiter as a pressure floor rather than a temperature floor (as used by Schaye & Dalla Vecchia 2008) so that gas particles can continue to cool below the temperature corresponding to the pressure floor, and thus will evolve towards thermal and chemical equilibrium for the given density.

5.2.2 Initial conditions

We ran simulations of isolated disc galaxies using initial conditions based on the model of Springel et al. (2005). These initial conditions were generated using a modified version of a code that was kindly provided to us by Volker Springel. Each galaxy has a total mass within $R_{200, \text{crit}}$ (i.e. the radius enclosing 200 times the critical density) of $M_{200} = 10^{11} M_{\odot}$. The galaxies initially consist of a rotating disc of gas and stars and a central stellar bulge, embedded in a dark matter halo. The initial stellar mass is $M_* = 1.4 \times 10^9 M_{\odot}$, which is consistent with the abundance matching results of Moster et al. (2013) corrected for baryonic effects according to the prescription of Sawala et al. (2015). Twenty per cent of the initial stellar mass is in the bulge, with the remainder in the stellar disc. We use a gas mass fraction in the disc of 30 per cent, which gives an initial gas mass of $1.8 \times 10^8 M_{\odot}$.

The gas and stellar discs initially have an exponential surface density profile with a radial scale length of 2.0 kpc. The vertical structure of the stellar disc has an isothermal profile with a scale height of ten per cent of the radial scale length, while the gas is initially in chemical equilibrium with a constant temperature of 10^4 K and a vertical structure set up in hydrostatic equilibrium using an iterative

Model	M_{200} (M_{\odot})	c_{200}	$M_{*,\text{init}}$ (M_{\odot})	$M_{\text{gas,init}}$ (M_{\odot})	$f_{\text{d,gas}}$	m_{baryon} (M_{\odot})	ϵ_{soft} (pc)	Z (Z_{\odot})	UV Field
ref	10^{11}	8.0	1.4×10^9	4.8×10^8	0.3	750	3.1	0.1	ISRF ^a
hiZ	10^{11}	8.0	1.4×10^9	4.8×10^8	0.3	750	3.1	1.0	ISRF
lowISRF	10^{11}	8.0	1.4×10^9	4.8×10^8	0.3	750	3.1	0.1	10% ISRF

^aISRF of Black (1987)

Table 5.1: Properties of the galaxy simulations used in this paper: total mass M_{200} within the radius $R_{200,\text{crit}}$ enclosing a mean density of 200 times the critical density of the Universe at redshift zero, NFW concentration c_{200} of the dark matter halo, initial stellar mass $M_{*,\text{init}}$, initial gas mass $M_{\text{gas,init}}$, disc gas mass fraction $f_{\text{d,gas}}$, mass per gas or star particle m_{baryon} , gravitational softening length ϵ_{soft} , gas metallicity Z , and UV radiation field.

procedure. At this temperature, most of the hydrogen is in HII in chemical equilibrium. The stellar bulge has a Hernquist (1990) density profile, and the dark matter halo follows a Hernquist (1990) profile that is scaled to match a Navarro et al. (1996) (NFW) profile in the inner regions with a concentration $c_{200} = 8.0$, which agrees with the redshift zero mass-concentration relation of Duffy et al. (2008).

We use a resolution of $750 M_{\odot}$ per gas or star particle, with 100 SPH neighbours, and a gravitational softening length of 3.1 pc, and we model the dark matter halo using a static potential. Each simulation initially contains 6.45×10^5 gas particles and 1.88×10^6 star particles.

We include a constant, uniform UV radiation field, along with a local self-shielding prescription, and the gas metallicity is held fixed, with dust-to-gas mass ratios of $2.4 \times 10^{-3} Z/Z_{\odot}$ and $4.0 \times 10^{-3} Z/Z_{\odot}$ for graphite and silicate grain species, respectively. These dust-to-gas ratios were taken from the ‘ISM’ grain abundances used by the photoionisation code CLOUDY⁵ version 13.01 (Ferland et al. 2013), and we assume that they scale linearly with metallicity, Z .

In paper I, we ran six simulations with different combinations of metallicity and UV radiation field. Each simulation was repeated twice, once with the full non-equilibrium chemical model of Richings et al. (2014a,b), and once using cooling rates computed assuming chemical equilibrium. In this paper, we focus on three of these simulations: ref (ten per cent solar metallicity and the local ISRF of Black 1987), hiZ (solar metallicity and the Black 1987 ISRF), and lowISRF (ten per cent solar metallicity and ten per cent of the Black 1987 ISRF), all evolved using the full non-equilibrium chemical model. We focus on these as they are the most relevant for conditions in molecular clouds in low-mass galaxies. Of the three remaining simulations in paper I, lowZ (with one per cent solar metallicity) did not form dense clouds, as the gas was mostly unable to cool to a cold (~ 100 K) phase; UVB (evolved with the redshift zero UV background of Haardt & Madau 2001) used an extragalactic UV radiation field that is more relevant for the circum- and intergalactic medium than for molecular clouds; and UVBthin neglected self-shielding of UV radiation, which is necessary for the formation of molecules. The properties of our simulations are summarised in Table 5.1.

⁵<http://nublado.org/>

5.3 Analysis methods

In this section we describe the methods that we use to analyse gas clouds in our simulations, including the algorithm that we use to identify clouds (§5.3.1), how we link clouds to their progenitors and descendants to define their mass evolution (§5.3.2), and how we create maps of CO emission from individual clouds (§5.3.3).

5.3.1 Clump finding algorithm

Observationally, molecular clouds are typically identified as regions detected in emission from a molecular tracer (often CO) above an intensity threshold (e.g. Larson 1981; Solomon et al. 1987). This is approximately equivalent to selecting regions above a molecular gas surface density threshold. However, as we are interested in the atomic to molecular transition, we do not want to select only clouds that are already molecular. We therefore need a criterion that is based on the total gas content, and not just on the molecular content.

Furthermore, Dobbs et al. (2015) found that using a grid-based approach to identify clouds above a surface density threshold in simulations can create problems for studying the cloud evolution. They found that clouds that are identified with such a method appear to evolve on shorter time-scales than is seen in the three-dimensional particle distribution. These errors arise due to the projection onto a two-dimensional grid, as the gas moves relative to the grid.

We therefore base our clump finding algorithm on the particle-based approach used by Dobbs et al. (2015). This is a Friends-of-Friends (FoF) algorithm that acts on dense gas particles. We first select gas particles with a hydrogen number density, n_{H} , above a threshold $n_{\text{H},\text{min}}$. We then link together nearby dense particles by taking each particle in turn and identifying particles that lie within a linking length, l .

There are two parameters in this method, $n_{\text{H},\text{min}}$ and l . However, as noted by Dobbs et al. (2015), they are degenerate, as denser particles will be closer together. We use a density threshold of $n_{\text{H},\text{min}} = 10 \text{ cm}^{-3}$, which is comparable to (or slightly lower than) the density at which we expect the transition from atomic to molecular hydrogen to occur (e.g. Schaye 2001; Gnedin et al. 2009). This ensures that we focus on clouds that are likely to become molecular. We then use a linking length $l = 10 \text{ pc}$, which corresponds approximately to the mean spacing between gas particles at the density threshold, $n_{\text{H},\text{min}}$, for our resolution of $750 M_{\odot}$ per particle.

Fig. 5.1 shows maps of the gas surface density in each of our three simulations after 500 Myr. Each map is 8 kpc across and views the disc face-on. We also zoom in (by a factor 13) on the six most massive clouds in each simulation. We see that these clouds show a wide range of morphologies. Some are approximately spherical, while others have been stretched into long, thin filaments by shear in the rotating disc. We also see some clouds with two or more density peaks, which suggests that they consist of multiple clumps that are in the process of merging.

Fig. 5.2 shows the cloud mass functions for each simulation. Here we have identified clouds in snapshots at 100 Myr intervals, from 100 Myr to 900 Myr, and

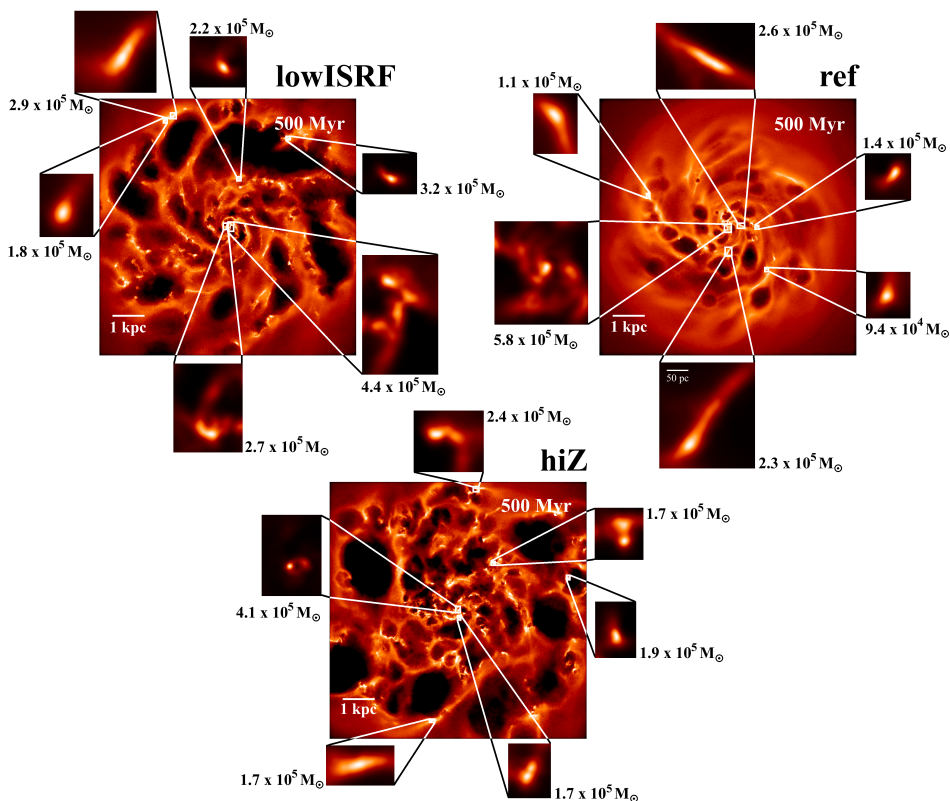


Figure 5.1: Maps of gas surface density after 500 Myr from simulations lowISRF ($0.1 Z_{\odot}$, ten per cent of the Black (1987) ISRF; top left), ref ($0.1 Z_{\odot}$, Black (1987) ISRF; top right) and hiZ (Z_{\odot} , Black (1987) ISRF; bottom). Each map is 8 kpc across and views the disc of the galaxy face-on. We also zoom in (by a factor 13) on the most massive clouds in each simulation, and we give the mass of dense gas (with $n_{\text{H}} \geq 10 \text{ cm}^{-3}$) in each cloud. We see a wide range of morphologies, including nearly spherical clouds, clouds that have been sheared into long filaments, and clouds with multiple density peaks that are indicative of cloud mergers.

combined the different snapshots into a single mass function for each simulation. We will show in the next section that the clouds have lifetimes < 100 Myr if we define lifetimes using the particles originally in the cloud when it is identified, so we do not double-count cloud mass by combining snapshots in this way. However, if we follow the total mass of cloud progenitors/descendants, we find that individual cloud structures can survive for > 100 Myr, although new gas has cycled through them. Such long-lived cloud structures will appear multiple times in Fig. 5.2.

All three simulations show similar cloud mass functions. For the remainder of this study, we shall focus on clouds that contain at least 50 gas particles to avoid poorly resolved clouds in our analysis (but see Appendix A for the effects of the pressure floor on low-mass clouds). This corresponds to a mass of $3.75 \times 10^4 M_{\odot}$, shown by the vertical dotted line in Fig. 5.2.

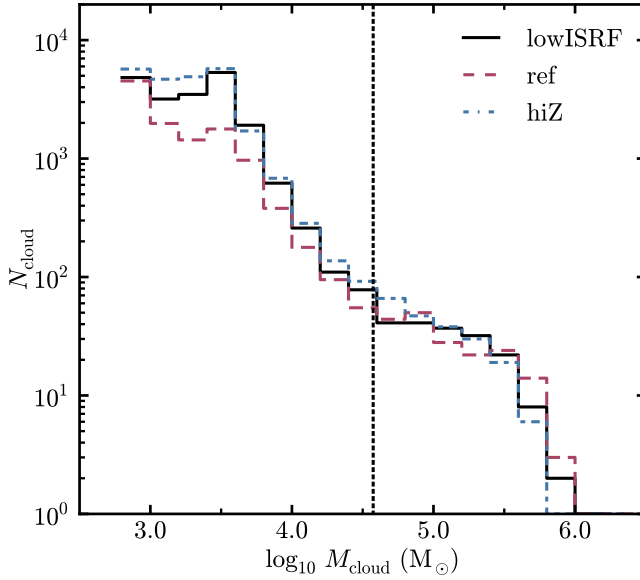


Figure 5.2: Cloud mass functions from simulations lowISRF (*black solid curve*), ref (*red dashed curve*) and hiZ (*blue dot-dashed curve*), taken from snapshots at 100 Myr intervals from 100 Myr to 900 Myr. The vertical dotted line shows a mass of $3.75 \times 10^4 M_{\odot}$, which corresponds to the mass of a cloud containing 50 particles. We consider only clouds above this mass for the remainder of this study. All three simulations show similar cloud mass functions.

We also need to define the radius of each cloud, which will be important for comparing to the observed molecular cloud scaling relations (see §5.4). We determine the radius by finding the 3-dimensional ellipsoid that approximately encloses the particles in the cloud. First, we compute the moment of inertia tensor, I :

$$I_{ij} = \sum_{k=1}^N m_k (|\mathbf{r}|^2 \delta_{ij} - r_{k,i} r_{k,j}), \quad (5.3)$$

where m_k is the mass of the k^{th} particle, \mathbf{r}_k is the position vector of the k^{th} particle in the cloud's centre of mass frame, the summation is over the N particles in the cloud, i and j index the Cartesian directions ($i, j = 1, 2, 3$ in 3d), and δ_{ij} is the Kronecker delta function. The eigenvectors of I give the directions of the principle axes of the cloud. We then determine the maximum extent of the particle distribution along each principle axis to obtain the semi-major, intermediate and minor axes, a , b and c respectively, of the ellipsoid that approximately encloses the particles in the cloud. Finally, we define the cloud radius, R_{mean} , to be the geometric mean of these three axes, i.e.:

$$R_{\text{mean}} = (abc)^{1/3}. \quad (5.4)$$

The above cloud definition is based on a density threshold. However, observations define molecular clouds based on a CO intensity threshold. We therefore also consider an alternative cloud definition, based on the CO emission, which we discuss in section 5.3.3.

5.3.2 Cloud mass evolution

To follow the mass evolution of individual clouds, and hence determine their ages and lifetimes, we first ran the clump finding algorithm described above on all snapshots, taken at intervals of 1 Myr. We then took each massive cloud (containing at least 50 particles) in a given snapshot and traced back its main progenitor in preceding snapshots, and its main descendant in subsequent snapshots.

There are a couple of different ways in which we can link a given cloud to its progenitors and descendants. In the first method that we use, we first take all particles in a given cloud in snapshot i . We then look for these particles in the preceding snapshot, $i-1$, and we identify the cloud that contains the most of these particles. This cloud is selected as the main progenitor. We then take all of the particles in the main progenitor, and we look for these particles in snapshot $i-2$. We repeat this process to find the main progenitor in each preceding snapshot until we can no longer identify a progenitor. Finally, we repeat the above procedure in the snapshots following i to identify the main descendants.

The above method allows us to follow the evolution of the total mass of the cloud. In this way, we can trace coherent cloud structures through time. However, gas will cycle through individual clouds, with new gas being added to the cloud via smooth accretion or mergers, while existing gas can break off into smaller clouds or disperse into the ISM. Therefore, after some time, it is possible that a cloud will no longer contain any of the material that was originally in the cloud in snapshot i .

We therefore also considered an alternative method to link clouds with their progenitors and descendants, in which we consider only gas particles that were originally in the cloud in snapshot i . This is similar to how Dobbs & Pringle (2013) trace the evolution of GMCs in their simulations of an isolated disc galaxy. We first take the particles in the cloud in snapshot i and identify the main progenitor in snapshot $i-1$ that contains the most of these particles, as before. However, we then take only the particles in the main progenitor that were originally in the cloud in snapshot i (and not all of the main progenitor's particles), and we trace these back to snapshot $i-2$ to find the preceding main progenitor, and so on. We then repeat this procedure in later snapshots to identify the main descendants. In this way we can trace the evolution of only gas that was originally in the cloud in snapshot i .

In Fig. 5.3 we show examples of the mass evolution of individual clouds selected at 500 Myr from the ref simulation. For each cloud we show the evolution of the total cloud mass (black solid curves), using the first method described above, and of the mass of original particles that were in the cloud at 500 Myr (blue dashed curves), using the second method described above. The horizontal dotted line in each panel indicates half of the mass of the cloud at 500 Myr, which we use to define the age and lifetime of the cloud (see below).

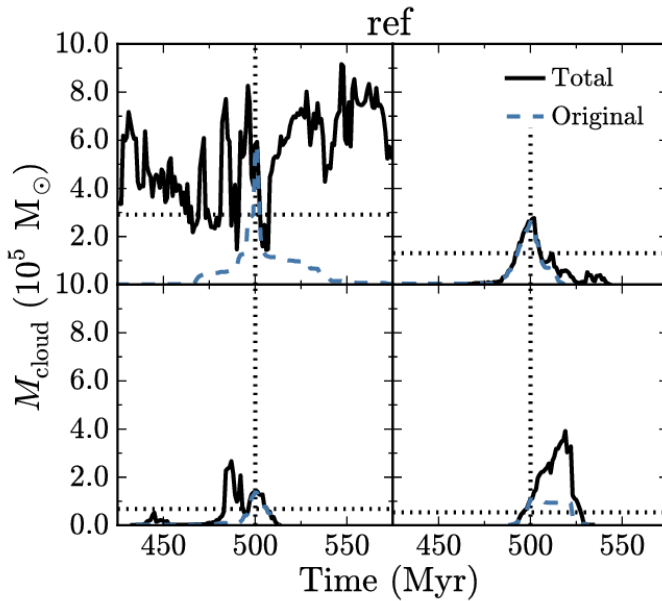


Figure 5.3: Mass evolution of four clouds selected at 500 Myr from the ref simulation. We show the evolution of the total cloud mass (*black solid curves*) and of the mass of particles originally in the cloud at 500 Myr (*blue dashed curves*). The horizontal dotted lines indicate half of the mass of the cloud at 500 Myr, which we use to define the cloud ages and lifetimes (see text).

For some clouds, the evolution of the total and original mass are similar (e.g. the top right panel). These are clouds that reach their peak mass close to 500 Myr, and have fairly simple evolutionary histories, for example with no significant cloud mergers bringing in new material at later times.

In many other clouds, the evolution is more complex. For example, in the bottom right panel, the cloud is still growing at 500 Myr. The total mass of the cloud therefore quadruples over the following 19 Myr, after which it rapidly declines. However, by definition, the original mass is a maximum in the original snapshot (at 500 Myr in this example). We see that the original mass in this example remains nearly constant over the same period.

Finally, in some clouds (e.g. the top left panel), we find that the progenitors and descendants traced by the total mass extend over a much longer time period than those traced only by the original particles at 500 Myr. These are clouds that are constantly cycling through new gas, via accretion and cloud mergers, while existing gas breaks away or is blown away and disperses. The cloud in the top left panel is located at the centre of the galaxy. We saw in Fig. 5.1 that there is more dense gas near the centre, with several clouds packed closely together within the central few hundred parsecs. This explains why we see a strong cycling of gas through individual clouds in this region.

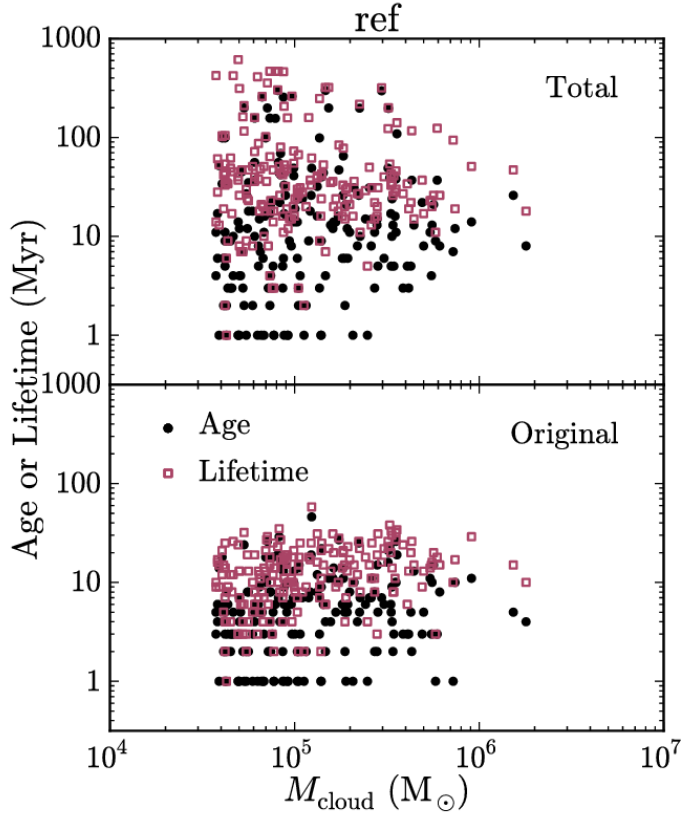


Figure 5.4: Cloud ages (*black circles*), defined as the time since the cloud’s main progenitor had half of its current mass, and cloud lifetimes (*red squares*), defined as the period from when the main progenitor had half of its current mass to when the main descendant is reduced to half of its current mass. We define ages and lifetimes using either the total progenitor/descendant mass (*top panel*), or the mass of particles that were originally part of the cloud, i.e. at the time the cloud was identified (*bottom panel*). We show all clouds with at least 50 particles, selected in snapshots at 100 Myr intervals from 100 Myr to 900 Myr, from the ref simulation. Our other two simulations (lowISRF and hiZ; not shown) have similar distributions of cloud ages and lifetimes.

We can now use the mass evolution of a cloud’s progenitors and descendants to determine the age and lifetime of the cloud, based on either the total mass of the cloud or the mass of original particles. We define the age of the cloud as the time since the mass was half of its current value, and we define its lifetime to be the total period over which its mass is greater than half of its current value. For example, suppose we identify a cloud at time t_{now} . In the past, its main progenitor had half of its current mass at time t_{past} , and in the future, its main descendant is reduced to half of its current mass at time t_{future} . The age is then $t_{\text{now}} - t_{\text{past}}$, and the lifetime is $t_{\text{future}} - t_{\text{past}}$. The ages and lifetimes will depend on the mass frac-

tion that we use to define them. For example, if we use the time when the main progenitor/descendant was a quarter of the cloud's current mass, rather than half, the median lifetimes are increased by ≈ 50 per cent. However, by using a factor of half, there can only be one 'main' progenitor/descendant in each snapshot over the cloud's lifetime, and we avoid ambiguities arising from multiple progenitors/descendants with equal mass.

In Fig. 5.4 we plot the ages (black circles) and lifetimes (red squares) of clouds from the ref simulation versus their current mass, using the total progenitor/descendant mass (top panel) or the mass of original particles (bottom panel). Our other two simulations (lowISRF and hiZ; not shown) have similar distributions of cloud ages and lifetimes. We show all clouds with at least 50 particles identified in snapshots at 100 Myr intervals, from 100 Myr to 900 Myr. Note that, while we only show clouds with at least 50 particles, we still identify clouds with as few as 25 particles, so we can trace the clouds in Fig. 5.4 to the time when they had, or will have, half of their current mass.

If we use the total cloud mass (top panel), we find a median cloud age of 12 Myr, and a median lifetime of 33 Myr. There is a lot of scatter in cloud ages and lifetimes, with many having ages and lifetimes of a few hundred Myr. Note that, since we combine snapshots at 100 Myr intervals in this figure, evolutionary tracks will appear multiple times if they have a lifetime longer than this interval.

In the bottom panel, we see that cloud ages and lifetimes defined using only the original particles are shorter than those defined from the total mass. Using this definition, we find a median age of 5 Myr and a median lifetime of 13 Myr. There is again a lot of scatter in cloud ages and lifetimes, but we find that most clouds have an age ≤ 30 Myr and a lifetime ≤ 40 Myr. Observational estimates, typically based on associated signatures of star formation such as young stellar clusters and HII regions, find GMC lifetimes $\approx 20 - 40$ Myr (e.g. Bash et al. 1977; Kawamura et al. 2009; Murray 2011; Miura et al. 2012), although Elmegreen (2000) and Scoville et al. (1979) find lifetimes of a few Myr and hundreds of Myr, respectively. We find no clear trend of age or lifetime with the current mass of the cloud.

Since we run each simulation for 1 Gyr, we follow the evolution of the galaxy for many cloud lifetimes. This is important as it ensures that the evolution of individual clouds is not strongly affected by the initial chemical state of the gas at the beginning of the simulation, when most of the hydrogen was in HII.

For the remainder of this paper, we will use cloud ages and lifetimes defined via the mass of original particles (i.e. the bottom panel of Fig. 5.4). This definition gives a better indication of how long the current material has been in the cloud. However, both age/lifetime definitions that we have considered here (using total or original mass) involve tracing individual particles through time in the simulations, which is not possible in observations. Observational estimates are typically based on nearby signatures of star formation, such as young stellar clusters and HII regions (e.g. Kawamura et al. 2009). It is not clear which of our definitions is likely to correspond more closely with these observational definitions, so we need to be careful when comparing to observed GMC lifetimes.

5.3.3 CO emission maps

We computed CO emission from the $J = 1 - 0$ line in our simulations in post-processing, using the publicly available Monte-Carlo radiative transfer code RADMC-3D⁶ (version 0.38), written by Cornelis Dullemond. This code follows emission from user-specified molecular and atomic lines, and also includes thermal emission, absorption and scattering from dust grains. We used molecular CO data from the LAMDA database⁷ (Schöier et al. 2005), including collisional excitation rates of CO by ortho- and para-H₂ (Yang et al. 2010). We assumed an ortho-to-para ratio of 3:1 for H₂. We included two species of dust grains, graphite and silicate, with dust opacities from Martin & Whittet (1990), who used the power-law size distribution of dust grains from Mathis et al. (1977).

Line emission from CO depends on the level populations of the CO molecule. The simplest method is to assume that the level populations are in Local Thermodynamic Equilibrium (LTE). However, this assumption may not always be valid. We therefore computed the level populations in non-LTE using the Local Velocity Gradient (LVG) method, also known as the Sobolev (1957) approximation. This method assumes that, due to gas motions, photons emitted from transitions in the CO molecule will become sufficiently Doppler shifted after travelling some distance that the photon can no longer be absorbed by the same transition that produced it. This allows us to define an escape probability for these photons based on their velocity gradient. We can then determine the level populations, including radiative excitation by line photons, from local quantities alone. A more detailed description of the LVG method, as implemented in RADMC-3D, can be found in Shetty et al. (2011a).

In addition to thermal broadening of the emission line, RADMC-3D also allows the inclusion of doppler broadening by unresolved microturbulence. In our simulations, we impose a density-dependent pressure floor, P_{floor} , on the gas to ensure that the Jeans mass is resolved by at least 4 SPH kernel masses, to prevent artificial fragmentation (see section 5.2.1). While the implementation of this pressure floor was motivated by numerical reasons, its effect on the cloud will be similar to a pressure term from unresolved turbulence. We can attribute a one-dimensional velocity dispersion, $\sigma_{\text{floor, 1D}}$, to the pressure floor according to $P_{\text{floor}} = \rho \sigma_{\text{floor, 1D}}^2$. Using equation 5.2 for P_{floor} , with our fiducial parameters $N_{j,m} = 4$, $m_{\text{gas}} = 750 M_{\odot}$ and $N_{\text{ngb}}^{\text{SPH}} = 100$, we find:

$$\sigma_{\text{floor, 1D}} = 1.18 \left(\frac{\rho}{10^{-24} \text{ g cm}^{-3}} \right)^{1/6} \text{ km s}^{-1}. \quad (5.5)$$

We therefore include microturbulent broadening due to this pressure floor when computing the CO line emission, with a velocity dispersion given by equation 5.5. The Doppler broadening due to this microturbulence is then added to the thermal broadening in quadrature.

For each cloud in our simulations, we extracted a region around the cloud and interpolated the gas density, temperature and velocities, along with the densities

⁶<http://www.ita.uni-heidelberg.de/~dullemond/software/radmc-3d/>

⁷<http://home.strw.leidenuniv.nl/~moldata/>

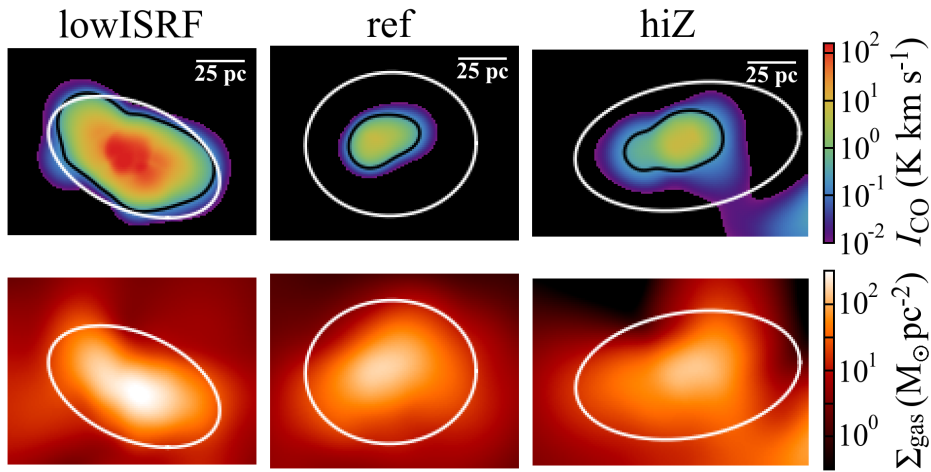


Figure 5.5: CO $J = 1-0$ line emission maps (*top row*) and gas surface density maps (*bottom row*) of molecular clouds from the lowISRF (*left*), ref (*centre*) and hiZ (*right*) simulations. The white ellipse in each panel indicates the boundary of the cloud, defined by gas particles with a density above a threshold $n_{\text{H}, \text{min}} = 10 \text{ cm}^{-3}$. The black contours in the top row show $I_{\text{CO}} = 0.25 \text{ K km s}^{-1}$, which corresponds to the 3σ intensity threshold for the Small Magellanic Cloud in the observations of Leroy et al. (2011). In the examples from the ref and hiZ simulations, only the centres of the clouds would be detectable in a typical CO survey.

of CO and H_2 , onto a 3d Cartesian grid with a resolution of 1 pc, using the same C^2 Wendland (1995) kernel with 100 SPH neighbours as was used in the simulations. We used RADMC-3D to compute the total emission from the $J = 1-0$ line and thermal dust emission in 480 wavelength bins covering a velocity range $\pm 60 \text{ km s}^{-1}$ centred on the line, which we projected onto a plane parallel to the galactic disc. We then repeated this without line emission to create a map of the thermal dust emission only, which we finally subtracted from the total emission to produce a continuum-subtracted map of CO $J = 1-0$ line emission.

In Fig. 5.5 we show examples of CO emission maps from individual molecular clouds in the lowISRF, ref and hiZ simulations (left, centre and right columns, respectively). The top and bottom rows show maps of the CO emission and gas surface density, respectively.

The white ellipse in each panel shows the boundary of the cloud, defined by gas particles with a density above a threshold $n_{\text{H}, \text{min}} = 10 \text{ cm}^{-3}$. This ellipse was computed by projecting the 3d ellipsoid that approximately encloses the particles in the cloud onto the image plane, where the 3d ellipsoid is based on the principle axes of the moment of inertia tensor, as described in section 5.3.1. For comparison, the black contours in the top row show $I_{\text{CO}} = 0.25 \text{ K km s}^{-1}$. This corresponds to the 3σ intensity threshold for the observations of the Small Magellanic Cloud in Leroy et al. (2011). In the examples from the ref and hiZ simulations (centre and right columns, respectively), only the centres of the clouds are above this detection

threshold.

We thus see that our standard definition of a cloud, based on a fixed density threshold, includes a larger region than if we had defined clouds based on the observable CO emission. We therefore also consider an alternative cloud definition, in which we only include regions in the 2d maps of CO emission with $I_{\text{CO}} > 0.25 \text{ K km s}^{-1}$. For this alternative cloud definition, we also compute the projected cloud mass, M_{proj} , and size, $R_{\text{proj}} = (A/\pi)^{1/2}$, from the 2d maps, rather than from the 3d particle distribution, where M_{proj} and A are the total mass and area, respectively, of pixels above the CO intensity threshold. This alternative cloud definition provides a fairer comparison with observations.

It is important to note that these CO emission maps may be sensitive to resolution. In particular, high-resolution simulations of dense clouds find that most CO is concentrated in compact structures, with sizes $\sim 1 \text{ pc}$ and densities $\sim 10^3 \text{ cm}^{-3}$ (e.g. Glover & Clark 2012). Such structures are poorly resolved in our simulations, which may make the predicted CO emission uncertain.

5.4 Cloud scaling relations

Observations of molecular clouds find strong relations between their properties such as size, velocity dispersion and mass, both in Milky Way GMCs (e.g. Larson 1981; Solomon et al. 1987; Heyer et al. 2009) and in extragalactic GMCs (e.g. Bolatto et al. 2008). For example, building on the original relations identified by Larson (1981), Solomon et al. (1987) studied a sample of GMCs in the Milky Way, and found that the line of sight velocity dispersion, σ , follows a power law relation with cloud radius, R :

$$\sigma = 0.72 \left(\frac{R}{\text{pc}} \right)^{0.5} \text{ km s}^{-1}. \quad (5.6)$$

By assuming that the clouds are in virial equilibrium, they estimated the cloud masses, M , and they found a power-law relation between M and σ :

$$M = 2000 \left(\frac{\sigma}{\text{km s}^{-1}} \right)^4 M_{\odot}. \quad (5.7)$$

Combining equations 5.6 and 5.7 produces the following relation between M and R :

$$M = 540 \left(\frac{R}{\text{pc}} \right)^2 M_{\odot}, \quad (5.8)$$

which implies that the clouds in their sample have a constant mean surface density of $\Sigma = 170 M_{\odot} \text{ pc}^{-2}$. Later studies have corrected this value to $200 M_{\odot} \text{ pc}^{-2}$ to account for an updated estimate for the Sun's galactocentric radius of 8.5 kpc, rather than 10 kpc as originally used (see e.g. Heyer et al. 2009). The corrected mass-size relation is then:

$$M = 625 \left(\frac{R}{\text{pc}} \right)^2 M_{\odot}. \quad (5.9)$$

The updated galactocentric radius of the Sun will also affect the size-linewidth relation in equation 5.6. However, the correction for this relation is smaller than the errors.

Heyer et al. (2009) re-examined the sample of Solomon et al. (1987), and used the ^{13}CO luminosities of the clouds to estimate their molecular hydrogen masses. They found a median molecular surface density of $42 M_{\odot} \text{pc}^{-2}$, lower than the value determined by Solomon et al. (1987) from the virial mass. Furthermore, they found that Σ is not constant, and that $\sigma/R^{0.5}$ varies systematically with surface density as $\Sigma^{0.5}$.

Roman-Duval et al. (2010) studied the properties of molecular clouds in the BU-FCRAO Galactic Ring Survey (Jackson et al. 2006) and the UMSB survey (Clemens et al. 1986; Sanders et al. 1986) in the Milky Way. They found the following mass-size relation:

$$M = 228 \left(\frac{R}{\text{pc}} \right)^{2.36} M_{\odot}, \quad (5.10)$$

based on ^{13}CO line emission.

Fig. 5.6 shows the cloud mass-size relation from the ref simulation, where the cloud radius, R_{mean} , was calculated from the 3d particle distribution (see equation 5.4). Our other two simulations (lowISRF and hiZ; not shown) have very similar cloud mass-size relations. We show all clouds with at least 50 particles identified in snapshots at 100 Myr intervals from 100 Myr to 900 Myr. The colour scale indicates the age of the cloud, defined from the particles originally in the cloud in the current snapshot, as described in section 5.3.2. The black solid and dashed lines show the observed relations of Solomon et al. (1987) and Roman-Duval et al. (2010), respectively, i.e. equations 5.9 and 5.10.

Our simulated clouds follow a similar slope to the observed relations, but the normalisation is a factor ≈ 4 lower than is observed. The lower normalisation is determined by the density threshold that we use to define a cloud, and suggests that our definition includes a larger region around the cloud than would be included in a typical observational survey based on CO emission. Indeed, we saw in Fig. 5.5 that only the central regions of our simulated clouds have velocity-integrated CO intensities above a threshold of 0.25 K km s^{-1} . For a fairer comparison with observations, we therefore also considered an alternative cloud definition in which we include only regions above this CO intensity threshold, and compute cloud properties in projection, as described in section 5.3.3.

Fig. 5.7 shows the mass-size relation computed using only CO-detectable regions, for the ref simulation. Compared to Fig. 5.6, for a density-based cloud definition, the clouds lie much closer to the observed relations of Solomon et al. (1987) and Roman-Duval et al. (2010) (black solid and dashed lines, respectively), although the normalisation of this relation in our simulations is still a factor ≈ 2 lower than is observed (compared to a factor ≈ 4 in Fig. 5.6). However, even our

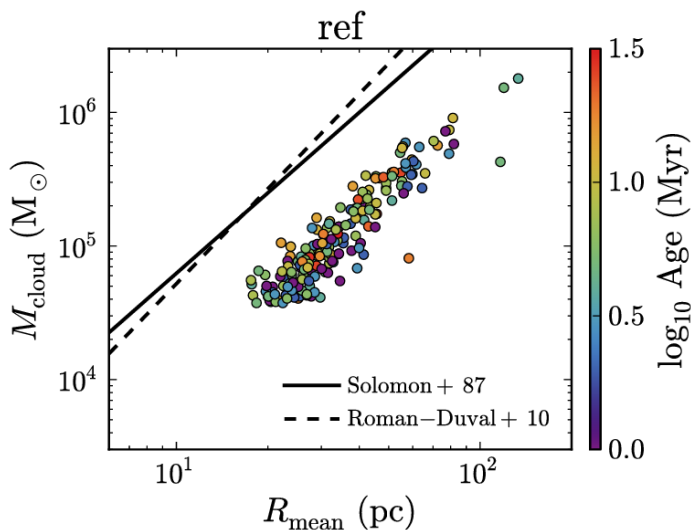


Figure 5.6: Cloud mass, M_{cloud} , versus cloud radius, $R_{\text{mean}} = (abc)^{1/3}$, for all clouds with at least 50 particles identified in snapshots at 100 Myr intervals from 100 Myr to 900 Myr in the ref simulation. Our other two simulations (not shown) have very similar cloud mass-size relations. The colour scale indicates the cloud age. The black lines show the observed relations of Solomon et al. (1987) (*solid*; our equation 5.9) and Roman-Duval et al. (2010) (*dashed*; our equation 5.10). Our simulated clouds follow a similar slope to the observed relations, but the normalisation, which depends on the cloud definition, is a factor ≈ 4 lower than is observed.

CO-based cloud definition is not identical to the definitions used in these two observational studies. Our criterion is based on a minimum velocity-integrated CO intensity in the projected, two-dimensional position-position space of the CO emission maps. However, Solomon et al. (1987) define clouds as regions above a minimum CO brightness temperature of 1 K in the three-dimensional position-position-velocity space. Roman-Duval et al. (2010) use a minimum velocity-integrated intensity of $4\sigma = 0.23 \sqrt{N_v} \text{ K km s}^{-1}$, where N_v is the number of velocity channels, but for ^{13}CO line emission, rather than ^{12}CO as used by us. Additionally, when measuring ^{13}CO column densities to compute the cloud mass, they include only velocity channels above a ^{13}CO brightness temperature of $4\sigma = 1 \text{ K}$. Therefore, the remaining discrepancy in the normalisation of the cloud mass-size relation is likely due to the different CO thresholds that we use. Given that observational studies use a range of cloud definitions, with different clump finding algorithms and using different molecular emission lines, we keep our CO-based definition general, rather than try to match a particular observational study.

We saw in Fig. 5.1 that the clouds in our simulations exhibit a wide range of morphologies, from nearly spherical to highly elongated. We can use the axis ratios of the ellipsoid enclosing the 3d particle distribution, as defined in section 5.3.1, to study the shapes of these clouds. Fig. 5.8 shows the ratio of minor to

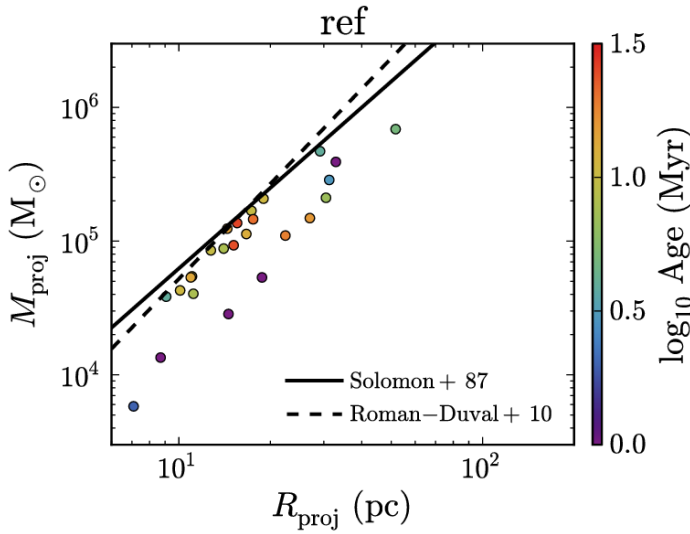


Figure 5.7: As Fig. 5.6, but for cloud masses and projected sizes determined from CO-detectable ($I_{\text{CO}} > 0.25 \text{ K km s}^{-1}$) regions only. The normalisation of this relation in our simulations is a factor ≈ 2 lower than the observed relations (Solomon et al. 1987 and Roman-Duval et al. 2010; black solid and dashed lines respectively) when we include only CO-detectable regions, compared to a factor of four lower than is observed when we used a density-based cloud definition (see Fig. 5.6).

major axes, c/a , plotted against M_{cloud} for the ref simulation. The colour scale indicates the cloud ages. There is a large scatter in cloud shapes, with $0.1 \lesssim c/a \lesssim 1.0$. The most massive clouds ($M_{\text{cloud}} \gtrsim 6 \times 10^5 M_{\odot}$) tend to be less spherical ($c/a \lesssim 0.4$), which may suggest that these are merging systems, although this could also be caused by shear. This may also be a resolution effect, as the lowest-mass clouds in Fig. 5.8 are resolved with as few as 50 SPH particles, which will tend to make them more spherical. However, for most clouds there is no clear trend of shape with mass or age.

Fig. 5.9 compares the velocity dispersion-cloud size relation from the ref simulation (coloured points) to the observed relation from Solomon et al. (1987), i.e. our equation 5.6 (black solid line), for our standard density-based cloud definition. In the top panel of Fig. 5.9, we plot the one-dimensional velocity dispersion, $\sigma_{1\text{D}} = \sigma_{3\text{D}}/\sqrt{3}$, where the three-dimensional velocity dispersion is $\sigma_{3\text{D}}^2 = \sigma_x^2 + \sigma_y^2 + \sigma_z^2$, and $\sigma_i^2 = \langle v_i^2 \rangle - \langle v_i \rangle^2$ for the i^{th} component of the particle velocities, v_i , where angular brackets indicate a mass-weighted average over all particles in the cloud. The colour scale in the top panel of Fig. 5.9 indicates the cloud age.

We see that the relation between $\sigma_{1\text{D}}$ and R_{mean} is steeper than observed. In particular, we find very low velocity dispersions, $\sigma_{1\text{D}} < 1 \text{ km s}^{-1}$, far below the observed relation of Solomon et al. (1987). However, these measurements of

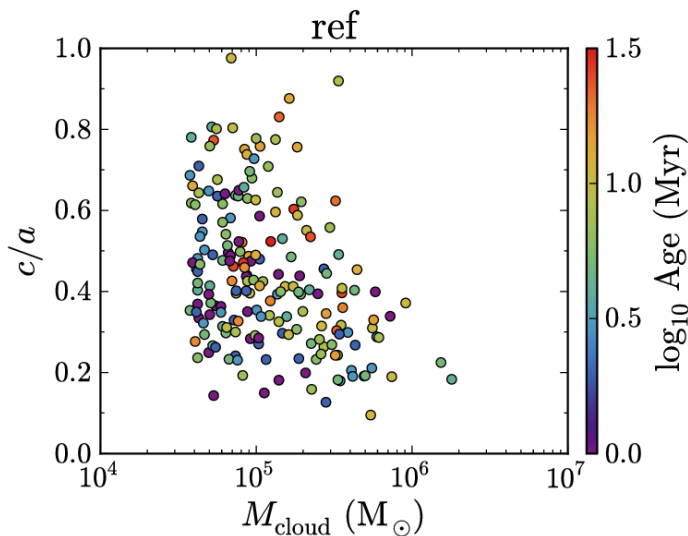


Figure 5.8: Minor-to-major axis ratio, c/a , plotted against cloud mass for clouds with at least 50 particles, selected from snapshots at intervals of 100 Myr from 100 Myr to 900 Myr in the ref simulation. Our other two simulations (not shown) have very similar distributions of cloud shapes. The colour scale indicates the cloud age. Whilst the most massive clouds ($M_{\text{cloud}} \gtrsim 6 \times 10^5 M_{\odot}$) tend to be less spherical ($c/a \lesssim 0.4$), for the remaining clouds there is no clear trend of shape with mass or age.

σ_{1D} in the simulations do not account for unresolved turbulence. As noted in section 5.3.3, the pressure floor that we impose on the gas to ensure that the Jeans mass is always well-resolved will have a similar effect on the cloud as a pressure term from unresolved turbulence, with a turbulent velocity dispersion, $\sigma_{\text{floor}, 1D}$, given by equation 5.5. We therefore need to include the effects of this pressure floor.

In the bottom panel of Fig. 5.9, we compute $\sigma_{\text{floor}, 1D}$ for each cloud using its mean density, add this to σ_{1D} in quadrature, and plot the total velocity dispersion against cloud radius. By accounting for the pressure floor in this way, we avoid unrealistically low velocity dispersions (the lowest value is now $\approx 2.3 \text{ km s}^{-1}$). This will be important for computing CO emission in our simulated clouds, as the CO $J = 1 - 0$ line is often optically thick in molecular clouds, so the line intensity will depend on the line width.

The observed velocity dispersions will also include a component due to the thermal broadening of the molecular lines that are used to measure σ_{1D} . For CO, with a mean molecular weight $\mu = 28$, the thermal velocity is $\sigma_{\text{th}, 1D} = \sqrt{k_B T / \mu m_p} = 0.17 \text{ km s}^{-1}$ at a temperature $T = 100 \text{ K}$, where k_B and m_p are the Boltzmann constant and proton mass, respectively. Thus, $\sigma_{\text{th}, 1D}$ is small compared to $\sigma_{\text{floor}, 1D}$ in our simulations, so we do not include $\sigma_{\text{th}, 1D}$ in Fig. 5.9, although we do account for thermal broadening when we compute CO line emission, as described in section 5.3.3.

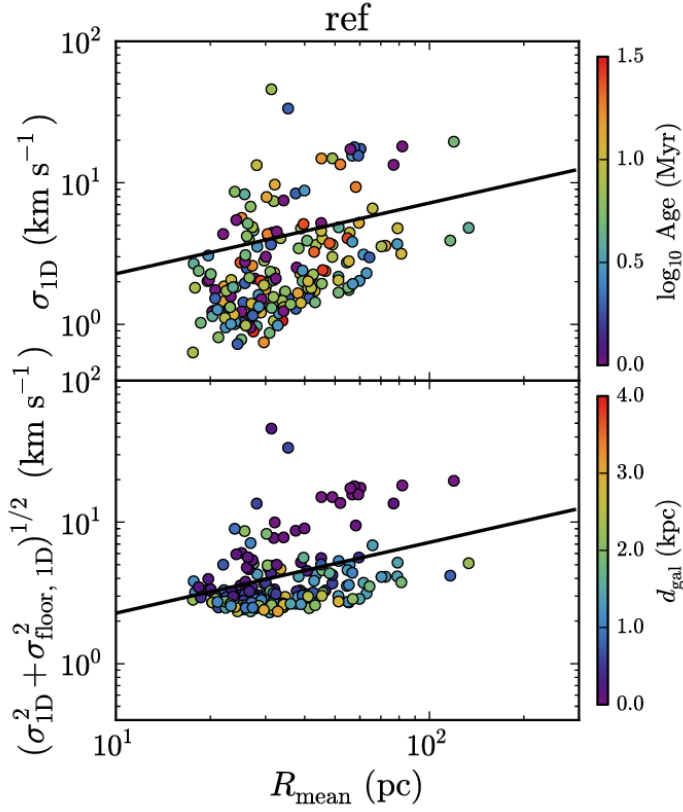


Figure 5.9: One-dimensional velocity dispersion, measured from gas particle motions only (σ_{1D} ; *top panel*), and including the contribution from the pressure floor ($\sigma_{\text{floor}, 1D}$; *bottom panel*), plotted against cloud radius. The colour scale in the top panel indicates the cloud age, while in the bottom panel it indicates the distance of the cloud’s centre of mass from the galaxy centre. The black lines indicate the observed relation of Solomon et al. (1987). We show only the ref simulation here, although the relations in our other two simulations are very similar. If we do not account for the pressure floor (top panel), we find unrealistically low velocity dispersions ($< 1 \text{ km s}^{-1}$). When we include the pressure floor as an unresolved turbulence term (bottom panel), we find velocity dispersions $> 2.3 \text{ km s}^{-1}$ for all clouds, although there remains a large scatter in this relation. The clouds with the highest velocity dispersion tend to be close to the galaxy centre.

Even accounting for the pressure floor, we still find a lot of scatter in this relation in our simulations, with some clouds showing velocity dispersions $> 10 \text{ km s}^{-1}$. In the top panel of Fig. 5.9, we found no trend in this relation with the cloud age. However, in the bottom panel, the colour scale indicates the distance of the cloud’s centre of mass from the centre of the galaxy. We see that clouds with the highest velocity dispersions ($\gtrsim 10 \text{ km s}^{-1}$) are generally found within the central $\approx 1 \text{ kpc}$ of the galaxy. We also find that many of these high velocity dispersion clouds contain

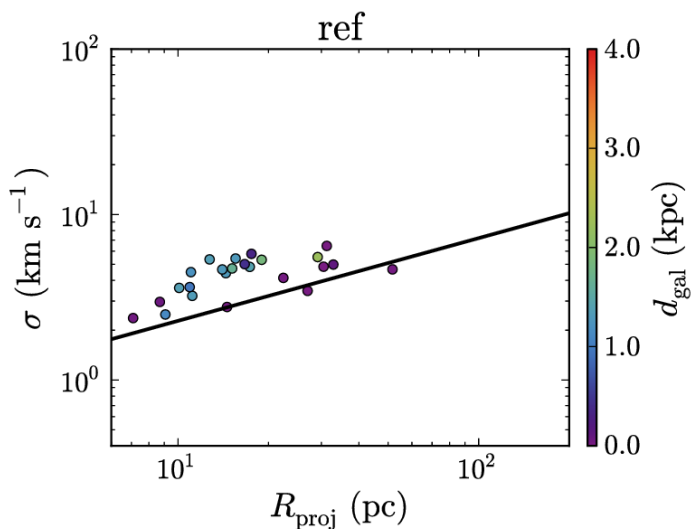


Figure 5.10: As Fig. 5.9, but measured from CO-detectable ($I_{\text{CO}} > 0.25 \text{ K km s}^{-1}$) regions of each cloud only. Also, we use projected sizes and compute the velocity dispersion by fitting a single Gaussian component to the CO spectrum. We exclude all clouds that show multiple peaks in their CO spectrum, as they cannot be fit with a single velocity component, and likely consist of multiple clouds that are undergoing mergers. We find better agreement with the observed relation of Solomon et al. (1987) (*black line*) than we saw in Fig. 5.9.

multiple density peaks that indicate substructures within the cloud. Therefore, some of the scatter towards high velocity dispersions is likely to be caused by motions of substructures within the cloud, possibly created by ongoing cloud-cloud mergers, which are more common in the centre of the galaxy. Interestingly, observations of molecular clouds in the centre of the Milky Way also find higher velocity widths compared to the linewidth-size relation of nearby molecular clouds in the Galactic disc (e.g. Oka et al. 2001).

Fig. 5.10 shows the velocity dispersion-size relation in the ref simulation using our CO-based cloud definition, i.e. restricted to CO-detectable regions and with cloud sizes computed in projection. The 1d velocity dispersion of each cloud was measured by fitting a single Gaussian component to the CO spectrum extracted from pixels above the I_{CO} threshold. We visually inspected each spectrum and excluded those with multiple peaks, which cannot be fit with a single velocity component. These systems are likely multiple clouds that are undergoing mergers. The velocity dispersion was then obtained from the width of the best-fitting Gaussian. The width of the CO spectrum includes microturbulent Doppler broadening by the pressure floor. By defining clouds above a CO intensity threshold, measuring the velocity dispersion from the width of the CO spectrum rather than motions of the gas particles, and excluding merging systems with multiple velocity components, we find better agreement with the observed relation of Solomon et al. (1987) than we saw in Fig. 5.9.

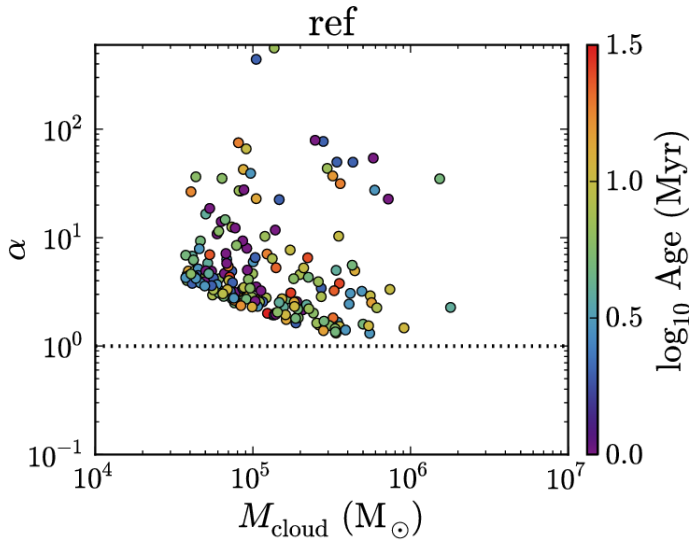


Figure 5.11: Virial parameter, α , versus cloud mass for all clouds with more than 50 particles in snapshots at 100 Myr intervals from 100 Myr to 900 Myr, from the ref simulation. Clouds in our other simulations (lowISRF and hiZ; not shown) have similar distributions of α . The colour scale indicates the cloud age. The horizontal dotted line shows $\alpha = 1$, below which clouds are gravitationally bound. We see that all of our simulated clouds have $\alpha > 1$, i.e. they are unbound. However, the lower envelope of points is caused by the pressure floor; so this is likely to be an effect of limited resolution.

In Fig. 5.11 we plot the virial parameter, α , against M_{cloud} , from the ref simulation, where:

$$\alpha = \frac{5\sigma^2 R_{\text{mean}}}{GM_{\text{cloud}}} \quad (5.11)$$

(e.g. Bertoldi & McKee 1992; Dobbs et al. 2011), and we include the pressure floor in the velocity dispersion, i.e. $\sigma^2 = \sigma_{\text{1D}}^2 + \sigma_{\text{floor, 1D}}^2$. The numerical factor on the right hand side depends weakly on the density profile of the cloud. The value of 5 that we use here corresponds to a cloud with constant density; for comparison, in a cloud with a power-law density profile $\rho \propto r^{-2}$, this numerical factor would be 3.

The horizontal dotted line shows $\alpha = 1$, which corresponds to virial equilibrium, with $2K + W = 0$, where K and W are the kinetic and gravitational potential energies, respectively. A cloud that is gravitationally bound, with $K + W < 0$, requires $\alpha < 2$. While we do find clouds with $\alpha \approx 1 - 2$ in our simulations, which are marginally bound (but not virialised), most have $\alpha > 2$, and thus are unbound. Dobbs et al. (2011) similarly found that most (but not all) GMCs in their simulations of isolated disc galaxies are gravitationally unbound. They attributed this to cloud-cloud collisions and stellar feedback, which regulate the velocity dispersion within the clouds. However, in our simulations, the lack of clouds with low virial

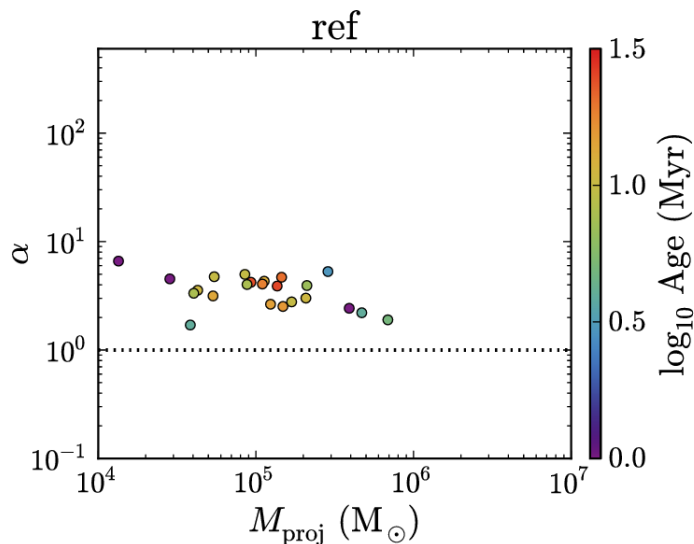


Figure 5.12: As Fig. 5.11, but measured from CO-detectable regions only, and with α calculated from velocity dispersions measured from the simulated CO spectra. Compared to Fig. 5.11, for a density-based cloud definition, the dependence of the lower envelope of α on cloud mass is weaker. However, we still find that all clouds are unbound ($\alpha > 1$), even for a CO-based cloud definition.

parameters is partially due to the pressure floor, at least for masses $\lesssim 3 \times 10^5 M_\odot$. We find a lower envelope of $\alpha \propto M^{-2/3}$ in Fig. 5.11, whereas observations find that α is approximately constant with mass (e.g. Rosolowsky 2007). This scaling of α with cloud mass is what we would expect when the virial parameter is determined by the pressure floor, with $\sigma_{\text{floor, 1D}} \propto \rho^{1/6}$ (equation 5.5) and $R_{\text{mean}} \propto M^{1/2}$ (as seen in Fig. 5.6). It is therefore apparent that the pressure floor prevents the low-mass clouds from becoming gravitationally bound in our simulations.

Some observational studies also suggest that molecular clouds may be gravitationally unbound (e.g. Heyer et al. 2001). Dobbs et al. (2011) also demonstrated that many of the GMCs in the sample of Heyer et al. (2009) have $\alpha > 2$ (see, for example, the centre bottom panel of fig. 1 of Dobbs et al. 2011). However, there are still some GMCs in this sample with $\alpha < 1$, which we do not see in our simulations. Furthermore, other studies suggest that molecular clouds may be marginally gravitationally bound, with $\alpha \approx 1$ (see e.g. McKee & Ostriker 2007).

To test how the pressure floor affects our results, we repeated the ref model twice, with the pressure floor lowered by factors of 4 and 16 in terms of the Jeans mass, corresponding to $N_{\text{J,m}} = 1$ and 0.25, respectively. We present these comparisons in Appendix A, but we summarise the main results here.

As we lower the pressure floor, the low-mass ($\lesssim 3 \times 10^5 M_\odot$), most poorly resolved clouds become more compact. They extend to lower values of α and can become strongly gravitationally bound, with $\alpha < 1$, and thus they can survive for

longer, with ages up to ≈ 50 Myr. However, clouds with higher masses than this are unaffected by the pressure floor. This also means that the mass-size relation becomes flatter when we lower the pressure floor, and no longer agrees with the observed slope of this relation. It is therefore not clear whether the trend of more compact clouds when we lower the pressure floor is physically correct, or if it is an artifact of spurious fragmentation and collapse that may arise when we do not fully resolve the Jeans scale (e.g. Bate & Burkert 1997; Truelove et al. 1997). To determine which is the physically correct solution, we will need to repeat these tests at a higher resolution.

Despite the differences that arise from lowering the pressure floor, we find that the median relations of molecule abundances with cloud age, and of CO intensity and X_{CO} factor with dust extinction, which we present for our fiducial simulations in the next two sections, are insensitive to the pressure floor, although the scatter in these relations does increase as we lower the pressure floor.

Fig. 5.12 shows the virial parameter plotted against cloud mass for our CO-based cloud definition, including only regions above the I_{CO} threshold, and using velocity dispersions measured by fitting a single Gaussian component to the simulated CO spectra, as described above. We show clouds from the ref simulation (using our fiducial pressure floor, with $N_{\text{I,m}} = 4$), and we exclude those with multiple peaks in the CO spectrum, which cannot be fit by a single Gaussian component. Compared to Fig. 5.11 (for a density-based cloud definition), the dependence of the lower envelope of α on cloud mass is weaker, which suggests that the impact of the pressure floor on the virial parameter is less severe when we use a CO-based cloud definition. However, we still find that all clouds in our simulations are unbound, with $\alpha > 1$.

5.5 Chemical evolution

We now look at the evolution of molecular abundances within the dense clouds that we have identified in our simulations. In particular, we investigate the time-scales over which these clouds become fully molecular, and whether they remain close to chemical equilibrium throughout their evolution. As in the previous section, we consider two cloud definitions: one based on a minimum density threshold ($n_{\text{H}} > 10 \text{ cm}^{-3}$), and one based on a minimum velocity-integrated CO intensity threshold ($I_{\text{CO}} > 0.25 \text{ K km s}^{-1}$). We consider two molecular species: H_2 , which is the most prevalent molecule in interstellar gas, and CO, which is the most easily observed molecule.

5.5.1 Molecular hydrogen

Fig. 5.13 shows the molecular hydrogen fraction, $f_{\text{H}_2} = M_{\text{H}_2}/M_{\text{H,tot}}$ (where M_{H_2} is the mass of H_2 and $M_{\text{H,tot}}$ is the total mass of hydrogen in the cloud), for all clouds with at least 50 particles identified in snapshots at 100 Myr intervals from 100 Myr to 900 Myr, using our density-based cloud definition. In the top row of Fig. 5.13 we plot f_{H_2} against the age of the cloud, and in the bottom row we plot the ratio

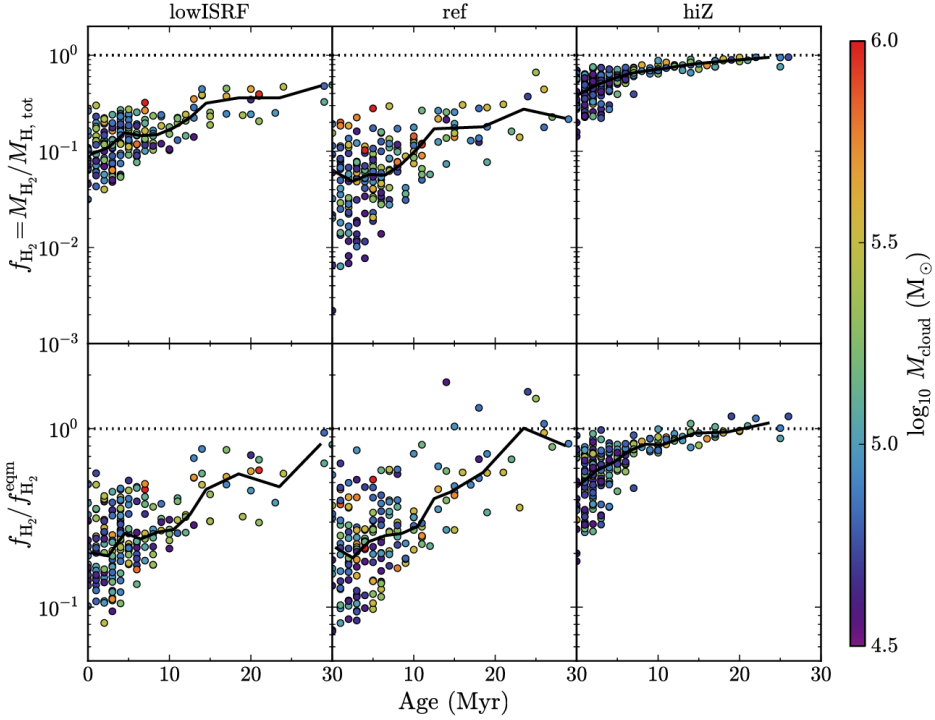


Figure 5.13: Molecular hydrogen fraction, f_{H_2} (top row), and the ratio of the H_2 fraction to the H_2 fraction in chemical equilibrium, $f_{\text{H}_2}/f_{\text{H}_2}^{\text{eqm}}$ (bottom row), plotted against cloud age for all clouds with at least 50 particles identified in snapshots at 100 Myr intervals from 100 Myr to 900 Myr in our three simulations: lowISRF (left column), ref (centre column) and hiZ (right column). The dotted horizontal lines indicate a value of unity, and the colour scale indicates cloud mass. We also show the median f_{H_2} or $f_{\text{H}_2}/f_{\text{H}_2}^{\text{eqm}}$ in bins of age (solid curves). We see that f_{H_2} increases, and moves closer to chemical equilibrium, with increasing cloud age, and does so faster for higher metallicity.

$f_{\text{H}_2}/f_{\text{H}_2}^{\text{eqm}}$, where $f_{\text{H}_2}^{\text{eqm}}$ is the molecular hydrogen fraction if all gas particles are set to chemical equilibrium. The three columns in Fig. 5.13 correspond to our three simulations (lowISRF, ref and hiZ), and the colour of each point indicates the mass of the cloud. The black curve in each panel shows the median in bins of age.

The top row of Fig. 5.13 shows that the H_2 fraction increases with age, while there does not appear to be any significant trend with cloud mass. The simulation using solar metallicity (hiZ, right column) shows the highest H_2 fractions for a given cloud age. This is as expected, as we assume that the formation rate of H_2 on dust grains scales linearly with metallicity. In contrast, our reference simulation (ref, centre column), with a metallicity of ten per cent solar, shows the lowest H_2 fractions.

In run hiZ, the median cloud H_2 fraction reaches $f_{\text{H}_2} = 0.5$ after ≈ 3 Myr. In the ref simulation, with a factor of ten lower metallicity than hiZ, molecular hydrogen

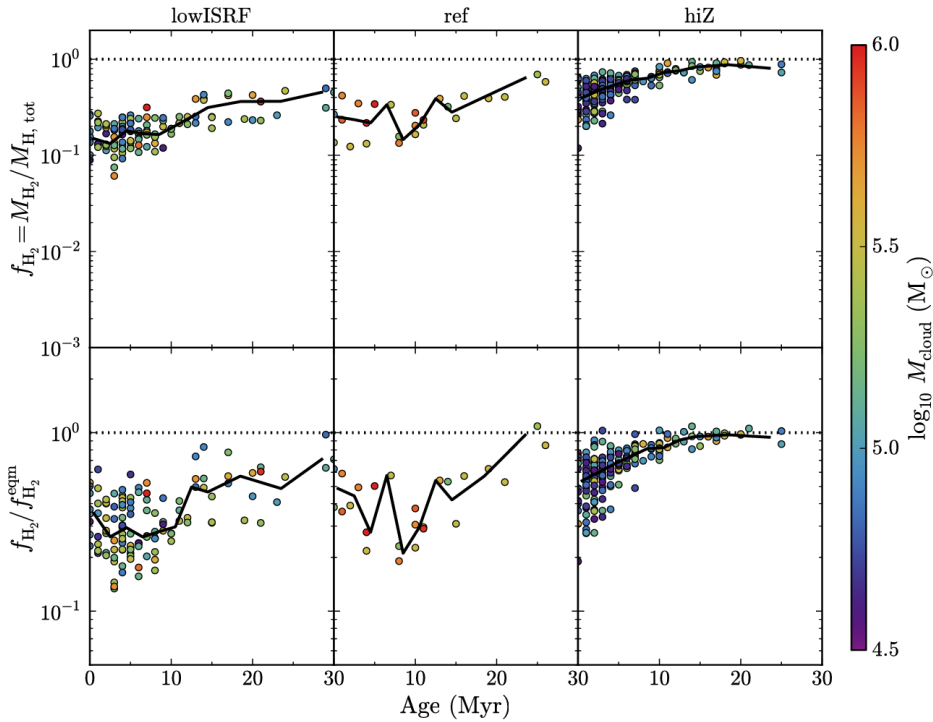


Figure 5.14: As Fig. 5.13, but only for the region within each cloud with $I_{\text{CO}} > 0.25 \text{ K km s}^{-1}$. By restricting the cloud definition to CO-detectable regions, we find less scatter in the H_2 fraction for the lowISRF and ref simulations, while the hiZ simulation is mostly unaffected.

takes longer to build up, and only reaches $f_{\text{H}_2} \approx 0.2$ after ≈ 30 Myr. Finally, in run lowISRF (left column), with ten per cent solar metallicity and ten per cent of the ISRF used in the other two simulations, the median H_2 fraction is always a factor ≈ 2 higher than for ref. Thus, the time-scale for forming molecular H_2 in dense clouds is shorter at higher metallicity and (to a lesser extent) in the presence of a weaker UV radiation field.

In the bottom row of Fig. 5.13, we see that the H_2 fraction in young clouds is below what we would expect in chemical equilibrium. The clouds in the run at solar metallicity (hiZ) reach chemical equilibrium the fastest, with the median $f_{\text{H}_2} / f_{\text{H}_2}^{\text{eqm}}$ already at 50 per cent after ≈ 1 Myr (which is the smallest time-scale that we show here, as we only have snapshots at 1 Myr intervals). After ≈ 13 Myr, f_{H_2} has reached 90 per cent of its equilibrium value.

At lower metallicity, clouds take longer to reach chemical equilibrium. For example, clouds in the ref and lowISRF simulations reach 50 per cent of the equilibrium H_2 fraction after ≈ 16 Myr, and they reach 90 per cent after ≈ 22 Myr and ≈ 30 Myr respectively. In the ref simulation, clouds still have a low H_2 fraction ($f_{\text{H}_2} \approx 0.2$) after 30 Myr, although they have reached chemical equilibrium by this time. In other words, these clouds are still not fully molecular, even in chemical

equilibrium. This suggests that, in the reference simulation, the HI-to-H₂ transition, which depends on both metallicity and radiation field, lies further above the density threshold that we use to define our clouds ($n_{\text{H},\text{min}} = 10 \text{ cm}^{-3}$) than in the other two simulations. In the ref simulation our definition of a dense cloud therefore includes a greater proportion of the HI envelope.

In Fig. 5.14 we repeat Fig. 5.13, but for our CO-based cloud definition, i.e. including only regions with $I_{\text{CO}} > 0.25 \text{ K km s}^{-1}$. We compute f_{H_2} by projecting the H₂ column density onto the same image grid as was used for the CO emission maps, and selecting pixels above the I_{CO} threshold.

In the top row of Fig. 5.14, the H₂ fraction in the lowISRF and ref simulations shows less scatter than we previously saw in Fig. 5.13, and the values of f_{H_2} are higher, as we exclude the outer atomic envelope of the cloud. The ratio of H₂ fraction in non-equilibrium and H₂ fraction in equilibrium in the bottom row of Fig. 5.14 also shows less scatter.

The lowISRF run shows similar trends with cloud age as previously, whereas the ref run shows weaker evolution with age, with H₂ fractions closer to equilibrium (within a factor $\approx 2-5$) in young clouds when we include only CO-detectable regions. The ref simulation contained the most CO-faint pixels, because its combination of low metallicity and high radiation field resulted in the lowest CO fractions (see Fig. 5.15 in the next section). Therefore, restricting our cloud definition to CO-detectable regions has the strongest effect for the ref run. The CO-detectable regions are located in the dense cores of the clouds, which we would expect to reach chemical equilibrium faster, since collisional reaction rates typically scale with n^2 , where n is the density. This likely explains why the H₂ fraction in the ref simulation reaches equilibrium faster when we select only CO-detectable regions.

In the hiZ simulation, the H₂ fraction is mostly unaffected by restricting the cloud definition to CO-detectable regions, with similar scatter and trends with age as in Fig. 5.13.

One caveat to note is that these conclusions on the formation time-scale of H₂ may be sensitive to resolution. In particular, small-scale turbulence makes the gas form dense clumps, which increases the formation rate of H₂ in turbulent clouds (e.g. Glover & Mac Low 2007b; Micic et al. 2012). However, our simulations do not resolve this small-scale turbulence, so it is likely that we underestimate the formation rate of H₂.

Krumholz & Gnedin (2011) compared the equilibrium H₂ model of Krumholz et al. (2008, 2009) and McKee & Krumholz (2010) to the non-equilibrium H₂ model of Gnedin & Kravtsov (2011), applied to cosmological zoom-in simulations of a Milky Way progenitor galaxy and to a simulation of a cosmological box, $25h^{-1}$ Mpc on a side, run with the Adaptive Refinement Tree (ART) code (Kravtsov 2003). They found excellent agreement at metallicities $\gtrsim 10^{-2} Z_{\odot}$, suggesting that non-equilibrium effects are unimportant for H₂ at the metallicities that we consider here. However, their simulations were run at a lower resolution than we use. For example, their cosmological zoom-in simulations had a maximum resolution of 65 pc, compared to a gravitational softening of 3.1 pc in our simulations.

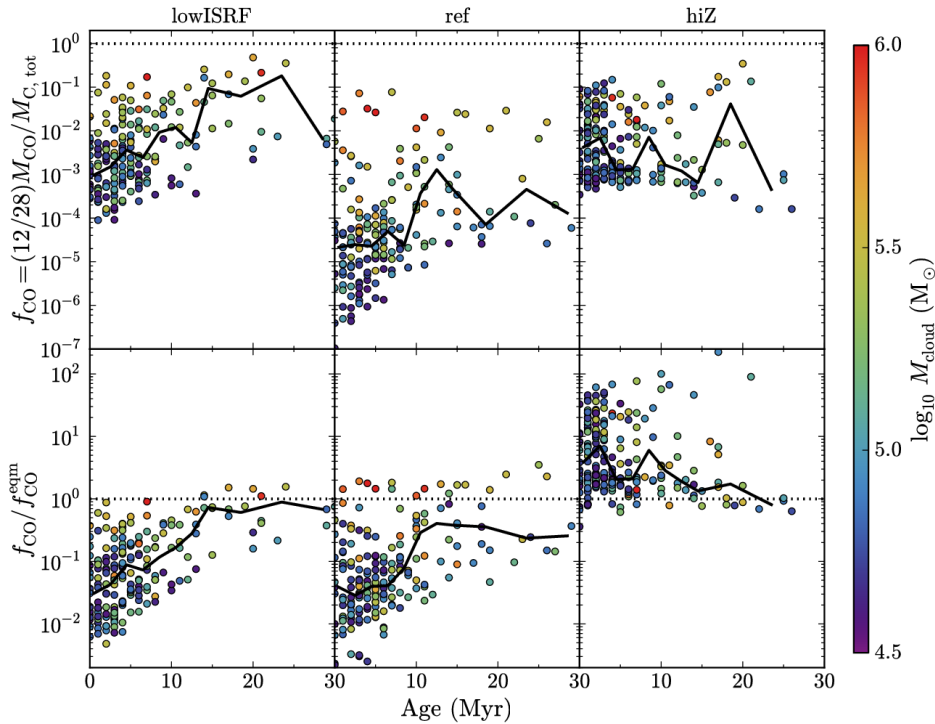


Figure 5.15: As Fig. 5.13, but for the CO fraction, $f_{\text{CO}} = (12/28)M_{\text{CO}}/M_{\text{C,tot}}$ (top row), and the ratio of the CO fraction to the equilibrium value, $f_{\text{CO}}/f_{\text{CO}}^{\text{eqm}}$. We define f_{CO} as the fraction, by mass, of carbon in CO molecules (hence the factor of $(12/28)$). The lowISRF and ref runs show increasing f_{CO} and $f_{\text{CO}}/f_{\text{CO}}^{\text{eqm}}$ with cloud age and mass, while the hiZ run shows no strong trends. For lowISRF and ref the CO fraction in young clouds is typically lower than in equilibrium, whereas for hiZ it is typically higher than in equilibrium.

5.5.2 Carbon monoxide

The top row of Fig. 5.15 shows the mass fraction of carbon in CO, $f_{\text{CO}} = \frac{12}{28} \frac{M_{\text{CO}}}{M_{\text{C,tot}}}$, for each cloud as a function of cloud age, where M_{CO} and $M_{\text{C,tot}}$ are the CO and total carbon masses respectively, while the bottom row shows $f_{\text{CO}}/f_{\text{CO}}^{\text{eqm}}$, where $f_{\text{CO}}^{\text{eqm}}$ is the CO mass fraction in chemical equilibrium. The colour scale indicates cloud mass, the black curves show the median in bins of age, and the left, centre and right columns show runs lowISRF, ref and hiZ respectively.

In runs lowISRF and ref, which both assume $0.1 Z_{\odot}$, we see that f_{CO} tends to increase with cloud age. However, there is more scatter in f_{CO} at fixed age than we saw for f_{H_2} in Fig. 5.13. A handful of clouds reach $f_{\text{CO}} \approx 0.5$ in the lowISRF run, but many are several orders of magnitude below unity.

In the bottom left and bottom centre panels, we see that f_{CO} in young clouds ($\lesssim 10 - 15$ Myr) tends to be below equilibrium by 1 – 2 orders of magnitude in the lowISRF and ref runs, while clouds older than this are typically closer to equilib-

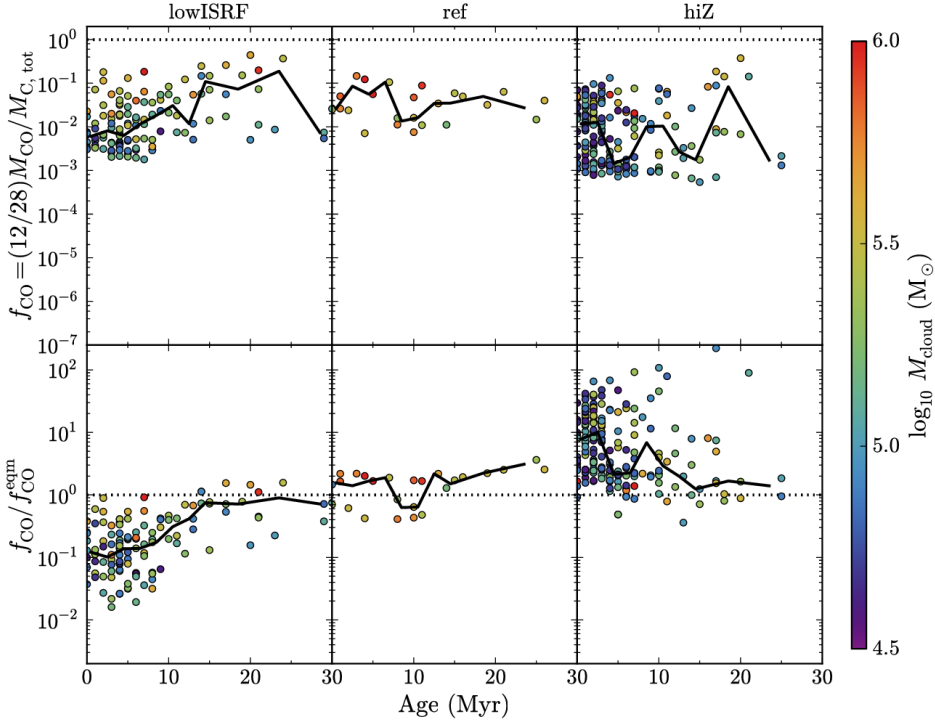


Figure 5.16: As Fig. 5.15, but only for the region within each cloud with $I_{\text{CO}} > 0.25 \text{ K km s}^{-1}$. The CO fraction in CO-detectable regions in the ref simulation is now close to equilibrium, even in young clouds, whereas with our previous cloud definition it was an order of magnitude below equilibrium in clouds younger than $\approx 10 \text{ Myr}$. However, for lowISRF and hiZ the median CO fraction in young clouds remains an order of magnitude lower and higher than in equilibrium, respectively.

rium, although for ref the median $f_{\text{CO}}/f_{\text{CO}}^{\text{eqm}}$ is still only $0.2 - 0.5$. However, these non-equilibrium effects do not fully explain the very low CO fractions that we find in the top row. These low values of f_{CO} are partly due to the density threshold, $n_{\text{H},\text{min}} = 10 \text{ cm}^{-3}$, that we use to define a cloud. This is close to the density of the H_I-to-H₂ transition, which can occur once H₂ becomes self-shielded. However, CO forms once it becomes shielded from dissociating radiation by dust, which typically occurs at higher densities.

The lowISRF and ref runs also show trends of f_{CO} with cloud mass, with more massive clouds showing higher CO fractions that are closer to equilibrium. This is because massive clouds are more likely to contain higher density regions where dust shielding is sufficient to form CO.

The simulation using solar metallicity (hiZ; right column) has higher CO fractions than the ref simulation. This is due to the higher dust abundance at higher metallicity, and hence stronger dust shielding from dissociating radiation. We see no strong trend of f_{CO} with cloud age in the hiZ simulation. In the bottom right

panel, we see that the CO fraction is either close to equilibrium or enhanced, by up to two orders of magnitude in some cases. The enhanced CO fractions that we see in the hiZ run are due to fluctuations in the dust extinction seen by individual particles within the cloud. Particles with enhanced CO abundances had $A_v \gtrsim 1$ within the previous few Myr, but A_v has since declined. Since the photodissociation rate of CO decreases exponentially with A_v , a small decrease in A_v can produce a large increase in photodissociation rate. However, it takes a finite time for the CO to be destroyed, thus we see enhanced CO abundances. We see much less enhancement of CO at lower metallicity (lowISRF and ref) because, in these runs, A_v rarely exceeds unity, thus CO rarely becomes fully shielded from dissociating radiation.

Fig. 5.16 shows CO fractions of clouds using a CO-based cloud definition, i.e. including only regions above the I_{CO} threshold. The effects of limiting our cloud definition to CO-detectable regions on CO fractions are similar to the effects it had on H_2 fractions that we saw in the previous section. In the lowISRF and ref runs, CO fractions are higher and show less scatter. The trends with cloud age in the lowISRF run are similar to those for a density-based cloud definition, while the ref simulation shows weaker evolution and is close to equilibrium, even in young clouds. The CO fractions in the hiZ run are mostly unaffected by the choice of cloud definition, and hence for young clouds they remain strongly enhanced compared to equilibrium.

5.6 CO emission and the X_{CO} factor

Observations of molecular clouds often use CO emission as a tracer of molecular gas. The H_2 column density is then determined from the CO intensity using a conversion factor, X_{CO} , as given in equation 5.1 (see Bolatto et al. 2013 for a recent review). If the abundances of H_2 and CO are out of equilibrium in young clouds, as we found to be the case in the previous section, then this may affect the X_{CO} factor. To investigate this, we used our maps of CO emission from the clouds in our simulations to measure X_{CO} .

The CO properties of a cloud are expected to depend on the dust extinction, as dust shields the cloud from photodissociating radiation, enabling the formation of CO (e.g. Lombardi et al. 2006; Pineda et al. 2008; Feldmann et al. 2012; Lee et al. 2015). Fig. 5.17 shows the mean velocity-integrated CO intensity (I_{CO} ; top row) and the mean X_{CO} factor (bottom row) in each cloud (using our density-based cloud definition) from our three simulations (lowISRF, ref and hiZ, in the left, centre and right columns respectively), as a function of the mean dust extinction, A_v . In each cloud, we average I_{CO} , A_v and the H_2 column density, N_{H_2} , over all pixels within the projected ellipse containing the cloud particles, i.e. the white ellipses in Fig. 5.5. The mean X_{CO} factor is then $\langle N_{H_2} \rangle / \langle I_{CO} \rangle$. The horizontal dotted line in the top row indicates $I_{CO} = 0.25 \text{ K km s}^{-1}$, which corresponds to the 3σ intensity threshold for the Small Magellanic Cloud in the observations of Leroy et al. (2011), and is the minimum I_{CO} threshold that we use in our CO-based cloud definition. In the bottom row, the horizontal dotted line shows a value of $X_{CO} = 2 \times 10^{20} \text{ cm}^{-2} (\text{K km s}^{-1})^{-1}$, typical of molecular clouds in the Milky Way

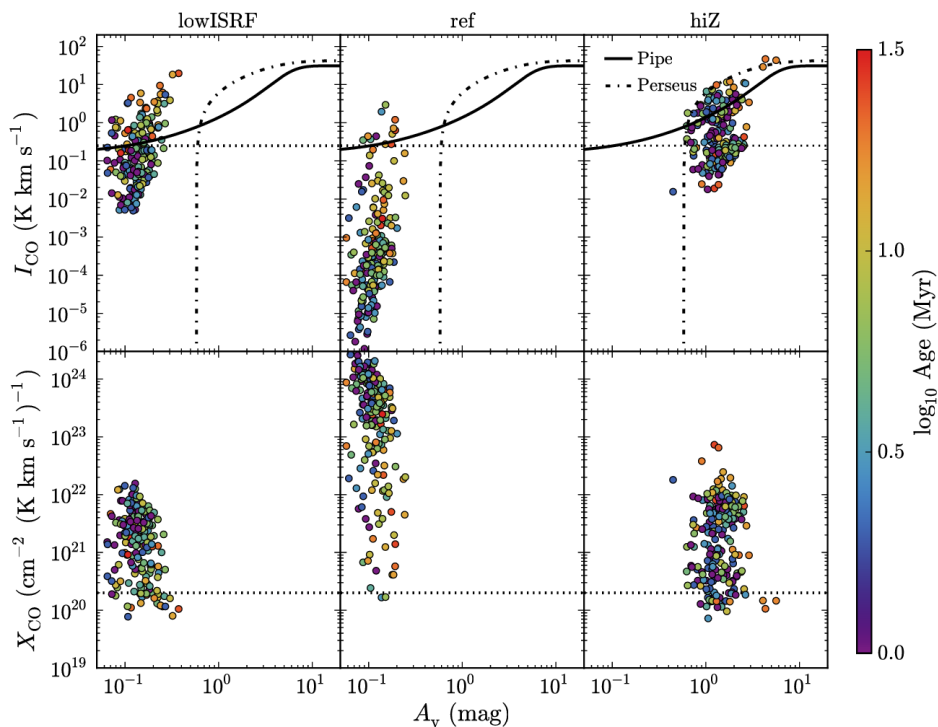


Figure 5.17: Mean velocity-integrated CO intensity, I_{CO} (top row), and X_{CO} factor (bottom row), plotted against mean dust extinction, A_v , for clouds from the lowISRF (left), ref (centre) and hiZ (right) simulations. We include all clouds with at least 50 particles in snapshots from 100 Myr to 900 Myr, in 100 Myr intervals. The colour scale indicates cloud age. In the top row, we also show the $I_{\text{CO}} - A_v$ relations observed in the Pipe nebula (Lombardi et al. 2006; solid curves) and the Perseus cloud (Pineda et al. 2008; dot-dashed curves) in the Milky Way. The horizontal dotted line in the top row indicates $I_{\text{CO}} = 0.25 \text{ K km s}^{-1}$, which corresponds to the 3σ intensity threshold for the Small Magellanic Cloud in the observations of Leroy et al. (2011). In the bottom row, the horizontal dotted line indicates the typical value measured in molecular clouds in the Milky Way, $X_{\text{CO}} = 2 \times 10^{20} \text{ cm}^{-2} (\text{K km s}^{-1})^{-1}$ (e.g. Bolatto et al. 2013).

(Bolatto et al. 2013). The colour scale in both rows indicates cloud age.

In the top row, we see that I_{CO} increases steeply with A_v , particularly in the lowISRF and ref simulations. For comparison, we also show the observed $I_{\text{CO}} - A_v$ relations seen in the Pipe nebula (Lombardi et al. 2006) and the Perseus cloud (Pineda et al. 2008) in the Milky Way. The observations of Pineda et al. (2008) in particular find that I_{CO} cuts off at low A_v , below a threshold $A_v = 0.58$. This is unsurprising, as CO typically relies on dust to become shielded from dissociating radiation before it can form. Therefore, the steep $I_{\text{CO}} - A_v$ relation that we find in our simulations is likely due to this threshold effect, with most clouds lying close to the threshold. Since A_v depends on the column density, along with metallicity, this

strong $I_{\text{CO}}-A_v$ relation reflects the fact that it is the column density, rather than the volume density, of a cloud that determines the molecular properties of the cloud, as this determines whether the cloud is shielded from dissociating radiation.

At high A_v , observations find that I_{CO} becomes saturated as the CO line becomes optically thick (e.g. Lombardi et al. 2006; Pineda et al. 2008). The lowISRF and ref simulations do not extend above $A_v \approx 0.4$ and so do not saturate, but the hiZ run contains clouds up to $A_v \approx 6$. These high- A_v clouds in the hiZ run do suggest a much shallower relation than at lower A_v in the same simulation, and are consistent with the observed saturation in Pineda et al. (2008), although we only have a few high- A_v clouds, so it is not clear if this relation is truly saturated in our simulations at high A_v .

Comparing the different panels in the top row, we see that the threshold A_v below which I_{CO} is strongly suppressed increases with metallicity (centre versus right) and, to a lesser extent, with the intensity of the radiation field (left versus centre). The dependence on radiation field is understandable, as a stronger radiation field requires a higher dust extinction before CO can become shielded.

However, the reason for the dependence on metallicity is more complicated. If CO is shielded only by dust, then the dissociation rate decreases $\propto \exp(-\gamma_d A_v)$, where $\gamma_d = 3.53$ (van Dishoeck et al. 2006). The threshold, A_v^{thresh} , then arises from the exponential cut off due to shielding. The formation of CO proceeds via a series of reactions, so the overall formation rate, R_{form} , will be determined by the rate-limiting step. These reactions are typically two-body interactions, so R_{form} scales with density squared. It also depends on the availability of carbon and oxygen, with densities $n_{\text{C,tot}}$ and $n_{\text{O,tot}}$ respectively, so $R_{\text{form}} \propto n_{\text{C,tot}} n_{\text{O,tot}} \propto Z^2 n_{\text{H,tot}}^2$, where Z is the metallicity and $n_{\text{H,tot}}$ is the total hydrogen number density. However, the rate-limiting step may depend on only Oxygen or Carbon, and not both (e.g. if the formation of an intermediate species such as CH_2^+ is the slowest step), in which case $R_{\text{form}} \propto Z n_{\text{H,tot}}^2$. If we define A_v^{thresh} to be when the CO fraction is some value, say $f_{\text{CO}} = 0.1$, then $\exp(-\gamma_d A_v^{\text{thresh}}) \propto Z^i n_{\text{H,tot}}^2$, where $i = 1$ or 2 , depending on the rate-limiting step in the formation of CO. Since the clouds in all three of our simulations follow the same mass-size relation, and have the same distribution of cloud masses (Fig. 5.2), the average cloud surface density and volume density are independent of Z . Thus, the metallicity dependence of A_v^{thresh} is given by:

$$A_v^{\text{thresh}} = -\frac{i}{\gamma_d} \ln(Z) + \text{constant}. \quad (5.12)$$

We therefore expect A_v^{thresh} to decrease weakly with increasing metallicity, if the attenuation of CO photodissociation is due to dust shielding. However, this is opposite to what is seen in Fig. 5.17.

The reason for this discrepancy is that, in the ref simulation, with ten per cent solar metallicity, the shielding of CO is primarily due to H_2 , and not dust. H_2 shielding will cut off the CO dissociation rate at a threshold H_2 column density, $N_{\text{H}_2}^{\text{thresh}} = f_{\text{H}_2} N_{\text{H,tot}}^{\text{thresh}}$, where f_{H_2} is the H_2 fraction of the cloud and $N_{\text{H,tot}}^{\text{thresh}}$ is the total hydrogen column density at the threshold. Then $A_v^{\text{thresh}} \propto Z N_{\text{H,tot}}^{\text{thresh}}$. If $N_{\text{H,tot}}^{\text{thresh}}$ is constant, A_v^{thresh} will increase linearly with Z . However, $N_{\text{H}_2}^{\text{thresh}}$ decreases logarithm-

mically with Z due to the increased CO formation rate, as described above, and f_{H_2} is generally higher in the hiZ run (Fig. 5.15). Additionally, dust shielding becomes more important at high metallicity, which further reduces $A_{\text{v}}^{\text{thresh}}$, and CO self-shielding also plays a role in some clouds. We thus find a sub-linear increase in $A_{\text{v}}^{\text{thresh}}$ with Z .

Pineda et al. (2008) find that the $I_{\text{CO}} - A_{\text{v}}$ relation in separate regions of the Perseus cloud also varies, suggesting that this relation depends on the physical conditions in the cloud. Using the Meudon PDR code (Le Petit 2006), they find that the variations in the $I_{\text{CO}} - A_{\text{v}}$ relation that they observe can be explained by variations in physical conditions, particularly volume density and internal gas motions. They also find that the $I_{\text{CO}} - A_{\text{v}}$ relation moves to higher A_{v} in the presence of stronger radiation fields in their models, consistent with what we see in our simulations. However, they do not consider variations in metallicity, which we find to be more important. Lee et al. (2015) measure the $I_{\text{CO}} - A_{\text{v}}$ relation in the Large and Small Magellanic Clouds, and compare these to the Milky Way. They find that, at fixed A_{v} , I_{CO} decreases with increasing dust temperature, suggesting a dependence on radiation field strength that is consistent with our simulations. However, they find that the $I_{\text{CO}} - A_{\text{v}}$ relations in these three galaxies are similar, despite their different metallicities.

The bottom row of Fig. 5.17 shows a large range in X_{CO} , spanning from two (lowISRF) to four (ref) orders of magnitude. We find no strong trends of X_{CO} with A_{v} . However, if we look at the highest- A_{v} clouds in the ref run ($A_{\text{v}} > 4$), the scatter in X_{CO} is much smaller, and the clouds lie within a factor two of the Milky Way value. We see a similar trend at high A_{v} when we lower the pressure floor in the ref run (see the bottom right panel of Fig. 5.24). As we discuss further in Appendix A, when we lower the pressure floor the clouds become more compact and extend to higher A_{v} . In the run with the lowest pressure floor ($N_{\text{J,m}} = 0.25$), the scatter in X_{CO} at $A_{\text{v}} > 0.3$ is reduced by a factor four compared to the whole sample, and at $A_{\text{v}} > 0.6$ the clouds are consistent with the Milky Way value of X_{CO} . This suggests that the large scatter arises because the clouds are diffuse, with low A_{v} , and the scatter is greatly reduced at high A_{v} . However, this is based on a small number of clouds.

Bell et al. (2006) find a strong relation between X_{CO} and A_{v} in their one-dimensional PDR models. However, the $X_{\text{CO}} - A_{\text{v}}$ relations that they consider show how X_{CO} varies with depth in a given cloud, whereas in Fig. 5.17 we show the mean X_{CO} and A_{v} for individual clouds. Indeed, Bell et al. (2006) show that their $X_{\text{CO}} - A_{\text{v}}$ relation varies with cloud properties such as density and turbulent velocity. The scatter that we find in X_{CO} in our simulations is therefore likely driven by the wide range of cloud properties in our sample.

In the two runs at $0.1 Z_{\odot}$ (lowISRF and ref), we find a trend of increasing I_{CO} with cloud age. This is consistent with the trend of increasing f_{CO} with age that we saw in Fig. 5.15. These two runs also show a trend of decreasing X_{CO} with increasing cloud age. The median X_{CO} factor in bins of age decreases by more than an order of magnitude for 0 to 15 Myr, although there is a large scatter (two and four orders of magnitude in lowISRF and ref, respectively) in X_{CO} at fixed age. The trend in X_{CO} at ages > 15 Myr is uncertain, as there are few clouds at

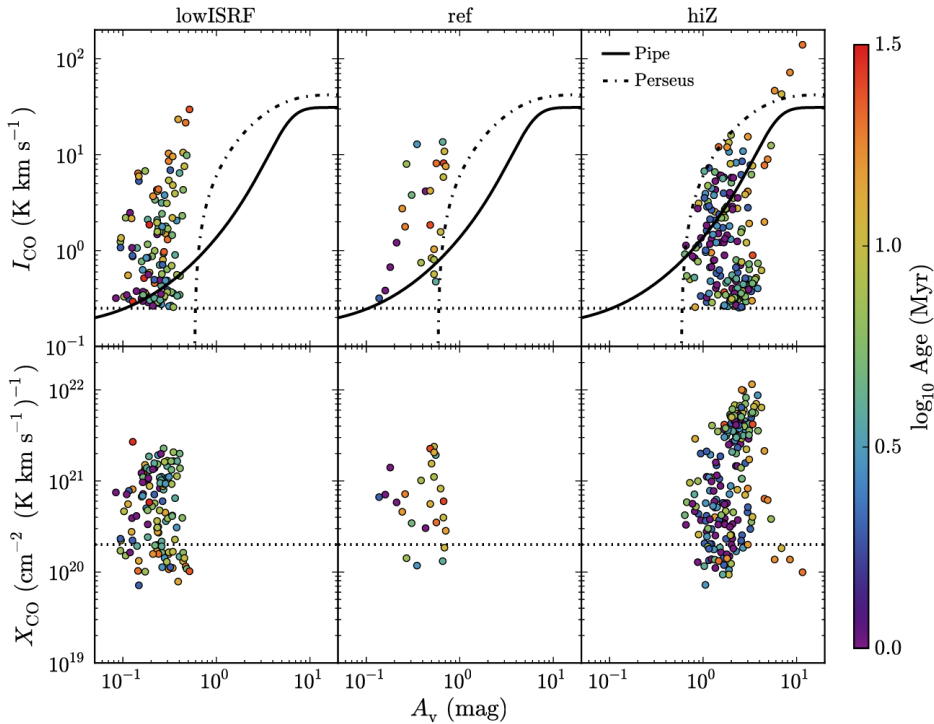


Figure 5.18: As Fig. 5.17, but for I_{CO} , X_{CO} and A_v averaged over only pixels with $I_{\text{CO}} > 0.25 \text{ K km s}^{-1}$. Note that the ranges of the y-axes are much smaller than in Fig. 5.17. There is much less scatter in I_{CO} and X_{CO} at fixed A_v compared to Fig. 5.17, as we exclude CO-faint pixels that would be undetectable in typical CO surveys of molecular clouds.

high ages. We see no strong trends of I_{CO} or X_{CO} with age at solar metallicity (hiZ), as the time-scales to reach equilibrium are shorter at higher metallicity, as we saw in Figs. 5.13 and 5.15.

In Fig. 5.18 we plot I_{CO} (top row) and X_{CO} (bottom row) versus A_v for our CO-based cloud definition, where these three quantities are now averaged over only pixels within the cloud with $I_{\text{CO}} > 0.25 \text{ K km s}^{-1}$. Note that the ranges of the y-axes are much smaller than in Fig. 5.17. In the lowISRF and ref simulations (left and centre columns), there is much less scatter in both I_{CO} and X_{CO} than we saw in Fig. 5.17, for a density-based cloud definition. The reduction in scatter in the hiZ simulation is more modest. We also see more clearly how the $I_{\text{CO}} - A_v$ relation shifts towards higher A_v at higher metallicity and, to a lesser extent, at higher radiation field strength. While most high- A_v clouds in the hiZ run remain consistent with the observed saturation of I_{CO} , there are now two clouds that lie a factor of $\approx 2 - 3$ above the observed relation. We again find no strong trends of X_{CO} with A_v , except that clouds with $A_v > 6$ in the hiZ run show much less scatter and are within a factor two of the Milky Way value. In the lowISRF run, the trend of median X_{CO} with cloud age is similar to that using a density-based

cloud definition, while the trend of X_{CO} with age in the ref run is much weaker when we use a CO-based cloud definition.

It is important to note that the values of the X_{CO} factor that we have presented in this section may be sensitive to resolution. In particular, as we noted in section 5.3.3, high-resolution simulations of dense clouds (e.g. Glover & Clark 2012) have found that most CO is concentrated in dense ($\sim 10^3 \text{ cm}^{-3}$), compact ($\sim 1 \text{ pc}$) structures that are poorly resolved in our simulations. This will make the predicted CO emission, and hence the X_{CO} factor, uncertain.

Smith et al. (2014) studied the molecular gas and CO properties in high resolution simulations of Milky Way-type galaxies, run with the moving mesh code AREPO (Springel 2010) and with time-dependent chemistry based on Glover & Mac Low (2007a,b) and Nelson & Langer (1997). They considered four simulations of galaxies with different surface densities and radiation field strengths, all assuming solar metallicity. The mean X_{CO} factor averaged over the galaxy in their four simulations was $3.89 - 13.1 \times 10^{20} \text{ cm}^{-2} (\text{K km s}^{-1})^{-1}$ when all gas was included. However, 42 – 85 per cent of the molecular mass in their simulations was ‘CO-dark’, with a CO intensity $\leq 0.1 \text{ K km s}^{-1}$. When they included only gas with $I_{\text{CO}} > 0.1 \text{ K km s}^{-1}$, the mean X_{CO} factor in their simulations was $1.48 - 2.28 \times 10^{20} \text{ cm}^{-2} (\text{K km s}^{-1})^{-1}$. In other words, when they included only CO-bright regions, the mean X_{CO} factor decreased. This agrees with the trend that we find in our simulations. Furthermore, the values of the mean X_{CO} factor found by Smith et al. (2014), averaged over the whole galaxy, overlap with the lowest values that we find for individual clouds, although we also find a large scatter in X_{CO} between clouds.

5.7 Conclusions

We have presented an analysis of GMCs identified in high-resolution ($750 M_{\odot}$ per particle and a gravitational softening of 3.1 pc) SPH simulations of isolated disc galaxies, with a particular emphasis on the evolution of molecular abundances and the implications for CO emission and the X_{CO} factor. Our simulations include a treatment for the non-equilibrium chemistry of 157 species, including 20 molecules (Richings et al. 2014a,b).

We define dense clouds in our simulations using two different methods, one that is physically motivated and another that is observationally motivated. First, we define clouds to be regions with a density above a threshold of $n_{\text{H}} = 10 \text{ cm}^{-3}$, which, depending on the metallicity and radiation field, is comparable to, or slightly lower than, the density of the HI-to-H₂ transition (e.g. Schaye 2001; Gnedin et al. 2009). We group gas particles above this threshold into clouds using a Friends-of-Friends (FoF) algorithm, with a linking length of $l = 10 \text{ pc}$.

The observationally motivated cloud definition is based on CO emission, where we restrict the cloud boundary to regions with a velocity-integrated CO intensity above a threshold of 0.25 K km s^{-1} . This allows for fairer comparison with observations, as it excludes CO-faint regions that would be undetectable in typical CO surveys of molecular clouds.

To highlight the effects of metallicity and radiation field, we run our simula-

tions at constant metallicity and with a uniform background UV radiation field, along with a prescription for local self-shielding by gas and dust (Richings et al. 2014b). Our three simulations cover two metallicities ($0.1 Z_{\odot}$ and Z_{\odot}) and two UV radiation fields (the ISRF of Black 1987, measured in the local solar neighbourhood, and ten per cent of this ISRF).

Our main results are as follows:

- (i) Our simulated clouds have a median lifetime of 13 Myr (Fig. 5.4), defined by the period over which at least half of the particles originally in the cloud when it was identified were in the main progenitor/descendant. This is consistent with observational estimates (e.g. Bash et al. 1977; Kawamura et al. 2009; Murray 2011; Miura et al. 2012), although see Elmegreen (2000) and Scoville et al. (1979) for examples of shorter and longer observational estimates of GMC lifetimes, respectively. If we instead define the cloud lifetime by tracking the total mass of its main progenitor/descendant, rather than only the original particles, we find that clouds survive longer, with a median lifetime of 33 Myr, as new gas cycles through the cloud.
- (ii) Simulated clouds follow a mass-size relation $M \propto R^2$, as observed in molecular clouds (e.g. Solomon et al. 1987; Roman-Duval et al. 2010). If we define clouds by a density threshold of $n_{\text{H}} = 10 \text{ cm}^{-3}$, then the normalisation is a factor ≈ 4 below the observed relation (Fig. 5.6). However, if we restrict our cloud definition to CO-detectable regions, we find better agreement with observations, with a normalisation that is a factor ≈ 2 below the observed relation (Fig. 5.7).
- (iii) The most massive clouds ($\gtrsim 6 \times 10^5 M_{\odot}$) tend to be aspherical, with minor-to-major axis ratios $\lesssim 0.4$ (Fig. 5.8), while clouds at lower masses show a wide range of minor-to-major axis ratios (0.1 – 1.0).
- (iv) Clouds defined by a density threshold approximately follow the observed velocity dispersion-size relation if we account for the contribution of the pressure floor in the velocity dispersion (Fig. 5.9), although there is a large scatter in the simulated relation. In particular, clouds within 1 kpc of the galactic centre typically lie 0.5 dex above the observed relation. We find better agreement with the observed relation when we use a CO-based cloud definition (Fig. 5.10).
- (v) Most clouds in our simulations are gravitationally unbound, with a virial parameter $\alpha > 2$ (Fig. 5.11). While some clouds are marginally bound, with $\alpha \approx 1 - 2$, all clouds have $\alpha > 1$, i.e. no clouds are virialised. However, this is partially due to the pressure floor, at least in low-mass clouds ($\lesssim 3 \times 10^5 M_{\odot}$). When we repeat the ref run with a lower pressure floor, reduced by a factor of 16 in terms of the Jeans mass, we do find some low-mass clouds with $\alpha < 1$ (Fig. 5.22).
- (vi) At ten per cent solar metallicity, young GMCs ($\lesssim 10 - 15$ Myr) are underabundant in H_2 and CO compared to chemical equilibrium, by factors ≈ 3

and 1 – 2 orders of magnitude respectively (Figs. 5.13 and 5.15). These non-equilibrium effects are less apparent at solar metallicity. The H_2 fraction at solar metallicity reaches within a factor 2 of equilibrium at 1 Myr, while the CO fraction at solar metallicity either remains close to equilibrium or becomes enhanced by up to two orders of magnitude compared to equilibrium. These non-equilibrium effects therefore depend strongly on metallicity, with no strong dependence on radiation field.

- (vii) If we restrict our analysis to CO-detectable regions (with $I_{\text{CO}} > 0.25 \text{ K km s}^{-1}$), we find higher H_2 and CO fractions, as we exclude the atomic outer envelope of clouds (Figs. 5.14 and 5.16). The simulation with a low metallicity and a low UV radiation field (lowISRF) shows similar trends of f_{H_2} and f_{CO} with age as for our standard cloud definition, although the simulation at low metallicity and for a high UV radiation field (ref) shows weaker evolution of f_{H_2} and f_{CO} with age.
- (viii) The mean CO intensity, I_{CO} , is strongly suppressed towards low dust extinction, A_v , and may become saturated at high A_v (Fig. 5.17), in agreement with observations (e.g. Pineda et al. 2008). Our simulated $I_{\text{CO}} - A_v$ relation moves towards higher A_v at higher metallicities and, to a lesser extent, for stronger UV radiation fields.
- (ix) There is large scatter (2 – 4 orders of magnitude) in the mean X_{CO} factor of individual clouds (Fig. 5.17). There are no strong trends with the mean dust extinction of the cloud, except that clouds at high A_v show much less scatter in X_{CO} and are within a factor of 2 of the Milky Way value (see also Fig. 5.24).
- (x) At ten per cent solar metallicity, we find weaker CO emission in young clouds, with ages $\lesssim 10 - 15 \text{ Myr}$ (Fig. 5.17), consistent with the trends we find for f_{CO} . This is also reflected in the median X_{CO} factor in bins of cloud age, which decreases by more than an order of magnitude from 0 to 15 Myr, although there is a large scatter in X_{CO} at fixed age. There are no strong trends with age at solar metallicity.
- (xi) By restricting our analysis to CO-detectable regions, we find less scatter in X_{CO} ($\approx 1 - 2$ orders of magnitude; Fig. 5.18). We also find better agreement with observed GMC scaling relations (Figs. 5.7 and 5.10).

We have therefore shown that, at ten per cent solar metallicity, clouds younger than $\approx 10 - 15 \text{ Myr}$ are likely to be underabundant in H_2 and CO compared to chemical equilibrium. CO is more strongly underabundant than H_2 in young clouds, which results in a trend of decreasing X_{CO} with increasing age from 0 to 15 Myr, albeit with a large scatter. Clouds at solar metallicity reach chemical equilibrium faster (within $\approx 1 \text{ Myr}$).

However, there are several caveats that we need to consider. Firstly, our simulations use a constant, uniform UV background. While we do include self-shielding

by gas and dust, which varies both spatially and temporally, the interstellar radiation field itself should also vary, due to the birth and evolution of nearby stars and due to relative motions between the gas and the stars. If the fluctuations in the radiation field occur on time-scales shorter than the chemical time-scale, they can drive abundances out of equilibrium (e.g. Oppenheimer & Schaye 2013). Additionally, radiative feedback from young, massive stars (due to photoionisation heating and/or radiation pressure) may disrupt their natal clouds and inhibit further formation of dense clouds (e.g. Dale et al. 2005; Krumholz & Matzner 2009; Hopkins et al. 2012; Walch et al. 2012; Rosdahl et al. 2015). These effects are not included in our simulations.

Secondly, the presence of turbulence can drive chemical abundances out of equilibrium, if the time-scale associated with the turbulence is short compared to the chemical time-scale (e.g. Gray et al. 2015). If we do not fully resolve small-scale turbulence in our simulations, we may therefore underestimate the effects of non-equilibrium chemistry. Conversely, the presence of unresolved turbulence will also create small-scale regions with higher densities than we resolve. The formation time-scales of molecules are shorter at higher densities, so they would reach equilibrium sooner in these unresolved high-density regions. This could lead us to overestimate the non-equilibrium chemistry.

Furthermore, our simulations include a density-dependent pressure floor to ensure that we always resolve the Jeans mass by at least four times the kernel mass. However, in the lowest-mass clouds ($\lesssim 3 \times 10^5 M_{\odot}$) this pressure floor prevents clouds from becoming gravitationally bound. In Appendix A we repeat our ref model with different pressure floors, to explore how this affects our results. As we lower the pressure floor, the lowest-mass, most poorly resolved clouds ($\lesssim 2 - 3 \times 10^5 M_{\odot}$) become more compact, more strongly gravitationally bound, and can live longer (up to ≈ 50 Myr). However, at higher masses clouds are unaffected. This also means that the run with the lowest pressure floor no longer reproduces the observed slope of the mass-size relation. It is therefore not clear whether using a lower pressure floor gives the physically correct solution, or if it is the result of artificial fragmentation and collapse that may arise when we do not fully resolve the Jeans scale (e.g. Bate & Burkert 1997; Truelove et al. 1997). To determine which is the physically correct solution, we would need to repeat these tests at higher resolution.

Despite these differences when we vary the pressure floor, we find that our main results for the median relations of molecule abundances with cloud age, and of CO intensity and X_{CO} factor with dust extinction, are insensitive to the pressure floor, although there is more scatter in these relations when we use a lower pressure floor.

A final caveat to note is that these conclusions depend on how the cloud age is defined. We have defined the cloud age from the time when half of the particles currently in the cloud were in a cloud progenitor. However, as we discussed in section 5.3.2, alternative definitions can result in different ages. Furthermore, our definition requires that we trace individual gas particles back in time. This is trivial in SPH simulations, but is not possible in observations, for which we only have a single snapshot of the cloud at the present day. Observational estimates of GMC

ages and lifetimes typically use nearby signatures of star formation, such as young stellar clusters and HII regions (e.g. Kawamura et al. 2009). We therefore need to be careful when comparing cloud ages from our simulations with observational estimates, as the two definitions may not be equivalent.

Acknowledgments

We are very grateful to Volker Springel for sharing GADGET3 and his initial conditions code, to Claudio Dalla Vecchia for allowing us to use ANARCHY, and to Benjamin Oppenheimer for code contributions. We gratefully acknowledge support from the European Research Council under the European Union’s Seventh Framework Programme (FP7/2007-2013) / ERC Grant agreement 278594-GasAroundGalaxies. This work used the DiRAC Data Centric system at Durham University, operated by the Institute for Computational Cosmology on behalf of the STFC DiRAC HPC Facility (www.dirac.ac.uk). This equipment was funded by BIS National E-infrastructure capital grant ST/K00042X/1, STFC capital grant ST/H008519/1, and STFC DiRAC Operations grant ST/K003267/1 and Durham University. DiRAC is part of the National E-Infrastructure. This work also used computer resources provided by the Gauss Centre for Supercomputing/Leibniz Supercomputing Centre under grant:pr83le. We further acknowledge PRACE for awarding us access to resource Supermuc based in Germany at LRZ Garching (proposal number 2013091919).

5.8 Appendix A: Effects of the pressure floor

In our simulations we impose a density-dependent pressure floor (equation 5.2) to ensure that we always resolve the Jeans mass by at least a factor $N_{J,m} = 4$ times the kernel mass. However, we saw in Fig. 5.11 that this pressure floor prevents the lowest-mass clouds ($\lesssim 3 \times 10^5 M_{\odot}$) from becoming gravitationally bound. While the pressure floor could represent sources of pressure that are not explicitly included in our models, such as unresolved turbulence, its functional form was motivated by numerical reasons, so we may overestimate the true pressure.

Conversely, if we remove the pressure floor entirely, so that we no longer resolve the Jeans mass in cold, dense gas, we may experience artificial fragmentation and collapse in gas that should be Jeans-stable. Bate & Burkert (1997) considered the resolution requirements in SPH simulations that include self-gravity, applied to the collapse and fragmentation of molecular clouds. In simulations where the gravitational softening length, ϵ_{soft} , is smaller than the SPH smoothing length, h_{sml} , which is the case for nearly all gas particles in our simulations (we use $\epsilon_{\text{soft}} = 3.1 \text{ pc}$), they found that, if the Jeans mass is not resolved by at least two times the kernel mass, gas can artificially undergo collapse when it should be Jeans-stable. The reason is that the thermal pressure is smoothed on scales of h_{sml} , while the gravitational force is smoothed on scales of ϵ_{soft} . Therefore, once a gas cloud becomes unresolved, the pressure force will be smoothed out before the gravitational force. Hence it will artificially lose pressure support against gravity and will undergo gravitational collapse.

A number of approaches have been proposed in the literature to alleviate these problems of artificial fragmentation that may occur when the Jeans scale is unresolved. Booth et al. (2007) developed a prescription for star formation and feedback in disc galaxies in which unresolved molecular gas is modelled by ‘sticky particles’ that coagulate when they collide. Narayanan et al. (2011) also use a subgrid prescription to model the unresolved cold, molecular gas, which involves hybrid SPH particles that include both the warm and the cold ISM phases. Robertson & Kravtsov (2008) imposed a pressure floor in their SPH simulations of disc galaxies by setting a minimum internal energy (i.e. a temperature floor). They explored a range of temperature floors, corresponding to $N_{J,m} = 2 - 200$ in our nomenclature (see their appendix A), and they used a fiducial floor with $N_{J,m} = 30$. Hopkins et al. (2011) used the pressure floor of Robertson & Kravtsov (2008) in their SPH simulations of disk galaxies, with $N_{J,m} = 10$ (although they also consider $N_{J,m} = 4 - 15$, see their appendix A). Schaye & Dalla Vecchia (2008) imposed a polytropic equation of state, $P \propto \rho^{\gamma_{\text{eff}}}$, in their SPH simulations of disc galaxies. They used $\gamma_{\text{eff}} = 4/3$ so that m_{gas}/M_J and h_{sml}/L_J are constant, where m_{gas} is the SPH particle mass, h_{sml} is the SPH smoothing length, and M_J and L_J are the Jeans mass and length, respectively. They set the normalisation of the equation of state such that $N_{J,m} = 6$.

However, not all simulation studies have imposed a Jeans limiter. For example, Clark & Glover (2015) simply ended their SPH simulations of molecular clouds once the Jeans scale became unresolved. However, they used a very high resolution ($0.005 M_{\odot}$ per particle and 50 SPH neighbours), so they could follow the gravitational collapse up to a density of $\sim 10^6 \text{ cm}^{-3}$. Walch (2015) also did not include a Jeans limiter in their SPH simulations of supernova feedback in molecular clouds. The densities in some of their simulations extended up to $\sim 10^6 \text{ cm}^{-3}$ (see their fig. 3), but they used a lower resolution than Clark & Glover (2015), with $0.1 M_{\odot}$ per SPH particle, so the Jeans scale will be unresolved in some of their simulations. However, unlike the simulations of Bate & Burkert (1997) and Clark & Glover (2015), Walch (2015) included stellar feedback, which may help to alleviate the problem of artificial fragmentation by heating the gas before it can collapse. There are also other studies that do not explicitly include a Jeans limiter, for example Gnedin & Kravtsov (2011); Glover & Mac Low (2011); Shetty et al. (2011a,b); Dobbs & Pringle (2013).

To explore how the pressure floor affects our results, we repeated the ref model twice, with the pressure floor reduced by factors of 4 and 16 in terms of the Jeans mass (i.e. with $N_{J,m} = 1$ and 0.25, respectively). These simulations were run for 100 Myr, and we then compared clouds at 100 Myr in these runs with the ref model (whereas previously we have been combining clouds from nine snapshots at 100 Myr intervals).

Fig. 5.19 shows the cloud mass functions, which are similar for the three pressure floors. In Fig. 5.20 we show the cloud age as a function of mass, where the cloud age is defined by the time when half of the particles that were originally in the cloud in the current snapshot (100 Myr) were in a progenitor of that cloud, i.e. our fiducial age definition (see section 5.3.2). The left, centre and right panels show the results for a pressure floor with $N_{J,m} = 4, 1$ and 0.25, respectively. In

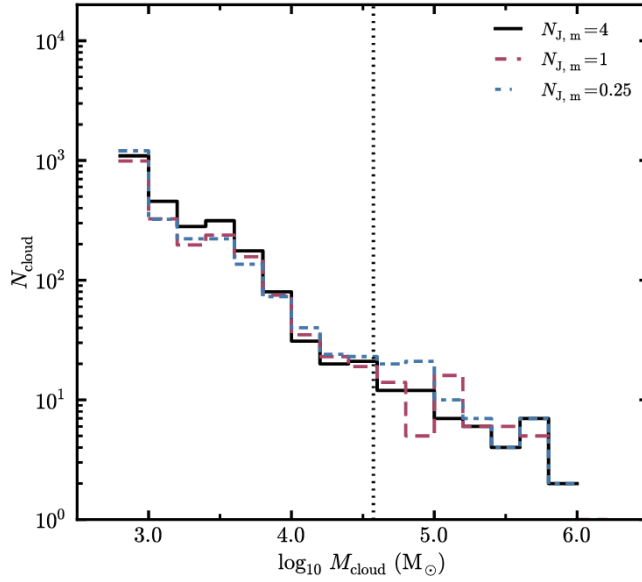


Figure 5.19: Cloud mass functions for the ref model, using a pressure floor with $N_{J,m} = 4$ (black solid curve), $N_{J,m} = 1$ (red dashed curve) and $N_{J,m} = 0.25$ (blue, dot-dashed curve), where $N_{J,m}$ is the ratio of the minimum Jeans mass to the mass within the SPH kernel. The cloud mass function is insensitive to the pressure floor.

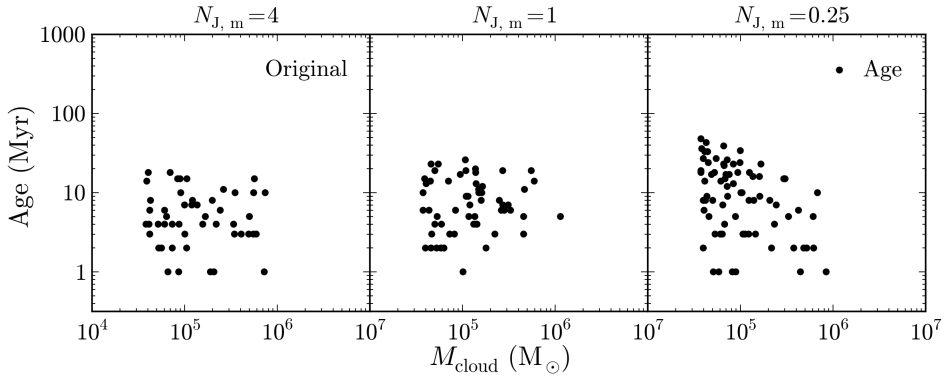


Figure 5.20: Cloud age versus mass for all clouds in the snapshot at 100 Myr in the ref model with three different pressure floors: $N_{J,m} = 4$, 1 and 0.25 (left, centre and right panels, respectively). In the run with the lowest pressure floor (right panel), low-mass clouds can survive for longer (up to 50 Myr) than in the run with our fiducial pressure floor (left panel).

the run with the lowest pressure floor (right panel), we find clouds extending up to higher ages (up to 50 Myr). However, the longest-lived clouds (≥ 30 Myr) in this simulation are only found in the lowest-mass, most poorly resolved clouds ($M_{\text{cloud}} \lesssim 10^5 M_{\odot}$), whereas we see no trends between cloud age and mass with

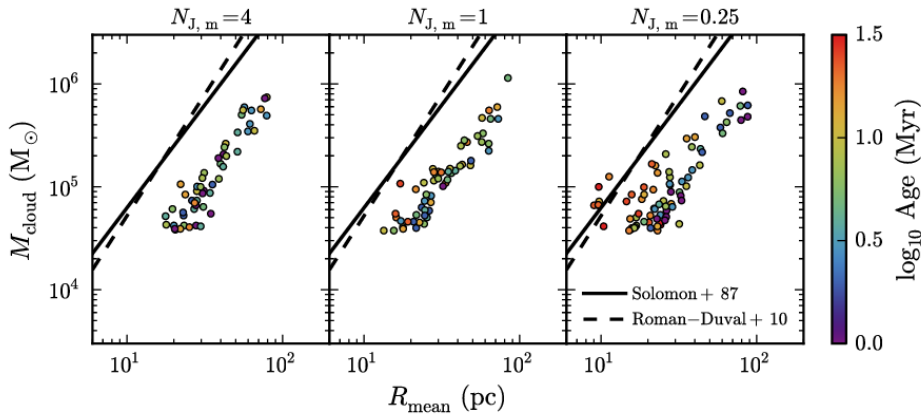


Figure 5.21: Mass-size relation for clouds in the snapshot at 100 Myr, from the ref model with three different pressure floors: $N_{J,m} = 4$, 1 and 0.25 (left, centre and right panels, respectively). The colour scale indicates the cloud age. We also show the observed relations from Solomon et al. (1987) (solid curves) and Roman-Duval et al. (2010) (dashed curves). In the run with $N_{J,m} = 0.25$, low-mass clouds are more compact, but this run no longer reproduces the observed slope of this relation.

higher pressure floors.

Fig. 5.21 shows the mass-size relation for clouds with the different pressure floors. The colour scale indicates the cloud age, and the black solid and dashed curves show the observed relations of Solomon et al. (1987) and Roman-Duval et al. (2010), respectively. The run with the lowest pressure floor (right panel) shows more scatter in this relation, with clouds of the same mass generally being more compact than in the $N_{J,m} = 4$ run. Additionally, the most compact clouds, i.e. those that lie to the left of the relation, tend to be older ($\gtrsim 30$ Myr). This is understandable, as more compact objects will be more strongly gravitationally bound, and thus can survive for longer. This explains the longer cloud ages that we saw in Fig. 5.20 in the $N_{J,m} = 0.25$ run.

However, it is only the lowest-mass, most poorly resolved clouds that are more compact in the $N_{J,m} = 0.25$ run than in the $N_{J,m} = 4$ run. The highest-mass clouds ($\gtrsim 3 \times 10^5 M_{\odot}$) appear unaffected by the pressure floor. This also means that the mass-size relation in the $N_{J,m} = 0.25$ run is flatter than is observed. While the clouds in the $N_{J,m} = 4$ run lie further from the observed relations, they do recover the same slope, and the difference in normalisation can be explained by the differences in cloud definition (as seen in Figs. 5.6 and 5.7). Therefore, it is not clear whether the more compact clouds that we find when we lower the pressure floor are physically correct, or if they are an artifact of spurious fragmentation and collapse that may arise when we do not fully resolve the Jeans scale. To determine what the physically correct solution is, we would need to repeat these tests at a higher resolution.

Fig. 5.22 shows the virial parameter, α , as a function of cloud mass, for the

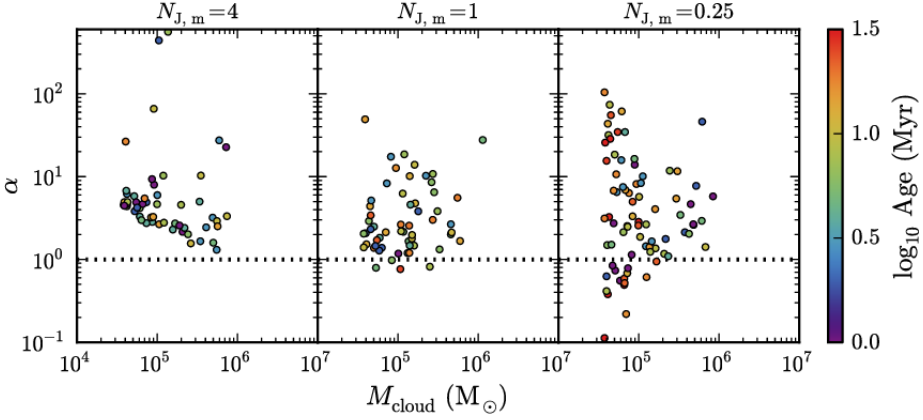


Figure 5.22: Cloud virial parameter, α , versus mass, for the ref model with three different pressure floors: $N_{J,m} = 4$, 1 and 0.25 (left, centre and right panels, respectively). The colour scale indicates the cloud age, and the horizontal dotted lines show a value of $\alpha = 1$, below which clouds are gravitationally bound. The lower envelope of α decreases as we lower the pressure floor, with some low-mass clouds in the $N_{J,m} = 0.25$ run becoming strongly gravitationally bound. However, it is not clear whether this result is physically correct, or if it is an artifact of spurious collapse that may arise when we do not fully resolve the Jeans scale (see text).

three pressure floors (in different panels). The horizontal dotted line indicates a value of $\alpha = 1$, below which clouds are gravitationally bound. In the left panel, for our fiducial pressure floor, $N_{J,m} = 4$, we see a lower envelope in α that declines with cloud mass as $\alpha \propto M_{\text{cloud}}^{-2/3}$. This scaling is due to the pressure floor, as discussed in section 5.4, and means that, in the $N_{J,m} = 4$ run, the pressure floor prevents the lowest-mass clouds from becoming gravitationally bound.

As we lower the pressure floor, the low-mass clouds extend to lower values of α , and can become strongly gravitationally bound in the $N_{J,m} = 0.25$ run (although there are still clouds with high values of α as well). This is consistent with the more compact low-mass clouds that we saw in this run in Fig. 5.21. However, as noted above, it is not clear whether this result is the physically correct one, or if it is an artifact of spurious fragmentation and collapse. In particular, it is only the low mass, most poorly resolved clouds that become more strongly gravitationally bound when we lower the pressure floor. High-mass clouds ($\gtrsim 2 \times 10^5 M_{\odot}$) are unaffected.

We now need to consider whether varying the pressure floor affects the evolution of molecular abundances, the CO emission or the X_{CO} factors of individual clouds. Fig. 5.23 shows the H_2 fraction, f_{H_2} (top row), and the ratio of f_{H_2} to the equilibrium H_2 fraction, $f_{\text{H}_2}^{\text{eqm}}$ (bottom row), plotted against cloud age, for the three pressure floors (in different columns). As we lower the pressure floor (left to right), clouds extend to higher ages, as we saw in Fig. 5.20. However, the median values of f_{H_2} and $f_{\text{H}_2}/f_{\text{H}_2}^{\text{eqm}}$ at fixed cloud age are similar, regardless of the pressure

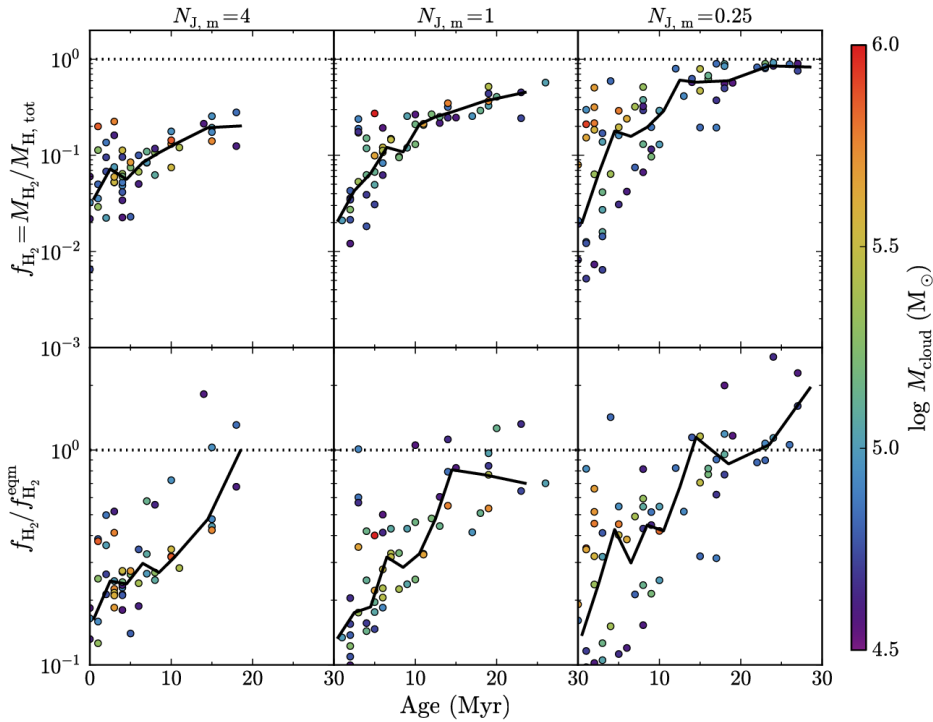


Figure 5.23: H_2 fraction, f_{H_2} (top row), and the ratio of f_{H_2} to the H_2 fraction in equilibrium, $f_{\text{H}_2}^{\text{eqm}}$, plotted against cloud age, for clouds in the snapshot at 100 Myr from the ref model with three different pressure floors: $N_{J,m} = 4$, 1 and 0.25 (left, centre and right columns, respectively). The colour scale indicates the cloud mass, the solid curves indicate the median relation in bins of age, and the horizontal dotted lines indicate a value of unity. As we lower the pressure floor, clouds extend to higher ages, but continue to follow similar median relations of f_{H_2} and $f_{\text{H}_2} / f_{\text{H}_2}^{\text{eqm}}$ with age, albeit with more scatter.

floor. Thus, by lowering the pressure floor, we simply extend the same median relations of f_{H_2} and $f_{\text{H}_2} / f_{\text{H}_2}^{\text{eqm}}$ versus cloud age to higher ages, although the scatter also increases. In particular, in all three runs it takes $\approx 10 - 15$ Myr for the median f_{H_2} to reach within a factor two of its equilibrium value.

When we lower the pressure floor, the CO fractions (not shown) also follow similar median relations with cloud age as for our fiducial pressure floor, albeit with more scatter.

Fig. 5.24 shows the mean CO intensity, I_{CO} (top row), and the mean X_{CO} factor (bottom row) of each cloud for the three pressure floors as a function of mean dust extinction, A_v . As we lower the pressure floor, clouds extend to higher A_v , as they become more compact. However, they continue to follow a similar trend of I_{CO} with A_v , although there is more scatter in this relation with a lower pressure floor. In particular, the threshold A_v below which I_{CO} cuts off does not appear to be strongly affected by the pressure floor, i.e. the $I_{\text{CO}} - A_v$ relation does not move horizontally in this plot. However, the increased scatter as we reduce the

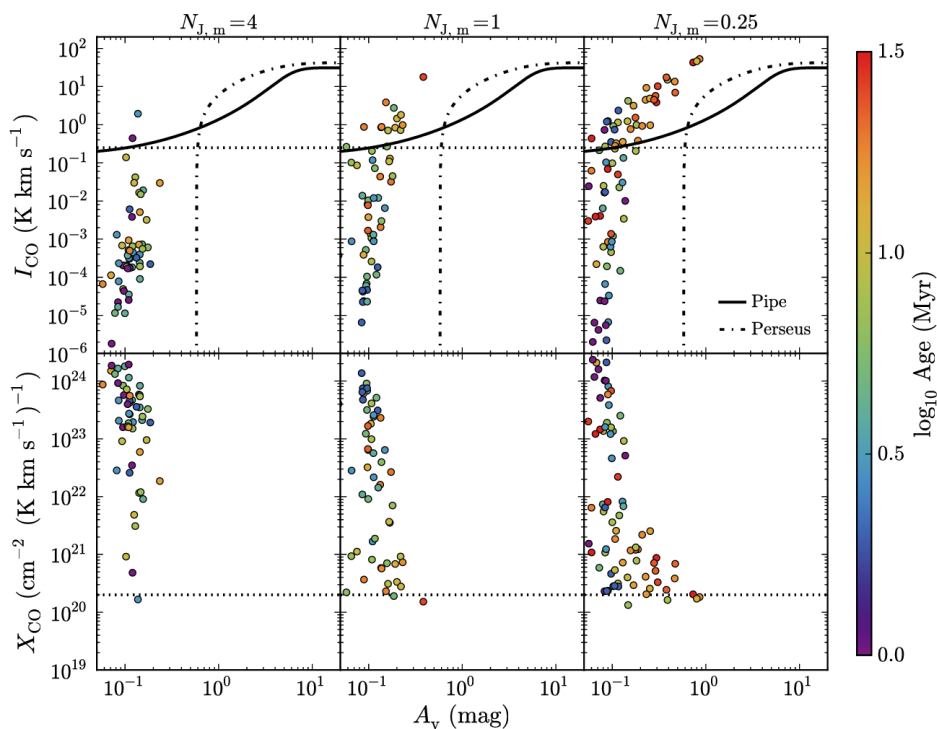


Figure 5.24: Mean CO intensity, I_{CO} (top row), and X_{CO} factor (bottom row), plotted against mean dust extinction, A_v . The colour scale indicates the cloud age. In the top row, we also show the $I_{\text{CO}} - A_v$ relations observed in the Pipe nebula (Lombardi et al. 2006; solid curves) and the Perseus cloud (Pineda et al. 2008; dot-dashed curves). The horizontal dotted lines in the top row indicate a value of $I_{\text{CO}} = 0.25 \text{ K km s}^{-1}$, which corresponds to the 3σ intensity threshold for the Small Magellanic Cloud in the observations of Leroy et al. (2011). In the bottom row, the horizontal dotted lines indicate the typical value measured in the Milky Way, $X_{\text{CO}} = 2 \times 10^{20} \text{ cm}^{-2} (\text{K km s}^{-1})^{-1}$ (e.g. Bolatto et al. 2013). As we lower the pressure floor, clouds extend to higher A_v , as they become more compact. However, for the values of A_v where the different runs overlap, the $I_{\text{CO}} - A_v$ relations are consistent, albeit with more scatter, particularly in I_{CO} , and with a shallower cut-off in I_{CO} towards low A_v .

pressure floor means that we find some low- A_v clouds ($A_v \approx 0.06$) with higher CO intensities ($I_{\text{CO}} \approx 0.3 \text{ K km s}^{-1}$), so the cut-off in I_{CO} at low A_v is less steep than in the $N_{\text{J},m} = 4$ run.

The X_{CO} factors all show similar scatter of four orders of magnitude, regardless of pressure floor. In the $N_{\text{J},m} = 0.25$ run, the high- A_v clouds (≥ 0.3) show less scatter in X_{CO} (one order of magnitude) and suggest a trend of decreasing X_{CO} with increasing A_v . This trend cannot be verified in the $N_{\text{J},m} = 4$ run, because it does not include these high- A_v clouds. However, for the range of A_v where these three runs overlap, they show consistent $X_{\text{CO}} - A_v$ relations.

To conclude, lowering the pressure floor results in low mass clouds ($\leq 3 \times 10^5 M_{\odot}$) becoming more compact, more strongly gravitationally bound, and able

to survive for longer. However, it is not clear whether this is the physically correct result, or if it is an artifact of spurious fragmentation and collapse that may arise when we do not fully resolve the Jeans scale. In particular, the run with the lowest pressure floor ($N_{J,m} = 0.25$) no longer reproduces the observed slope of the cloud mass-size relation (Solomon et al. 1987; Roman-Duval et al. 2010). To determine which is the physically correct solution, we would need to repeat these tests at a higher resolution.

Furthermore, we find similar median trends of f_{H_2} and $f_{\text{H}_2}/f_{\text{H}_2}^{\text{eqm}}$ versus cloud age, and I_{CO} and X_{CO} versus A_v , regardless of pressure floor. Lowering the pressure floor simply extends these relations to higher ages and A_v , albeit with more scatter.

References

- Abdo A. A. et al., 2010, *ApJ*, 710, 133
Ackermann M. et al., *A&A*, 538, 71
Bash F. N., Green E., Peters W. L., III, 1977, *ApJ*, 217, 464
Bate M. R., Burkert A., 1997, *MNRAS*, 288, 1060
Bell T. A., Roueff E., Viti S., Williams D. A., 2006, *MNRAS*, 371, 1865
Bertoldi F., McKee C. F., 1992, *ApJ*, 395, 140
Black J. H., 1987, *ASSL*, 134, 731
Bolatto A. D., Leroy A. K., Rosolowsky E., Walter F., Blitz L., 2008, *ApJ*, 686, 948
Bolatto A. D., Wolfire M., Leroy A. K., 2013, *ARA&A*, 51, 207
Booth C. M., Theuns T., Okamoto T., 2007, *MNRAS*, 376, 1588
Cazaux S., Tielens A. G. G. M., 2002, *ApJ*, 575, L29
Chabrier G., 2003, *PASP*, 115, 763
Clark P. C., Glover S. C. O., 2015, arXiv:1506.06503
Clemens D. P., Sanders D. B., Scoville N. Z., Solomon P. M., 1986, *ApJS*, 60, 297
Cullen L., Dehnen W., 2010, *MNRAS*, 408, 669
Dabrowski I., 1984, *Can. J. Phys.*, 62, 1639
Dale J. E., Bonnell I. A., Clarke C. J., Bate M. R., 2005, *MNRAS*, 358, 291
Dalla Vecchia C., Schaye J., 2012, *MNRAS*, 426, 140
Dame T. M., Hartmann D., Thaddeus P., 2001, *ApJ*, 547, 792
Dobbs C. L., Burkert A., Pringle J. E., 2011, *MNRAS*, 413, 2935
Dobbs C. L., Pringle J. E., 2013, *MNRAS*, 432, 653
Dobbs C. L., Pringle J. E., Duarte-Cabral A., 2015, *MNRAS*, 446, 3608
Duffy A. R., Schaye J., Kay S. T., Dalla Vecchia C., 2008, *MNRAS*, 390, 64
Durier F., Dalla Vecchia C., 2012, *MNRAS*, 419, 465
Elmegreen B. G., 2000, *ApJ*, 530, 277
Feldmann R., Gnedin N. Y., Kravtsov A. V., 2012, *ApJ*, 747, 124
Ferland G. J. et al., 2013, *RMxAA*, 49, 137
Frerking M. A., Langer W. D., Wilson R. W., 1982, *ApJ*, 262, 590
Glover S. C. O., Mac Low M.-M., 2007a, *ApJS*, 169, 239
Glover S. C. O., Mac Low M.-M., 2007b, *ApJ*, 659, 1317
Glover S. C. O., Mac Low M.-M., 2011, *MNRAS*, 412, 337
Glover S. C. O., Clark P. C., 2012, *MNRAS*, 426, 377

- Gnedin N. Y., Tassis K., Kravtsov A. V., 2009, *ApJ*, 697, 55
Gnedin N. Y., Kravtsov A. V., *ApJ*, 728, 88
Gray W. J., Scannapieco E., Kasen D., 2015, *ApJ*, 801, 107
Haardt F., Madau P., 2001, in Neumann D. M., Tran J. T. V., eds, *XXIst Moriond Astrophys. Meeting, Clusters of Galaxies and the High Redshift Universe Observed in X-rays* Editions Frontieres, Paris, 64
Hernquist L., 1990, *ApJ*, 356, 359
Heyer M. H., Carpenter J. M., Snell R. L., 2001, *ApJ*, 551, 852
Heyer M., Krawczyk C., Duval J., Jackson J. M., 2009, *ApJ*, 699, 1092
Hopkins P. F., Quataert E., Murray N., 2011, *MNRAS*, 417, 950
Hopkins P. F., Quataert E., Murray N., 2012, *MNRAS*, 421, 3488
Hopkins P. F., 2013, *MNRAS*, 428, 2840
Jackson J. M. et al., 2006, *ApJS*, 163, 145
Kawamura et al., 2009, *ApJS*, 184, 1
Kravtsov A. V., 2003, *ApJ*, 590, L1
Krumholz M. R., McKee C. F., Tumlinson J., 2008, *ApJ*, 689, 865
Krumholz M. R., Matzner C. D., 2009, *ApJ*, 703, 1352
Krumholz M. R., McKee C. F., Tumlinson J., 2009, *ApJ*, 693, 216
Krumholz M. R., Gnedin N. Y., 2011, *ApJ*, 729, 36
Larson R. B., 1981, *MNRAS*, 194, 809
Lee C., Leroy A. K., Schnee S., Wong T., Bolatto A. D., Indebetouw R., Rubio M., 2015, *MNRAS*, 450, 2708
Le Petit F., Nehmé C., Le Bourlot J., Roueff E., 2006, *ApJS*, 164, 506
Leroy A. K. et al., 2011, *ApJ*, 737, 12
Lombardi M., Alves J., Lada C. J., 2006, *A&A*, 454, 781
Martin P. G., Whittet D. C. B., 1990, *ApJ*, 357, 113
Mathis J. S., Rumpl W., Nordsieck K. H., 1977, *ApJ*, 217, 425
McKee C. F., Ostriker E. C., 2007, *ARA&A*, 45, 565
McKee C. F., Krumholz M. R., 2010, *ApJ*, 709, 308
Micic M., Glover S. C. O., Federrath C., Klessen R. S., 2012, *MNRAS*, 421, 2531
Miura R. E. et al., 2012, *ApJ*, 761, 37
Moster B. P., Naab T., White S. D. M., 2013, *MNRAS*, 428, 3121
Murray N., 2011, *ApJ*, 729, 133
Narayanan D., Krumholz M., Ostriker E. C., Hernquist L., 2011, *MNRAS*, 418, 664
Narayanan D., Krumholz M. R., Ostriker E. C., Hernquist L., 2012, *MNRAS*, 421, 3127
Navarro J. F., Frenk C. S., White S. D. M., 1996, *ApJ*, 462, 563
Nelson R. P., Langer W. D., 1997, *ApJ*, 482, 796
Oka T., Hasegawa T., Sato F., Tsuboi M., Miyazaki A., Sugimoto M., 2001, *ApJ*, 562, 348
Oppenheimer B. D., Schaye J., 2013b, *MNRAS*, 434, 1063
Pineda J. E., Caselli P., Goodman A. A., 2008, *ApJ*, 679, 481
Planck Collaboration XIX, 2011, *A&A*, 536, 19
Portinari L., Chiosi C., Bressan A., 1998, *A&A*, 334, 505
Price D. J., 2008, *J. Comput. Phys.*, 227, 10040

- Richings A. J., Schaye J., Oppenheimer B. D., 2014a, MNRAS, 440, 3349
Richings A. J., Schaye J., Oppenheimer B. D., 2014b, MNRAS, 442, 2780
Richings A. J., Schaye J., 2015, arXiv:1506.08829
Robertson B. E., Kravtsov A. V., 2008, ApJ, 680, 1083
Roman-Duval J., Jackson J. M., Heyer M., Rathborne J., Simon R., 2010, ApJ, 723, 492
Rosdahl J., Schaye J., Teyssier R., Agertz O., 2015, MNRAS, 451, 4553
Rosolowsky E., 2007, ApJ, 654, 240
Sanders D. B., Clemens D. P., Scoville N. Z., Solomon P. M., 1986, ApJS, 60, 1
Sawala T. et al., 2015, MNRAS, 448, 2941
Schaye J., 2001, ApJ, 562, L95
Schaye J., Dalla Vecchia C., 2008, MNRAS, 383, 1210
Schaye J. et al., 2015, MNRAS, 446, 521
Schöier F. L., van der Tak F. F. S., van Dishoeck E. F., Black J. H., 2005, A&A, 432, 369
Scoville N. Z., Solomon P. M., Sanders D. B., 1979, in Burton W. D., ed., Proc. IAU Symp. 84, The Large-Scale Characteristics of the Galaxy, Reidel, Dordrecht, p. 277
Scoville N. Z., Yun M. S., Clemens D. P., Sanders D. B., Waller W. H., 1987, ApJS, 63, 821
Shetty R., Glover S. C., Dullemond C. P., Klessen R. S., 2011a, MNRAS, 412, 1686
Shetty R., Glover S. C., Dullemond C. P., Ostriker E. C., Harris A. I., Klessen R. S., 2011b, MNRAS, 415, 3253
Smith R. J., Glover S. C. O., Clark P. C., Klessen R. S., Springel V., 2014, MNRAS, 441, 1628
Sobolev V. V., 1957, SvA, 1, 678
Solomon P. M., Rivolo A. R., Barrett J., Yahil A., 1987, ApJ, 319, 730
Springel V., 2005, MNRAS, 364, 1105
Springel V., Di Matteo T., Hernquist L., 2005, MNRAS, 361, 776
Springel V., 2010, MNRAS, 401, 791
Sternberg A., Le Petit F., Roueff E., Le Bourlot J., 2014, ApJ, 190, 10
Strong A. W., Mattox J. R., 1996, A&A, 308, L21
Tielens A. G. G. M., Hollenbach D., 1985, ApJ, 291, 722
Truelove J. K., Klein R. I., McKee C. F., Holliman J. H. II, Howell L. H., Greenough J. A., 1997, ApJ, 489, L179
van Dishoeck E. F., Black J. H., 1988, ApJ, 334, 771
van Dishoeck E. F., Jonkheid B., van Hemert M. C., 2006, Faraday Discuss., 133, 231
Visser R., van Dishoeck E. F., Black J. H., 2009, A&A, 503, 323
Walch S. K., Whitworth A. P., Bisbas T., Wunsch R., Hubber D., 2012, MNRAS, 427, 625
Walch S., Naab T., 2015, MNRAS, 451, 2757
Wendland H., 1995, Adv. Comput. Math. 4, 389
Williams J. P., Bergin E. A., Caselli P., Myers P. C., Plume, R., 1998, ApJ, 503, 689
Yang B., Stancil P. C., Balakrishnan N., Forrey R. C., 2010, ApJ, 718, 1062

THESIS SUMMARY AND FUTURE OUTLOOK

Galaxies are gravitationally bound objects consisting of stars and gas, embedded within extended haloes of non-luminous ‘dark matter’, which interacts only via gravity. Understanding how galaxies form and evolve is an exciting area of research that has made great progress in recent decades.

In our current picture of galaxy formation, most of the matter in the Universe is in the dark matter component, which dominates the large-scale structure. Since dark matter interacts only via gravity, it is dissipationless, meaning that it cannot cool and radiate away its energy. Therefore, as it collapses under the influence of gravity, it forms extended, approximately spherical haloes. Gas, on the other hand, is dissipative, so it can cool radiatively. As the gas cools and loses support from thermal pressure, it falls into the gravitational potentials of the dark haloes. At the centre of the halo, it forms a rotating disc, and, as it continues to cool, it fragments to form molecular clouds and ultimately stars.

This simple picture of galaxy formation explains how systems of gas and stars are assembled to form the galaxies that we see in the night sky, and it explains the large-scale distribution of galaxies, which follow a ‘Cosmic Web’ of filamentary structures, as observed in deep galaxy surveys. However, there are a wide range of physical processes that complicate this simple picture. For example, as stars form within the galaxy, they inject energy and momentum into the surrounding gas via stellar winds, radiation and supernovae. Additionally, all massive galaxies contain a supermassive black hole (SMBH) at their centre. As the SMBH accretes material, it also releases energy into the surrounding gas. These feedback processes heat and disrupt the gas, and drive outflows that deplete the galaxy’s gas reservoir. They can therefore inhibit further star formation in the galaxy.

On the smallest scales, chemical processes deal with the reactions between ions and molecules. This chemistry can influence galaxy formation in two ways. Firstly, the chemical composition of the gas determines how quickly it can cool, because different chemical species radiate away energy at different rates. This affects the dynamics of galaxy formation, such as how quickly gas cools and falls onto a galaxy to fuel star formation. Secondly, the chemical composition determines the

observable emission that can be seen from the emission lines of individual chemical species. This is important for interpreting observations of these lines, and for comparing our models of galaxy formation to such observations.

The various physical processes involved in galaxy formation cover a wide range of scales, from millions of light-years down to atomic scales. This presents a significant challenge for attempts to model all of these processes self-consistently. One approach that is often employed to model galaxy formation is to use numerical simulations. Due to the complex interplay between the various physical processes involved in galaxy formation across a wide range of scales, this is a computationally demanding problem. Therefore, these simulations are typically run on supercomputers with hundreds or thousands of CPUs.

6.1 This thesis

In this thesis we used numerical simulations to explore the role that chemistry plays in galaxy formation. Simulations of galaxies often assume chemical equilibrium, in other words, that the chemical reactions between ions and molecules have reached an equilibrium or steady state. However, this assumption may not be valid if the physical conditions of the gas are evolving very rapidly. Therefore, for this thesis we have developed a chemical model to follow the non-equilibrium evolution of ions and molecules, and we incorporated this model into hydrodynamic simulations of galaxies.

In **chapter 2** we presented the chemical model that we developed for this thesis. We then applied this model to a range of physical conditions, with different densities, temperatures and UV radiation fields that are typical for the diffuse interstellar medium (ISM), i.e. the diffuse gas within galaxies. To confirm the accuracy of our model, we compared the chemical abundances and the cooling and heating rates in chemical equilibrium to those computed using the photoionisation code `CLOUDY`¹. This latter code uses a much more extensive chemical network than we use in our model, but it only computes abundances in chemical equilibrium, i.e. it does not follow the non-equilibrium evolution. We generally found good agreement between the two models. We also identified the chemical species that are most important for cooling in the range of physical conditions considered here. These include CII, SiII, FeII, OI and H₂.

To explore how non-equilibrium chemistry affects the cooling rate, we then considered idealised scenarios of gas that is cooling at constant density or constant pressure. At high temperatures, above 10⁴ K, non-equilibrium effects suppress the cooling rate, whereas below 10⁴ K the cooling rate is enhanced by up to two orders of magnitude in non-equilibrium. These effects are driven by recombination lags, as it takes a finite time for ions and electrons to recombine as the gas cools, thereby leaving the gas in a more highly ionised state than in equilibrium.

In **chapter 3** we extended our chemical model to account for gas that becomes shielded from the UV radiation, due to intervening gas and dust. We applied this model to one-dimensional photodissociation regions (PDRs), in which a slab of gas

¹<http://nublado.org/>

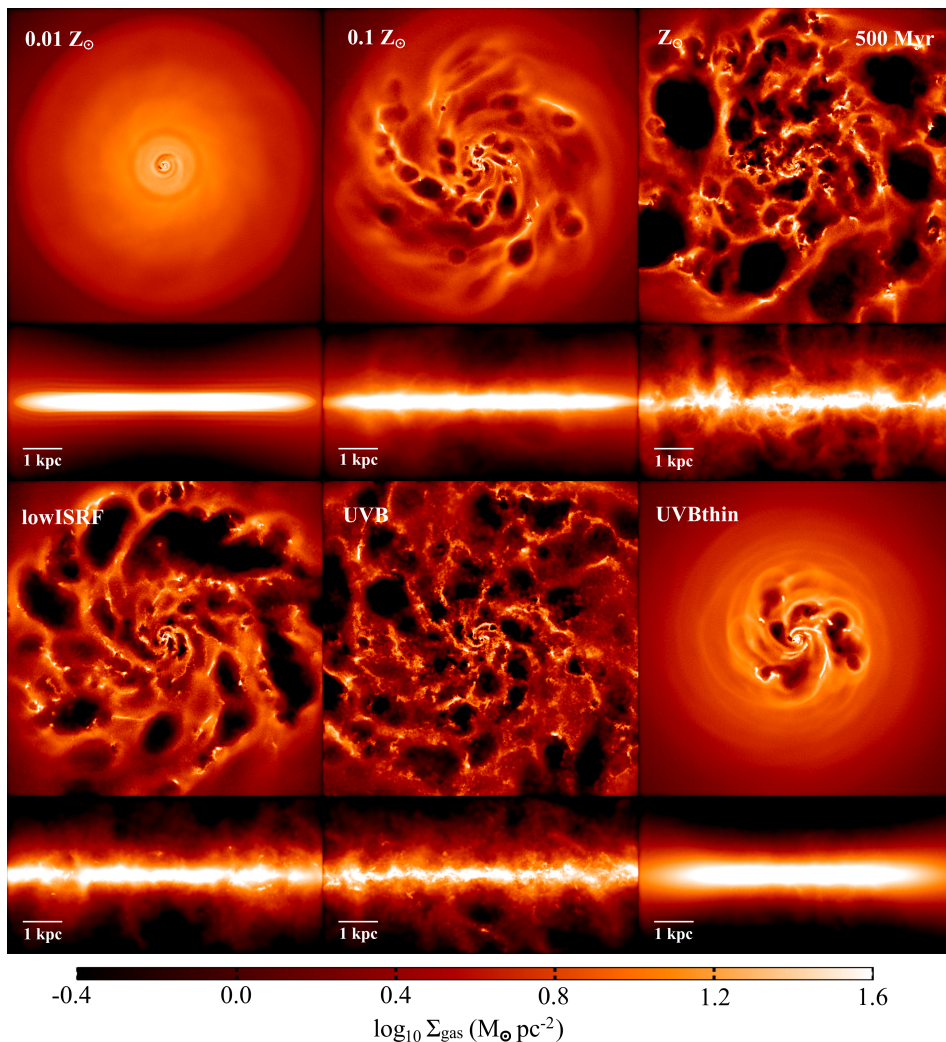


Figure 6.1: Maps of the gas surface density, Σ_{gas} , after 500 million years in the simulations of isolated disc galaxies presented in chapter 4. The top row shows galaxies with three different metallicities: $0.01 Z_{\odot}$ (*left*), $0.1 Z_{\odot}$ (*centre*) and Z_{\odot} (*right*), run with the local interstellar radiation field. The bottom row shows galaxies with a metallicity of $0.1 Z_{\odot}$, but with weaker radiation fields. In *lowISRF* (*left*), the radiation field was reduced by a factor of 10, while *UVB* (*centre*) used the extragalactic UV background, which is weaker by approximately another factor of 10. Finally, in *UVBthin* (*right*) we neglect self-shielding of gas. In each pair of panels we show the disc of the galaxy face-on (*top*) and edge-on (*bottom*).

is irradiated from one side by the interstellar radiation field, and we followed the chemical abundances throughout the cloud, as the UV radiation became absorbed. We then used these to explore the various heating and cooling mechanisms in different regions within the cloud. We also used these to investigate how the transition from atomic to molecular hydrogen depends on the physical conditions

of the cloud. We found that the column density where this transition occurs is lower at higher density and at higher metallicity. This agrees with the results of previous PDR models.

In **chapter 4** we incorporated our chemical model into hydrodynamic simulations of isolated disc galaxies, with an initial stellar mass 10^9 times the mass of the Sun. We ran six simulations with different metallicities (i.e. different proportions of elements heavier than helium) and different UV radiation fields using our full non-equilibrium chemical model (starting from chemical equilibrium at 10^4 K, with hydrogen mostly in HII), and then we repeated these simulations assuming chemical equilibrium. Using this suite of simulations, we explored how the properties of our model galaxies are influenced by metallicity, UV radiation and non-equilibrium chemistry.

Fig. 6.1 shows the gas surface density after 500 million years in the six simulations run with our full non-equilibrium chemical model, for different metallicities (top row) and different UV radiation fields (bottom row). In each pair of panels we show the galaxy disc face-on (top) and edge-on (bottom).

The total star formation rate is higher at higher metallicity and for weaker radiation fields. If the star formation rate is higher, there will be more stellar feedback, for example from supernovae, which heats the gas and drives gas out of the galaxy. We thus see in Fig. 6.1 that the gaseous disc becomes more disrupted at higher metallicity and for weaker radiation fields, as there are more supernovae creating hot bubbles in the disc. The mass outflow rate from the galaxy also increases with increasing metallicity and decreasing UV radiation, due to the increase in stellar feedback.

Unlike the metallicity and radiation field, non-equilibrium chemistry does not strongly influence the total star formation rate or outflow properties of the galaxy. However, it does affect the abundances of individual chemical species. For example, the mass of H_2 in molecular outflows is a factor ≈ 20 higher in non-equilibrium.

We then created maps of the observable line emission from CII and CO from our simulations in post-processing, using the publicly available code `RADMC-3D`². We found that CII and CO emission increases with increasing and decreasing UV radiation, respectively, and both increase with metallicity. Non-equilibrium chemistry generally has no strong effect on the CII emission, whereas it does change the CO emission by a factor of $\approx 2 - 4$ compared to equilibrium.

Finally, in **chapter 5** we focussed on the properties of Giant Molecular Clouds (GMCs) in our simulations. We defined clouds in two ways: firstly, as regions above a density threshold, and secondly, as regions above a CO intensity threshold. The latter definition is closer to how molecular clouds are defined in observations.

We found cloud lifetimes up to ≈ 40 million years, with a median of 13 million years. This is consistent with the lifetimes of observed molecular clouds. We also found similar cloud scaling relations, for example between cloud mass and radius, as seen in observations, although the normalisation of our simulated mass-size relation differed from the observed relation by a factor $2 - 4$, due to different

²<http://www.ita.uni-heidelberg.de/~dullemond/software/radmc-3d/>

cloud definitions.

We considered the molecular fractions of our simulated clouds as a function of cloud age to explore how long it takes for clouds to become fully molecular and reach chemical equilibrium. At ten per cent solar metallicity, the H_2 and CO fractions of clouds reach equilibrium after $\approx 10 - 15$ million years, while at solar metallicity they reach equilibrium within one million years.

We then computed the CO emission from our simulated clouds using RADMC-3D. The CO intensity is strongly suppressed in clouds with low dust extinction, as there is insufficient dust to shield the CO molecule from dissociating radiation. At high dust extinction, the CO intensity possibly saturates, as the CO line becomes optically thick. We also used these CO emission maps to compute the conversion factor, X_{CO} , between CO intensity and H_2 column density in our simulated clouds. This X_{CO} factor is commonly used by observations to infer the H_2 content from CO emission. At ten per cent solar metallicity, X_{CO} decreases with increasing cloud age up to 15 million years, albeit with a large scatter at fixed age, whereas there is no strong trend between X_{CO} and age at solar metallicity.

6.2 Future outlook

The simulations presented in this thesis include one of the most detailed treatments of non-equilibrium chemistry so far used in hydrodynamic simulations on galactic scales. However, they still contain several limitations.

Foremost among these limitations is the lack of a fluctuating UV radiation field due to the evolution and movement of local radiation sources, such as young stars. In our models, we consider a constant, uniform radiation field and apply a prescription for self-shielding by gas and dust. While the shielding of the radiation field does vary, both spatially and temporally, we do not include variations due to the evolving distribution of local sources. If these variations are rapid, on time-scales shorter than the chemical time-scale, then they could drive additional non-equilibrium effects in the chemistry. Furthermore, since the radiation field is not related to the young stars in our simulations, we also miss some feedback effects due to the heating of gas surrounding young stars by the UV radiation emitted by these stars. Additionally, the chemistry of the gas is not directly influenced by local star formation in our simulations, which will have an impact on the observational tracers of star formation. For example, we do not correctly model HII regions, which are regions of ionised gas created by the strong radiation from nearby young stars.

To include these effects in our simulations, we will need to model the evolution of radiation from local sources. This will involve solving the radiative transfer equation, which describes how the radiation propagates through the gas. There are already several numerical methods that are commonly used to solve this problem, which are broadly divided into two categories: ray-tracing methods and moment-based methods. We can then couple the evolving radiation field to our chemical model.

A second limitation of our simulations is that we include only a single, isolated

galaxy. In reality, galaxies form within large-scale structures, such as filaments of gas and dark matter, millions of light years long, that feed new material into the galaxy. Additionally, multiple galaxies can come together and interact or merge. These interactions and mergers disturb the gas within the galaxy, which could potentially drive non-equilibrium effects in the chemistry.

To include these cosmological processes while still maintaining a reasonably high resolution, we can use cosmological zoomed simulations. These start with a low-resolution simulation of a large volume of the Universe and then zoom in on an individual galaxy halo. This halo is then simulated at a much higher resolution, while still keeping the large-scale structure at a low resolution. Another advantage of this approach is that it follows the formation of the galaxy from the early Universe, rather than starting from an idealised model galaxy. We can then explore how the properties of the galaxy change at different epochs throughout the Universe's history, and we can compare these with observations.

Another limitation of our simulations is that they may not have sufficient resolution to follow small-scale turbulence in the ISM. Turbulence can drive non-equilibrium effects in the chemistry if the density and temperature are evolving very rapidly. Therefore, if we are missing small-scale turbulence, we may underestimate the importance of non-equilibrium chemistry. To explore the effects of turbulence on the chemistry, we will need to consider very high-resolution simulations of small regions of the ISM.

Furthermore, the prescription that we use for supernova feedback in our simulations is fairly simplistic. When a supernova explodes in our simulations, we heat neighbouring gas particles by $10^{7.5}$ K, to prevent overcooling. This is necessary at low resolution, but at high resolution we can implement more realistic supernova models.

Another physical process that is missing from our simulations is magnetic fields. This can provide an additional source of pressure that may have an important impact on the evolution of molecular clouds.

Addressing the above limitations will require additional computational expense (to include radiative transfer and magnetic fields, to add large-scale structure, and to use higher resolution). However, the non-equilibrium chemistry is already a computationally demanding task. For example, in the simulations presented in chapter 4, $\approx 90 - 95$ per cent of the CPU time was spent integrating the chemistry. Therefore, we need to consider how to speed up the chemistry solver.

One option is to reduce the size of the chemical network under certain physical conditions. Our chemical model spans a wide range of temperatures and densities, from cold, molecular gas to hot, highly ionised gas. It therefore includes many chemical species (157 in total). However, not all of these species will be important at any given time. Therefore, we could limit the network to only those species that are important given the current physical conditions. Another option is to determine if the chemical abundances are in equilibrium and are likely to remain in equilibrium as the gas cools. We can then switch off the chemistry solver and evolve the temperature of that particular gas particle or cell in chemical equilibrium, which is much faster. However, both of these options involve computational overheads. For example, for each gas particle or cell, we need to determine which

species to include, or whether the abundances are in equilibrium. These overheads may negate any potential speed up.

Finally, we saw in chapter 4 that the non-equilibrium chemistry has no strong effect on the dynamics of the galaxy, such as the total star formation rate. Instead, it is primarily important for observational diagnostics, particularly CO emission and molecular outflows. Therefore, we could evolve most of the simulation in equilibrium, and only use non-equilibrium chemistry for a short period of time at the end. This would greatly reduce the computational cost while still capturing the main non-equilibrium effects that we are interested in.

NEDERLANDSE SAMENVATTING

Sterrenstelsels zijn gravitationeel gebonden objecten bestaande uit gas en sterren, die zijn ingebed in grootschalige halo's van 'donkere materie', een vorm van materie die geen licht uitzendt en alleen interactie heeft via de zwaartekracht. De vorming en evolutie van sterrenstelsels is een interessante tak van onderzoek, die in de afgelopen decennia grote vooruitgang heeft geboekt.

Binnen onze huidige visie op de vorming van sterrenstelsels vormt donkere materie het grootste deel van alle materie in het Universum en bepaalt daarmee in hoge mate hoe de materie op grote schaal gestructureerd is. Omdat donkere materie alleen interactie heeft via de zwaartekracht, is deze dissipatieloos, wat betekent dat deze vorm van materie niet kan afkoelen en geen energie uitstraalt. Wanneer donkere materie onder de invloed van de zwaartekracht samentrekt, vormt het daarom uitgestrekte, overwegend sferische, halo's. Gas kan daarentegen wel energie uitstralen en is dus in staat om af te koelen. Naarmate gas afkoelt en de thermische druk in het gas afneemt, trekt het samen onder de invloed van de zwaartekracht die wordt uitgeoefend door de structuren van donkere materie. In het centrum van een donkere halo vormt het gas vervolgens een roterende schijf, waarin, naarmate het gas nog meer afkoelt, moleculaire wolken en uiteindelijke sterren ontstaan.

Deze eenvoudige voorstelling van de vorming van sterrenstelsels verklaart hoe uit gas en sterren de sterrenstelsels zijn gevormd die we nu aan de nachtelijk hemel zien. Het verklaart ook de verdeling van sterrenstelsels op grote schaal, het zogenaamde 'kosmische web', zoals we dat afleiden uit waarnemingen van het nabije en verre heelal. Er zijn echter een aantal fysische processen die deze simpele voorstelling gecompliceerder maken. Zo vindt er tijdens de evolutie van sterren binnen een sterrenstelsel overdracht plaats van energie en impuls naar het omringende gas. Dit gebeurt via stellaire winden, straling en supernovaexplosies. Bovendien bevindt zich in alle massieve sterrenstelsels een supermassive zwart gat (SMBH) in het centrum. Zwarte gaten trekken materie aan en stralen daarbij ook energie uit naar het omringende gas. Dergelijke processen, die we feedback-processen noemen, zorgen voor verhitting en verstoringen in het gas, waarbij ze galactische winden kunnen veroorzaken die het gasreservoir van het sterrenstelsel uitputten. Feedback-processen kunnen daardoor tot gevolg hebben dat een sterrenstelsel geheel stopt met het vormen van sterren.

Op de kleinste schalen binnen sterrenstelsels vinden reacties tussen ionen en moleculen plaats. Deze chemische processen kunnen de vorming van sterrens-

telsels op twee manieren beïnvloeden. Ten eerste bepaalt de chemische compositie van het gas hoe snel het afkoelt, doordat verschillende soorten deeltjes met verschillende snelheden hun energie uitstralen. Dit heeft effect op de dynamica van het gas in en rondom sterrenstelsels, bijvoorbeeld op de snelheid waarmee het gas afkoelt en neerdaalt op het sterrenstelsel. Ten tweede bepaalt de chemische compositie de sterkte van de verschillende emissielijnen die we van sterrenstelsels waarnemen. Dit is een belangrijk gegeven voor zowel de interpretatie van observaties van galactische emissielijnen, als voor vergelijkende studies tussen dergelijke observaties en modellen voor de vorming van sterrenstelsels.

De verschillende fysische processen die een rol spelen in de vorming van sterrenstelsels beslaan een groot bereik aan schalen, variërend van miljoenen lichtjaren tot de kleinste atomaire schalen. Dit betekent dat we voor een enorme uitdaging staan om al deze processen te modelleren op een manier die 'zelfconsistent' is. Een veelvoorkomende benadering is het gebruik van numerieke simulaties. Door de complexe wisselwerking tussen de verschillende fysische processen die op uiteenlopende schalen een rol spelen, is dit echter, rekenkundige gezien, een veeleisend probleem. Dit is de reden dat bij het draaien van deze simulaties meestal gebruikt wordt gemaakt van supercomputers met honderden of duizenden CPU's.

Dit proefschrift

In dit proefschrift maken we gebruik van numerieke simulaties om de rol van chemie in de vorming van de sterrenstelsels te bestuderen. In simulaties van sterrenstelsels wordt doorgaans aangenomen dat alle materie zich in een chemisch evenwicht bevindt, wat wil zeggen dat de chemische reacties tussen ionen en moleculen een evenwicht of rusttoestand hebben bereikt. Dit is echter niet noodzakelijk een geldige aanname wanneer de fysische toestand van het gas snel verandert. Wij hebben daarom voor dit proefschrift een chemisch model ontwikkeld voor de evolutie van ionen en moleculen terwijl deze zich niet in evenwicht bevinden, en dit geïmplementeerd in hydrodynamische simulaties van sterrenstelsels.

In **hoofdstuk 2** presenteren we het chemische model dat we voor dit proefschrift hebben ontwikkeld. We passen het model vervolgens toe op verschillende fysische condities, variërend in dichtheid, temperatuur en UV-stralingsveld, zoals die zich voordoen in het diffuse interstellair medium (ISM) van sterrenstelsels. Om na te gaan hoe nauwkeurig ons model is, vergelijken we de chemische abundanties en de snelheden waarmee gas afkoelt en opwarmt zoals gegeven door ons model in de evenwichtssituatie met de waarden berekend met de fotoionisatiecode CLOUDY³. Deze code maakt gebruik van een chemisch netwerk dat weliswaar omvangrijker is dan wat wij gebruiken in ons model, maar het berekent de abundanties alleen in de evenwichtssituatie. In het algemeen komen beide modellen in deze situatie goed overeen. We onderzoeken in dit hoofdstuk ook welke chemische deeltjes het belangrijkste zijn voor de koeling van gas in de verschillende fysische condities waarop we ons model toepassen. Dit zijn onder andere CII, SiII, FeII, OI en H₂.

³<http://nublado.org/>

Om te onderzoeken wat voor effect een niet-evenwichtsstoestand heeft op de snelheid waarmee het gas afkoelt, bekijken we verschillende geïdealiseerde scenario's van gas dat afkoelt bij ofwel een constante dichtheid ofwel een constante druk. Bij hoge temperaturen, boven de 10^4 K, daalt deze snelheid, terwijl bij temperaturen onder de 10^4 K de snelheid juist toeneemt, tot wel twee ordes van grootte groter dan in de evenwichtssituatie. Deze effecten worden voornamelijk veroorzaakt doordat de recombinatie van ionen en elektronen achterblijft ten opzichte van de koeling van het gas, waardoor het gas zich in een hogere ionisatietoestand bevindt dan wanneer het in evenwicht zou zijn.

In **hoofdstuk 3** breiden we ons chemisch model uit om ook rekening te houden met het gas dat wordt afgeschermd van UV-straling door tussenliggend gas en stof. We passen dit model toe op ééndimensionale fotodissociatieregio's (PDRs), waarbij een gaswolk van één kant bestraald wordt door een interstellair stralingsveld, en we volgen hoe de chemische abundanties door de gaswolk heen veranderen naarmate de UV-straling wordt geabsorbeerd. We gebruiken deze vervolgens om de verschillende verhittings- en koelingsmechanismen in de verschillende regio's binnen de wolk te bestuderen en om te onderzoeken hoe de transitie van atomair naar moleculair waterstof afhangt van de fysische condities in de wolk. We vinden dat de kolomdichtheid waarbij deze transitie plaatsvindt, lager is als de dichtheid of de metalliciteit hoger is. Dit komt overeen met eerdere bevindingen van PDR-modellen.

In **hoofdstuk 4** implementeren we ons chemisch model in hydrodynamische simulaties van geïsoleerde schijfstelsels met een initiële massa van 10^9 maal de massa van de zon. We draaien zes simulaties met verschillende metalliciteiten (d.w.z. verschillende massafracties van elementen zwaarder dan helium) en verschillende UV-stralingsvelden, waarbij we gebruik maken van ons volledige chemische model zonder de aanname van chemisch evenwicht te maken. Vervolgens herhalen we deze simulaties waarbij we wel uitgaan van een chemisch evenwicht. Aan de hand van deze sets van simulaties onderzoeken we hoe de eigenschappen van onze modelsterrenstelsels worden beïnvloed door de metalliciteit, de UV-straling en de chemische toestand van niet-evenwicht.

Fig. 7.1 toont de oppervlakedichtheid van het gas na 500 miljoen jaar in de zes simulaties die we gedraaid hebben met ons chemisch model (zonder de aanname van chemisch evenwicht te maken), waarbij we de resultaten voor verschillende metalliciteiten (bovenste rij) en verschillende UV-stralingsvelden (onderste rij) laten zien. We laten hierbij steeds de schijf van het stelsel van voren (bovenste paneel) en van de zijkant (onderste paneel) zien.

De snelheid waarmee sterren gevormd worden is groter bij een hogere metalliciteit en bij een zwakker stralingsveld. Wanneer deze snelheid groter is, is er ook meer feedback van stervorming, bijvoorbeeld van supernova's, waarbij het gas wordt verhit en uit het sterrenstelsel wordt geblazen. We tonen dan ook in Fig. 7.1 dat er bij een hogere metalliciteit of een zwakker stralingsveld meer verstoringen plaatsvinden in de gasschijf, omdat er door het toegenomen aantal supernovaexplosies meer hete gasbellen in de gasschijf worden geblazen. De uitstroom van massa uit het sterrenstelsel neemt daarom ook toe bij een hogere metalliciteit of zwakkere UV-straling als gevolg van de toename van de stellaire feedback.

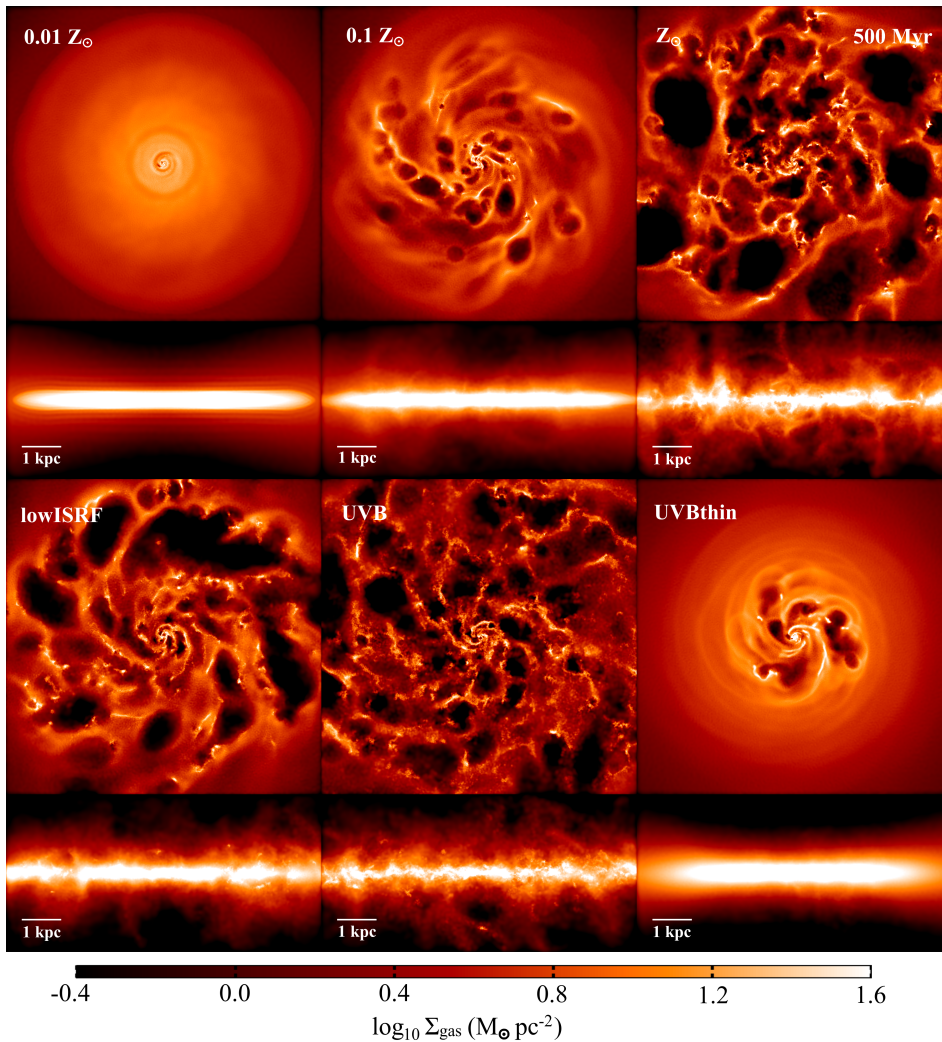


Figure 7.1: De oppervlakedichtheid, Σ_{gas} , van het gas na 500 miljoen jaar in de simulaties van geïsoleerde schijfstelsels uit hoofdstuk 4. De bovenste rij laat sterrenstelsels met drie verschillende metalliciteiten zien: $0.01Z_{\odot}$ (links), $0.1Z_{\odot}$ (midden) en Z_{\odot} (rechts). Hierbij is steeds dezelfde waarde van het lokale interstellaire stralingsveld aangenomen. De onderste rij laat sterrenstelsels zien met een metalliciteit van $0.1Z_{\odot}$, waarbij de sterkte van het stralingsveld wordt gevarieerd. In lowISRF (links) is de sterkte van het stralingsveld een factor 10 lager ten opzichte van de bovenste rij. In UVB (midden) is een stralingsveld aangenomen dat gelijk is aan die van de extragalactische UV-achtergrondstraling. Deze is nogmaals een factor 10 lager. Ten slotte is in UVBthin (rechts) aangenomen dat er geen afscherming van de UV-straling in het gas plaatsvindt. In elke twee panelen van deze figuur laten we de schijf van het sterrenstelsel zowel van voren (bovenste paneel) als van de zijkant (onderste paneel) zien.

Het feit dat het gas zich chemisch gezien niet in een evenwichtstoestand bevindt

heeft daarentegen weinig effect op de snelheid van de stervorming of de eigenschappen van de uitstroom van massa uit het sterrenstelsel. Het heeft echter wel effect op de abundanties van de afzonderlijke chemische deeltjes. Zo is de massa van H_2 in moleculaire uitstromen een factor ≈ 20 hoger dan in de evenwichtstoestand.

We brengen ook in kaart hoe sterk de waarneembare lijnemissie afkomstig van CII en CO is in onze simulaties. We doen dit in ‘post-processing’ (d.w.z. na het draaien van de simulatie) met de openbaar beschikbare code RADMC-3D⁴. We vinden dat de CII- en CO-emissie toeneemt naarmate de UV-straling respectievelijk toe- en afneemt en beide soorten emissie nemen toe naarmate de metalliciteit toeneemt. Het feit dat het gas niet in chemisch evenwicht verkeert heeft in het algemeen weinig op de CII-emissie, maar zorgt aan de andere kant wel voor een toename van de CO-emissie van een factor $\approx 2 - 4$ ten opzichte van de evenwichtstoestand.

In **hoofdstuk 5** richten we ons ten slotte op de eigenschappen van moleculaire reuzenwolken (GMC’s) in onze simulaties. We definiëren dergelijke wolken op de volgende twee manieren: als regio’s boven een bepaalde dichtheidsgrens en als regio’s boven een bepaalde CO-intensiteitsgrens. De tweede definitie komt hierbij het meest in de buurt van de definitie die gebruikt wordt in observaties.

We vinden dat de moleculaire wolken leeftijden kunnen hebben van wel ≈ 40 miljoen jaar, met een mediaan van 13 miljoen jaar. Dit komt overeen met de leeftijden van moleculaire wolken die men doorgaans vindt in observaties. Ook vinden we correlaties tussen de eigenschappen van deze wolken, zoals de correlatie tussen massa en radius, die vergelijkbaar zijn met die in de waarnemingen. De normalisatie van de relatie tussen massa en radius verschilt echter wel een factor $2 - 4$ van de waarnemingen. Dit komt doordat de gehanteerde definitie van een moleculaire reuzenwolk enigszins verschillend is.

Om te onderzoeken hoe lang het duurt voor een wolk volledig moleculair wordt en een toestand van chemisch evenwicht bereikt, kijken we naar de moleculaire fractie van onze gesimuleerde wolken als functie van hun leeftijd. Bij een metalliciteit die gelijk is aan 10 procent van die van de zon, bereiken de H_2 - en CO-fracties na $\approx 10 - 15$ miljoen jaar een evenwicht, terwijl ze bij een metalliciteit gelijk aan die van de zon binnen één miljoen jaar al een evenwicht bereiken.

Vervolgens gebruiken we RADMC-3D om de CO-emissie van onze gesimuleerde wolken te berekenen. We vinden dat de CO-intensiteit aanzienlijk lager is in wolken met weinig stof, doordat de CO-moleculen onvoldoende worden afgeschermd van straling die ervoor zorgt dat de moleculen worden ontleed. Als er wel veel stof aanwezig is, is het mogelijk dat er saturatie van de CO-emissie plaatsvindt wanneer de CO-emissielijn ‘optisch dik’ wordt. We gebruiken de in kaart gebrachte CO-intensiteit ook om de conversiefactor, X_{CO} , tussen de CO-intensiteit en de H_2 -kolomdichtheid in onze simulaties te bepalen. Deze X_{CO} -factor wordt doorgaans gebruikt in observaties om aan de hand van de waargenomen CO-emissie de hoeveelheid aanwezig H_2 te berekenen. Bij een metalliciteit gelijk aan 10 procent van die van de zon neemt X_{CO} af naarmate de leeftijd van de wolk toeneemt, een

⁴<http://www.ita.uni-heidelberg.de/~dullemond/software/radmc-3d/>

trend die doorzet tot een leeftijd van 15 miljoen jaar. De spreiding in X_{CO} bij een constante leeftijd is hierbij echter groot. Bij een metalliciteit gelijk aan die van de zon bestaat er daarentegen geen sterke relatie tussen X_{CO} en de leeftijd van de wolk.

Vooruitzichten

De simulaties die we voor dit proefschrift gebruiken, bevatten één van de meest gedetailleerde chemische modellen van niet-evenwicht dat tot dusver is gebruikt in hydrodynamische simulaties van sterrenstelsels. Toch bevat ook dit model nog enkele beperkingen.

De voornaamste beperking is het gebrek aan een fluctuerend UV-stralingsveld als gevolg van het feit dat lokale stralingsbronnen, zoals jonge sterren, veranderen en zich verplaatsen. Onze modellen bevatten een constant, uniform stralingsveld met daarbij een speciale aanpassing van het model wanneer het gas wordt afgeschermd van de straling door tussenliggend gas en stof. Ondanks dat deze afscherming van het stralingsveld varieert in zowel plaats als tijd, houden we in onze simulaties geen rekening met de verandering in de verdeling van lokale stralingsbronnen. In het geval dat de variaties plaatsvinden op tijdschalen korter dan de chemische tijdschaal, is het mogelijk dat ze voor extra verstoringen van het chemisch evenwicht zorgen. Bovendien is in onze simulaties het stralingsveld niet direct gerelateerd aan jonge sterren, waardoor we wellicht de feedback-effecten niet meenemen die worden veroorzaakt doordat jonge sterren het omringende gas verhitten met hun UV-straling. Daarnaast heeft de lokale stervorming in onze simulaties niet direct invloed op de chemische toestand van het gas, iets wat men wel zou vinden in observaties. Dit betekent dat onze gesimuleerde HII-regio's niet volledig realistisch zijn, doordat deze regio's in werkelijkheid ontstaan als gevolg van de sterke straling van nabije jonge sterren.

Om dergelijke effecten wel mee te nemen in de simulaties, zullen we de verdeling en evolutie van lokale stralingsbronnen moeten modelleren. Dit houdt in dat we de vergelijking voor stralingstransport zullen moeten oplossen: deze beschrijft hoe straling zich voortplant door een gas. Er bestaan echter al verschillende numerieke methoden die een oplossing voor dit probleem bieden. Deze zijn onder te verdelen in de volgende twee categorieën: 'ray-tracing' methoden en 'impulsgebaseerde' methoden. Door gebruik te maken van dergelijke methoden kunnen we het veranderende stralingsveld koppelen aan ons chemisch model.

Een tweede beperking van onze simulaties is het feit dat we alleen een enkel, geïsoleerd sterrenstelsel beschouwen. In werkelijkheid vormen sterrenstelsels alles behalve geïsoleerd. Ze vormen binnen de grootschalige structuur van het kosmisch web, bestaande uit filamenten van gas en donkere materie die zorgen voor de aanvoer van nieuw gas naar de sterrenstelsels. Hierin is het bovendien mogelijk dat meerdere sterrenstelsels zo dichtbij bij elkaar komen dat er interactie plaatsvindt of dat ze samenvoegen. Dergelijke processen zorgen voor verstoringen in het gas en zo mogelijk voor verstoringen van het chemisch evenwicht.

Om zowel de kosmologische processen te modelleren alsook voldoende hoge resolutie in onze simulaties te behouden, kunnen we gebruik maken van kosmol-

ogische ‘zoom’-simulaties. Bij het draaien van deze simulaties starten we op lage resolutie, waarbij we een groot volume van het universum modelleren, en zoomen we daarna in op een enkele galactische halo. Deze halo wordt vervolgens gesimuleerd bij een veel hogere resolutie, terwijl de structuur van het universum op grote schaal op de lagere resolutie blijft. Een bijkomend voordeel van deze benadering is dat het mogelijk is om de vorming van een sterrenstelsel al vanaf het vroege universum te volgen in plaats van op een later tijdstip te starten met een geïdealiseerd model van een sterrenstelsel. Dit betekent dat we de eigenschappen van sterrenstelsels op verschillende momenten in de geschiedenis van het universum kunnen onderzoeken en deze kunnen vergelijken met de waarnemingen.

Een andere beperking van onze simulaties is het feit dat ze waarschijnlijk onvoldoende resolutie hebben om de turbulentie in het interstellair medium op kleine schaal te volgen. Dergelijke turbulentie kan leiden tot verstoringen in het chemisch evenwicht als de dichtheid en temperatuur snel veranderen. Wanneer we deze turbulentie op kleine schaal meenemen in ons model, kan het daarom zijn dat we het belang onderschatten van het modelleren van gas buiten de chemische evenwichtssituatie. Om een goed beeld te krijgen van de effecten van turbulentie op de chemische gastoestand, zullen we gebruik moeten maken van simulaties die kleine regio’s van het interstellair medium simuleren met een hele hoge resolutie.

Om de bovengenoemde beperkingen van de huidige simulaties aan te pakken is meer computerkracht nodig (om het stralingstransport door te rekenen, om de grootschalige structuur van het heelal te simuleren en om gebruik te kunnen maken van een hogere resolutie). Het simuleren van de chemische gastoestand buiten chemisch evenwicht is echter al een, rekenkundig gezien, veeleisend probleem. Zo is voor de simulaties van hoofdstuk 4 $\approx 90 - 95$ procent van de CPU-tijd gebruikt voor het doorrekenen van de chemische gastoestand. Het is daarom noodzakelijk om te bekijken hoe dergelijke berekeningen sneller of efficiënter kunnen worden gemaakt.

Een mogelijke oplossing is om het netwerk van chemische reacties onder bepaalde fysische omstandigheden kleiner te maken. Ons chemisch model is toepasbaar op een groot bereik aan temperaturen en dichtheden, variërend van koud, moleculair gas tot heet, geïoniseerd gas. Het bevat daarom een groot aantal chemische deeltjes (157 in het totaal). Deze deeltjes zijn echter niet altijd even belangrijk voor de chemische toestand van het gas. Het uitsluiten van bepaalde deeltjes van de berekeningen in bepaalde fysische omstandigheden is daarom een manier om de grootte van het chemisch netwerk enigszins te beperken. Een andere manier is om op een gegeven tijd te bepalen of het gas in chemisch evenwicht is en dat waarschijnlijk, naarmate het afkoelt, ook zal blijven. Dan kunnen we vanaf dat moment de berekeningen met het volledige chemische model in het betreffende gasdeeltje of de betreffende gascel stopzetten en de verandering van de temperatuur slechts doorrekenen aan de hand een chemisch evenwichtsmodel. Dit zou veel sneller zijn dan de oorspronkelijke berekening. Beide opties vereisen echter wel extra rekenkracht, waardoor de verwachte snelheidstoename van de berekeningen kan tegenvallen. Zo moet in elk gasdeeltje of elke gascel worden gekeken welke chemische deeltjes moeten worden meegenomen in de berekeningen en of hun abundanties in chemisch evenwicht zijn of niet.

Ten slotte laten we in hoofdstuk 4 zien dat afwijkingen van het chemisch evenwicht weinig effect hebben op de dynamische eigenschappen van een sterrenstelsel, zoals de snelheid waarmee sterren gevormd worden. Deze afwijkingen zijn daarentegen wel belangrijk voor een aantal grootheden die we direct kunnen vergelijken met de observaties, in het bijzonder de CO-emissiesterkte en moleculaire uitstromen. We zouden daarom het grootste deel van de simulatie in de evenwichtstoestand kunnen draaien en alleen voor een korte tijdsperiode aan het einde van de simulatie de volledige chemische gastoestand kunnen doorrekenen, zonder daarbij een chemisch evenwicht aan te nemen. Op deze manier zou zowel de benodigde rekenkracht worden beperkt alsook de effecten van het feit dat het gas zich niet in de evenwichtstoestand bevindt, worden doorgerekend.

PUBLICATIONS

1. *The effects of metallicity, UV radiation and non-equilibrium chemistry in high-resolution simulations of galaxies*
A. J. Richings & J. Schaye
2015, arXiv:1506.08829, submitted to MNRAS
2. *Non-equilibrium chemistry and cooling in the diffuse interstellar medium - II. Shielded gas*
A. J. Richings, J. Schaye & B. D. Oppenheimer
2014, MNRAS, 442, 2780
3. *Non-equilibrium chemistry and cooling in the diffuse interstellar medium - I. Optically thin regime*
A. J. Richings, J. Schaye & B. D. Oppenheimer
2014, MNRAS, 440, 3349
4. *The connection between radio loudness and central surface brightness profiles in optically selected low-luminosity active galaxies*
A. J. Richings, P. Uttley & E. Körding
2011, MNRAS, 415, 2158
5. *The hot interstellar medium of the interacting galaxy NGC 4490*
A. J. Richings, G. Fabbiano, J. Wang & T. P. Roberts
2010, ApJ, 723, 1375
6. *Field and globular cluster low-mass X-ray binaries in NGC 4278*
G. Fabbiano, N. J. Brassington, L. Lentati, L. Angelini, R. L. Davies, J. Gallagher, V. Kalogera, D.-W. Kim, A. R. King, A. Kundu, S. Pellegrini, **A. J. Richings**, G. Trinchieri, A. Zezas & S. Zepf
2010, ApJ, 725, 1824

CURRICULUM VITAE

I was born on 29th June 1988 in Huntingdon, UK. I completed my pre-university education at Tavistock Sixth Form College in July 2006, with A-levels in Physics, Chemistry, Maths, Further Maths and Critical Thinking, and Advanced Extension Awards (AEAs) in Physics, Chemistry and Maths.

I started a four year undergraduate Master of Physics (M.Phys) course in Astrophysics at the University of Southampton in September 2006. During this time I had several opportunities to experience research in astronomy. In the summer of 2008 I undertook a research project with Dr. Phil Uttley at the University of Southampton, on *the connection between radio loudness and central surface brightness profiles in optically selected low-luminosity active galaxies*. This research was funded by a Nuffield Foundation undergraduate research bursary. For the final year of my degree I moved to the US to conduct a research project with Dr. Giuseppina Fabbiano at the Harvard-Smithsonian Center for Astrophysics, on *the hot interstellar medium of the interacting galaxy NGC 4490*. I graduated with first class honours in July 2010.

I then moved on to study for a Master of Advanced Studies (MASt) degree in Applied Mathematics at the University of Cambridge in October 2010. I graduated with distinction in July 2011.

In September 2011 I moved to the Netherlands to start a Ph.D. position at Leiden Observatory, under the supervision of Prof. dr. Joop Schaye. For my Ph.D. project, I worked on developing hydrodynamic simulations of galaxies, with a particular focus on modelling the non-equilibrium chemistry of ions and molecules in these simulations. During the course of my Ph.D. I presented my work at conferences and workshops in the Netherlands, Germany, the UK, Italy and Switzerland. I also attended the Jerusalem Winter School in January 2013, and the 43rd Saas-Fee Advanced Course in Switzerland in March 2013.

In January 2016 I will move to the US to start a Lindheimer fellowship at Northwestern University.

ACKNOWLEDGMENTS

I am very grateful to everyone who has helped and supported me throughout the course of my Ph.D., and have made this thesis possible.

Firstly, I would like to thank Joop for hiring me and giving me the opportunity to study here in Leiden, and for all of the help and support that you have given me over the last four years. I would also like to thank all of the members of Joop's group, both past and present: Ali, Antonella, Bart, Ben, Chris, Fabian, Freeke, Geert Jan, Gunjan, Joki, Jorryt, Lorrie, Marcel, Marco, Marijke, Milan, Monica, Paula, Rob and Sylvia, thank you for making our weekly group and preprint meetings so enjoyable! Ben, thank you for all of your support throughout my Ph.D. and for your advice when I was applying for postdoc positions, and thank you for showing me around Boulder! Marijke, thank you for translating my thesis summary into Dutch. Also, special thanks to my office mates, Marco and Monica, for making our office such a fun place to work!

I would also like to thank everyone at the Sterrewacht for creating such a fun, lively and sociable atmosphere, whether it was during coffee breaks, at the weekly borrel, or at the many parties and trips that were organised outside of work: thanks to Alex, Andra, Berenice, Bernard, Bram, Carl, Caroline, Christian, David, Emanuele, Fabian, Francisco, Gleb, Gerard, Heather, Henriette, Irene, Jeroen, Jesse, Leah, Luke, Maria, Marissa, Maryam, Mattia, Matteo, Mayuresh, Sebastiaan, Steven, Tiffany, Tim, Wendy and Willem, and to anyone else that I have forgotten!

Finally, I would like to say a very special thank you to Mum, Dad, Ollie, my grandparents and my whole family. You have always supported me and encouraged me to pursue my dreams, and I could not have done this without you.

